Mechanical modeling of superconducting cables for fusion under cyclic electromagnetic and thermal loads

Rebecca Riccioli

NNT/NL: 2021AIXM0657/042ED353

Ph.D. thesis

Defended at Aix-Marseille University
In co-supervision with University of Bologna
the 21st of December 2021 by

Rebecca Riccioli

Mechanical modeling of superconducting cables for fusion under cyclic electromagnetic and thermal loads

Discipline
Engineering sciences

Specialty
Solid mechanics

Ph.D. school
ED-353 Engineering sciences: Mechanics, Physics, micro and nano electronics

Laboratories/Partners
ASSYSTEM (France)

Jury composition

Laurent ORGEAS CNRS, Grenoble (FR)	Reviewer
Pasquale FABBRICATORE INFN, Genova (IT)	Reviewer
Damien DURVILLE CNRS, University of Paris-Saclay (FR)	Internal examiner
Laura SAVOLDI Politecnico di Torino (IT)	External examiner
Frédéric LEBON Aix-Marseille University (FR)	Ph.D. director
Marco BRESCHI University of Bologna (IT)	Ph.D. co-director
Alexandre TORRE CEA Cadarache (FR)	CEA supervisor
Neil MITCHELL ITER Organization	Invited
Arend NIJHUIS University of Twente	Invited

CONTENTS

ACKNOWLEDGMENT

Vorrei ringraziare nella mia lingua madre, ossia l'italiano, tutti coloro che hanno fatto parte di questo percorso. Un cammino, non solo di crescita professionale, ma anche di crescita personale. Sono grata per aver avuto l'opportunità di svolgere un eccelente lavoro di ricerca, il cui risultato é stato frutto di molteplici collaborazioni internazionali con entità di rilievo della comunità dei superconduttori. Sono inoltre grata al CEA per avermi ospitato durante il dottorato e alla Francia in generale, un Paese meraviglioso che ho potuto chiamare casa in questi tre anni.

Ringrazio innanzitutto i membri della commissione e in particolar modo i revisori del mio elaborato, Pasquale Fabbricatore e Laurent Orgéas, che hanno senz'altro contribuito al miglioramento della qualità del mio manuscritto. Ringrazio i miei due direttori di dottorato, Marco Breschi e Frédéric Lebon, e tutto il team composto da Alexandre Torre, Damien Durville e Louis Zani, che ha supervisionato e guidato il mio lavoro passo dopo passo, aiutandomi a crescere come ricercatrice.

Grazie a tutte le collaborazioni con laboratori esterni. Grazie a Pierre Manil, Christophe Mayri, David Vincent del CEA di Saclay. Grazie al LMA e in particolar modo a Frédéric e Joseph Moysan. Un enorme grazie a Véronique Aubin per i molteplici scambi e all'infinito supporto a distanza di Gilles Lenoir. Grazie al team del LIMSA e in particolare a Pier Luigi Ribani. Grazie anche alle collaborazioni con ITER e in particolare a Vladimir Tronza.

Ringrazio tutti i componenti fondamentali dell'IRFM che mi hanno aiutato giorno dopo giorni con i mille problemi tecnici che ho dovuto affrontare. Un grazie speciale a Ludovic Allegretti, Evelyne, Anne Coquillat, Sylvie Gibert, Christophe Roux.

Ringrazio inoltre tutto il gruppo GAIM-CRYO che é sempre stato pronto ad aiutarmi con consigli e/o supporto tecnico: Patrick Decool, Clément, Guilaume Jiolat, Valérie, Sévèrine, Gilles Gros, Daniel Cyazinski, Benoit, Sylvie Nicollet, Jérémy, Sylvain Girard, Manu, Patrick Prochet, Luca, Denis Arrend, Maxime Chiletti, Patrick Hartout, Pascal, Jean-Louis, Pierre, Cedric, Eric. Un grazie a Eric, David et Denis per le uscite e le risate, nella speranza di poter ritrovarci a ridere ancora insieme.

Grazie a tutti gli amici vecchi e nuovi che mi sono stati vicino in questo viaggio. Grazie al gruppo degli italiani del CEA che mi ha consentito di sentire un po' di calore dall'Italia. Grazie alle splendide amicizie che ho creato in Francia: Matteo, Carla, Ilaria, Eszter, Floriane, Valeria, Veronica. E grazie a tutte quelle persone del mio passato che conitnuano a battersi al mio fianco giorno dopo giorno: Silvia, Marianna, Francesca, Midori, Valentina, Elena.

Ringrazio inoltre di cuore Stéphanie, Alexandre Louzguiti, Denis Guibert, Daniela e Alexis per essere stati parte della famiglia che mi sono creata in Francia e per non avermi mai fatto sentire sola nel momento del bisogno.

Infine ringrazio la mia famiglia in Italia, mamma Nicoletta, Angelo e Riccardo, che mi ha permesso di spiegare le ali e prendere il volo, non avrei potuto essere più fortunata. Ma grazie anche a zii Carla e Beppe, Thomas e Monica, nonna Sandra per essere sempre stati parte del mio percorso e della mia vita e ovviamente grazie al mio compagno Michele che mi é stato vicino in questi ultimi anni di dottorato.

E' difficile riassumere tutto l'amore e il supporto che ho ricevuto in più di tre anni di vita in Francia, ma resta sempre in me la consapevolezza che questa tesi é il risultato di chi sono oggi grazie a tutti voi.

LIST OF ABBREVIATIONS

AC	Alternating Current
BC(s)	Boundary Condition(s)
BCS	Bardeen Cooper Schrieffer
BEAS	Bruker EAS GmbH
BR	Bronze Route
CC	Correction Coil
CD	Cool-Down
CEA	*Commissariat à l'Energie Atomique*
CICC, CICCs	Cable-In-Conduit-Conductor(s)
CNRS	*Centre Nationale de la Recherche Scientifique*
CPM	Cumulative Polar Map
CS	Central Solenoid
DTT	Divertor Tokamak Test
ECS	*Ecole Centrale Supélec*
EM	ElectroMagnetic
EMP	ElectroMagnetic Peak
EMR	ElectroMagnetic Release
EPSIC	Experimental Protocol to measure Strands In Compression
FBM	Fully Bonded Model
FC	Friction Coefficient
FE	Finite Element(s)
F4E	Fusion 4 Energy
FM	Fluid Model
GAIM	*Group* AIMants
HFZ	High Field Zone
HRL	High Resistivity Limit
HT	Heat Treatment
HTS	High Temperature Superconductor
IO	International Organization
IT	Internal Tin
ITER	International Thermonuclear Experimental Reactor
ITSCOTT	Internal Tin Superconductors Tensile Tests
JET	Joint European Torus
JT-60SA	Japanese Tokamak Super Advanced
LCSE	*Laboratoire de Cryogénie et des Stations d'Essais*
LHC	Large Hadron Collider
LHe	Liquid Helium
LMA	*Laboratoire de Mécanique et Acoustique*

LN_2	Liquid Nitrogen
LRL	Low Resistivity Limit
LTS	Low Temperature Superconductor
LTP	Long Twist Pitch
MULTIFIL	MULTIFIL-aments
MUNDA	MUltifil Numerical Dataset Analysis
NDT	Non-Destructive Testing
NMR	Nuclear Magnetic Resonance
OST	Oxford Superconducting Technology
PIT	Powder In Tube
PF	Poloidal Field
RM	Rigid Model
RRP	Rod Restacked–Rod Process
RRR	Residual Resistance Ratio
RT	Room Temperature
RRT	Round Robin Test
R&D	Research and Development
SCUTT	Strand Configuration for Uniaxial Tensile Test
SS	Stainless Steel
STP	Short Twist Pitch
TARSIS	Test ARrangement for Strain Influence on Strands
TEMLOP	Transverse ElectroMagnetic Load OPtimization
TF	Toroidal Field
THELMA	Thermal-Hydraulic-ELectro-MAgnetic
TIG	Tungsten Inert Gas
TP, TPs	Twist Pitch(s)
TRL	Technological Readiness Level
VF	Void Fraction
WUCD	Warm-Up-Cool-Down

ABSTRACT

This Ph.D. dissertation was conducted in the framework of R&D for magnetic fusion. In Tokamak-type experimental reactors, an ionized gas reaching millions of degrees is confined by high magnetic fields produced by powerful electro-magnets. In order to reduce the thermal dissipation, modern tokamaks use superconducting materials at cryogenic temperatures. These materials can carry large currents without electrical resistance. However, for advanced superconductors, this current-carrying capability is also a function of the mechanical strain state of the material.

In the ITER Tokamak, currently under assembling in France, the toroidal field magnets cables are composed of hundreds of Nb_3Sn composite superconducting wires sensitive to strain. During machine operation, these cables are submitted to cyclic mechanical loads of electromagnetic and thermal nature. It has been observed that these repetitive loads trigger a gradual but steady decrease of the electrical performance of the cable. Up to now, the exact mechanisms relying this macroscopic loss of electrical performance to the local strain state of the superconducting wires are still partially unknown. This issue is extremely complex because of its multi-scale and multi-physics nature. The goal of the Ph.D. thesis is to shed some light on both cable and strand scales by developing a solid numerical electromechanical model to simulate the superconducting cables in operation. This model is meant to identify and understand the main causes of performance degradation as well as to obtain a predictive tool to assess cable behavior for new superconducting cables.

During the three years of this Ph.D., both experimental and numerical activities were performed to tackle this issue. A major effort was applied to the development of a numerical model, based on the MULTIFIL code, permitting the mechanical modelling of a *Cable-In-Conduit Conductor* (CICC), typical of modern cables for fusion reactors. Several upgrades of the model were made to reach a satisfying representativeness of the cable in operation. In parallel, the experimental activities focused on the mechanical characterization of Nb_3Sn wires under cyclic compressive and tensile stresses, at both room and cryogenic temperature. Thanks to these test campaigns, specific experimental protocols were developed and important behaviors and trends about cyclic loading of

superconducting wires were identified. Finally, the modelling of complete cables under representative loading permitted a new interpretation of the mechanisms driving the electrical performance degradation in the ITER TF magnet conductors. Moreover, parametric studies demonstrated the impact of certain design parameters of the cables on their global mechanical behavior. This opened the way to studies of cables from other and new fusion projects, thus demonstrating the versatility of the model developed.

RESUME

Cette thèse s'inscrit dans le cadre de la recherche sur la fusion par confinement magnétique. Les réacteurs expérimentaux, de type Tokamak, confinent un gaz ionisé, chauffé à plusieurs millions de degrés, grâce à un fort champ magnétique créé par de puissants électro-aimants. Pour limiter la dissipation d'énergie thermique, les tokamaks modernes utilisent des matériaux supraconducteurs à température cryogénique. Ces matériaux peuvent transporter sans résistance électrique des courants très importants. Cependant, pour les supraconducteurs avancés, cette capacité de transport du courant est aussi fonction de l'état mécanique de déformation du matériau.

Dans le tokamak ITER, en construction en France, les câbles qui composent les aimants toroïdaux sont faits de centaines de brins supraconducteurs en Niobium-Étain (Nb3Sn) sensibles à la déformation. Au cours de l'opération de la machine, les câbles sont soumis à des chargements mécaniques de type électromagnétique et thermique, et ce de manière cyclique. Il est apparu que ces sollicitations répétées provoquaient une dégradation des performances électriques du câble. Jusqu'à présent, ces mécanismes reliant la perte de performance macroscopique du câble avec les champs de déformation des brins supraconducteurs, au niveau local, n'avaient été que très partiellement expliqués. Cette problématique est extrêmement complexe car à la fois multi-échelle et multi-physique. L'objectif de la thèse est donc d'essayer d'éclairer et de relier ces deux échelles en développant un modèle numérique électromécanique robuste pour simuler les câbles supraconducteurs en opération. Ce modèle doit permettre d'identifier et de comprendre les causes de la dégradation des performances et d'obtenir un outil prédictif pour de nouveaux câbles supraconducteurs.

Pendant ces trois années de thèse la problématique a été abordée à travers des activités tant expérimentales que numériques. Un effort conséquent a été investi dans le développement du code MULTIFIL, permettant la modélisation mécanique de câbles multi-torsadés de type *Cable-In-Conduit Conductor* (CICC), typiques des réacteurs de fusion récents. Plusieurs améliorations du modèle ont été nécessaires pour arriver à une représentativité satisfaisante du comportement du câble en opération. En parallèle, afin d'investiguer les propriétés mécaniques locale, des activités expérimentales ont été conduites pour caractériser la mécanique des brins composites en Nb_3Sn soumis à des efforts cycliques. Grâce à ces essais il a été possible de développer des protocoles

expérimentaux ad hoc et d'identifier des comportements et des tendances liées au chargements cycliques de ces brins. Enfin, la modélisation de câbles complets sous chargements représentatifs a permis de nouvelles interprétations des mécanismes mécaniques engendrant la dégradation des performances électriques du câble de l'aimant toroïdal d'ITER. Grâce à des études paramétriques, le code a mis en évidence l'impact de certains paramètres de design sur le comportement global du câble, ouvrant ainsi la voie à l'étude de câbles différents et nouveaux, tout en démontrant la versatilité du modèle développé.

RESUME ETENDU

I. Première partie – Contexte de la thèse et défis scientifiques

L'objectif de cette partie est de présenter le cadre dans lequel cette thèse s'inscrit en introduisant tout d'abord la supraconductivité, son application dans le monde de la fusion et la problématique principale de la thèse.

A. Supraconductivité

La supraconductivité est un état physique de certains matériaux qui leur permet de transporter du courant avec une résistance électrique nulle en dessous d'une certaine température. Une deuxième caractéristique typique des supraconducteurs est le diamagnétisme parfait, appelé Effet Meissner.

L'état supraconducteur est maintenu si le matériau est en dessous d'une surface critique identifiée par *(B,J,T)* en Figure 1. Les intersections de la surface avec les axes T et B fournissent les valeurs critiques T_c et B_c du matériau.

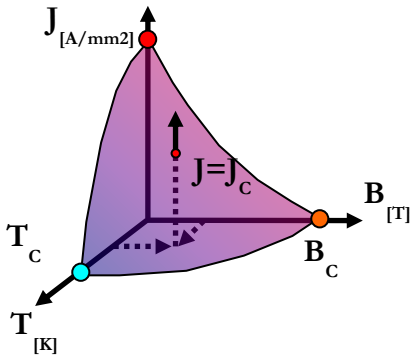

Figure 1. Surface critique d'existence de l'état supraconducteur.

La densité de courant critique J_c est souvent présentée comme fonction du champ et de la température $J_c(B,T)$ et elle définit la surface critique. Elle représente le maximum de densité de courant qui peut être transportée par le matériau sans perdre la supraconductivité.

Grâce à ses propriétés, les pertes par dissipation thermique des supraconducteurs sont négligeables, ce qui rend les supraconducteurs intéressants pour plusieurs

applications basées sur des électroaimants. Pourtant les aimants sont réalisés à partir de câbles, composés de brins composites multifilamentaires : matrice en bronze ou en cuivre avec milliers de microfilaments supraconducteurs torsadés comme montré en Figure 2 pour des raisons de stabilité thermique et électrique.

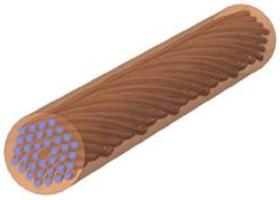

Figure 2. Schéma brin multifilamentaire de (Wang 2016).

La définition de la densité de courant critique d'un brin supraconducteur est faite à l'apparition d'un champ électrique graduel et la communauté a fixé cette valeur à 10 µV/m correspondant au *champ électrique critique* E_0. La température mesurée à cette valeur de champ électrique est appelée *température de partage de courant* T_{cs}. Plus cette température est faible, plus on risque de transiter à l'état résistif tôt. En plus, la transition du brin est décrite par la *Loi de puissance* suivante où *n* représente l'*indice de transition* appelé aussi *n-value* :

$$E = E_0 \left(\frac{J}{J_c(B,T)} \right)^n [V/m]. \quad (1)$$

Ce travail de thèse se base sur le supraconducteur Nb_3Sn qui est particulièrement intéressant pour ses propriétés critiques élevées. Cependant, pour ce matériau la densité de courant critique est aussi fonction de la déformation. Cela signifie que la capacité de transport de courant des brins est affectée par l'état mécanique des filaments comme en Figure 3.

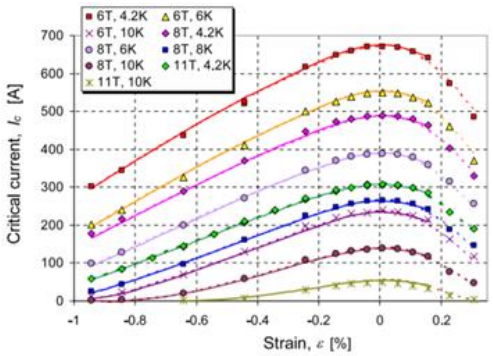

Figure 3. Courant critique pour un brin Nb_3Sn en fonction de la déformation à différents champs et températures (Ilyin 2007).

B. Energie et câbles de fusion

Les réacteurs à fusion par confinement magnétique sont l'une des technologies qui doit se baser sur les aimants supraconducteurs à cause des hautes intensités de champ et courant requises. La configuration la plus utilisée aujourd'hui est le *Tokamak* et

notamment le projet ITER, actuellement en construction en France depuis 2007, devra démontrer la faisabilité de production d'énergie à partir de réactions de fusion d'atomes de Deutérium et Tritium. Grâce à un système d'aimants très complexe, reporté en Figure 4a), le réacteur confine les atomes sous forme de gaz ionisé à 150 millions de °C, appelé *plasma*, qui aura une forme toroïdale donnée principalement par les aimants toroïdaux (Figure 4b)).

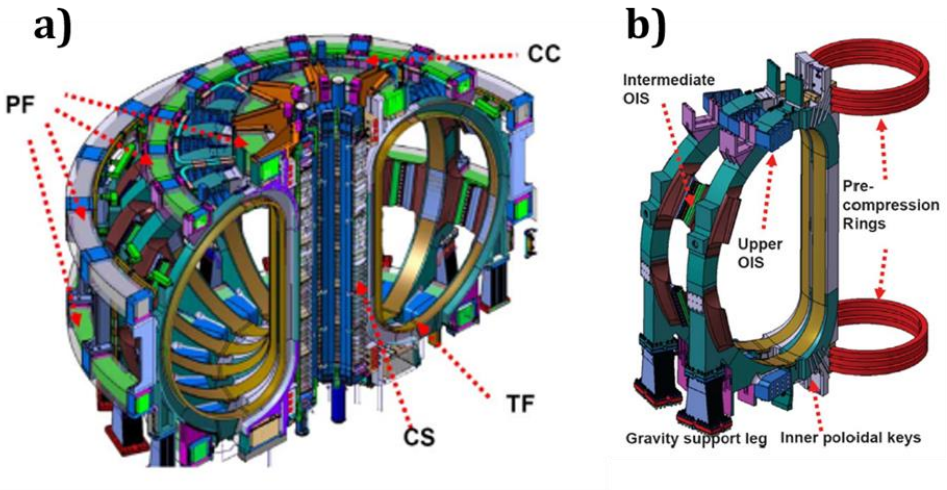

Figure 4. a) Système aimants d'ITER ; b) Aimants toroïdaux (Mitchell 2008).

Les aimants toroïdaux (*TF coils*) travaillent sous 12 T de champ maximum et à 68 kA de courant nominal, pourtant ils sont faits par des câbles en Nb_3Sn refroidis par Hélium liquide. Le design du câble TF est de type Câble-en-Conduit (CICC), c'est-à-dire plus de 1000 brins multi-torsadés selon plusieurs étages de câblage pour une répartition correcte des courants transportés par les brins et intégrés dans une gaine en acier inox servant de support mécanique (Figure 5). Au centre du câble est positionnée une spirale en acier pour le passage d'hélium, autour de laquelle sont torsadés six sous-parties de câble, appelées *pétales*, séparées par une feuille en acier. Chaque pétale a un cœur de 12 brins cuivre, puis les éléments de câblage sont des triplets de brins fait par 2 brins Nb_3Sn et un brin cuivre. Le cuivre sert toujours pour des raisons de stabilité thermique et électrique.

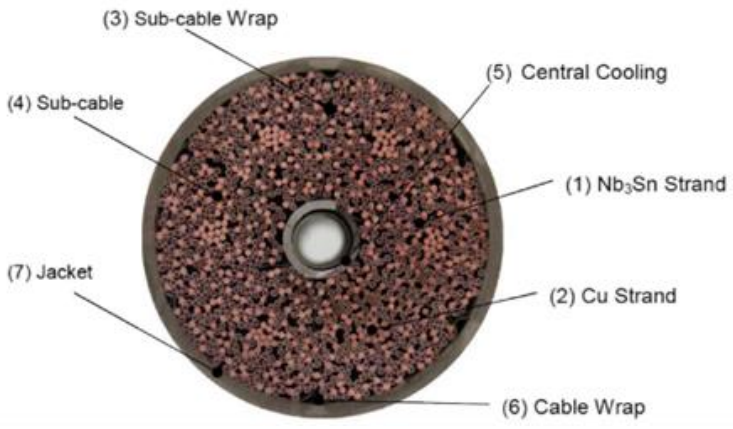

Figure 5. Section typique d'un conducteur du TF d'ITER (Boutboul 2014).

Pendant le fonctionnement de la machine les conducteurs sont soumis à plusieurs chargements mécaniques de différentes natures. Les forts courants et l'intense champ créent des forces électromagnétiques qui atteignent 800 kN/m dans la direction transverse au conducteur. Ces forces sont également de nature cyclique (~1000 cycles EM). En plus, à cause du retrait thermique différentiel entre la gaine en acier et le câble interne, à chaque fois qu'il y a un changement de température dû à la mise en froid du conducteur qui travaille à 4 K, le câble est soumis par la gaine à des forces de traction/compression s'il est réchauffé ou refroidi. A cause de ces chargements mécaniques, la capacité de transport de courant des brins est affectée.

Les conducteurs ont été testés dans la station d'essai SULTAN (PSI, Suisse) qui permets d'évaluer le comportement du conducteur en configuration droite soumis aux mêmes chargements prévus par l'opération. Pendant la phase de qualification des conducteurs du TF d'ITER, on a pu observer la dégradation de la T_{cs} avec l'application des cycles EM jusqu'à ne pas respecter le critère de 5.7 K fixé par ITER comme montré en Figure 6.

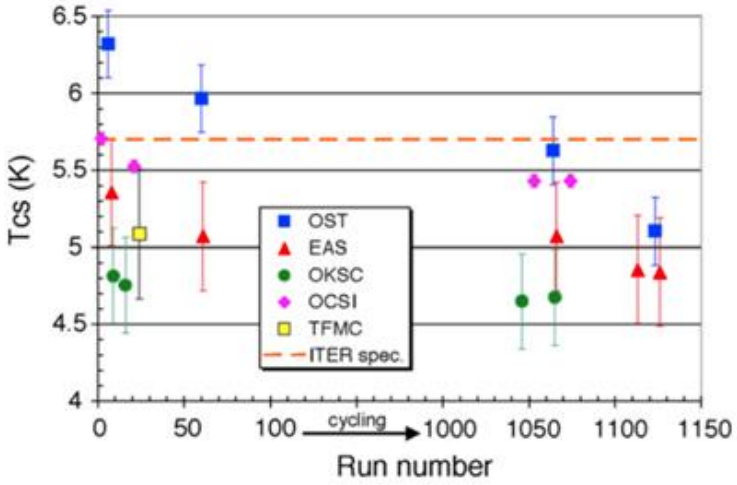

Figure 6. Dégradation de la Tcs à cause de cycles EM pendant un essai typique dans SULTAN (Ciazynski 2007).

Les années suivantes ont été dédiées à un programme d'essais avec pour objectif final la compréhension des mécanismes de dégradation des performances électriques des câbles CICC. Les expériences et investigations expérimentales menées montrent que les filaments des brins tendent à fracturer avec l'application des cycles EM à cause du flambement des brins et suggèrent que les designs devraient mieux supporter mécaniquement les brins.

Cependant, les mécanismes de dégradation sont encore partiellement inconnus et aujourd'hui il n'existe pas un outil fiable qui permette prédire le comportement d'un certain conducteur en phase de design. C'est en réponse de cette exigence que la thèse a lieu à travers à la fois une piste expérimentale et numérique.

II. Seconde partie – Comportement mécanique des brins en Nb_3Sn

Les données expérimentales sont un outil important pour l'étude du comportement mécanique des fils composites, mais elles sont aussi largement utilisées pour la définition de lois de comportement des matériaux à mettre en œuvre dans des codes numériques. Même si des protocoles expérimentaux ont été définis sur la base de plusieurs études pour le comportement en traction, la littérature scientifique manque d'informations sur le comportement en compression des fils supraconducteurs, car en raison du petit diamètre (<1mm) la charge critique pour éviter la flexion du brin est trop petite. De plus, il n'existe qu'une seule étude, à connaissance des auteurs, sur le comportement en fatigue en traction. Ainsi, les études expérimentales réalisées au cours de ce doctorat visent à étudier le comportement en fatigue des brins en Nb_3Sn pour des sollicitations de traction et de compression à température ambiante et cryogénique. En particulier, les essais de traction s'appuient sur les travaux de G. Lenoir (Lenoir 2017) avec quelques adaptations, tandis que pour les essais de compression un protocole expérimental spécifique a été élaboré.

A. Essais de traction

Les activités expérimentales ont été menées à la fois au CEA Paris-Saclay (Laboratoire LCSE) et au CEA Cadarache (Laboratoire GAIM). Les tests au LCSE ont été utiles pour apprendre le protocole expérimental pour tester les brins de Nb_3Sn très fragiles sous sollicitations de traction aussi bien à température ambiante qu'à température d'azote liquide. Ces tests préliminaires ont permis à ce doctorat de développer une procédure utilisée ensuite avec la machine de traction au laboratoire GAIM permettant des essais plus variés et plus nombreux. En particulier, la machine de traction GAIM est très utile car elle permet d'effectuer des milliers de cycles. Même si la machine a déjà été utilisée à température ambiante pour des tests mécaniques réguliers sur de grands échantillons d'acier, cuivre, résines, etc…, plusieurs adaptations, concernant le logiciel de la machine, l'extensomètre et le système de serrage de l'échantillon, ont été nécessaires pour tester ces fils fragiles spécifiques.

Le protocole développé par G. Lenoir se base sur une configuration particulière de l'échantillon qui s'appelle SCUTT, reportée en Figure 7, qui prévoit la soudure sur chaque côté d'une bille en laiton et la présence d'un tube libre coincé par la bille.

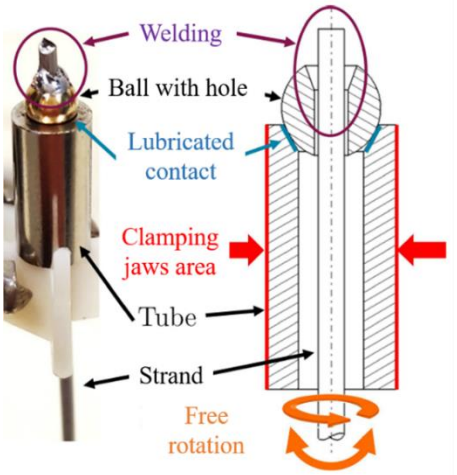

Figure 7. Dispositif SCUTT développé par G. Lenoir (Lenoir 2017).

Les principaux avantages de l'utilisation de la configuration SCUTT sont la minimisation de la contrainte de flexion grâce à l'alignement du toron avec les mâchoires de serrage, la transmission de l'effort de traction, mais aussi la rotation du toron autour de son axe, la limitation les dommages dus à la manipulation du toron lors du serrage dans la machine de traction et l'application d'une contrainte uniaxiale. La Figure 8 montre la configuration typique des essais en traction réalisés au GAIM.

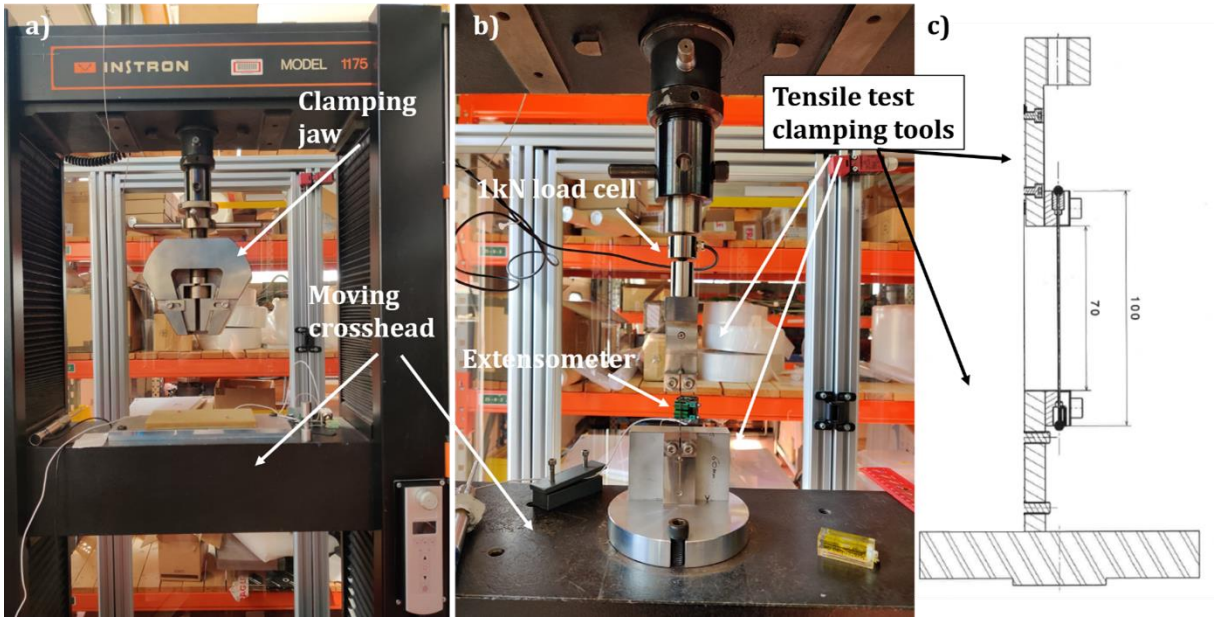

Figure 8. a) Machine de traction ; b) Mise en place pour l'essai de traction ; c) Outillage pour le serrage en traction.

Plusieurs essais ont été faits pour valider le protocole et s'assurer de la fiabilité des résultats. Tous les essais du GAIM commencent pour une montée monotone en traction avec quelque décharge suivie par 1000 cycles de charge-décharge à une effort fixe de 150 MPa. Les essais du LCSE ont servi pour la validation de l'essai mais à cause des limites de la machine ça n'a pas été possible de faire 1000 cycles. La Figure 9 illustre des

courbes typiques contrainte-déformation pour les montées monotones en omettant les cycles, démontrant la bonne réussite et reproductibilité des résultats.

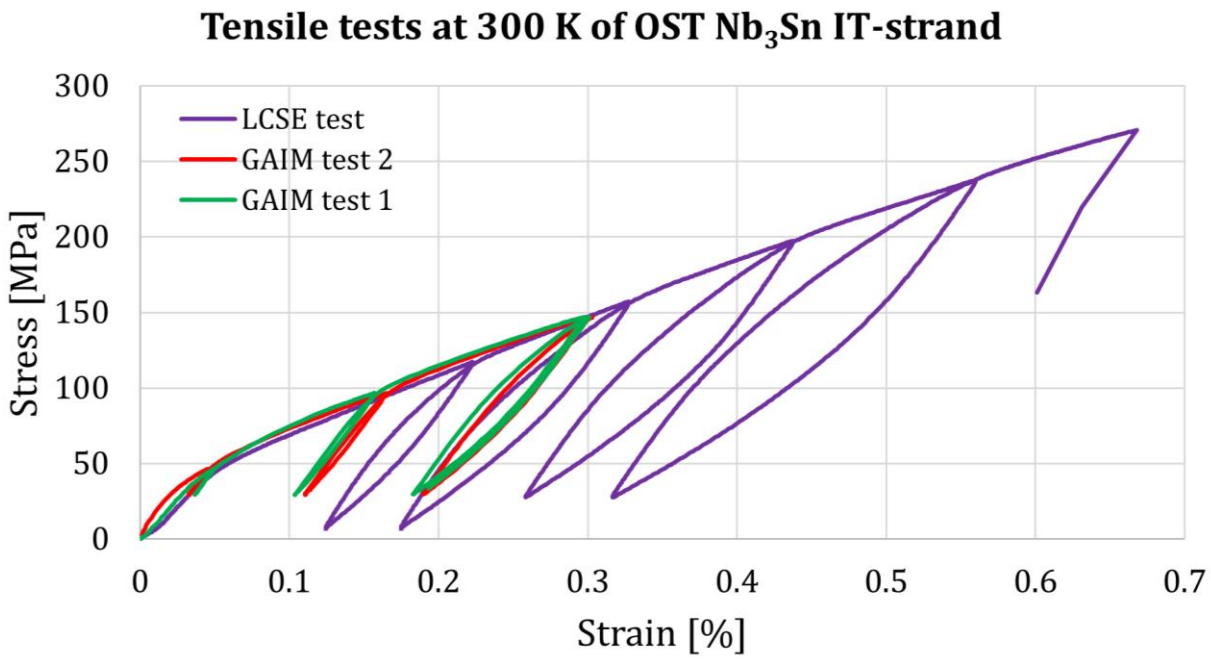

Figure 9. Essais de traction à température ambiante.

Après validation de la procédure plusieurs essais avec 1000 cycles ont été réalisés au GAIM et la Figure 10 montre un exemple du comportement observé.

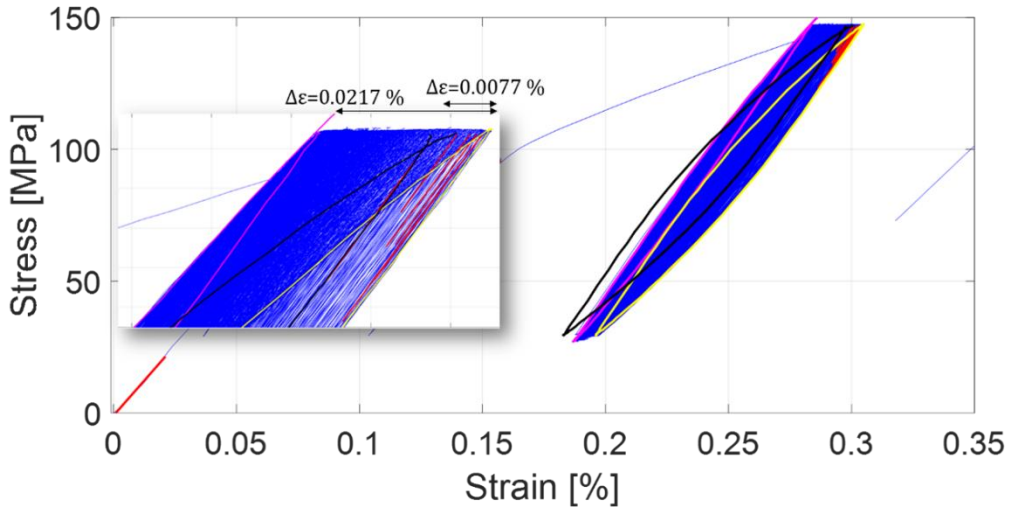

Figure 10. Courbe contrainte-déformation avec 1000 cycle à 150 MPa à température ambiante pour un brin Nb_3Sn.

La différence entre le premier cycle (noir) et le 13ème cycle (jaune) correspond à un Δε de +0,0077%, tandis que du 13ème cycle au millième cycle (rose) il y a une variation de Δε = -0,0217 %. En effet, selon (Bajas 2011) au cours des 15 premiers cycles, il y a une accumulation de la déformation plastique irréversible due à un effet Ratcheting. Le même effet est observé dans la présente étude pour les premiers cycles, mais ensuite un

durcissement progressif, probablement dû à la plastification de la matrice comme expliqué par (Sheth 2011), prédomine et l'effet global est la diminution de la déformation moyenne. Le comportement observé est très probablement affecté par des phénomènes structure à cause de la nature composite du brin : les filaments torsadés tendent à s'aligner et le brin devient par conséquent de plus en plus rigide. Cette observation est cohérente avec l'augmentation progressive du module d'élasticité avec les cycles. Ces tests révèlent ainsi une évolution dynamique en deux étapes du comportement composite constitué de l'ÉTAPE 1 [~1 → 15 cycles] : Effet Ratcheting ; et de l'ÉTAPE 2 [>15 cycles] : Durcissement cinétique.

Des essais à température cryogénique ont été également réalisés, mais l'outillage développé par la thèse pour faire des essais en bain d'azote liquide (77 K) est cause d'un fort bruit dans la mesure. Les résultats préliminaires sont cohérant avec la littérature, mais aucun mécanisme à double dynamique n'a été observé comme pour les essais à chaud. Des essais supplémentaires sont recommandés pour améliorer la stabilité de la mesure.

B. Essais de compression

Cette section présente le nouveau protocole expérimental nommé EPSIC (*Experimental Protocol to measure Strands In Compression*) qui a été entièrement développé au cours de cette thèse. L'idée principale derrière la conception de l'échantillon EPSIC est de concevoir et de tester un faisceau de fils parallèles compactés au lieu d'un seul fil, en déduisant la loi de compression du brin simple en mettant les résultats à l'échelle de la section transversale du fil unique. La fabrication du fagot EPSIC prend près d'un mois et les nombreuses étapes qui le caractérisent se résument en Table 1.

Table 1. Etapes principales de la manufacture d'un échantillon EPSIC.

ETAPE I – Bobinage des brins	Enroulement des brins Nb_3Sn plaqués Cr.	
ETAPE II – Suppression de l'épaisseur Cr	Retrait du placage Cr avec un traitement chimique HCl.	

ETAPE III – Fagot pré-compactage + Enrubannage	Utilisation de pinces mécaniques pour serrer le faisceau et réduire le diamètre. Emballage de paquet avec une feuille en acier.	
ETAPE IV – Tube + Compactage	Insertion du faisceau dans deux tubes en acier inox et compactage avec la machine de compaction radiale.	 
ETAPE V – Soudage des bouts	Soudage TIG des extrémités des faisceaux.	
ETAPE VI – Traitement thermique	Traitement thermique de 20 jours à 650°C.	
ETAPE VII – Coupe et polissage	L'échantillon est usiné radialement jusqu'aux dimensions nominales, et un polissage des extrémités est effectué pour l'analyse de la section.	
ETAPE VIII – Usinage de tubes inox	Usinage du faisceau pour ouvrir la zone de test de l'échantillon.	

La mise en place des tests, Figure 11, est une phase importante du protocole expérimental et elle est aussi importante que la fabrication des échantillons pour un résultat optimal. Il est extrêmement important de garantir autant que possible une application uniaxiale uniforme de la contrainte de compression.

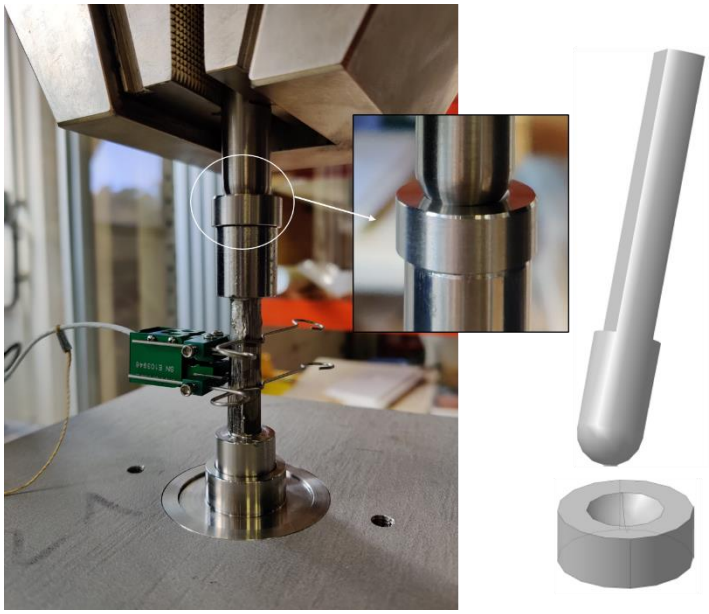

Figure 11. Mise en place des tests de compression.

Les activités expérimentales de compression EPSIC ont été réalisées à la fois au Laboratoire LMA de l'Institut CNRS et au CEA Cadarache (Laboratoire GAIM). La collaboration avec le LMA a été très utile pour développer la méthode et les outils pour tester les échantillons EPSIC en compression. Un essai type est reporté en Figure 12 avec 200 cycles à effort constant. La différence entre les deux pics de déformations diminue de 0,125 % à 0,0956 % pour l'essai de compression. Pour l'essai de traction on obtient les mêmes diminutions en 1000 cycles. En fait la différence initiale est de 0,115 % et après 1000 cycles arrive à 0,0958 %. En compression, il n'y a pas de comportement en deux étapes et le comportement est plus similaire à un effet Rochet, puisque la déformation moyenne continue d'augmenter avec les cycles et le module d'élasticité reste constant avec les cycles.

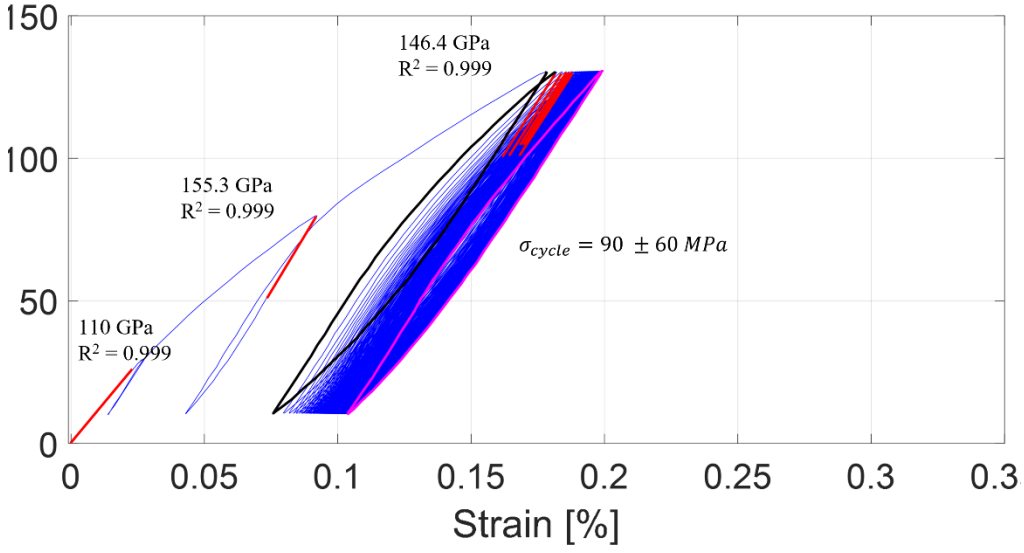

Figure 12. Courbe de contrainte-déformation en compression à température ambiante.

La Figure 13 montre une comparaison directe entre les résultats de traction et de compression, où le tracé de compression a été basculé sur la déformation positive pour le comparer à l'échelle de déformation de l'essai de traction. Les deux courbes sont tracées en enlevant la précharge. L'enveloppe de la courbe de compression est assez différente de celle de traction, avec une tendance qui implique un comportement plus rigide. Cette différence pourrait être expliquée par une plastification de la matrice cuivre des brins induite par le retrait thermique différentiel entre acier et brins pendant le refroidissent de l'échantillon de la température du traitement thermique et température ambiante.

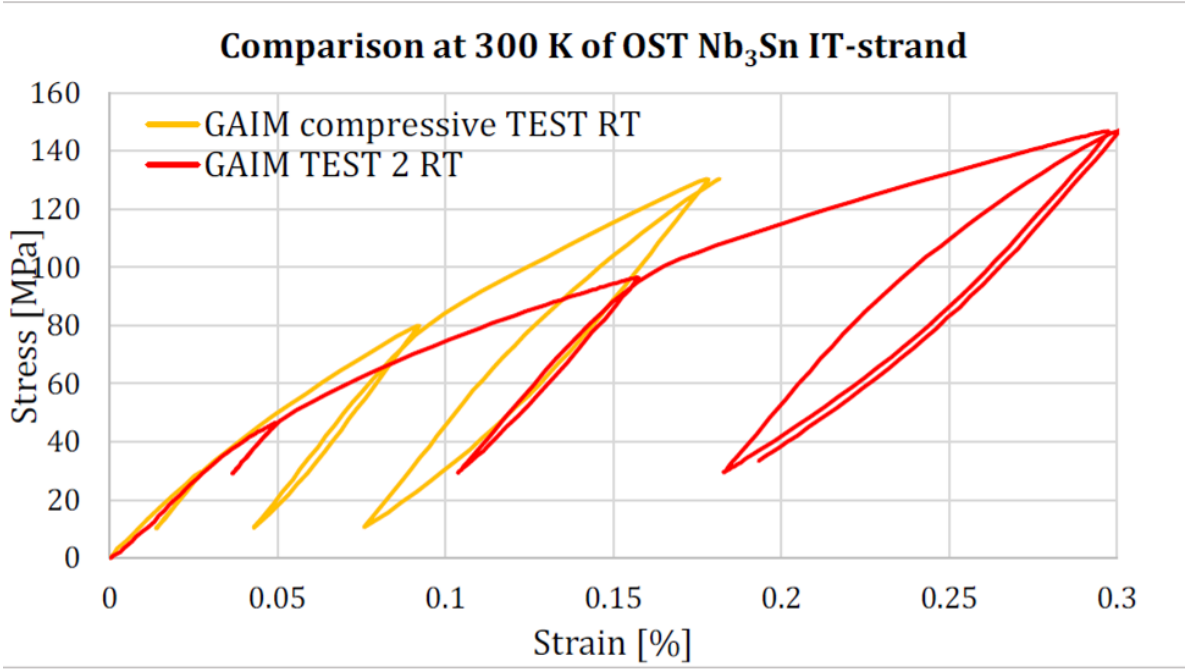

Figure 13. Comparaison entre les essais de traction et de compression GAIM à température ambiante.

III. Troisième partie – Modélisation mécaniques des CICCs en Nb_3Sn

Dans la communauté des supraconducteurs, il existe de nombreux modèles traitant des conducteurs CIC, qu'ils soient analytiques ou numériques. Selon l'objectif visé, certains modèles visent à reproduire uniquement la géométrie du câble, d'autres l'état mécanique du câble, parfois jusqu'aux performances électriques, et certains traitent même de la stabilité thermo-hydraulique du câble. L'état de l'art sur la modélisation des CICC met en évidence quelques difficultés concernant les simulations mécaniques. Tout d'abord, l'incapacité de fournir l'état de déformation local pour une géométrie de câble complexe à grande échelle, et ainsi de reproduire les phénomènes mécaniques macroscopiques se produisant à l'intérieur du câble sous des chargements. Deuxièmement, tous les modèles numériques considèrent généralement la déformation thermique comme une variable d'entrée. L'ancienne version du code mécanique MULTIFIL couvrait en partie ces problématiques puisqu'il était capable d'évaluer l'impact

des sollicitations thermiques et électromagnétiques sur les trajectoires des fils et les déformations locales. Cependant, il y avait encore des limites de modélisation et des inconvénients liés à ce code. C'est pourquoi la modélisation mécanique au cours de ce travail de thèse s'est appuyée sur le code MULTIFIL développé à ECS lors de la thèse de Bajas en 2010-2012. Depuis, le cœur du code a été profondément modifié, notamment en termes de définition des conditions aux limites. Les améliorations apportées au modèle de câble à fusion MUTIFIL dans le cadre de cette thèse, décrites ci-dessous, se sont concentrées sur trois aspects principaux : l'intégration de la nouvelle version du code pour l'étude des câbles de fusion, la mise à niveau des conditions aux limites tout en passant à un modèle de câble complet et le développement d'un protocole numérique standardisé pour simuler les câbles CICC.

A. Modélisation mécanique des CICCs avec MULTIFIL

Le code MULTIFIL permet de résoudre les équations d'équilibre mécanique entre plusieurs fibres en utilisant le modèle cinématique de poutre enrichie. Les brins supraconducteurs sont vus comme des poutres qui interagissent à travers des contacts de frottement. Grâce à la dernière version du code, les brins sont organisés selon une structure hiérarchique qui suit les étages de câblage principales. Les lois de comportement intégrées dans MULTFIL permettent une description assez riche de la déformation plastique que dans la direction longitudinale. Les contacts sont gérés avec une méthode de pénalisation en direction normale et un modèle de frottement en direction tangentielle.

Le code permet de simuler la mise en forme initiale du câble à l'aide d'une série de surface analytiques rigides qui compactent l'ensemble de brins jusqu'au taux de vide nominal, comme montré en Figure 14.

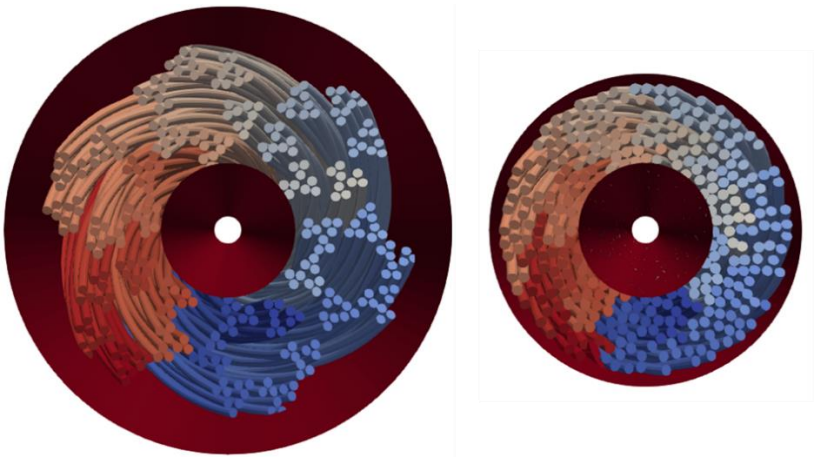

Figure 14. Assemblage des fils simulé par MULTIFIL grâce aux outils rigides (Bajas 2011).

Au cours de cette thèse deux améliorations du code ont été implémentées concernant la mise en forme initiale : codage de surface analytique hélicoïdales et codage de hiérarchie complexe pour la simulation de la géométrie complète d'un câble de fusion (voir Figure

15). Avant cette thèse c'était possible de simuler qu'une partie du câble, le pétale (237 brins au lieu de 1422 pour le TF d'ITER).

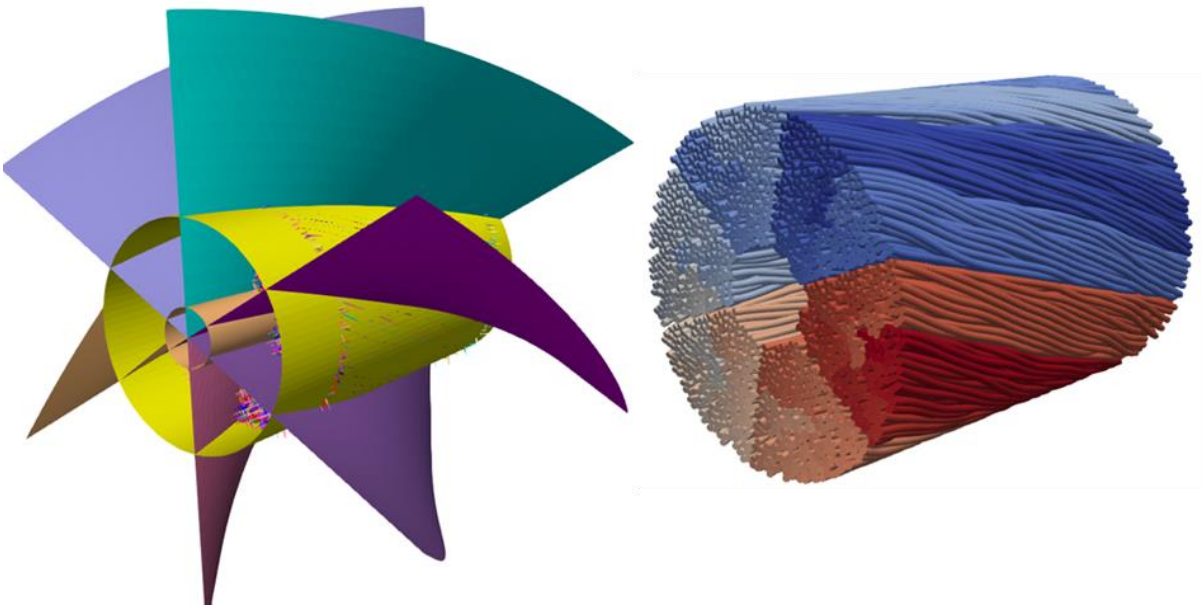

Figure 15. Implémentation du modèle de câble complet du TF d'ITER dans le code MULTIFIL.

Après la géométrie initiale, le traitement thermique typique de ces conducteurs pour la création de la phase supraconductrice est simulée par mise à zéro des contraintes dans les brins. Ensuite, la phase de mise en froid de la température de traitement thermique (650 °C) à la température d'opération (4.5 K) est simulée par une graduelle compression appliquée au câble simulé et causée par la présence de la gaine en acier. D'une façon similaire, à travers l'application d'efforts de traction et compression, les éventuels réchauffages et refroidissements sont simulés. Enfin, le code permet de simuler l'application de forces électromagnétiques perpendiculaires aux trajectoires des brins supraconducteurs.

Pour la simulation des chargements thermiques, des routines analytiques ont été développées en support de la simulation numérique afin de prendre en compte la présence de la gaine en acier. En particulier on simule la compression progressive du câble pendant le refroidissement et on compare la courbe avec le comportement d'une gaine virtuelle en acier. Le point de rencontre représente le point d'équilibre mécanique qu'on suppose avoir lieu réellement entre gaine-câble. Figure 16 montre le schéma conceptuel de cette étude. La même logique est appliquée lors de l'application des cycles EM, car il y a également un impact sur le point d'équilibre gaine-câble.

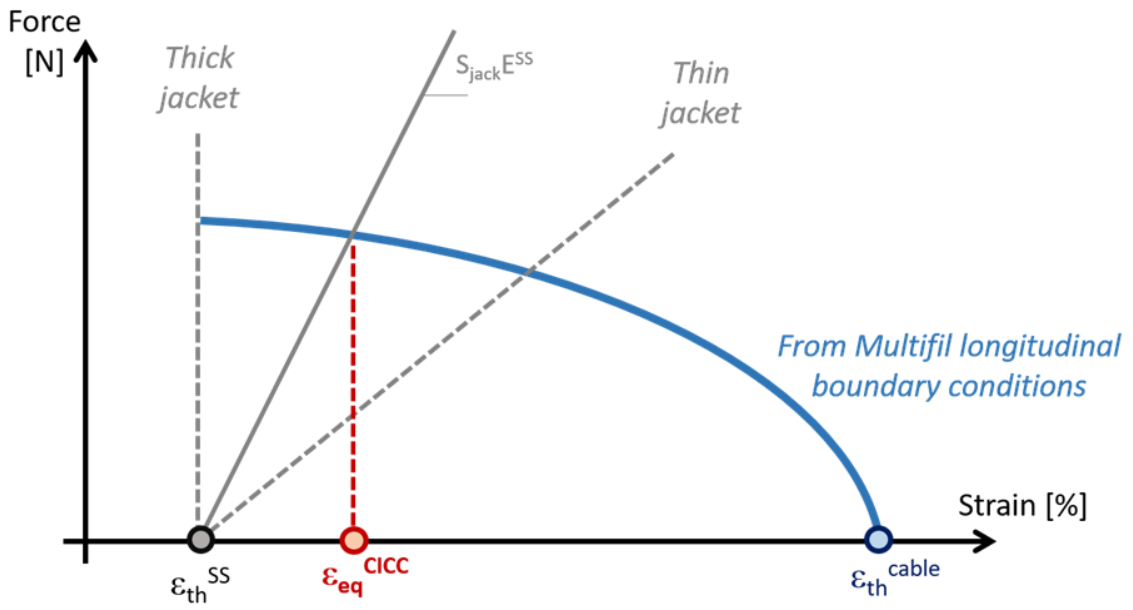

Figure 16. Etude de l'équilibre entre gaine en acier analytique virtuelle et câble MULTIFIL.

En plus, en tout début de thèse, une modification majeure a été faite au cœur du code pour la simulation des chargements thermique. Cette amélioration visait à avoir une distribution de la déformation homogène qui était compromise par des interactions de frottement entre les brins et les surfaces rigides.

Enfin des routines analytiques ont aussi été développées en appui à la simulation du chargement EM ainsi que dans le cas de la simulation du seul pétale pour trouver les bonnes conditions aux limites à prendre en compte pour considérer les forces supplémentaires des pétales autour de celui simulé.

Grâce à tout ce travail, la thèse a amélioré la fiabilité du modèle aussi bien du câble complet que du pétale pour la simulation du comportement mécanique d'un câble de fusion. En fait, même si le modèle du câble complet est fondamental, il y a une grande différence de temps de calcul par rapport au modèle du pétale. Pourtant il a été jugé important de développer un modèle de sous-échelle fiable d'un câble qui pourrait encore être un outil utile pour des analyses plus rapides.

B. Protocole numérique de simulation des câbles de fusion

A cause de la complexité de simulation des différentes étapes, comme présenté par la section précédente, un protocole numérique a été formalisé pour éclaircir le traitement des données à utiliser pour la simulation de chaque phase de la vie d'un conducteur en opération en utilisant MULTIFIL.

Ce protocole identifie plusieurs étapes numériques, alternées avec des études analytiques, pour supporter et fournir les paramètres nécessaires aux simulations numériques. Un schéma de cette procédure est reporté sur la Figure 17.

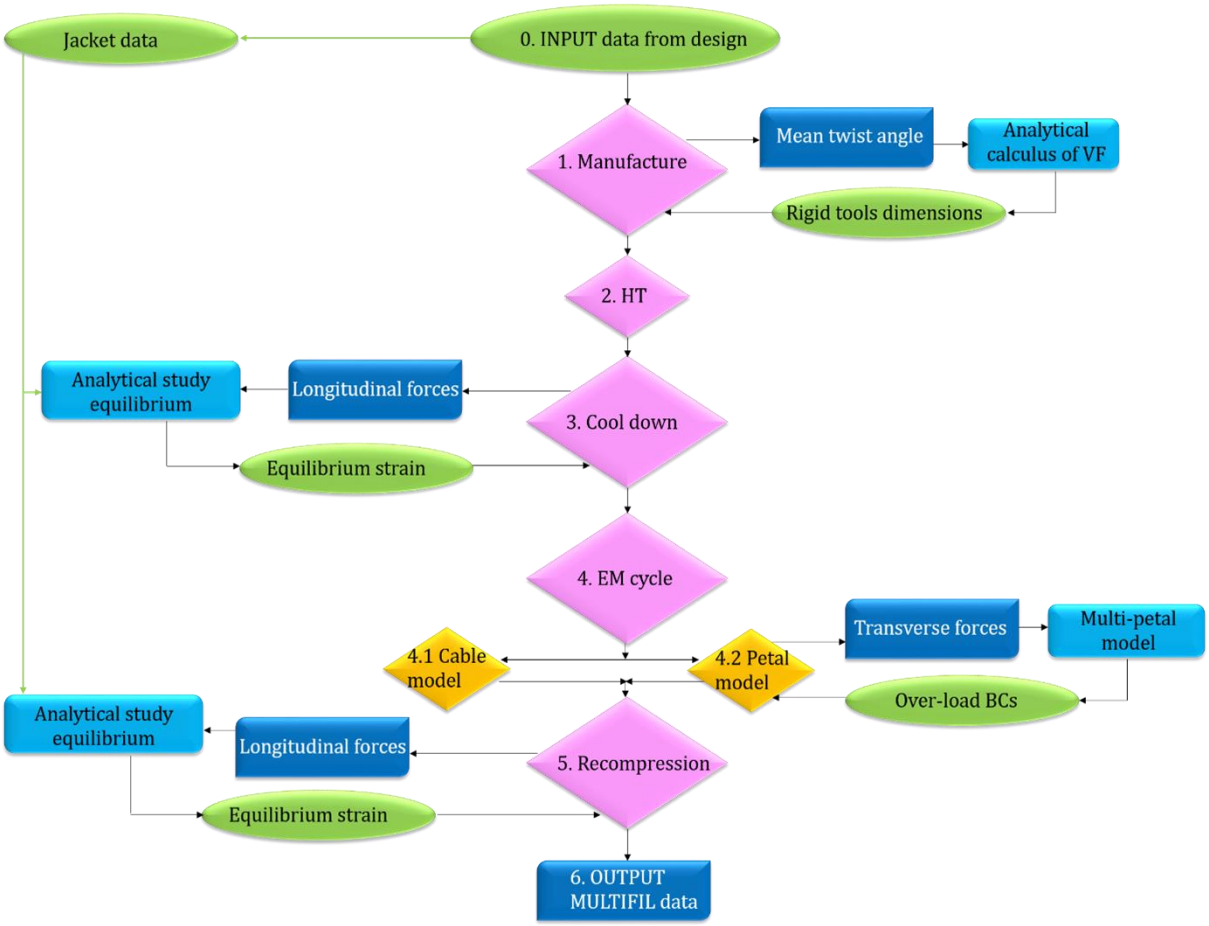

Figure 17. Protocole numérique des simulations de câbles de fusion avec le code MULTIFIL.

Le losange rose central représente les principales étapes de la durée de vie du câble simulée par MULTIFIL ; les détails de chaque étape de simulation sont donnés dans (Riccioli 2019), (Riccioli 2020). Les ovales verts sont les données d'entrée pour la simulation fournie par la conception ou les routines analytiques (rectangles bleu clair) qui post-traitent les données de la simulation (rectangles bleu foncé). Par exemple, les dimensions finales du câble/pétale simulé sont ceux qui produisent le taux de vide nominal; pour le calculer, la connaissance de l'angle de torsion moyen à partir de la simulation est nécessaire, comme expliqué dans (Riccioli 2021).

A la fin de la chaîne de simulation avec MULTIFIL, les données de sortie sont des valeurs de la déformation en neuf points sur chaque section de brin (Figure 18), une sur l'axe et huit à la périphérie à un rayon R_m qui ne correspond pas au rayon du brin R_s ou au rayon filamentaire R_{fil} (rayon de la zone où il y a les filaments supraconducteurs).

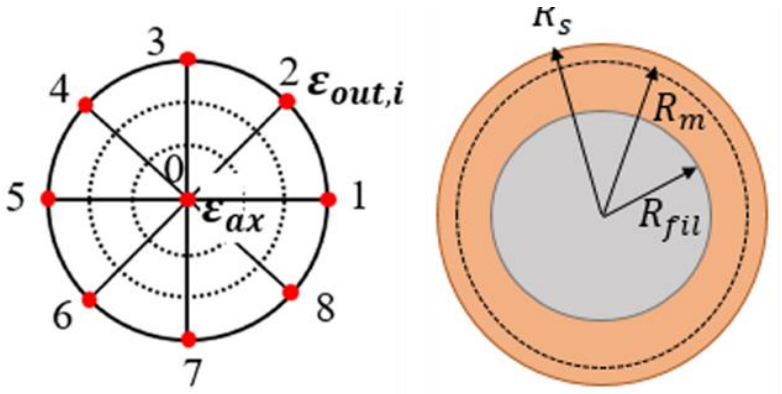

Figure 18. Emplacement des valeurs de la déformation sur la section du fil.

Ces valeurs sont utilisées comme données d'entrée de routines analytiques électriques ou de codes numériques électromagnétiques pour l'évaluation des caractéristiques électriques du câble simulé. Une partie du travail a été dédiée au couplage du code mécanique MULTIFIL au code électromagnétique THELMA de l'Université de Bologne pour déduire une valeur de T_{cs} du conducteur simulé.

IV. Quatrième partie – Simulations et analyses

Le code MULTIFIL appliqué aux câbles à fusion ayant atteint un stade de développement permettant de modéliser et d'analyser un ensemble plus riche et plus varié de cas d'étude, il a été nécessaire de rationaliser le processus d'analyse, en définissant des catégories et des niveaux d'analyse. Par conséquent, un protocole d'analyse a été développé pour extraire des indicateurs et des paramètres utiles à la fois quantitatifs et qualitatifs qui peuvent être utilisés pour un assez large éventail d'objectifs : comparaison et vérification numérique des études expérimentales, validation du code MULTIFIL, définition de comparaison standardisée de différents modèles de conducteurs et définition d'indicateurs mécanique d'analyse. Les trois sections suivantes reportent les résultats principaux des simulations les plus pertinentes.

A. Etudes phénoménologiques de la dégradation cyclique

Le CICC du TF d'ITER a été le cas de référence pour la plupart des travaux de cette thèse.

Table 2. Principaux paramètres de simulation pour les modèles de câbles en pétales et complets par rapport à la conception ITER TF CICC.

	TF d'ITER CICC	Modèle pétale	Modèle câble complet
Disposition câblage	((2Nb_3Sn+1Cu)x3x5x5 +(3x4Cu))x6		
Diamètre spirale	10 mm		
Diamètre câble	39.7 mm	38.44 mm	38.854 mm
Diamètre brin	0.82 mm		
Nombre brins	1422	237	1422
Frottement brins	[-]	0.1	0.1

Diamètre externe gaine	43.7 mm		
Angle de torsion	0.97	0.988	0.967
Taux de vide	29.7 %	29.7 %	29.8 %
Longueur	760 m in coil, 0.45 m high field in SULTAN	0.3 m	0.15 m
SULTAN conditions	(11.78 T, 68 kA)		

Le modèle du pétale :

La Figure 19 rapporte la force de réaction longitudinale du pétale lorsqu'il est soumis à certaines chargements, dans ce cas spécifique : un refroidissement de la température du traitement thermique (CD) et trois cycles EM.

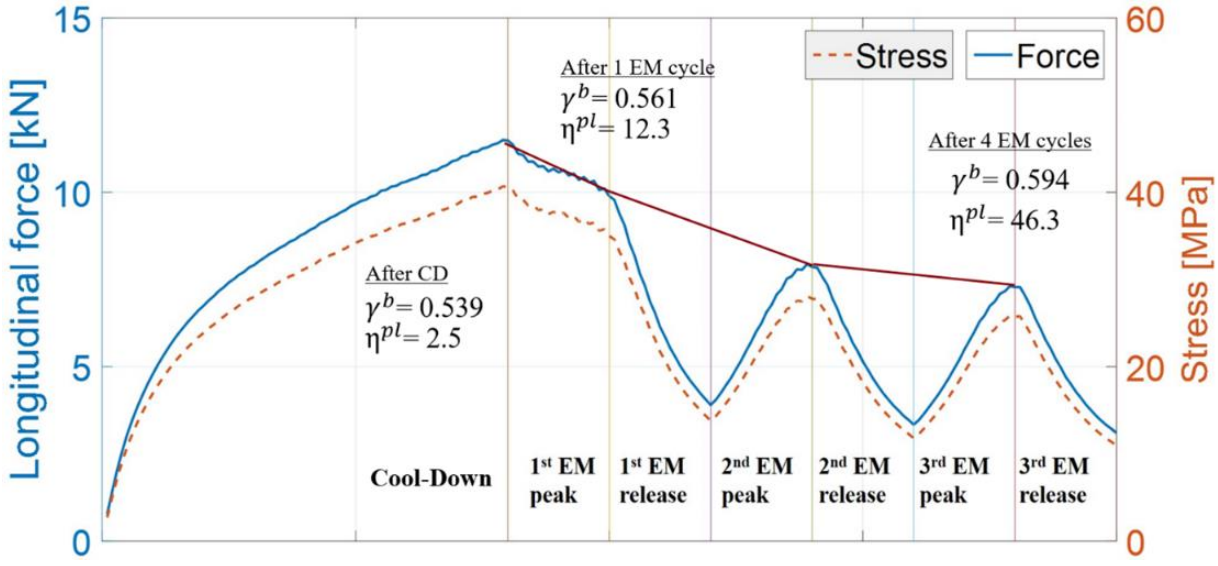

Figure 19. Force de réaction longitudinale F_z et contrainte σ_z du câble pour la séquence de chargements donnée appliquée à l'étude de cas nominale (Riccioli 2021).

La force de réaction longitudinale du câble diminue lors de l'application de la force de Lorentz. Même si la déformation axiale moyenne est presque constante à –0,45 % pour le CD et après le premier cycle EM, le rapport de plasticité change radicalement de 2,5 à 12,3. Ces résultats suggèrent que l'effet majeur du premier cycle EM est la plastification du câble. Comme la force de réaction longitudinale diminue considérablement, il est raisonnable de s'attendre à ce qu'un nouvel équilibre entre la gaine et le câble soit établi. Pour atteindre le nouvel équilibre, une recompression du câble de –0,042 % est requise par rapport à l'équilibre trouvé à la fin du CD comme montré en Figure 20.

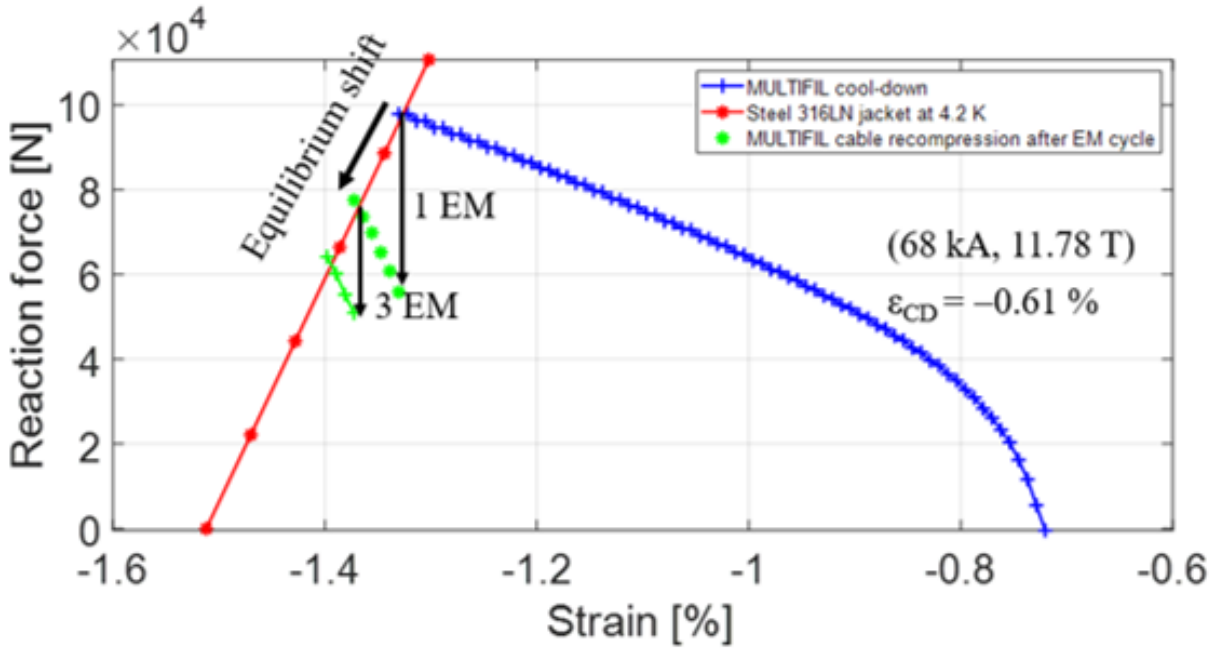

Figure 20. Equilibre gaine-câble après chaque chargement.

Lorsque le câble plastifie, la gaine se détend et tend vers son point de repos comme si elle était libre. La déformation initiale calculée après CD est +0,18 % pour la gaine et –0,61 % pour le câble par rapport à leurs positions de repos à 4,2 K. Cela signifie qu'après CD la gaine a une contrainte de compression « de réserve » de –0,18 % qu'elle applique au câble pendant le cycle EM en raison du ramollissement du câble. Le calcul montre qu'après ~100 cycles EM, le point de repos de la gaine est atteint. La plastification progressive du câble et la relaxation correspondante de la gaine pourraient expliquer la chute initiale de la T_{cs} observée dans plusieurs conducteurs TF (Breschi 2017). Les mesures de déformation résiduelle le long de la longueur de la gaine sur les conducteurs testés sont en bon accord avec cette théorie. En particulier, les échantillons SULTAN, après cyclage, sont coupés en plusieurs points, le câble est extrait de la gaine, et la déformation différentielle est mesurée (Decool 2008), (Hemmi 2012). Toutes les études montrent une relaxation quasi nulle de la gaine dans la zone à haut champ (à pleine charge électromagnétique), si on la compare à la zone à bas champ, confirmant ainsi que les câbles sont plastifiés si soumis à chargement EM.

Une évaluation de la T_{cs} a été faite en couplant les résultats MULTIFIL avec le code électromagnétique THELMA et une comparaison avec les résultats expérimentaux de (Breschi 2017) est proposée dans la Figure 21.

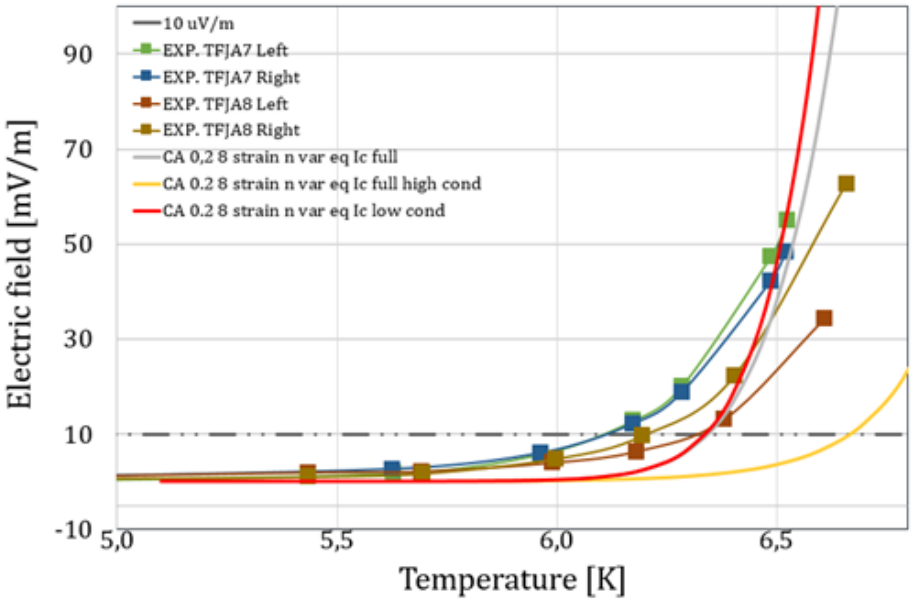

Figure 21. Évaluation de la T_{cs} avec THELMA pour trois valeurs de conductance différentes.

La T_{cs} trouvée avec le modèle pétale est dans l'ordre de grandeur des valeurs expérimentales. Même si le modèle EM repose sur des hypothèses qu'il est recommandé d'approfondir, le résultat obtenu est déjà relevant par rapport aux travaux précédents (Breschi 2012b). Le modèle précédent de MULTIFIL devait interpoler la T_{cs} trouvé par THELMA pour trouver la contrainte thermique correcte pour la simulation du CD. Grâce aux améliorations du modèle apportées par ce doctorat, il est désormais possible de trouver des valeurs T_{cs} cohérentes sans ce paramètre libre supplémentaire.

Le modèle du câble complet :

Même si le modèle à pétale unique a déjà dévoilé l'impact des cycles EM sur le comportement mécanique d'un sous-câble multi-torsadé, la mise à l'échelle du modèle était nécessaire pour une analyse complète des phénomènes inter-pétales ainsi que pour la description adéquate du comportement du câble. Les paragraphes suivants présentent les résultats et les analyses pour le modèle de câble complet, avec un accent particulier sur le comportement inter-pétales. Néanmoins, certains phénomènes sont similaires à ceux observés pour le modèle à pétale unique et ne seront pas détaillés.

A la différence du modèle à pétale unique (Riccioli 2021), l'angle de torsion moyen modélisé correspond désormais à la valeur de 0,97, comme prévu par la conception, grâce à la présence du dernier étage de câblage. Même si le taux de vide (VF) final est de 29,7 % pour les deux modèles, un angle de torsion moyen différent correspond à un comportement mécanique différent. En particulier, dans le sens longitudinal le câble complet est moins rigide que son homologue pétale droit. En fait, la distribution des contraintes après CD rapportée sur la Figure 22 montre le CICC du TF d'ITER pour les modèles à simple pétale et à câble complet. La seule différence entre les deux modèles est la présence du dernier étage de câblage, mais la distribution est plus pointue et plus

étroite pour le pétale droit (STRAIGHT), avec la valeur moyenne déplacée vers les contraintes de compression. La répartition obtenue avec le modèle de câble complet (FULL) est plus large et plus exposée à la flexion, aux efforts de traction et donc au risque de rupture des filaments. La contrainte thermique appliquée au câble (ε_{CD}) donnée par l'équilibre gaine-câble due au CD est plus compressive pour le modèle de câble complet, qui se comporte comme un câble « plus mou ».

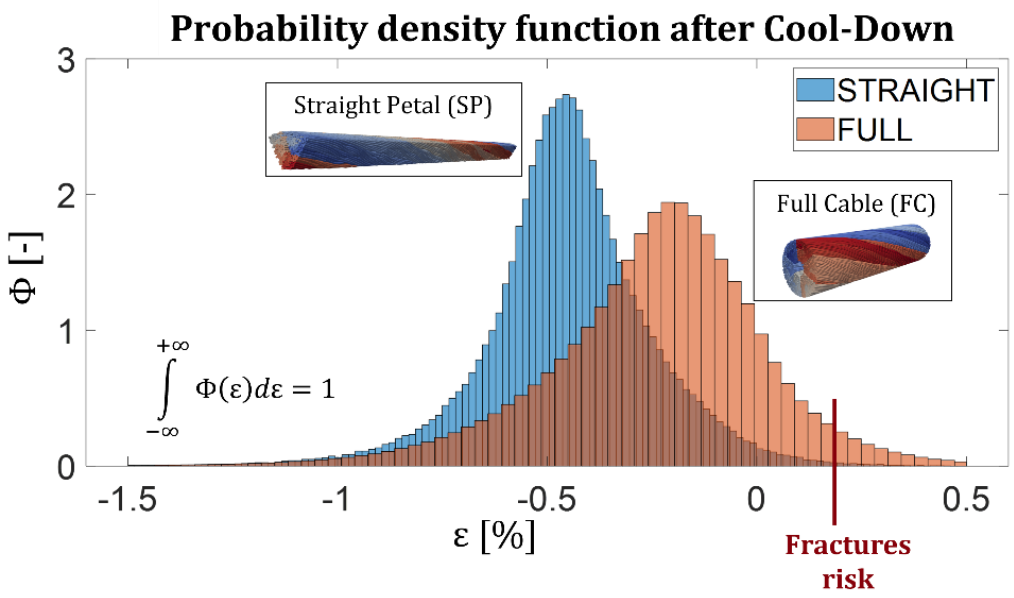

Figure 22. Comparaison de la distribution de la déformation après CD pour le modèle à pétale droit simple et le modèle à câble complet.

Le modèle de câble complet révèle l'effet des cycles EM sur le déplacement des brins du côté de la basse pression EM, qui n'a pas été détecté par le modèle de pétale. A pleine charge EM, le déplacement des brins devient important (quelques diamètres de brin), et un espace s'ouvre du côté basse pression EM du câble comme montré par la section en Figure 23. Bien que le relâchement de la charge EM diminue cet effet, certains brins sont déformés plastiquement et ne retrouvent pas leur position initiale. Un comportement similaire a été observé lors de l'examen destructif de l'échantillon JACS01 R du CS d'ITER testé par ITER (Hemmi 2012).

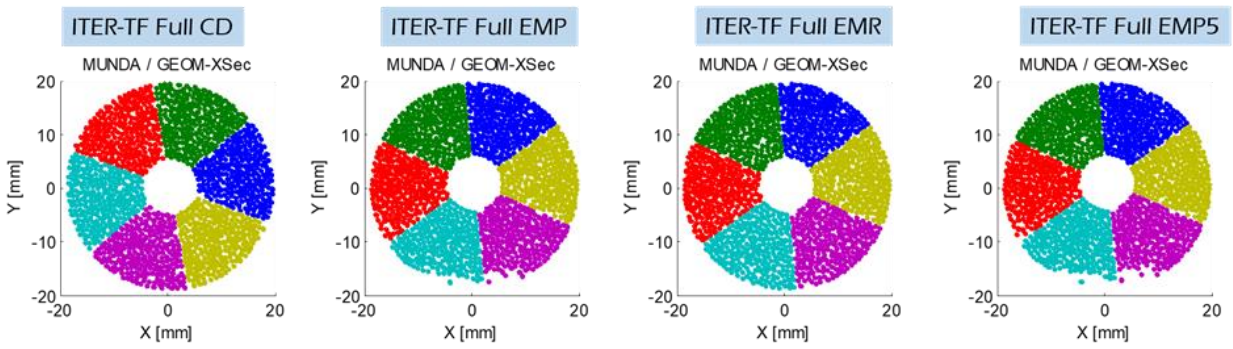

Figure 23. Pour chaque chargement, position des brins sur une section générique à 75 mm de longueur de câble simulée. La direction de la force EM correspond avec la direction positive de l'axe y.

Ce phénomène s'exprime également par l'évolution de la fraction de vide (VF) locale illustrée sur la Figure 24 : la zone de basse pression EM est caractérisée par une augmentation drastique de la VF locale du côté basse pression EM, et par une réduction, plus graduelle, du VF du côté des hautes pressions EM, bien que les valeurs moyennes ne changent que légèrement. La Figure 24 montre également la distribution transversale de l'angle de torsion local et met en évidence une augmentation localisée du flambement dans la zone de basse pression EM, correspondant à des déplacements importants dans cette zone. Ce flambement a également été observé expérimentalement du côté basse pression EM des conducteurs ouverts après essai (Hemmi 2012).

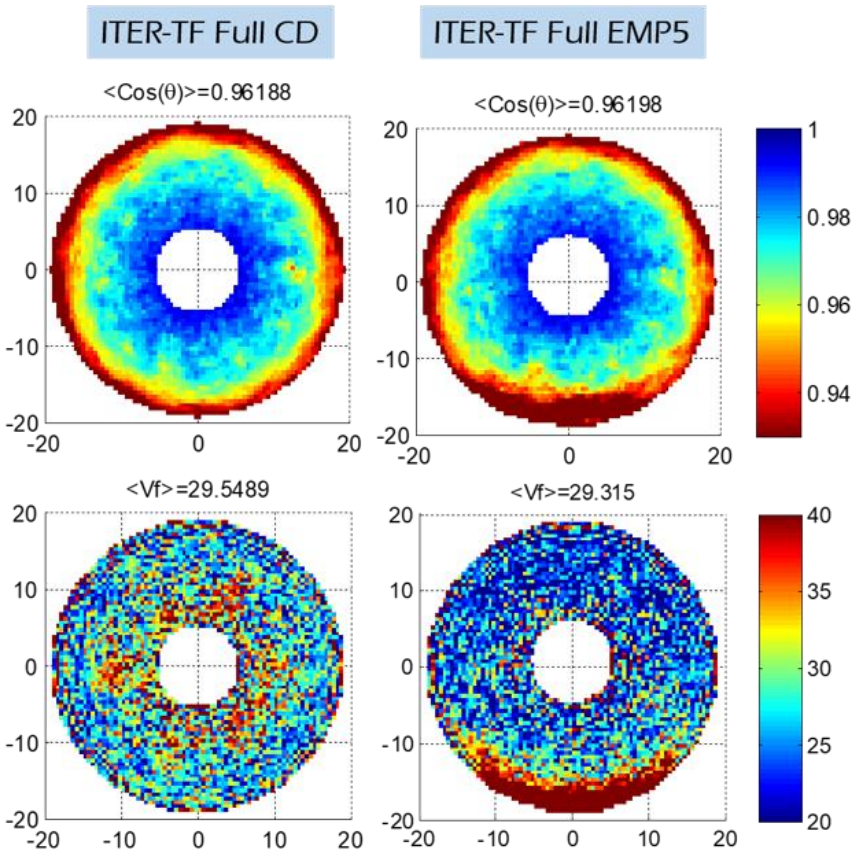

Figure 24. Première ligne : carte polaire cumulée de l'angle de torsion moyen pour différents chargements ; deuxième ligne : carte polaire cumulée de la fraction de vide locale pour différents chargements. La direction de la force EM correspond avec la direction positive de l'axe y.

La Figure 25 rapporte les cartes polaires cumulées des déformations axiales, élastiques et plastiques. Après CD, toutes les déformations sont relativement axisymétriques sur la section transversale. L'effet des cycles EM est une augmentation progressive des déformations plastiques de compression du côté de la haute pression EM, rompant la symétrie initiale, tandis que la déformation élastique est marginale dans la déformation axiale totale. Ce ramollissement global du câble par plastification peut être lié à des mesures expérimentales de contrainte résiduelle nulle dans la gaine dans la zone à haut champ de l'échantillon SULTAN (Hemmi 2012).

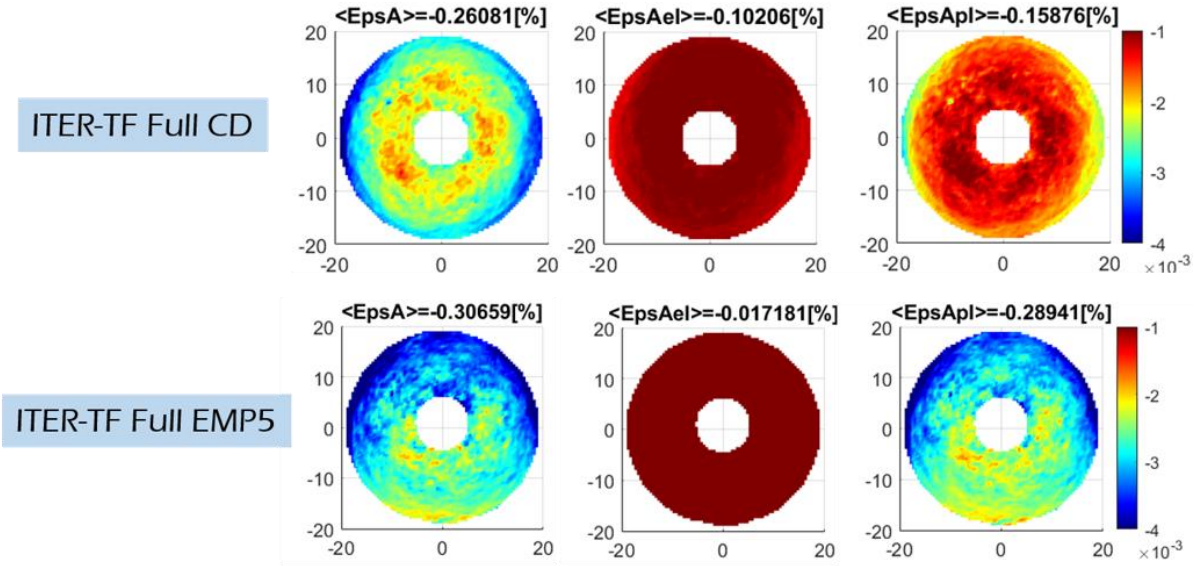

Figure 25. Première ligne : carte polaire cumulée des déformations axiales, élastiques et plastiques après CD ; deuxième ligne : carte polaire cumulée des déformations axiales, élastiques et plastiques au pique du 5ème cycle EM. La direction de la force EM correspond avec la direction positive de l'axe y.

La Figure 26 montre que les forces de contact entre brins ont tendance à diminuer ou même à disparaître du côté basse pression EM du câble. Cette chute drastique de l'amplitude de la force de contact et du nombre de contacts est un autre phénomène révélé par cette étude. Il démontre que cette conception de câble (ITER-TF) n'est pas en mesure de maintenir de bons contacts entre brins pendant son fonctionnement, diminuant ainsi, probablement, sa capacité de redistribution. Ceci est conforme à la diminution drastique des pertes AC dans les câbles du TF d'ITER après une charge cyclique (facteur ~5-10 de (Bessette 2014)), et montre un phénomène cohérent avec les mesures directes des résistances de contact inter-brins effectuées par Twente (Nijhuis 2004).

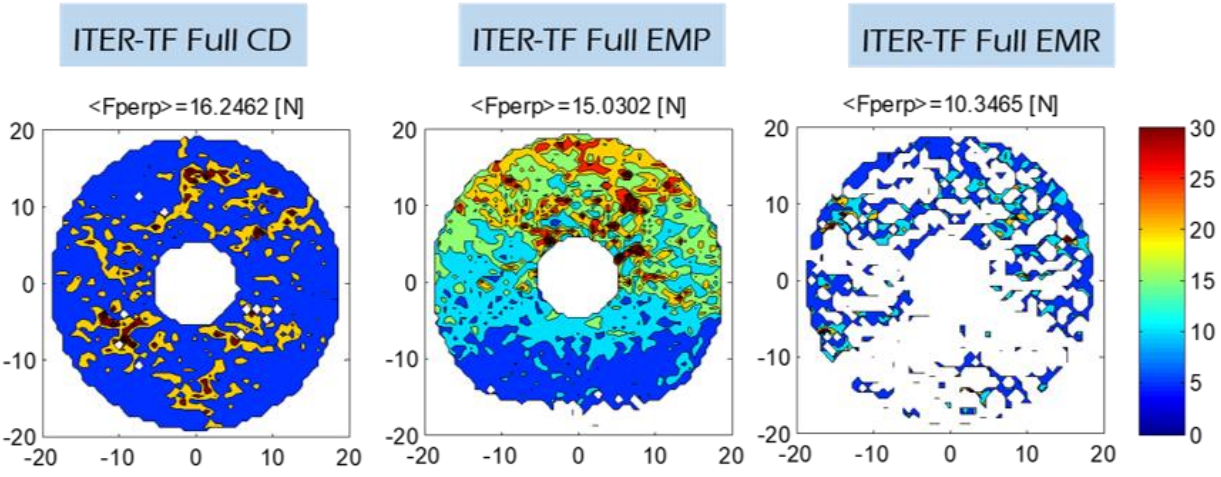

Figure 26. Carte polaire cumulée des forces perpendiculaires de contact. La direction de la force EM correspond avec la direction positive de l'axe y.

B. Comportement mécanique des CICCs : paramètres de design

L'objectif principal de cette section est de discuter de l'impact du taux de vide (VF) et du coefficient de frottement sur le comportement mécanique du câble. Le cas d'étude

nominal est caractérisé par un VF de 29,7 % et un coefficient de frottement entre brins de 0,1. Quatre autres cas ont été étudiées avec un VF de 27,8 %, 32,7 %, 35,3 % et 36 % respectivement. Pour tous, une séquence de CD et un cycle EM a été appliquée. Le CD a été analysé en fonction de différents coefficients de frottement allant de 0,1 à 0,9.

Les cartes de déformation illustrées dans la figure ci-dessous montrent un flambement sensiblement plus important pour les câbles les moins compactés, car les fils ont tendance à se plier davantage lorsque le CD compressif se produit.

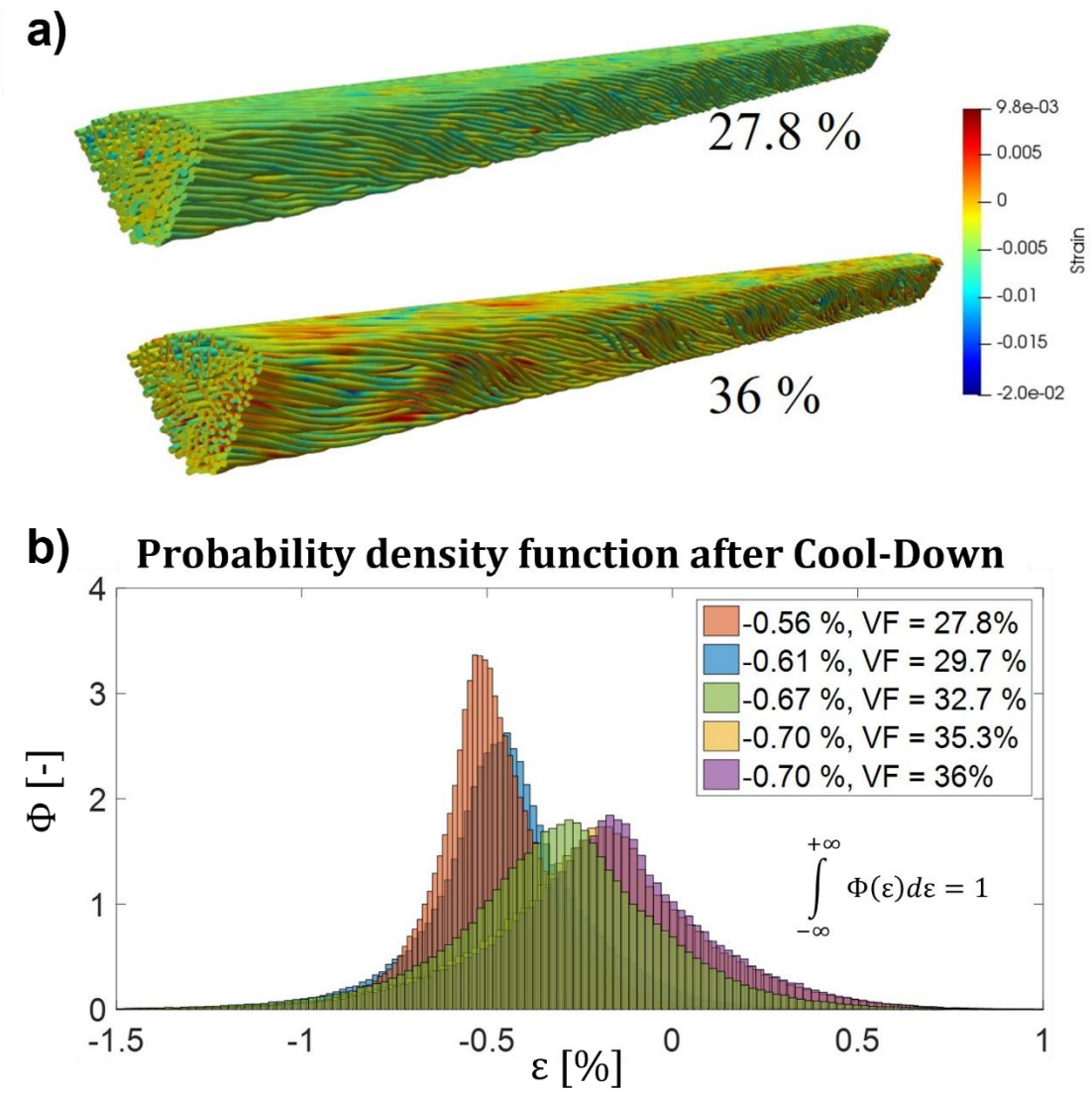

Figure 27. a) Carte des déformations simulées par MULTIFIL après CD pour deux VF différents ; b) Répartition des déformations après CD en fonction du VF (Riccioli 2020).

La Figure 27b) montre que la distribution passe clairement d'étroite et pointue à une plus grande et plus large pour des fractions de vide plus importantes, détectant ainsi un effet de seuil autour de 32 % de taux de vide. Les câbles au taux de vide plus élevés seront majoritairement exposés à la fracture des filaments comme illustré aussi par Figure 28a).

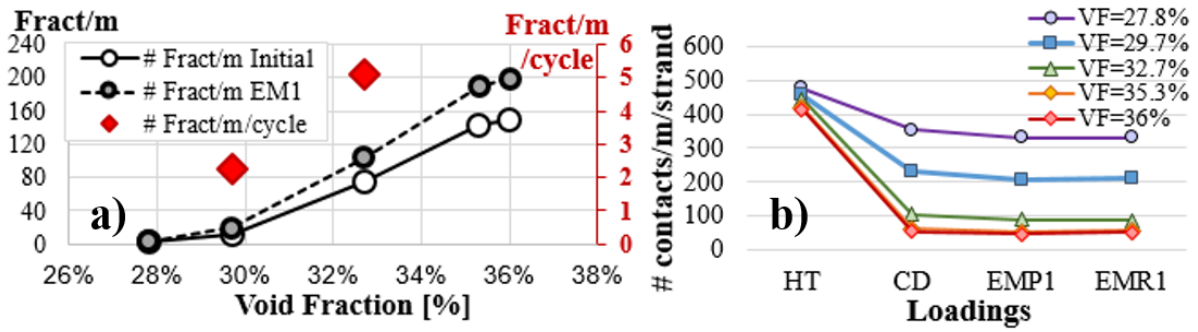

Figure 28. a) Pour chaque chargement, variation du nombre de fractures par mètre en fonction des VF. b) Pour chaque chargement, variation du nombre de contacts par mètre et par brin en fonction des VF.

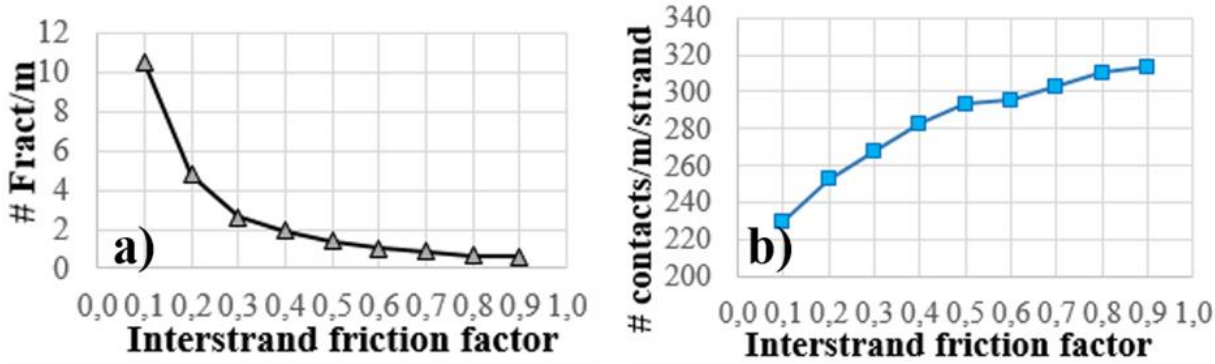

Figure 29. a) Variation du nombre de fractures par mètre en fonction du coefficient de frottement après CD. b) Variation du nombre de contacts par mètre et brin en fonction du coefficient de frottement après CD.

L'analyse réalisée à la fin du CD (Figure 29a)) confirme que si les coefficients de frottement augmentent, les fractures par mètre diminuent, et un seuil autour de 0,2-0,3 est observé.

L'étude des contacts (Yagotintsev 2019) est importante pour l'analyse des pertes AC, car ils affectent les résistances inter-brins (Nijhuis 2004). Les graphiques de la Figure 28b) et de la Figure 29b) indiquent le nombre de contacts, qui sont les mêmes qu'après la simulation du traitement thermique. Cette étude est centrée sur les contacts créés au cours de la fabrication du câble, qui se caractérisera par une résistance faible (Yagotintsev 2019) et vise à étudier leur évolution lors des sollicitations mécaniques. La Figure 29a) montre que les câbles les plus compactés se caractérisent par des contacts plus forts après la phase de fabrication.

La Figure 29b) se réfère aux contacts après CD, et montre que des coefficients de frottement plus élevés font que le câble préserve les contacts forts créés lors de la fabrication.

C. Etude et comparaison d'autres designs de CICCs

L'objectif principal de cette section est d'illustrer la polyvalence du protocole numérique et du modèle MULTFIL pour simuler différents CICCs en Nb_3Sn : CICC du CS d'ITER (Bessette 2014), CICC du CS de JT60-SA (Yoshida 2010) et CICC du TF du DTT (Giannini 2021).

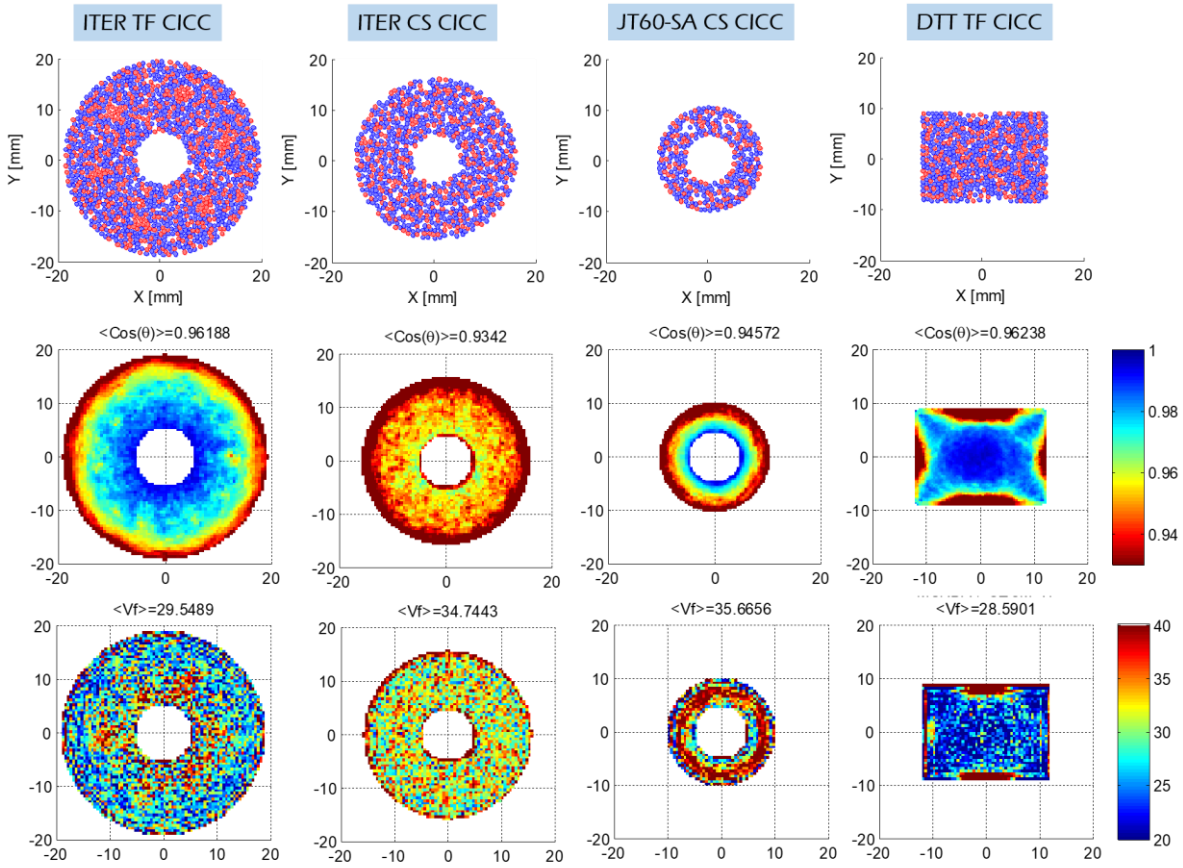

Figure 30. Première ligne : pour chaque design, position des brins Cu et Nb_3Sn sur la section à 75 mm ; deuxième ligne : carte polaire cumulée de l'angle de torsion local pour différents designs ; troisième ligne : carte polaire cumulée de la fraction de vide locale pour différents modèles.

La position des brins de Cu (voir la première ligne de la Figure 30) montre bien l'absence de noyaux de Cu dans les pétales des JT-60SA CS et ITER CS CICC par rapport à le CICC du TF d'ITER. Les noyaux de Cu sont non visibles pour le conducteur du TF du DTT, du fait du fort compactage du câble les fils des pétales ont tendance à se mélanger les uns aux autres. Tous les câbles circulaires présentent, comme attendu des hélices de câblage, un gradient radial présentant des fils plus rectilignes vers le centre du câble (voir Figure 30, ligne 2). De toute évidence, le câble du CS d'ITER se caractérise par un angle d'inclinaison plus élevé par rapport à l'axe du câble, en raison de sa conception à pas courts torsadés. Une distribution intéressante est illustrée par la géométrie rectangulaire avec des fils plus droits jusqu'aux coins des câbles. Les trois câbles circulaires présentent un taux de vide (VF) constant en fonction de la coordonnée angulaire. Cependant, les cartes présentent une distribution radiale complètement différente selon le cas de test, ce qui indique que la distribution VF locale est également fonction des dimensions, ainsi que du VF moyen lui-même. De plus, le VF local pour le rectangulaire montre une distribution particulière avec des pics minimaux correspondant aux angles.

V. Conclusions et perspectives

Les travaux présentés dans ce doctorat visent à mieux comprendre l'un des enjeux majeurs liés aux systèmes magnétiques d'ITER. Le supraconducteur Nb_3Sn composant les câbles de la bobine TF est fragile et sensible aux contraintes et cette particularité influence la capacité de transport de courant du supraconducteur. Parallèlement, des essais expérimentaux ont montré qu'après 1000 chargements cycliques aux conditions nominales de fonctionnement (68 kA et 11,8 T), les CICCs de la bobine TF se caractérisent par une dégradation des performances. Cependant, même si plusieurs travaux attribuent la perte de performance à des phénomènes mécaniques réversibles ou irréversibles se produisant à l'échelle des brins, il n'est pas possible de mesurer la déformation locale à l'intérieur des câbles et ainsi de s'attaquer à la cause profonde de la dégradation. L'Organisation Internationale ITER et le CEA ont donc favorisé l'adaptation du code MULTIFIL, capable de simuler l'interaction mécanique de centaines de brins, pour étudier les CICCs d'ITER afin de reproduire les chargements thermomécaniques et électromécaniques appliqués à ces conducteurs, en calculant les cartes de déformation au niveau des brins individuels. Une ancienne version du code a créé un modèle sous-échelle du CICC du TF d'ITER afin de simuler le comportement du conducteur lorsqu'il est soumis aux mêmes chargements que ceux appliqués aux échantillons SULTAN. Il a néanmoins laissé de nombreux développements inachevés et de nombreuses questions ouvertes. Le projet de thèse a tenté de répondre aux besoins d'ITER et de la communauté de la fusion à travers la création d'un modèle fiable de simulation des câbles de fusion en termes de représentabilité et de compréhension du fonctionnement des phénomènes mécaniques à l'échelle locale. De plus, le projet a abordé la question de la dégradation cyclique à la fois par des activités expérimentales et par la modélisation numérique.

Les activités expérimentales visaient à étudier le comportement en fatigue en traction et compression des brins Nb_3Sn soumis à des milliers de cycles de chargements uniaxiaux. Plusieurs campagnes expérimentales ont été réalisées à la fois à température ambiante et cryogénique. Ces activités expérimentales ont permis une caractérisation mécanique complète des propriétés du brin plus détaillées que les études présentées dans la littérature pour les essais de traction des brins en Nb_3Sn pendant des centaines de cycles. De plus, grâce aux travaux de ce doctorat, un tout nouveau protocole expérimental a été développé pour tester des fils supraconducteurs très fragiles et de petite taille en compression. Les perspectives de ce travail expérimental seraient de nouvelles campagnes cryogéniques pour confirmer les résultats de traction et de compression obtenus, tandis que les essais de traction cyclique à température ambiante sont aptes à fournir des lois de comportement mécaniques à implémenter dans des codes numériques.

Grâce aux travaux numériques basés sur le code MULTIFIL, un nouveau modèle fiable et solide pour la simulation des CICC a été créé pour évaluer l'état de déformation

local et global pour une géométrie de câble complexe à pleine échelle. De plus, un protocole numérique et des routines de post-traitement ont été développés ad hoc pour l'étude MULTIFIL des câbles de fusion. Ce qui a permis la compréhension phénoménologique des mécanismes mécaniques macroscopiques affectant la dégradation globale des performances électriques du conducteur et de l'impact des paramètres de conception sur le comportement électromécanique du câble. Les simulations du modèle du CICC du TF d'ITER ont mis en évidence une plus grande exposition à la contrainte de traction du modèle de câble complet que dans le modèle à pétale unique. Par conséquent, le modèle à pétale unique utilisé jusqu'à présent dans les travaux antérieurs ne pouvait pas être complètement représentatif des principaux mécanismes se produisant à l'intérieur d'un conducteur plein.

Les études paramétriques réalisées montrent une transition nette du comportement bloqué au comportement lâche à travers l'évolution des ruptures, des contacts et des rapports de flexion et de plasticité. Le coefficient de frottement est fixe à 0,1 et toutes les principales études ont été réalisées à cette valeur. Cependant, le coefficient de frottement réel entre brins en contact est inconnu, et probablement plus complexe qu'un simple coefficient de frottement. Des futurs travaux et investigations, avec un tribomètre par exemple, sont recommandés pour en déduire un modèle de contact plus réaliste pour les simulations.

Le protocole numérique MULTIFIL développé pour façonner les câbles de fusion et le protocole de post-traitement MUNDA pour étudier les principaux paramètres géométriques ont également été appliqués avec succès à d'autres câbles tokamak. Des analyses préliminaires de comparaison géométrique de ces conducteurs ont mis en évidence des caractéristiques mécaniques importantes qui pourraient affecter le comportement électrique des câbles, telles que la distribution locale du taux de vide. Les futures études devraient se concentrer sur l'étude mécanique des différents conducteurs sous sollicitations thermiques et électromagnétiques similaire aux études réalisées pour le CICC du TF d' l'ITER.

I. FIRST PART – Ph.D. SCIENTIFIC CONTEXT AND CHALLENGES

LIST OF SYMBOLS

B	$[T]$	Magnetic field/Toroidal field
B_c	$[T]$	Critical magnetic field
B_{c1}	$[T]$	Lower critical magnetic field
B_{c2}	$[T]$	Upper critical magnetic field
B_{op}	$[T]$	Operating magnetic field
Cu	$[-]$	Copper
CuNi	$[-]$	Copper-Nickel
Cr	$[-]$	Chrome
E	$[\mu V/m]$	Electric field
E_0	$[\mu V/m]$	Critical electric field
F_p	$[N]$	Pinning force
I	$[A]$	Current
I_c	$[A]$	Critical current
I_{op}	$[A]$	Operating current
J	$[A/mm^2]$	Current density
J_c	$[A/mm^2]$	Critical current density
Jc_E, Jc_{eng}	$[A/mm^2]$	Engineering critical current density
J_{op}	$[A/mm^2]$	Operating current density
Nb	$[-]$	Niobium
Nb_3Sn	$[-]$	Niobium-three-Tin
$NbTa$	$[-]$	Niobium-Tantalium
$NbTi$	$[-]$	Niobium-Titanium
n	$[-]$	n-value
$\hat{n}$	$[10^{19}m^{-3}]$	Particles density
P_{ext}	$[J]$	External heating power
P_{fus}	$[J]$	Fusion power
Q	$[-]$	Amplification factor
R	$[m]$	Plasma radius
S	$[mm^2]$	Strand cross-section
Sn	$[-]$	Tin
T	$[K]$	Temperature
T_c	$[K]$	Critical temperature
T_{cs}	$[K]$	Temperature of current sharing
T_{op}	$[K]$	Operating temperature
ΔT_{cs}	$[K]$	Temperature margin
α	$[-]$	Helium nucleus
ε	$[\%]$-$[-]$	Strain
λ	$[nm]$	London penetration depth

μ_m	***[H/m]-[N/A²]***	Magnetic permeability
μ_0	***[H/m]-[N/A²]***	Vacuum permeability
τ_E	***[s]***	Energy confinement time
χ_m	***[-]***	Magnetic susceptibility

I.1 CHAPTER – SUPERCONDUCTIVITY

The objective of this chapter is to introduce the superconducting phenomenon, which plays a key role in the presented dissertation. The information of this chapter is partially based on the books (Evans 2018), (Tixador 1995) and (Wilson 1983). Section I.1.1 presents superconductors and focuses on the properties defining them. Section I.1.2 describes the complexity of the wires made of superconducting materials and section I.1.3 presents the main industrial applications of these materials.

I.1.1 Superconducting properties

The physicist Kamerlingh Onnes discovered superconductivity in 1911 while performing experiments with liquefied helium, which boils at 4.2 K at the atmospheric pressure, to study the electrical resistance of metals at cryogenic temperatures. The following paragraphs present the two main properties defining a superconducting material and the physical conditions at which superconductivity exists.

I.1.1.1 Electrical resistance

The superconductivity is a typical property of some materials related to a non-measurable electrical resistance. Commonly, the electrical resistance of the conductors decreases with temperature. This happens because resistivity depends on the material imperfections and on the thermal vibration of the ions. When the temperature decreases the atoms vibrate less and less and the resistance tends to a lower limit defined by the material imperfections. However, K. Onnes observed that for some materials the resistance dropped close to zero below a certain temperature. The experience of K. Onnes with mercury below 4.2 K is illustrated in Figure I.1.1, taken from the site (Khachan).

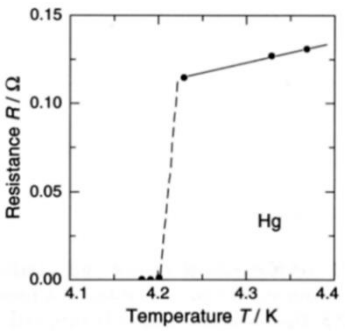

Figure I.1.1 The resistance of mercury as a function of temperature measured by K. Onnes in 1911 (Khachan).

The classical conducting laws do not apply to superconductors, but they follow the BCS (Bardeen Cooper Schrieffer) theory developed in 1957 by John Bardeen, Leon Cooper and J. Robert Schrieffer. This theory is based on quantic phenomena that include the creation of the *Cooper pairs* made of two electrons that "attract" each other. The passage of the first electron of the pair temporary deforms the lattice and offers an easier passage through the lattice to the second one. This natural vibration of the lattice is called *phonon*. The interaction between a Cooper pair is temporary and each electron is attracted to every other electron forming a large network of interactions thanks to a temporary accumulation of positive charges due to the passage of the previous electrons.

An electrical resistance almost zero means that the Joule's effect does not occur and consequently there is not heat dissipation in the superconductor when the current flows. In fact, the superconductor can usually be considered as an equipotential domain when it is far from its critical surface. This property of superconductors makes them a powerful tool for carrying large currents and thus producing large magnetic fields, which is important in numerous R&D and industrial applications. Some of them are presented in section I.1.3.

I.1.1.2 Meissner's effect

Another feature of superconductors, called *Meissner's effect*, was experimentally observed in 1933 by Walter Meissner and Robert Ochsenfeld and related to the so-called perfect-diamagnetic behavior. They observed that at the temperature of the transition from normal to superconducting state, the magnetic behavior of the material changed from non-magnetic to almost perfectly diamagnetic. An example of this transition is given in Figure I.1.2.

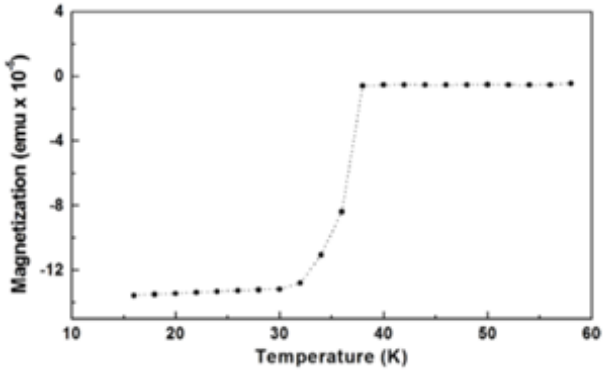

Figure I.1.2. Superconducting transition of the MgB_2 at 38 K measured with the magnetization (Jha 2009).

A diamagnetic material is characterized by a magnetic field that opposes the applied external one. The magnetic permeability μ_m in the diamagnetic materials is smaller than the vacuum permeability μ_0 and in most of them is smaller than one or equals to zero. Therefore, the magnetic susceptibility $\chi_m = \mu_m - 1$ is usually negative for diamagnetic materials and it means that these materials are repelled by the applied

magnetic field. Superconductors are perfectly diamagnetic because they are able to completely expel the applied magnetic field, except for an external layer called *London penetration depth* λ. The transition superconducting-normal state is a reversible thermodynamic transition and does not depend on the presence of the external magnetic field. Figure I.1.3 illustrates this effect.

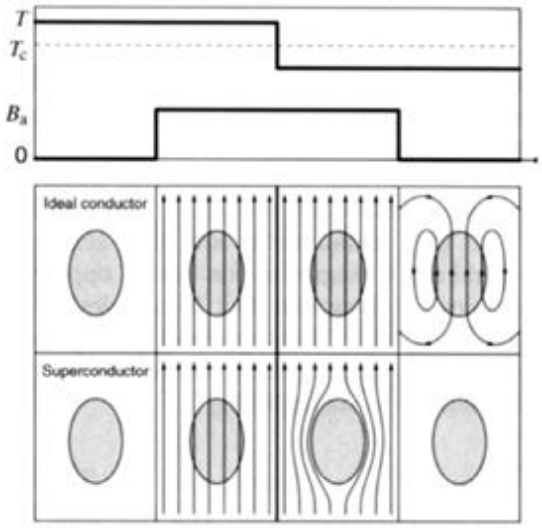

Figure I.1.3. Meissner's effect and difference between an ideal conductor and a superconductor (Khachan).

I.1.1.3 Critical surface

As explained in the sections above, superconductivity is a physical state of some materials that can be either simple elements or compounds. However, this state is only maintained as long as the material is below a certain critical surface identified in the *(B,J,T)* space and defining the superconducting domain for this specific material. The intersections of the surface with axes *T* and *B* give the intrinsic critical values of temperature T_c and magnetic field B_c for this material. An illustration of critical surface is given in Figure I.1.4.

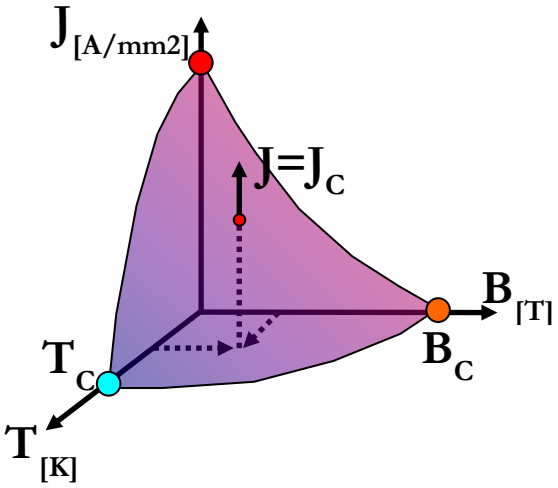

Figure I.1.4. Critical surface inside which the superconducting state exists.

The critical temperature T_c is the temperature defining the transition from the normal to the superconducting state when no external field is applied and no current flows in the material. Figure I.1.5 reports examples of T_c values for several superconductors as a function of the year of discovery.

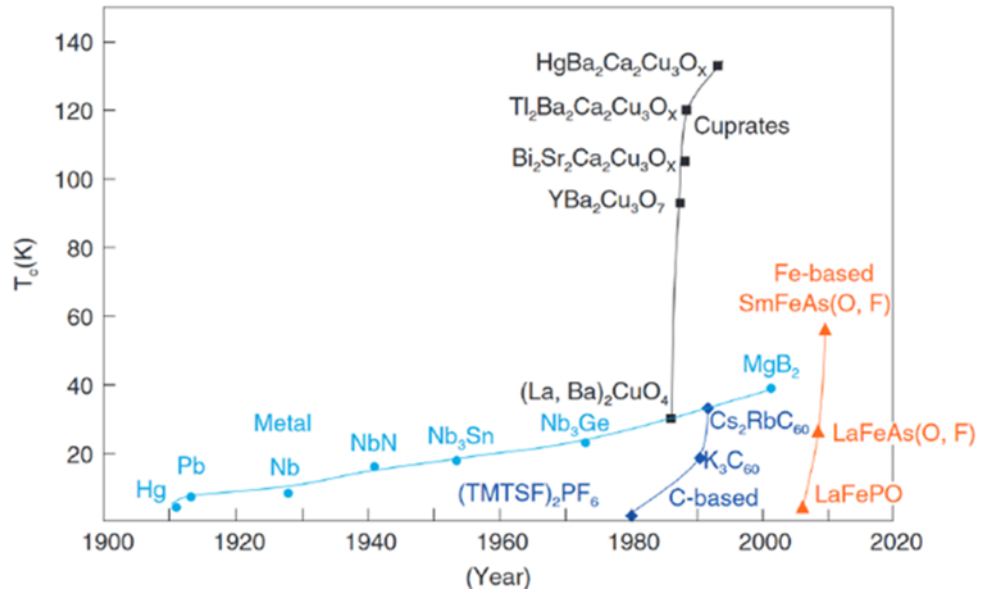

Figure I.1.5. Critical values of the temperatures for some superconductors as a function of their discovery (Shibata 2011).

Superconductors can be classified in *low temperature superconductors* (LTS) and *high temperature superconductors* (HTS). For critical temperatures below 77 K, it is common to talk about LTS and they are usually cooled with liquid helium (LHe). The superconductors belonging to the HTS group have a critical temperature above 77 K and they can thus be cooled in liquid nitrogen (LN_2).

The critical magnetic field B_c corresponds to the highest external field that can be tolerated by the superconductor without losing its superconductivity at 0 K and without current. Plotting the magnetic field developed inside the superconductor as a function of the external magnetic field to which it is exposed, two different behaviors are observed and illustrated in Figure I.1.6.

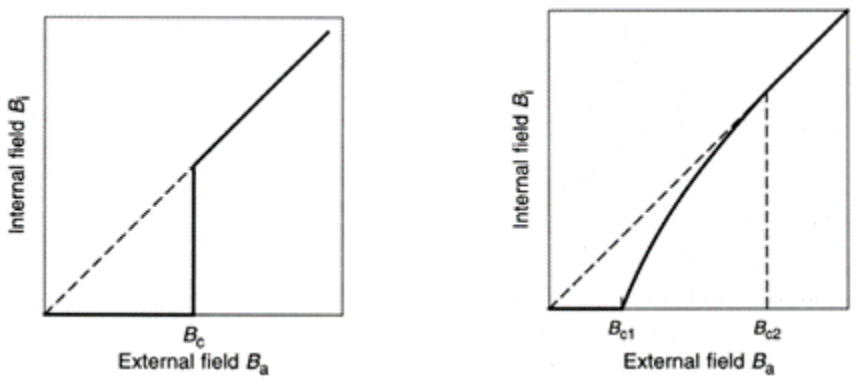

Figure I.1.6. a) Type-I superconductor, b) Type-II superconductor (Khachan).

Figure I.1.6a) shows the behavior of type-I superconductors, which have a sudden transition from the perfect diamagnetic behavior (magnetic susceptibility is negative $\chi_m = -1$) to the normal state at a specific value of the external magnetic field B_c. Figure I.1.6b) shows the behavior of type-II superconductors that have two critical fields B_{c1} and B_{c2}. The Meissner's effect happens below the lower limit B_{c1}, which is usually very small (few mT), while between B_{c1} and B_{c2} the field partially penetrates into the superconductor, but superconductivity is maintained. In this case, the superconductor is in the so-called mixed state. The magnetic field penetrates into the superconductor through tubes of magnetic flux called vortex or fluxoids, represented in Figure I.1.7. The mixed state makes the type-II superconductors exploitable for industrial application since B_{c2} can reach several dozens of Tesla. For example, wires made of Nb_3Sn have a B_{c2} limit at 24.5 T.

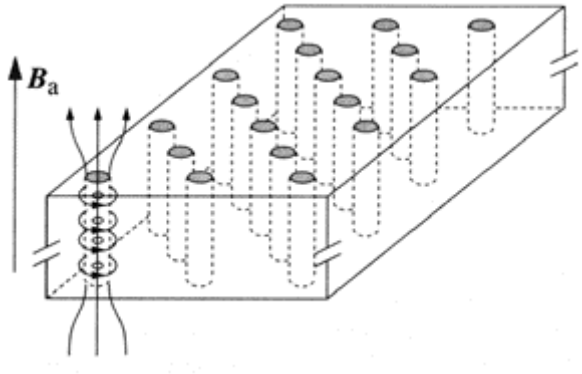

Figure I.1.7. Vortices of normal state in the superconductor during the mixed state (Khachan).

The critical current density J_c is the maximum transport current density that can flow in a given superconducting material while in superconducting state. It is generally given as a function of the applied field and temperature $J_c(B,T)$ and it is, thus, the one defining the critical surface. For the type-I superconductors, it corresponds to the maximum transport current density that can flow on the surface of the superconductor to attenuate the penetration of the external magnetic field. Concerning the type-II superconductors, the fluxoids tends to dispose themselves following a regular lattice to minimize the energy. However, it is necessary to have a gradient of the fluxoids density, so that the vortices currents create a macroscopic net current that is not zero. The gradient originates also a macroscopic net force per unit volume corresponding to the Lorentz force that interacts with the magnetic field and makes the fluxoids move. In this case, the flux flow regime is established inside the superconductor and thermal dissipation occurs. In order to prevent this phenomenon, the vortices are pinned thanks to imperfections, dislocations, defaults of the lattice and they do not move until when the Lorentz force is greater than the pinning force F_p. The critical current density in type-II superconductors is the transport current per unit area needed to unlock the vortices. The higher the critical current density, the more the material has an inhomogeneous distribution of the fluxoids.

Differently from the critical temperature and magnetic field, which are intrinsic physical properties of the superconducting material, the critical current density depends on imperfections and impurities introduced during manufacture to increase the pinning force of type-II superconductors. For example, Nb_3Sn wires manufactured by different routes may exhibit different J_c and thus different critical surfaces.

The use of superconducting electromagnets permits a negligible energy dissipation by Joule heating. The current can permanently flow as long as the superconductor stays below its critical surface and so the magnetic field can be easily maintained at the cost of the cryogenic cooling.

I.1.2 Superconducting wires

Nowadays, the most exploited superconducting materials are NbTi and Nb_3Sn, but the work done in this dissertation focuses on Nb_3Sn and its role in the cables for fusion reactors. Therefore, the next paragraphs describe the properties of the Nb_3Sn wires.

I.1.2.1 Nb_3Sn wires structure

Nb_3Sn superconductors are usually found as composite wires, or strands, with thousands of twisted superconducting filaments embedded in a copper matrix, as shown in Figure I.1.8. This structure is referred to as *multifilamentary composite*.

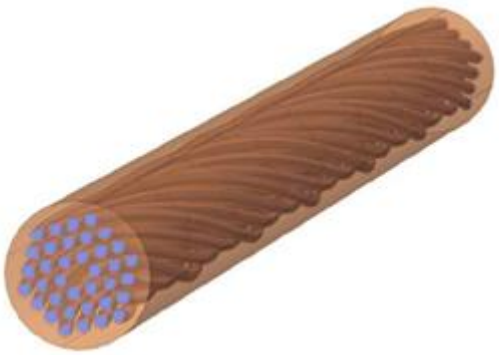

Figure I.1.8. Superconducting strand model by (Wang 2016).

The origin of this structure relates to the need for stabilizing the superconductor when thermo-magnetic perturbations occur and avoiding the transition to the normal state, called *quench*. The superconductor is a metastable state, because its specific heat is extremely low at cryogenic temperature. Hence, the slightest energy dissipation can cause a strong increase of the temperature and the transition of the superconductor.

One of the causes of energy dissipation is the movement of the superconductor under electromagnetic load and it is thus necessary to support the fine superconducting filaments by a mechanical matrix. The copper matrix thermal conductivity improves the thermal conduction of the material, since at low temperatures the superconductor is not a good conductor, and so its capability to conduct heat. The placing of the superconductor

in a good thermal and electrically conductive matrix reduces its sensitivity to perturbations. Moreover, the multi-filamentary structure prevents any temperature increase when a change of current or magnetic field occurs. The filaments are said *coupled through the matrix* and they are twisted to reduce the length of the induced currents loops and the associated losses. The twist pitch is usually not smaller than four/five times the strand diameter for mechanical reasons. Moreover, a CuNi barrier can be added around the filaments to increase the transversal resistivity of the matrix since $\rho_{CuNi} \sim 2000\rho_{Cu}$ at 4 K. The internal structure of modern strands is complex and reflects the application for which it is designed (high J_c, low losses etc…), as well as its manufacturing process.

I.1.2.2 Superconducting materials for wires

The choice of the superconductor is based on several considerations regarding its physical properties and performance, its cost, its workability or how easily it can be worked into a new shape. Figure I.1.9 plots J_c-B characteristics for some of the existing superconducting wires when the temperature is set at the usual operating temperature of these wires. In this plot, the critical current density J_c is scaled to the whole wire cross-sectional surface, including the matrix and other non-superconducting materials in the strand usually called *Non-Cu materials*. This specific definition of J_c is the *engineering critical current density*, sometimes labelled Jc_E or Jc_{eng}. The plot shows that the operating range of classical LTS wires is around 10^2-10^3 A/mm² (below 10 T for NbTi and below 18 T for Nb_3Sn), while HTS wires bear the promise of higher current densities at much higher fields.

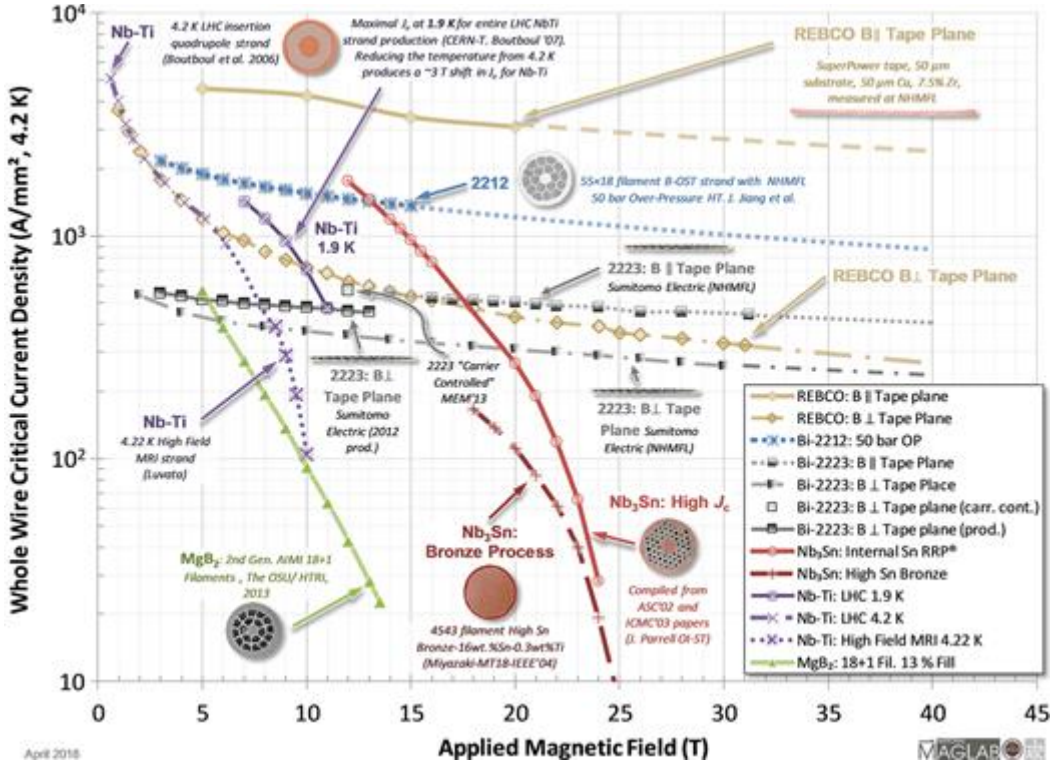

Figure I.1.9. Engineering critical current density vs applied magnetic field for the existing superconducting wires (Lee 2018).

Nb_3Sn and the NbTi have today the higher Technological Readiness Level (TRL), thanks to strong push by R&D projects (ITER/LHC) and NMR industrial market. In recent years, the need for higher operating fields has led to the use of Nb_3Sn because of its high critical magnetic field. Figure I.1.10 reports Nb_3Sn critical surface compared to the one of NbTi. As illustrated in the plot, Nb_3Sn exhibits a larger critical surface than NbTi.

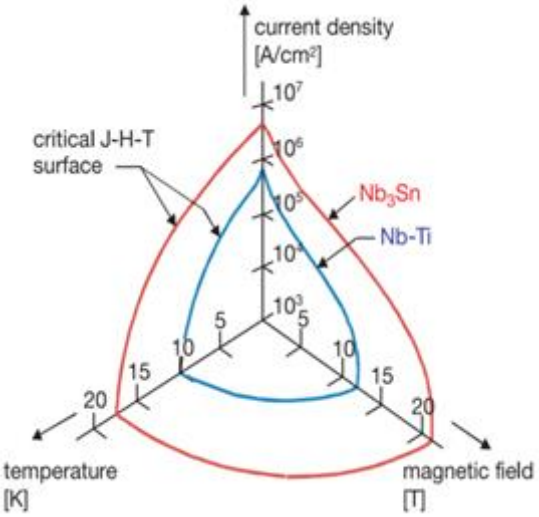

Figure I.1.10. Critical surface of the Nb_3Sn in red and NbTi in blue (Evans 2018).

Nb_3Sn belongs to the superconducting A15-type intermetallic compounds, with a body-centered cubic lattice of Sn atoms with two Nb atoms on each face of the cubic. As for critical current density, and similarly to other A15 compounds, grain boundaries are the main pinning centers. Therefore, to have a high J_c, the Nb_3Sn must be treated in such a way as to obtain a fine and homogeneous structure, with grains of diameters between 30 and 300 nm. The superconducting phase is, thus, obtained by a high and long temperature heat treatment, over 600 °C and 500 hours, which adds a considerable complexity in the manufacturing process of systems using this type of strands.

I.1.2.3 Wires operating conditions

The definition of the critical current of the superconducting wire corresponds to the appearance of an electric field. Due to the flux flow of the vortices, the increase in the electric field during the transition to the normal state is progressive, and the community conventionally chose a *critical electric field* E_0 at 10 µV/m for standard LTS. The critical surface is thus defined at an average electric field of E_0 inside the strand. The temperature measured when the electric field reaches E_0 is called the *current sharing temperature* T_{cs}.

The operating conditions of a wire are defined by the *operating magnetic field* B_{op}, which can include both external fields and self-field components, the *operating temperature* T_{op}, which is the temperature of the superconductor, and the *operating current density* J_{op}, referred to engineering current density unless otherwise stated, and usually chosen below the critical current density, as shown in Figure I.1.11. Indeed, in

order to have sufficient stability margin against perturbation and avoid quenches, the superconductor cannot operate too close to the critical surface, especially in perturbated environments as Tokamaks where heat fluxes have various sources (neutronic load, plasma, AC losses, etc…). This margin in operating current density can also be expressed as temperature margin as illustrated in Figure I.1.11. The *temperature margin* is an important design parameter and it is the difference between the current sharing temperature and the operating temperature: $\Delta T_{cs} = T_{cs} - T_{op}$.

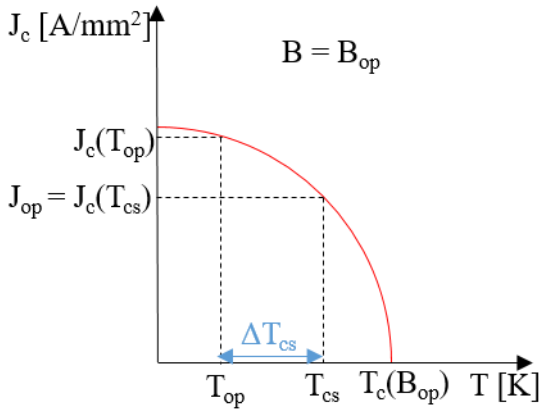

Figure I.1.11. *T-J_c* characteristic and illustration of the temperature margin.

The following sections and paragraphs, unless otherwise stated, might refer to J instead of J_{op} (A/mm² of superconducting strand), T instead of T_{op} (K), and B instead of B_{op} (T). Furthermore, for a given strand cross-section S (mm²) the *wire operating current* (or *transport current*) I_{op} is defined as the product of S by J_{op}.

I.1.2.4 Power law and superconducting transition

As aforementioned, the transition of the wire from the superconducting to the normal state is gradual and related to the increasing mean electric field inside the wire. The shape of this gradual transition is described by the so-called *power law* describing the relation between electric field and current. The superconductor electric field is thus described by a non-linear function of the current density given by:

$$E = E_0 \left(\frac{J}{J_c(B,T)} \right)^n [V/m] \qquad \text{(I. 1)}$$

In the equation (I.1), $J_c(B,T)$ is the critical current density of the wire, while n is called *transition index*, or *n-value,* and describes the steepness of the transition. The *n-value* is sometimes given as a function of J since the steepness of the transition varies with the transport current density. Moreover, for a wire, J and J_c both refer to the strand cross-sectional area, hence the equation (I.1) can be written also as follows:

$$E = E_0 \left(\frac{I}{I_c(B,T)} \right)^n [V/m]. \qquad \text{(I. 2)}$$

Figure I.1.12 reports an example of the *J-E* characteristic and shows the influence of the *n-value* on the steepness of the *E(J)* curve. A log-scale plot of the same curves emphasizes the difference of steepness due to the *n-value* exponent.

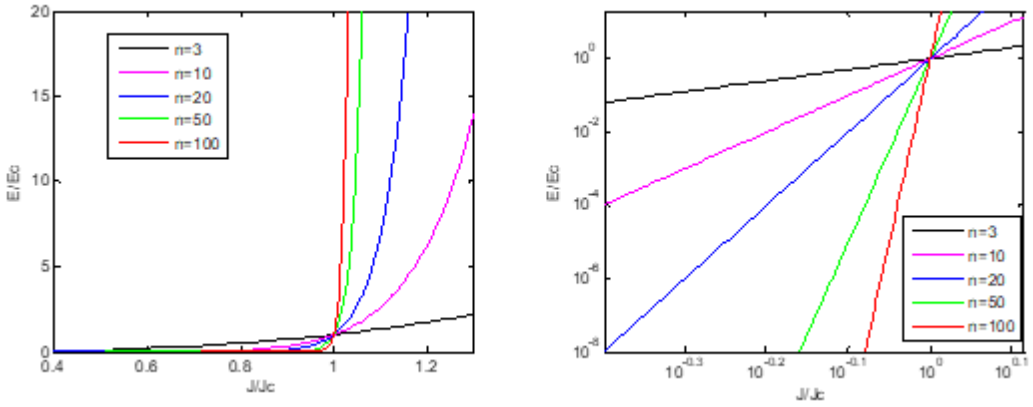

Figure I.1.12. The plot of the power law for a generic superconductor as a function of the *n-value*, for given magnetic field and temperature.

Typical *n-values* for single wires measured at 4.2 K and 12 T are in the range 20-30 for IT-wires and 30-50 for BR-wires (Mitchell 2003). From one hand, a high *n-value* means less losses developed below J_c. On the other hand, a faster transition makes the superconductor less stable when approaching the critical surface and implies more risks of undesired transitions due to perturbations. Moreover, lower *n-values* than expected are associated with non-uniform or broken filaments (Mitchell 2003).

I.1.2.5 Nb_3Sn IT-wires manufacture

The major drawbacks of Nb_3Sn are its manufacturing process, which requires a long heat treatment, and its extreme brittleness. There are three main processes to produce Nb_3Sn wires: *Bronze Route (BR)*, *Powder In Tube (PIT)* and *Internal Tin (IT)*. All of them involve procedures, like stacking, extrusion and drawing, to prepare the precursors of the Nb_3Sn that will react during the high temperature heat treatment (HT). The chosen method depends on the required wire properties, as well as on the manufacturer preferred industrial process.

Figure I.1.13 illustrates the main manufacturing steps for a generic IT-wire. Rods of Nb and NbTi are inserted into an Oxygen-Free Copper billet and the central hole hosts the Sn core making in this way a sub-bundle (Figure I.1.13a-b). After extrusion, several sub-element rods are then inserted into an Oxygen-Free Copper matrix composing the second stack (Figure I.1.13c). During the heat treatment the Sn cores diffuse to create the superconducting phase with the Nb rods, and a bronze matrix with the inner Cu. The final configuration foresees a diffusive barrier to avoid the diffusion of the Sn into the external copper layer during the HT, which remains pure for the wire stabilization. The purity of the Copper matrix is given by the *Residual Resistivity Ratio* (RRR), which is the ratio between the strand resistivity at 20 K and 273 K.

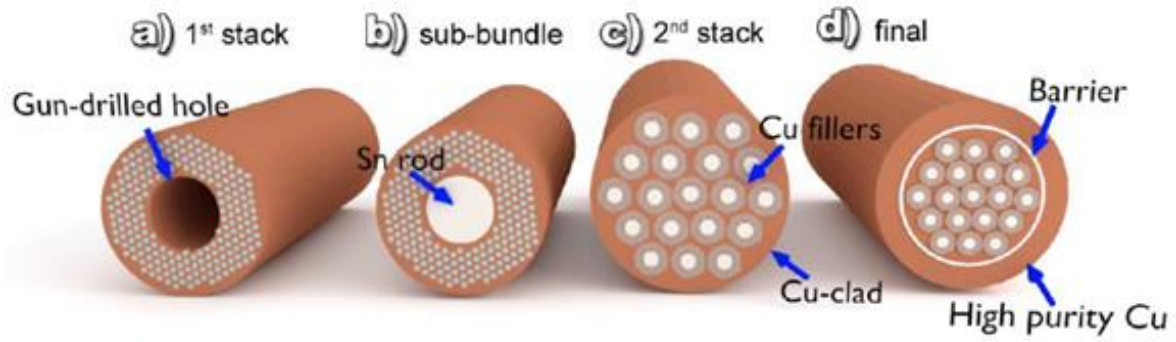

Figure I.1.13. Stacking steps of a generic IT-wire taken from (Sanabria 2017).

A very similar method is used for the BR wires, where each Nb or Nb-Ta rod is inserted into a bronze matrix and the sub-bundles are composed of these filaments. This manufacture is more complicated because at each drawing steps the bronze loses its ductility, so annealing steps are necessary to restore it.

The IT-wires produce a slightly higher J_c with respect to the BR wires as illustrated by typical values in Table I.1.1, at the cost of greater filaments diameter that can cause an increase of the hysteresis losses. Hence, the IT-wires might be suitable for constant peak-field operations that are ramped up slowly.

Table I.1.1. Summary of the main superconducting wires typical properties (from (Sanabria 2017)).

Typical parameters	*IT wires*	*BR wires*
Jc [A/mm^2] at (12 T,4.2 K)	1000	900
Filament diameter [μm]	3-6	2-4
Hysteresis losses [mJ/cm^3] for ±3 T	900	200

Figure I.1.14 shows typical cross-sections of BR and IT wires.

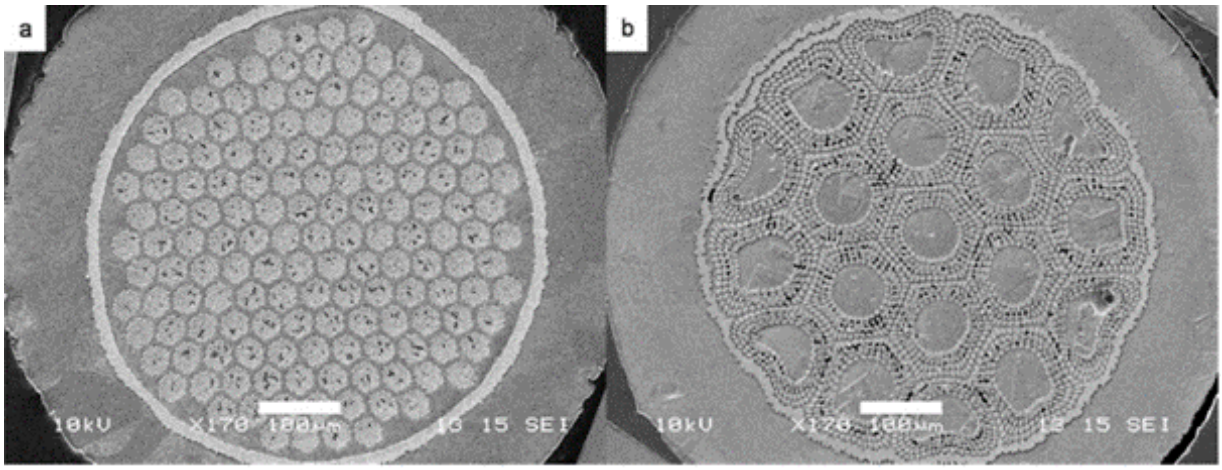

Figure I.1.14. Transverse cross-sections of BR wire (a) and IT wire (b) taken from (Miyoshi 2009).

The experimental work done in this dissertation refers to the IT-Nb_3Sn wires of Oxford Superconducting Technology (OST) type. For this strand, 156 Nb and NbTi rods are inserted into a Copper billet during manufacturing. The 19 sub-element rods are then

assembled with a Tantalum sheet into the Copper tube to constitute the final billet (Boutboul 2016). These wires can reach critical current densities of ~3000 A/mm² and filaments diameters of 40-70 µm.

Finally, the PIT wires follow a quite different strategy of stacking: $NbSn_2$ powders are inserted into a Nb tube with a Cu sheath between them. The final stack is characterized by the Cu external layer and the characteristics are considered intermediate between the ones of the IT and BR wires.

Figure I.1.15 summarizes the main Nb_3Sn wires manufacture methods.

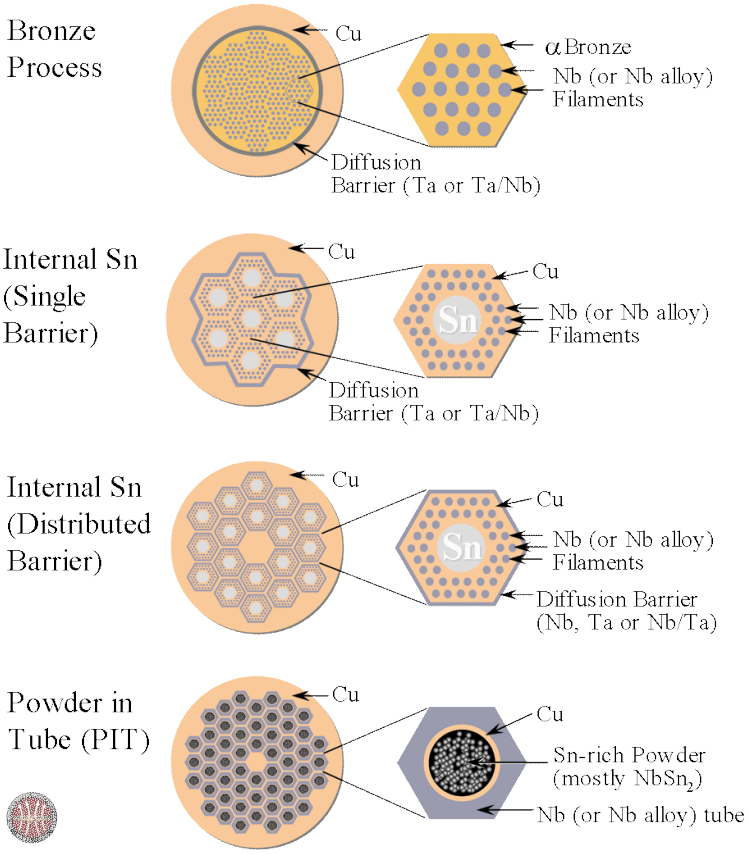

Figure I.1.15. Summary of the main Nb_3Sn wire manufacture processes (Lee 2018).

I.1.2.6 Mechanical sensitivity of Nb_3Sn strands

Differently from other common superconductors, Nb_3Sn wires critical current density is not just a function of magnetic field and temperature as defined by the critical surface illustrated in Figure I.1.4. There is also a sensitivity to the strain state of the superconducting filaments. Figure I.1.16 reports the critical current as a function of strain for an OST Nb_3Sn IT-strand at different temperatures and magnetic fields measured in the study (Ilyin 2007). Transport properties are thus hugely affected by strain, in particular below -1 % and above 0.2 % where filaments fracture occur.

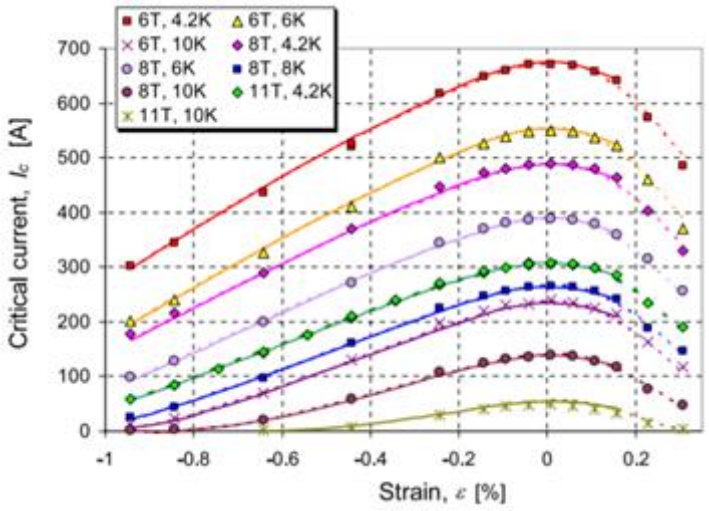

Figure I.1.16. Strain dependency of the critical current for the OST Nb_3Sn strand at different temperatures and magnetic fields (Ilyin 2007).

There are many possible fits of the experimental $I_c(B,T,\varepsilon)$ data points, but the *ITER scaling law* has been standardized by the relation defined in (ITER Organization 2008):

$$J_c = \frac{C}{B} s(\varepsilon)(1-t^{1.52})(1-t^2)b^p(1-b)^q, \tag{I.3}$$

where the variables are calculated by the formula defined in Table I.1.1.

Table I.1.2. ITER scaling law parameters formula (ITER Organization 2008).

Critical temperature [K]	$T_c^*(B,\varepsilon) = T_{c0max}^*[s(\varepsilon)]^{\frac{1}{3}}(1-b_0)^{\frac{1}{1.52}}$
Critical field [T]	$B_{c2}^*(T,\varepsilon) = B_{c20max}^* s(\varepsilon)(1-t^{1.52})$
Strain function	$s(\varepsilon) = 1 + \frac{1}{1-C_{a1}\varepsilon_{0,a}}\left[C_{a1}\left(\sqrt{\varepsilon_{sh}{}^2 + \varepsilon_{0,a}{}^2} - \sqrt{(\varepsilon-\varepsilon_{sh})^2 + \varepsilon_{0,a}{}^2}\right) - C_{a2}\varepsilon\right]$
	$\varepsilon_{sh} = \frac{C_{a2}\varepsilon_{0,a}}{\sqrt{C_{a1}{}^2 - C_{a2}{}^2}}$
Reduced magnetic field	$b = \frac{B}{B_{c2}^*(T,\varepsilon)}$
Reduced magnetic field at 0 K	$b_0 = \frac{B}{B_{c2}^*(0,\varepsilon)}$
Reduced temperature	$t = \frac{T}{T_c^*(0,\varepsilon)}$
C	Scaling constant
B_{c20max}^*	Upper critical field at 0 K and 0 strain
T_{c0max}^*	Critical temperature at 0 T and 0 strain
p	Low field exponent of the pinning force ($p \simeq 0.5$)
q	High field exponent of the pinning force ($q \simeq 2$)
C_{a1}	First strain fitting constant
C_{a2}	Second strain fitting constant

$\varepsilon_{0,a}$	Residual strain component

C, p and q are fitting parameters specific for each wire. $\varepsilon_{0,a}$ is the remaining strain component when the applied strain ε is zero.

I.1.3 Applications

The previous sections highlighted interesting current carrying capabilities of existing superconducting wires, which can be 100 times the typical densities of usual conductors. This feature makes superconductors of practical interest for the manufacture of compact and powerful electromagnets, at the cost of cryogenic cooling. The superconductors, like NbTi and Nb_3Sn, work at cryogenic temperatures in the range of 2-8 K and the refrigerant is usually Helium 4 while a large effort is now being devoted to the R&D of HTS cables to work with LN_2 and increase the magnets performance.

Nowadays, superconductivity plays a key role for some technological applications for which an equivalent competitor made with resistive conductors does not exist or is not as efficient. Generally, these technologies are needed for systems producing high magnetic inductions through large currents without heat dissipation. Even though there are several possible applications under study, the three main fields exploiting superconductivity are fusion reactors, particles accelerators and the Nuclear Magnetic Resonance (NMR). The framework of this Ph.D. work relies on the superconductivity for the magnetically confined fusion reactors. Although this application will be detailed in the next chapter, it is important to mention that NMR medical devices are presently the only widespread industrial application of superconductivity so far. At the same time in R&D, the high energies physics applications like the particles accelerators are the largest users of superconducting technology due to the need for very high fields in their magnets.

I.1.4 Conclusion

This chapter showed how superconductivity is a mandatory tool for high field applications and how to exploit it through multifilamentary structured wires. It provided the basis for the understanding of the main electro-mechanical phenomena concerning the wire as part of a more complex architecture given by the electromagnet system.

The most important laws and variables for superconductors, like critical current and current sharing temperature, are defined to make the reader understand the studies that will be performed in the following sections concerning superconducting wires and cables.

The work of this Ph.D. thesis refers to the Nb_3Sn material, which, with its high performance, is the most interesting and industrial-ready LTS for high field applications. However, its high strain-sensitivity is a major issue for projects and actors of the superconducting community, especially for high current & high field use, which

consequently involve extremely high mechanical loads. The next chapter presents the application of Nb_3Sn wires technology for controlled thermonuclear fusion reactors, which is the object of this dissertation.

I.2 CHAPTER – FUSION ENERGY

This chapter provides an introduction to fusion reactors based on (Hillairet 2021), with a particular attention to Tokamak machines and the ITER project in sections I.2.1 and I.2.2. Section I.2.3 deals with the design of the most used cables in the fusion machines and their operation for the ITER magnet system. Finally, section I.2.4 introduces the electrical performance degradation of the CICCs and the state-of-the-art about investigations and studies that have been performed on this particular issue.

I.2.1 Fusion energy overview

Controlled thermonuclear fusion reactors aim at reproducing the nuclear fusion reactions of the Sun. The fusion of two atoms, just like the fission of an atom, produces energy because of the conversion of the mass into energy following Albert Einstein's relation:

$$\Delta E = \Delta m \cdot c^2 \ [MeV] \tag{I.4}$$

where c is the *speed of light* and Δm is the *mass defect* during the nuclear reaction, generating the energy ΔE. The fusion reaction produces 4 times the energy produced by the fission reaction per nucleon. Hence, fusion is a very promising route for the production of carbon-free energy.

To make fusion reactions occur, the nuclei have to stay as close as possible (10^{-15} m) to overcome the electrostatic repulsion and at the same time this condition needs to be protracted in time as long as possible. Figure I.2.1 shows the impact of the temperature on the reaction rates for some of the best candidates to the fusion reactions.

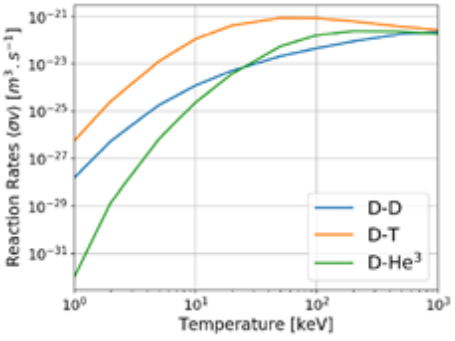

Figure I.2.1. Fusion reaction rates as a function of the temperature for some nuclei (Hillairet 2021).

The *D-T* reaction is the most suitable because it reaches the highest reaction rate at the lowest temperature (64 keV ~742·10^6 K). At this temperature, the fuel is an ionized gas called *plasma*. The desired fusion reaction is therefore between the Hydrogen isotopes Deuterium and Tritium:

$$D + T \rightarrow {}^4He\ (3.56\ MeV) + n\ (14.03\ MeV) \tag{I.5}$$

and the total released energy corresponds to 2.82·10^{-12} J per fusion reaction shared between the products of the reaction: the Helium nucleus, also labeled as α, and the neutron n. Hence, the fusion power is P_{fus} given by the sum of the neutron and α power:

$$P_{fus} = P_n + P_\alpha = \lambda P_\alpha, \qquad \lambda \approx 4.94. \tag{I.6}$$

The α-nuclei are the main driver of the heating of the plasma. An indicator of the reaction efficiency is the *amplification factor* Q, defined by the ratio of the fusion power to the external heating power:

$$Q = \frac{P_{fus}}{P_{ext}}. \tag{I.7}$$

Fusion ignition is reached when the heating provided by the reaction is sufficient to heat the plasma. At this point, P_{ext} is unnecessary and tends to 0, while Q tends to infinity. The product between the energy confinement time τ_E and particles density $\hat{n}$ can be plotted as a function of the temperature $\hat{T}$ to find the physical conditions to have ignition. Figure I.2.2 shows a minimum of $\tau_E\hat{n}$ product at 26.8 keV for any Q. At this minimum, ignition is reached for $\tau_E\hat{n} > 15 \cdot 10^{19} m^{-3} s$.

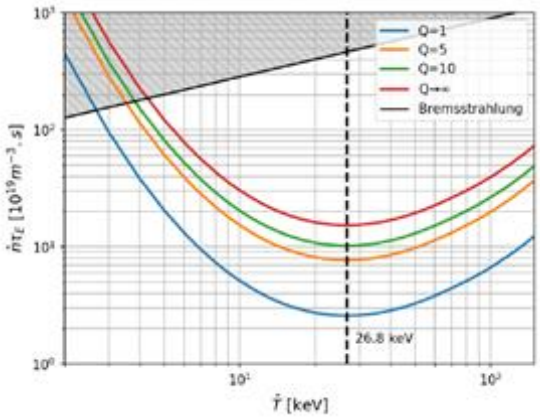

Figure I.2.2. $\tau_E\hat{n}$ product as a function of the temperature for different values of Q (Hillairet 2021).

I.2.2 Magnetic confinement reactors

One of the main problems in a nuclear fusion reactor is the confinement of the plasma reaching millions of degrees. Historically, several ways exist to confine plasma and one of them is the toroidal magnetic confinement. This kind of reactors is called *Tokamak*,

which is a Russian word standing for "magnetic confinement chamber". This section gives an overview on how the tokamaks work and the main projects relying on this technology.

I.2.2.1 Tokamaks machines & projects

The main idea is to exploit the charge of the particles in the plasma to guide them with toroidal magnetic lines, Figure I.2.3a).

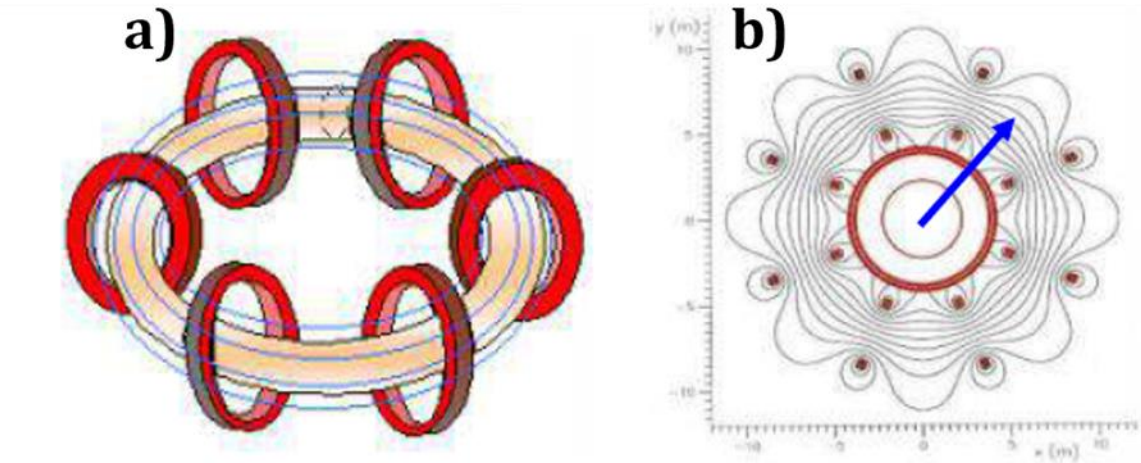

Figure I.2.3. a) Toroidal field, b) Toroidal field distortions (Devred 2017).

However, the discrete nature of the magnets makes distortions in the toroidal field lines, as a function of the plasma radius, Figure I.2.3b). A partial solution is to add a helical component to the magnetic lines. These field lines in Tokamaks are obtained thanks to the combination of a toroidal magnet system and the circulation of a transport current in the plasma, called *plasma current*. Thanks to this current, a poloidal field originates and sums to the toroidal field, giving thus resultant helical magnetic lines.

Up to 2020, the largest fusion machine was the *Joint European Torus* (JET) Tokamak in UK. This Tokamak relies on conventional magnets made of copper and so there is a strong power dissipation, more than 500 MW. This is the reason why the scaling up of these machines to produce electrical power requires the use of superconducting magnets to reduce the electrical power consumption and permit more compact windings.

The first Tokamak machine using the superconducting technology for the toroidal magnet is *Tore Supra* (CEA, France), today called *WEST*. It uses electromagnets for the toroidal coils made of NbTi. Some of the most relevant existing machines relying on superconductivity are listed in Table I.2.1.

Table I.2.1. Tokamak machines in order of time conception (Devred 2017).

Machine	*Major plasma radius*	*Where*
West (Tore Supra)	2.4 m	CEA, France
EAST	1.8 m	ASIPP, China
KSTAR	1.8 m	NFRI, Korea
SST-1	1.1 m	IPR, India

JT-60SA	3 m	JAEA, Japan
ITER	6.2 m	IO, France

The ITER project is the main project treated in this dissertation and its characteristics are introduced in the next paragraphs.

I.2.2.2 ITER project

The *International Thermonuclear Experimental Reactor* ITER is a very important project for fusion science, since its main challenge is to demonstrate the scientific and technological feasibility of fusion power. It is a demonstrative experimental reactor aiming to demonstrate the safety and environmental acceptability of fusion and to test the critical fusion technologies (Devred 2014). It is an international project supported by seven partners (CN, EU, IN, KO, JA, RF, US) and managed by the *International Organization* (IO). (Devred 2017)

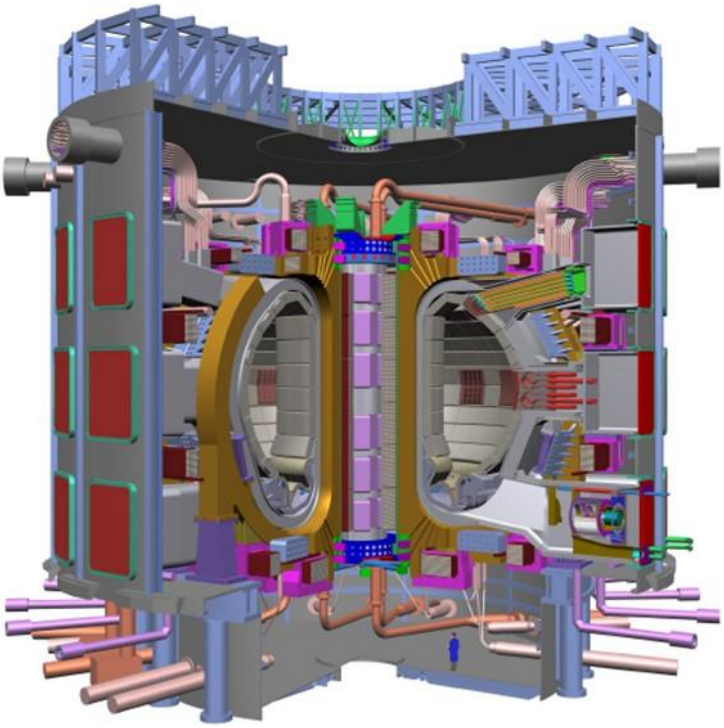

Figure I.2.4. ITER tokamak (ITER Organization web site).

The critical technological components that will be developed and tested in ITER are:

1. The vacuum vessel delimiting the plasma chamber (10^{-5}-10^{-6} Pa);
2. The blanket and divertor systems absorbing neutron flux and eliminating plasma ashes;
3. The magnet system controlling plasma confinement, shaping and stability;
4. The thermal shields and cryostat shielding the vacuum vessel and magnet system.

The scientific goal of ITER is to produce 500 MW of fusion power P_{fus} for pulses of 400 s with a power amplification factor Q of 10. Since P_{fus} scales with R^3B^4, where R is the

plasma radius and *B* is the toroidal field on the plasma toroidal axis, an adequate (*R,B*) doublet of (6.2 m, 5.3 T) was chosen for ITER.

I.2.2.3 ITER magnet system

The tokamak performance is driven by the magnets, which play a key role for the success of the reactor. Tokamak machines foresee a set of electromagnets, each of them can be made or not of superconducting conductors. Figure I.2.5 shows the general structure of the magnets needed to confine the plasma.

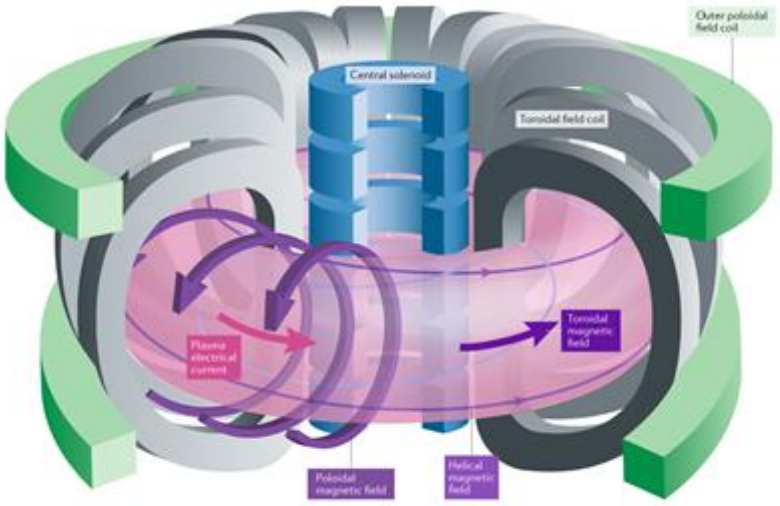

Figure I.2.5. The main electromagnets coils for a generic Tokamak reactor (Ham 2020).

The ITER magnet system, Figure I.2.6a), is completely made of superconducting coils providing an electromagnetic field of 5.3 T at the major plasma radius. Figure I.2.6b) shows the TF coils. The total weight of magnet system is ~10135 t for ~51 GJ of stored energy.

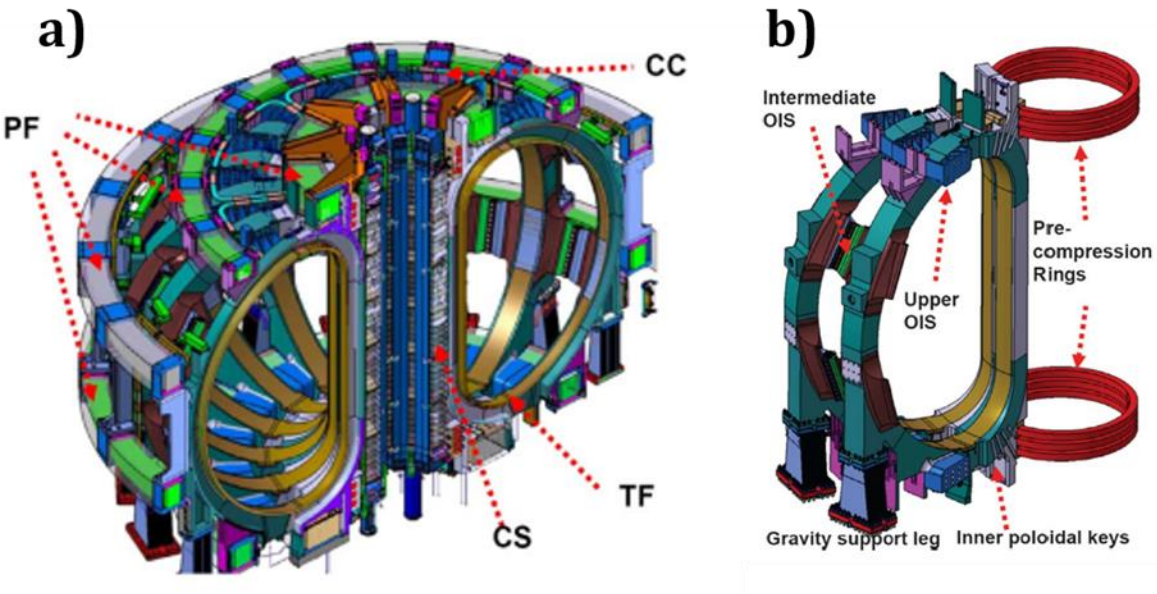

Figure I.2.6. a) ITER magnet system, b) Mechanical support to the TF coils (Mitchell 2008).

The system foresees several magnets, here briefly described. The Central Solenoid (CS) is composed of six independent modules and it is used for the plasma current initiation and the inductive drive. The 18 Toroidal Field (TF) coils provide the main confinement toroidal field. 6 Poloidal Field (PF) coils, supported on the TF structure, are used for plasma control and shaping. An additional set of 18 Correction Coils (CC) are placed between the TF and PF coils to correct error fields (Devred 2014). Figure I.2.7 shows the cross-section of the plasma chamber and the magnetic field lines.

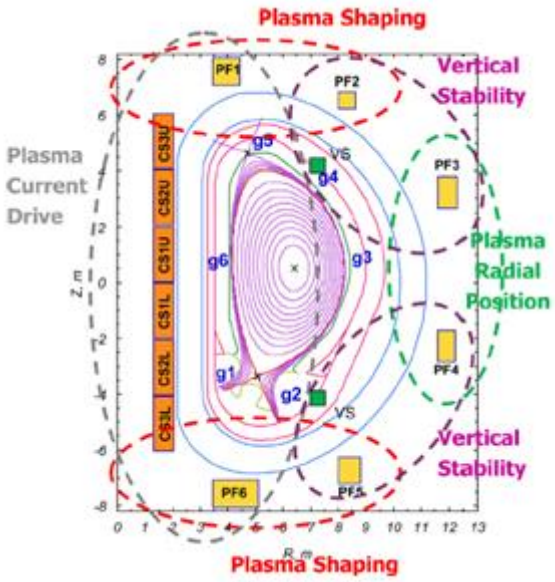

Figure I.2.7. Cross-section of the ITER plasma chamber (Mitchell 2017).

The TF coils are operated in steady-state regime while the CS modules and PF coils are pulsed magnets that undergo large current variations. The TF magnet system has been designed for 100 cool-down and warm-up cycles, 1000 TF charging cycles, 50 fast discharges and 10 quenches. ITER magnets are supplied with current and cryogenic fluids by 31 superconducting feeders that include BiSCCO-2223 HTS current leads.

Both CS and TF coils operate at high field and thus make use of Nb_3Sn wires, while PF coils and CCs use NbTi superconductor. All coils are cooled by supercritical Helium with a coil inlet temperature of 4.5 K. The ITER cryogenic power calls for 20 MW of power while it would have consumed 800 MW of power with resistive magnets. The main features of the coils are summarized in Table I.2.2.

Table I.2.2. Operating current for each ITER coil (Mitchell 2008).

Coil	TF	CS	PF
Nominal current	68 kA	45 kA	52 kA
Peak field	11.78 T	13 T	6 T
Superconductor	Nb_3Sn	Nb_3Sn	NbTi
Nominal temperature	5 K	4.5 K	4.5 K
Stored energy	41 GJ	6.4 GJ	4 GJ
Overall dimensions	14x9 m	12x4 m	8 to 24 m

Total weight	6540 t	974 t	2164 t

The work performed during this Ph.D. work focuses on the ITER TF coils, Table I.2.3 summarizes the main overall electromagnetic forces that these coils have to sustain.

Table I.2.3. ITER TF coil forces (Mitchell 2008).

Centering force per TF coil (MN)	403
Vertical force per half TF coil (MN)	205

The simultaneous presence of high magnetic induction and high current causes very large electromagnetic stresses. These stresses have to be sustained by mechanical components illustrated in Figure I.2.6b) for the specific case of the TF coil.

I.2.3 Fusion CICCs

Recent fusion magnets follow the *Cable-in-Conduit-Conductor (CICC)* design, which is characterized by a great number of multi-twisted strands inserted into a metallic jacket where the cooling fluid flows. This section provides an overview of the ITER TF Nb_3Sn CICCs.

Each TF conductor is composed of 900 superconducting and 522 Copper wires (Boutboul 2014). The two main companies that fabricated the Nb_3Sn wires for the EU TF coil conductors are Bruker EAS GmbH (BEAS) and Oxford Instruments Superconducting Technology (OST). Figure I.2.8a) shows the cross-sections of typical BEAS and OST wires.

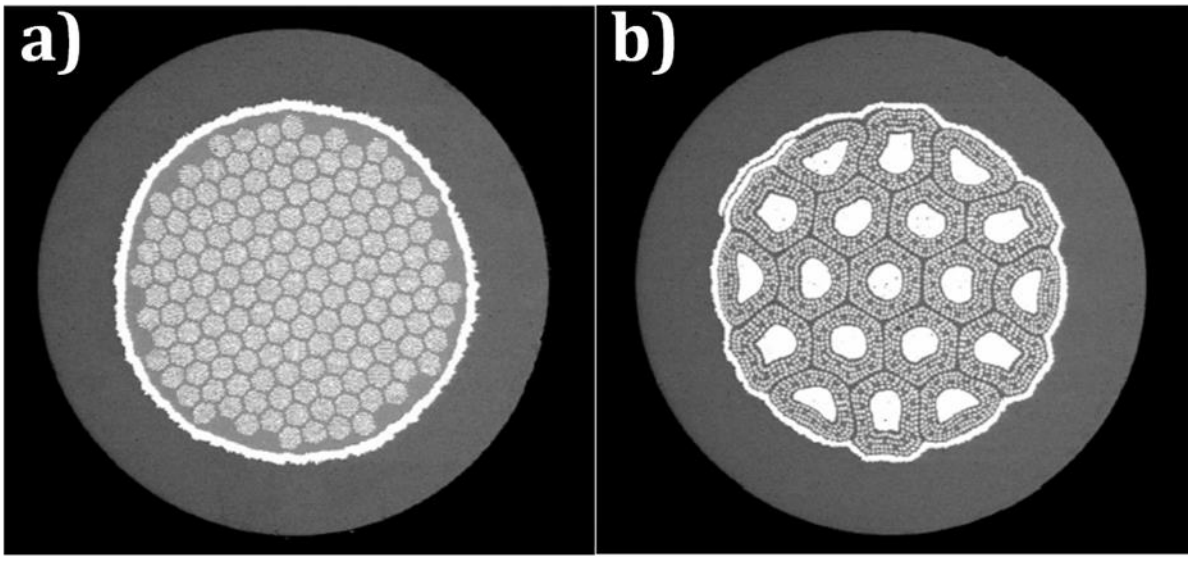

Figure I.2.8. a) BEAS Nb_3Sn BR-strand cross-section, b) OST Nb_3Sn IT-strand cross section (Boutboul 2016).

The Table I.2.4 summarizes the ITER TF Nb_3Sn wires main specifications.

Table I.2.4. ITER TF Nb_3Sn wires specification (Boutboul 2014).

Strand diameter	0.820 ± 0.005 mm
Strand twist pitch	15 ± 2 mm
Cr-plating thickness	1-2 µm

Strand piece length	> 1000 m
Cu/non-Cu volume ratio (χ)	1.0 ± 0.1
Critical current (12 T, 4.22 K)	> 190 A
n-value (12 T, 4.22 K)	> 20
RRR after heat treatment	> 100
Hysteresis losses (± 3 T cycle)	< 500 mJ/cm^3

The European wires used for the ITER TF conductors were object of a long qualification campaign to respect the specifications imposed in Table I.2.4 and the final parameters are listed in Table I.2.5.

Table I.2.5. Mean values for the European Nb_3Sn wires of the main parameters (Boutboul 2016).

Parameter	BEAS mean values	OST mean values
Critical current (A)	200	281
n-value	44	39
Cr-plating thickness	1.3	1.3
Cu/non-Cu	0.94	1.0
RRR	117	158
Hysteresis losses (mJ/cm^3)	65	264

The superconducting wires are twisted following a cabling process of five successive twisting stages and the final cable is then inserted into a stainless steel (SS) jacket. The cable is thus organized into multi-stages with SS/sub-cable wraps and a central cooling spiral. The jacket is afterwards compacted to its final dimensions that can be square, circular or circular-in-square. A typical cross-section of a CICC is reported in Figure I.2.9 for the ITER TF conductor.

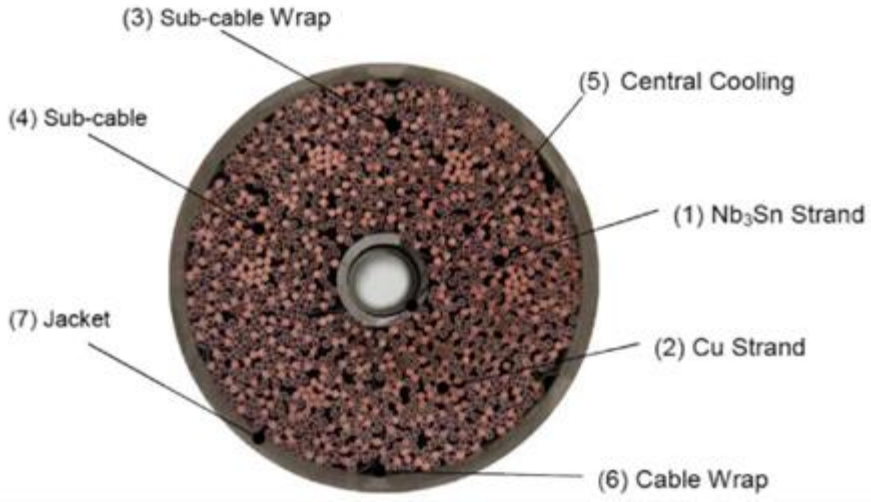

Figure I.2.9. Typical cross-section of an ITER TF conductor (Boutboul 2014).

A typical TF conductor unit length is 760 m requiring a minimum of 3.3 t of Nb_3Sn strands and 11.3 t of SS tubes. Figure I.2.10 reports the main steps of the ITER conductors manufacture.

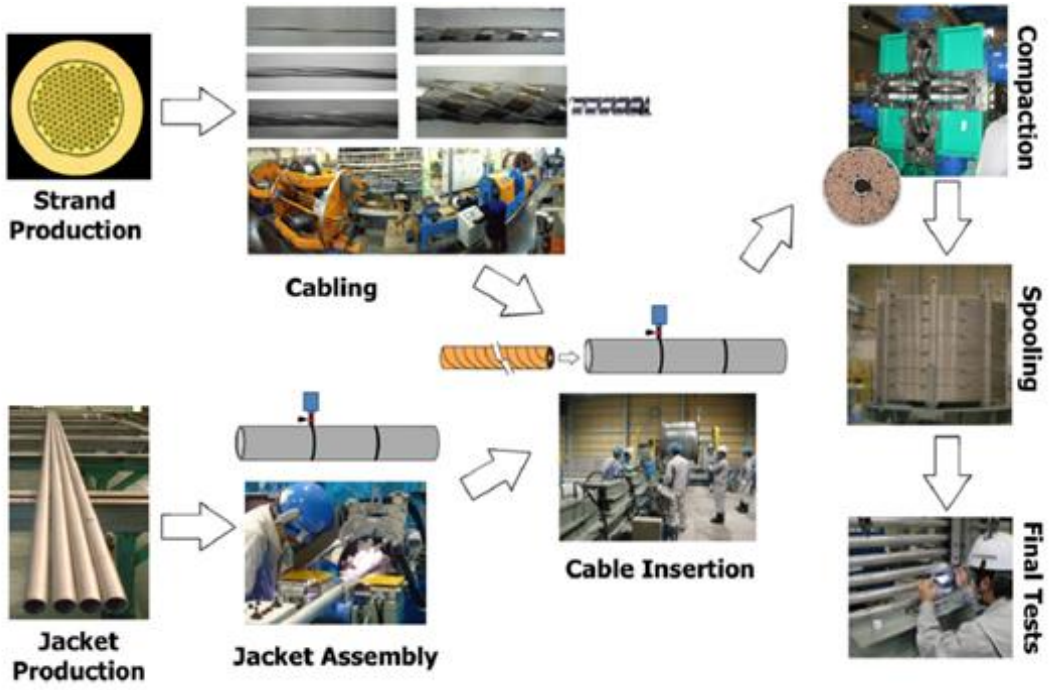

Figure I.2.10. Main steps of ITER CICC manufacture (Devred 2014).

As explained in (Devred 2014), the manufacture process starts with the strand production with the techniques reported in section I.1.2.5, then the wires are cabled together on a planetary machine. Simultaneously the jacket sections are produced by hot extrusion followed by cold drawing, and then welded together to achieve the cable length. The cable is inserted into the jacket by means of a pulling rope and compacted to the nominal dimension. Table I.2.6 reports the ITER Nb_3Sn CICCs main parameters.

Table I.2.6. Main design parameters for the ITER Nb_3Sn CICCs from (Devred 2012).

		TF CICC	CS CICC
SC strand type [-]		Nb_3Sn	Nb_3Sn
Wires diameter [mm]		0.82	0.83
Central spiral [mm]	Thick x Width	1x6	1x6
	Out diameter x Pitch	10x9	9x8.85
Cable wrap [mm]	Thick x Width	0.1x40	0.08x40
	Overlap [%]	40	40
Petals wrap [mm]	Thick x Width	0.1x(12-15)	0.05x20
	Coverage [%]	50	70
Cable layout		((2Nb_3Sn+1Cu)x3x5x5 +(3x4Cu))x6	(2Nb_3Sn+1Cu)x3x4x4x6
Twist pitches cable[mm]	1st stage	80	45
	2nd stage	140	85
	3rd stage	190	145
	4th stage	300	250
	Petal stage	420	450
Cu core inside petal		yes	no

Some of the information provided in Table I.2.6 is relevant to the simulations presented in part IV. A consideration can be here made on the role of the Twist Pitches (TPs). Conductors have AC losses associated with induced currents between strands when external magnetic field changes. This is a phenomenon similar to the one presented in chapter I.1 for the filaments scale. The choice of the TPs is related to the AC losses, and they are chosen to be non-integer multipliers to avoid the creation of large loops for coupling currents. However these losses cannot be completely removed and the TPs aims to achieve a good transposition, small AC losses and a great mechanical support of the strands. Furthermore, the successive twisting stage produces a transposed structure of the strands, differently form the filaments inside the wires, which is necessary for the homogeneous current sharing among strands and therefore each strand moves into every radial position in the cable (Mitchell 2005a).

I.2.4 CICC performance degradation

I.2.4.1 ITER TF CICCs loadings

During the reactor life, the conductors composing the coils are submitted to several mechanical loadings of different nature. In ITER, the large electromagnetic (EM) forces due to the Lorentz force (*IxB*) can reach values as high as 800 kN/m in the transverse conductor direction. Moreover, an additional loading, in the longitudinal direction, comes from the differential thermal contraction between the steel jacket and the wires composing the cable. This second phenomenon causes a longitudinal force acting on the cable each time the conductor is submitted to a temperature variation. This occurs for example during the Cool-Down (CD) of the conductor from the heat treatment temperature (HT) at 650 °C to the cryogenic temperature (4.5 K) as well as any time the magnet system is warmed-up (at 80 K or Room-Temperature (RT)) and cooled again. This thermal cycle is usually called Warm-Up-Cool-Down (WUCD).

The effect of these loadings is a cyclic mechanical solicitation of the superconductor during the machine operation. However, this affects the conductor performance because of the strain-sensitiveness of the Nb_3Sn current carrying capability.

The ITER full-size conductors were all tested and qualified in the SULTAN facility (PSI, Switzerland) (Bruzzone 2002), since it is the only facility able to provide the full TF conductor operating current and the background field needed to achieve the design peak field. Next paragraph provides an overview of the typical SULTAN tests.

I.2.4.2 SULTAN facility and tests

Figure I.2.11 reports an overview of the SULTAN facility and of the global sample orientation. In particular, the sample consists of two conductors, called “legs”, joined at the bottom and electrically connected at the top to the SULTAN superconducting transformer. The sample is placed vertically in the middle of a split-coil magnetic system,

but the peak background field applies only over a length of 0.45 m of the conductors. This means that there are also two lateral zones unexposed to magnetic field (and thus without EM load) (Breschi 2012a).

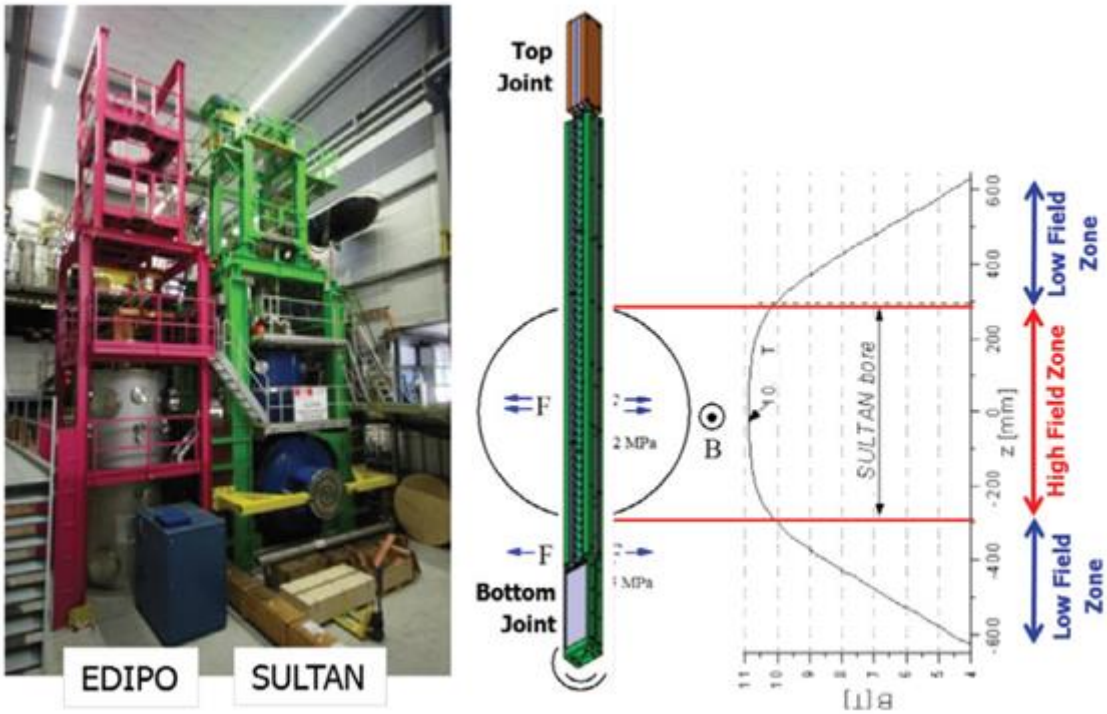

Figure I.2.11. View of EDIPO and SULTAN sample test facilities at CRPP (left) and SULTAN sample configuration (right) from (Devred 2014).

Figure I.2.12 reports a schematic drawing of the SULTAN samples and probes installed on the conductors jacket.

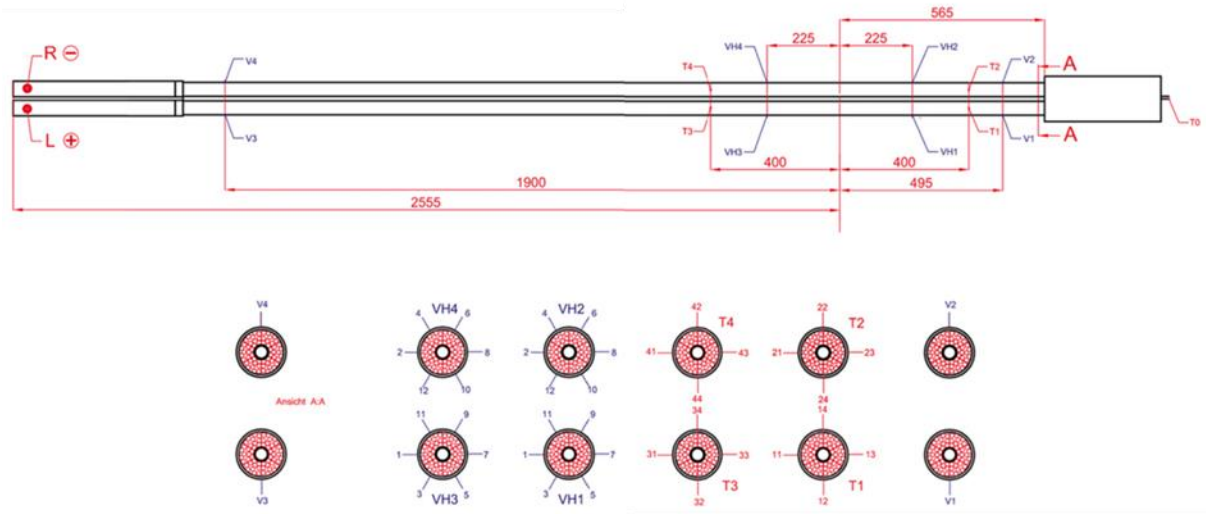

Figure I.2.12. Sketch of a typical SULTAN sample for TF conductors with upper terminations (on the left), bottom joint (on the right), temperature probes and voltage taps (Breschi 2012a).

Two crowns of six voltage taps are placed on each leg (VH1–VH4) around the high field zone, so the distance between the crowns on each leg is 450 mm. The leg is further

instrumented with four sets of temperature sensors (T1–T4). The temperature sensors are located upstream and downstream of the high field zone (HFZ) at an 800 mm distance from each other. They measure the conductor temperature and can be coupled to mass flow sensors to perform calorimetric assessments. Finally, the bottom joint allows both legs to be operated by a single power supply and provides the possibility of testing two conductors simultaneously. The two conductors are cooled through a forced flow of supercritical helium, usually flowing from the bottom joint to the upper terminations. Heaters are mounted on the helium inlet to control the sample test temperature and carry out the T_{cs} tests.

Tests aim to assess the performance of the conductors by measurements of the T_{cs}, ramping the temperature (T_{cs} run) at fixed current and field. The TF acceptance criterion is set at 5.8 K, for the T_{cs} measured after 1000 EM cycles at 68 kA in a SULTAN background field of 10.78 T (corresponding to a conductor peak field of 11.78 T). For each T_{cs} run, temperature is raised as shown in Figure I.2.13 until the superconductor transits to normal state. Finally, from the measurements of temperature and voltage the T_{cs} can be detected, see plot on the right of Figure I.2.13.

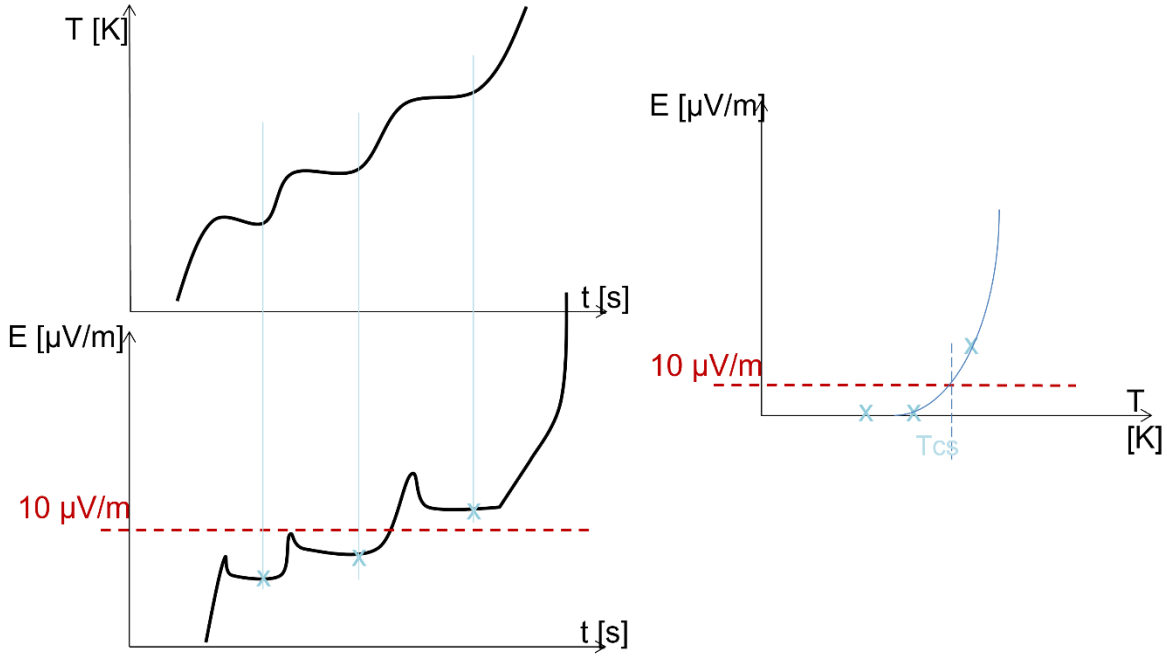

Figure I.2.13. Schematical drawing of a typical temperature ramp-up in SULTAN (plots on the left) and the T_{cs} assessment from the E-T characteristic (plot on the right).

SULTAN tests consist in several T_{cs} runs at the same operating conditions of the TF magnet system in the Tokamak by alternating electromagnetic loadings to thermal ones to assess the impact of the two of them on the conductor performance.

I.2.4.3 Performance degradation

During the qualification phase of ITER TF conductors, evidence was found that the cyclic loading of the conductor impacts the value of T_{CS} and that the temperature margin decreases with cycles number (Ciazynski 2007). A typical degradation curve is shown in Figure I.2.14 for several conductors.

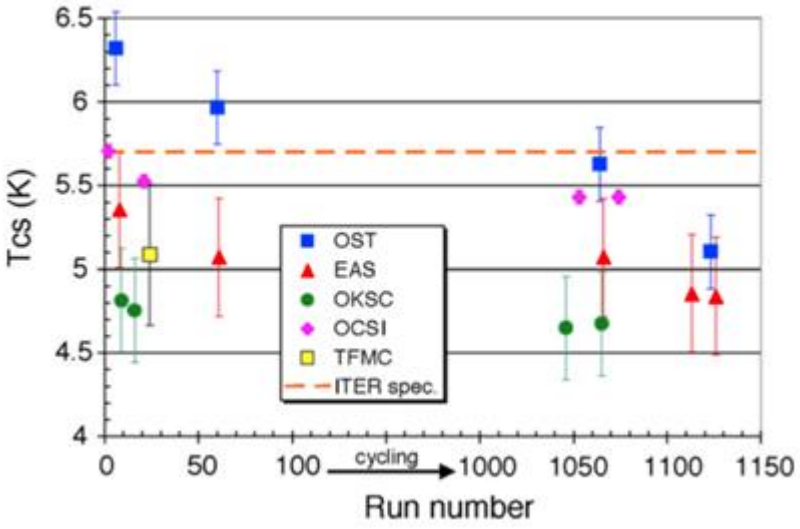

Figure I.2.14. T_{cs} degradation due to EM cycling in a typical SULTAN test (Ciazynski 2007).

In the following years, an extensive crash program (Devred 2014), (Breschi 2012a), (Breschi 2017) led to understand this behavior. Some of these findings are presented in paragraph I.2.4.4 as potential responsible.

The ITER CS CICC was a critical component since it is supposed to withstand 30000 EM cycles in the machine's lifetime. The problem was solved by changing the initial design that foresaw Long Twist Pitches (CS-LTP). The new design is characterized by the shortening of sub-cables twist pitches (CS-STP) and permitted to avoid degradation (Bessette 2014). This solution came from the intuition that locked strands would not move, and thus not degrade. However, even though this intuition proved to be experimentally efficient, the scientific understanding of such behavior is still unclear. Therefore, although 30 years of experience provided useful information on the Nb_3Sn conductors (Mitchell 2020), there is still not clarity about the mechanical phenomena at both micro and macro scales driving the performance degradation with cycling.

The present dissertation focuses on the ITER TF CICC, for which the design was not changed, and degradation is tolerated because of sufficient temperature margin to cope with 1000 EM cycles.

I.2.4.4 Experimental evidence and assumptions

This paragraph provides an overview of the extensive work that was done during the ITER conductors crash program, focusing on all findings that shed some light on the degradation mechanisms.

Moreover, (Mitchell 2020) provided a very comprehensive summary of Nb_3Sn used in fusion magnets. In particular, this paper introduces two main categories of phenomena affecting Nb_3Sn wires performance in a cable:

- **Type 1 Degradation:** Modification of performance due to the intrinsic critical current strain-sensitivity in Nb_3Sn. This phenomenon is directly linked to the complex local strain state of the filaments in a cable under loading and it is usually considered reversible.
- **Type 2 Degradation:** Alteration of current carrying capability due to physical damage to the superconducting filaments, typically under tensile strain. This type of degradation is usually considered reversible.

The difficulty is that both types of degradation are in any case present in a CICC and it is almost impossible to separate their respective effects. In order to get a better understanding of what is implied by Type 1 and Type 2 degradation and their potential explanations: Table I.2.7 lists experimental and/or numerical findings affecting the cable current carrying capability. These observations are related to either TF or CS-LTP conductor designs.

Table I.2.7 Summary of the phenomenological evidence that could induce degradation.

#	Short summary (Actor / Reference)	Tentative interpretation	Illustration
A	Destructive examination of LTP CS cables after cycling **(JAEA→QST /** (Hemmi 2012)**)**	LTP design shows large buckling of strands at HFZ. Buckling would induce extreme bending, exposure to tensile strains and thus fracture of filaments.	
B	Destructive examination of LTP CS cables after cycling **(JAEA→QST,** (Hemmi 2012)**)**	LTP design leaves too much space for strands movement at HFZ. These movements permit excessive strain that damages the filaments.	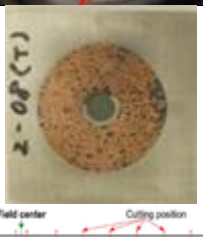
C	Residual strain measurements on LTP CS cable after cycling. **(JAEA→QST,** (Hemmi 2012)**)**	LTP cables can cumulate compressive strain by de-coupling of the cable and jacket. This additional compression might also induce additional bending, thus exposure to tensile strain.	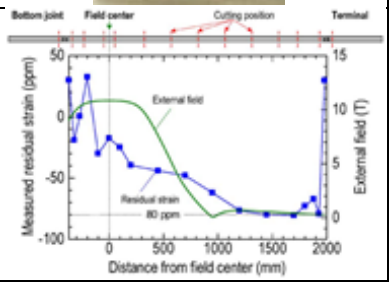

D	Susceptibility measurements by pick-up coils on CS samples **(CRPP→SPC / (Calzolaio 2013))**	During cycling, LTP shows a shift towards more compressive strain with broadening of distribution while STP shows a shift towards less compressive strain. Additional compressive strain would intrinsically reduce the current carrying capacity while the broadening can expose to tensile strain.	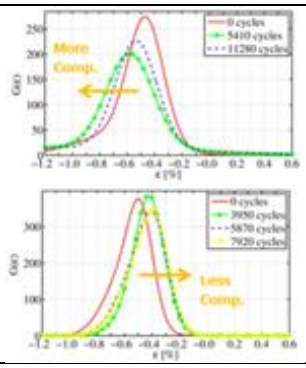
E	Filament fracture observation by polishing and microscopic analysis **(FSU /** (Sanabria 2012)**)**	Filament fractures are observed in CICC strands. STP has no cracks, showing much better support of strands.	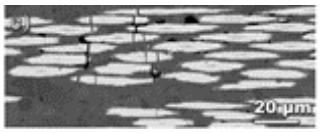
F	AC losses measurements variation before/after cycling **(CRPP→SPC & IO/** (Bessette 2014)**)**	AC losses of TF CICC are divided by a factor 10-20 after cycling, revealing a potential drastic increase in their inter-strand contact resistance. This would also impede their current redistribution capacity, and thus the global cable performance.	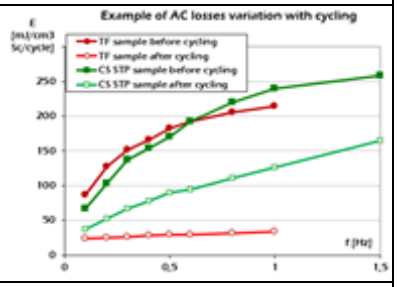
G	Evidence of « Ratcheting » effect on strands **(ECP→ECS /** (Bajas 2011)**)**	Cumulative strain can be obtained on single strand submitted to cyclic uniaxial loading. This might shift the strands local strain map in the compressive side for high cycles number (thus decreasing their current carrying capacity).	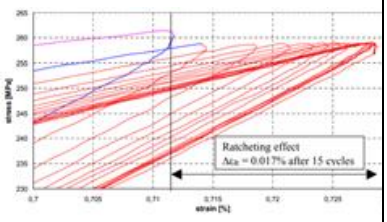

The above observations open several questions about the correct design of the CICC, since the difficulty is to be able to discriminate each observed phenomena and decide how to reduce, manage or eliminate their respective impacts.

Based on this overview, it is clear that even if the design issues of the ITER conductor have been temporary solved, the scientific community still needs for explanations about the strand-cable scale-up behavior as well as about the cyclic degradation. This Ph.D. project is born in a tentative effort of trying to answer to this call, focusing on the development of tools to shed light on the cyclic behavior of Nb_3Sn conductors through:

1) Experimental activities to investigate the cyclic behavior of the Nb_3Sn wires;

2) Numerical mechanical modelling to bridge the gap between the cable scale performances and the strand local strain map, thus permitting to identify the driving phenomena behind cable degradation.

I.2.5 Conclusion

The previous chapters of this first part of the dissertation contextualize the environment of the presented work and introduce the complexity of the use of superconductors in fusion reactors. It has been observed that a performance degradation issue may arise when using Nb_3Sn-based CICC in high-mechanically strained operating conditions (high current/high field). The precise understanding for this degradation of the CICCs that goes with the cyclic operation is still quite debated and it is one of the main issues treated in this dissertation.

The question that this Ph.D. thesis aims to answer is debated through both an experimental and modelling point of view. The experimental activities want to investigate the fatigue behavior in traction and compression of Nb_3Sn wires when submitted to thousands of cycles of uniaxial loadings. This activity would give the opportunity to understand if cyclic phenomena at strand-scale are dominant in the degradation process, and to enrich the sparse literature of fatigue behavior for this type of wire. On the other hand, the modelling work intends to build a solid and reliable model to simulate the fusion cables behavior in order to understand both macroscopic and local mechanical phenomena inside the cable affecting the electrical performance. The first studies focus on the ITER TF CICCs, and later, particular attention is paid to the design parameters and their impact on the electro-mechanical behavior of the cable.

II. SECOND PART – Nb_3Sn WIRES MECHANICAL BEHAVIOR

LIST OF SYMBOLS

$A_{elasticmax}$	*[-]-[%]*	Maximum elastic strain
Cu	*[-]*	Copper
Cr	*[-]*	Chrome
D_{sample}	*[mm]*	Sample diameter
E, E_0, E_u, E_N	*[MPa]*	Elastic modulus
F	*[N]*	Longitudinal applied force
HCl	*[-]*	Hydrochloric acid
I	$[mm^4]$	Momentum of inertia
I_c	*[A]*	Critical current
L_0	*[mm]*	Useful length
l	*[mm]*	Gauge length
l_0	*[mm]*	Initial gauge length
l_{eff}	*[mm]*	Effective length
Nb_3Sn	*[-]*	Niobium-three-Tin
N_c	*[N]*	Euler's critical load
R^2	*[-]*	Coefficient of determination
$R_{elasticmax}$	*[MPa]*	Maximum elastic stress
$R_{p0.2}$	*[MPa]*	Proof strength
S	$[mm^2]$	Cross-sectional area
S_0	$[mm^2]$	Initial cross-sectional area
$\beta_0 - \beta_1$	*[MPa]*	Coefficients of linear regression
ε	*[-]-[%]*	Strain
ε_{eng}	*[-]-[%]*	Engineering strain
ε_{true}	*[-]-[%]*	True strain
ν_{th}	*[Hz]*	Theoretical strain rate
σ	*[MPa]*	Stress
σ_c	*[MPa]*	Critical stress
σ_{eng}	*[MPa]*	Engineering stress
σ_{true}	*[MPa]*	True stress
Ø	*[mm]*	Diameter

II.1 CHAPTER – STATE OF THE ART

Nb_3Sn composite wires have been largely studied to investigate their mechanical behavior and the impact on the electrical behavior. Moreover, even though the wires in the cable are submitted to a pre-compression by the stainless-steel jacket, as explained in paragraph I.2.4.1, their mechanical characterization, due to their small diameter has been focused on their tensile behavior. This is why in literature only the tensile behavior has been investigated so far, assuming that their behavior in compression is the same as in tension. Paragraph II.1.2 presents the most relevant studies performed in literature on the IT-Nb_3Sn strands, but, first, section II.1.1 describes the wires to refer to for the experimental activities of this Ph.D. work and for the state of the art. Finally, paragraph II.1.3 illustrates the post-processing analysis applied to the experimental results.

II.1.1 Presentation of Nb_3Sn IT-wire samples

The samples for the Ph.D. experimental activities are European OST 01EX0796A01 Nb_3Sn IT-strands supplied by Fusion for Energy (F4E). It is important to mention that the wires used might differ marginally from the nominal one used in the coils, although representative of the OST-Type ITER production wire. A typical cross-section of this wire is the one previously shown in Figure I.2.8b).

These wires follow the internal tin process to create the superconducting phase, as explained in section I.1.2.5, and they were thermally treated under neutral gas atmosphere in the oven at CEA Cadarache. For more details about the heat treatment preparation and programming see Annex A.

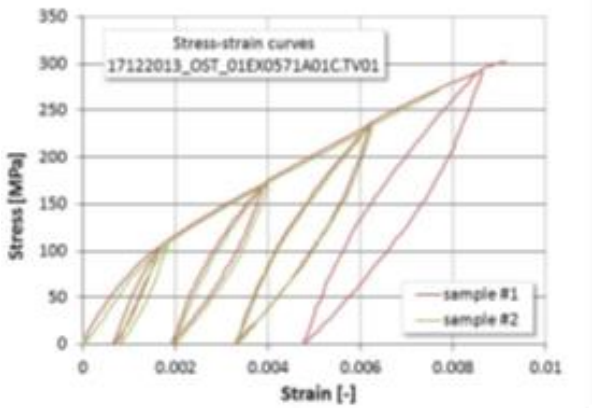

Figure II.1.1. Strain-stress curves at 4.2 K provided by the University of Twente (Nijhuis 2014).

The University of Twente has already tested a similar type of wire at 4.2 K and the stress-strain curve of Figure II.1.1 provides a reference for the present study.

The main characteristics of the sample used in the following tests are presented in Table II.1.1 and it is representative of strands used in the TFEU13 SULTAN left leg sample (ITER Organization 2015). The manufacture procedure is the one presented in paragraph I.1.2.5.

Table II.1.1. Main features of the Nb_3Sn wire sample for the experimental activities (ITER Organization 2015).

Diameter	0.820 ± 0.005 mm
Twist pitch	15 ± 2 mm (right hand twist)
Cr plating	2.0 μm
I_c (12 T, 4.2 K) on ITER barrel	253-320 A
RRR	> 100
n-value (12 T, 4.2 K)	> 20
Cu/non-Cu (unreacted, Cr plating)	1 ± 0.1
Strand losses (+/−3 T cycle, 4.2 K)	< 500 mJ/cm^3

II.1.2 Previous works on tensile tests

In literature, several studies have been performed so far on the tensile characterization of the Nb_3Sn wires. The following paragraphs report the more relevant studies that contribute to the definition of the experimental protocols used in this Ph.D. work with a major focus on the IT-wires to have a more appropriate reference for the results comparison.

II.1.2.1 RRT campaign & Nb_3Sn wires testing recommendations

The international *Round Robin Test (*RRT) campaign (Osamura 2008) had as major goal to provide recommendations to test Nb_3Sn wires at room temperature by testing different methods and tools. This campaign contributed to define the norm (IEC/CEI 61788-19 2013) presenting the main guidelines to test Nb_3Sn wires at RT.

For the strain measurement, it is recommended to use a double extensometer (Nyilas 2005) having a total weight of less than 30 g. The sample useful length should be at least 60 mm long and the test displacement driven at 0.1–0.5 mm/min.

Several recommendations are provided for the measurement of the elasticity modulus and the definition of the elastic region as well. The initial modulus of elasticity has to be measured on the initial slope but also on the linear part of the unloadings, as shown in Figure II.1.2. The elastic region is defined by the maximum stress $R_{elasticmax}$ and the maximum strain $A_{elasticmax}$ defining the transition from elastic to plastic regime. However, due to the difficult identification of the straight line, it is recommended to define the 0.2 % proof strength $R_{p0.2}$ using the elasticity modulus at the initial slope and on the linear parts of the unloadings, as shown in Figure II.1.2.

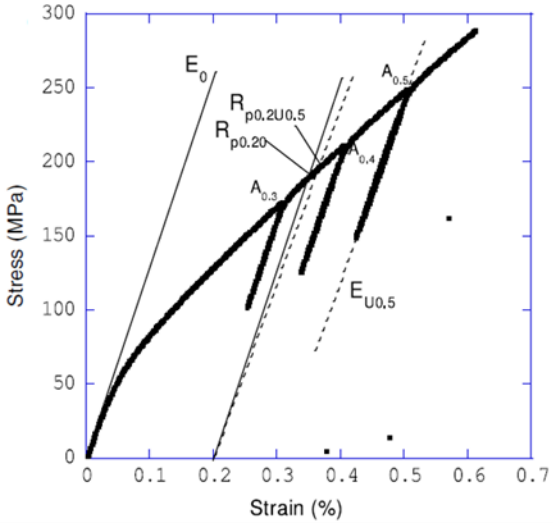

Figure II.1.2. Typical strain-stress curves and the measured parameters (Osamura 2008).

The tested clamping methods are numerous, but not presented here because not completely useful to the understanding of this Ph.D. experimental activities. However, the aforementioned guidelines were helpful in the fulfillment of the tensile test protocol.

Finally, the test is considered validated if the ratio between the moduli of elasticity E_0 at the initial slope and E_u calculated for an unloading between 0.3 % and 0.4 %, is within the 0.7–1.3 range.

II.1.2.2 TARSIS

The University of Twente has given one of the main contributions to the superconducting community concerning the mechanical characterization of Nb_3Sn wires (Van den Eijnden 2005) with the setup TARSIS (*Test ARrangement for Strain Influence on Strands*). The device allows the performance of several kinds of mechanical characterization like bending, pinching and axial tensile loading. Figure II.1.3 reports the configuration for strain-stress characterization in the TARSIS configuration.

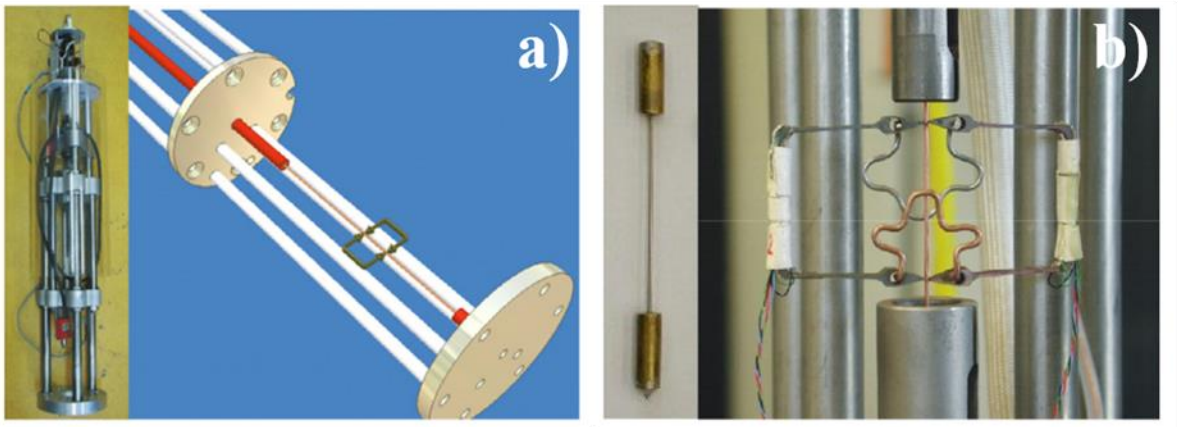

Figure II.1.3. a) TARSIS configuration for the axial tensile characterization, b) extensometer and sample configuration in TARSIS (Van den Eijnden 2005).

The strain measurement is performed thanks to a double extensometer configuration (Figure II.1.3 b)) to compensate the bending effects. The sample on the left of Figure II.1.3 b) foresees the soldering of brass tubes as intermediate component to ensure an aligned fixation and reduce the sample handling. Studies demonstrated that the soldering does not affect the mechanical properties of the superconducting wire according to (Van den Eijnden 2005). Moreover, the inner tube hole is slightly greater than the strand diameter to leave some space for eventual misalignment of the wire. The tests end with wire breakage close to the tube or in correspondence of the extensometer clamping points. For more details about the experimental procedure, one may refer to (Van den Eijnden 2005). The experimental protocol was validated thanks to the reproducibility of the results. Figure II.1.4 reports the measured strain-stress characteristics on an IT-wire by *Europa Metalli-LMI* with TARSIS for three different temperatures. The curves at 77 K and 293 K coincide.

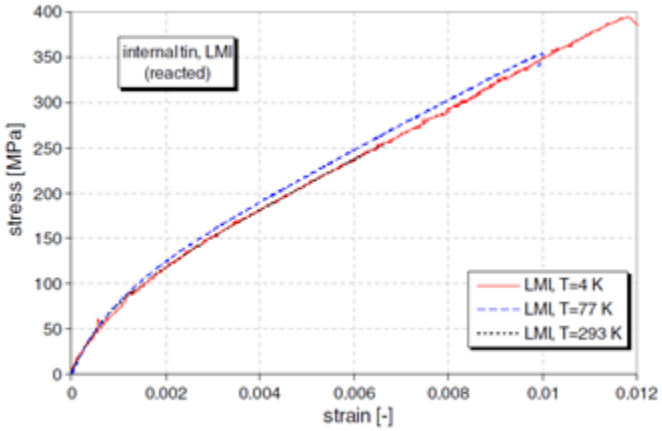

Figure II.1.4. Strain-stress characteristics of IT wires in TARSIS at three different temperatures (Van den Eijnden 2005).

II.1.2.3 SCUTT device

In the framework of G. Lenoir's Ph.D. thesis (Lenoir 2017), another experimental protocol to characterize superconducting wires was developed based on already existing methods and aiming to improve their limits. This protocol relies on the SCUTT (*Strand Configuration for Uniaxial Tensile Test*) device and will be better illustrated in section II.2.1 since the Ph.D. experimental protocol is partially based on it. The principle is similar to the TARSIS configuration, but instead of soldered brass tubes it is characterized by free conical tubes and soldered tin balls. The extensometer is not double but simple, very light and the knifes are glued directly on the wire. Figure II.1.5 reports the obtained strain-stress characteristic for the wire in blue line. The wire breakage occurs at the center of the sample.

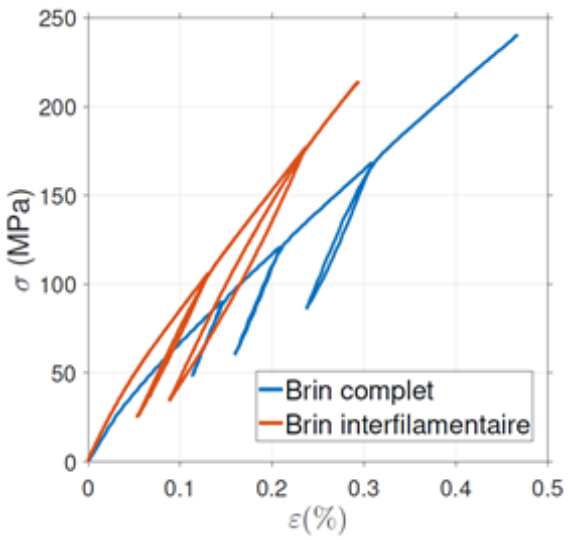

Figure II.1.5. Strain-stress characteristics for an RRP-wire (Lenoir 2017).

II.1.2.4 Fatigue uniaxial tensile tests

In the framework of another Ph.D. work (Bajas 2011) few uniaxial tensile cycles were performed at RT on ALSTOM IT-wires and EAS BR-wires by using keyless clamps. Figure II.1.6 reports the results with a focus on the IT-wire.

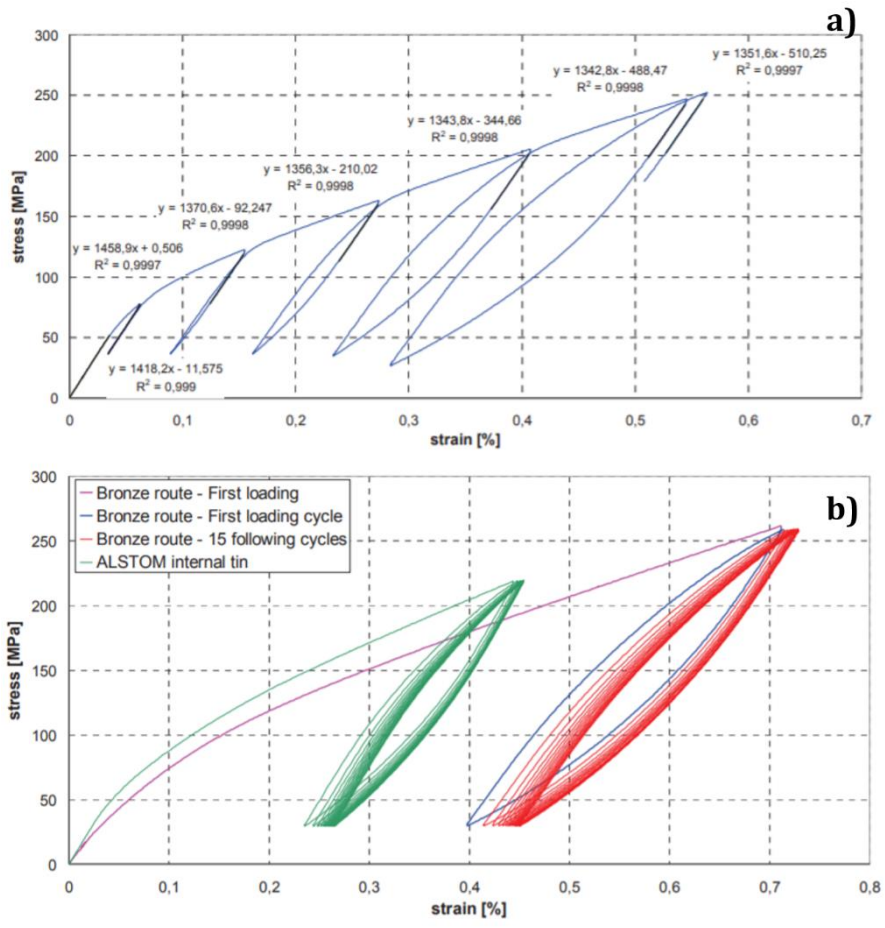

Figure II.1.6. a) Monotonous strain-stress characteristic of IT-wire with unloadings; b) cyclic strain-stress characteristics of Nb_3Sn wires (Bajas 2011).

These tests showed a Ratcheting effect after 15 cycles without stabilization of the phenomenon; hence, the study of additional cycles was recommended by (Bajas 2011).

Simultaneously, the fatigue behavior of the Nb_3Sn was investigated by the Ph.D. work of (Sheth 2011) with a major focus on the impact of cycling on the fractures/cracks in the microfilaments. In particular, he performed thousands of loading-unloading tensile cycles at 77 K with the setup reported in Figure II.1.7.

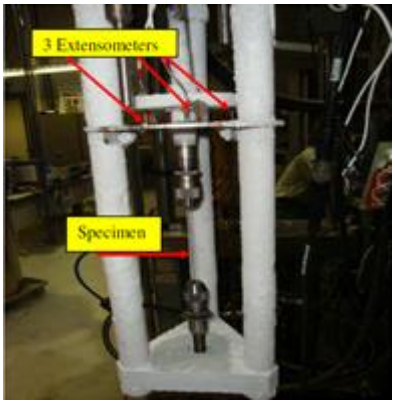

Figure II.1.7. Fatigue test setup with three extensometers (Sheth 2011).

The test is performed in displacement control (0.5 mm/min) until the performance of the first cycle, then thousands of cycles are performed under force control between 164 N and 20 N. The maximum and minimum displacements are recorded and monitored all over the 30000 cycles, see Figure II.1.8b).

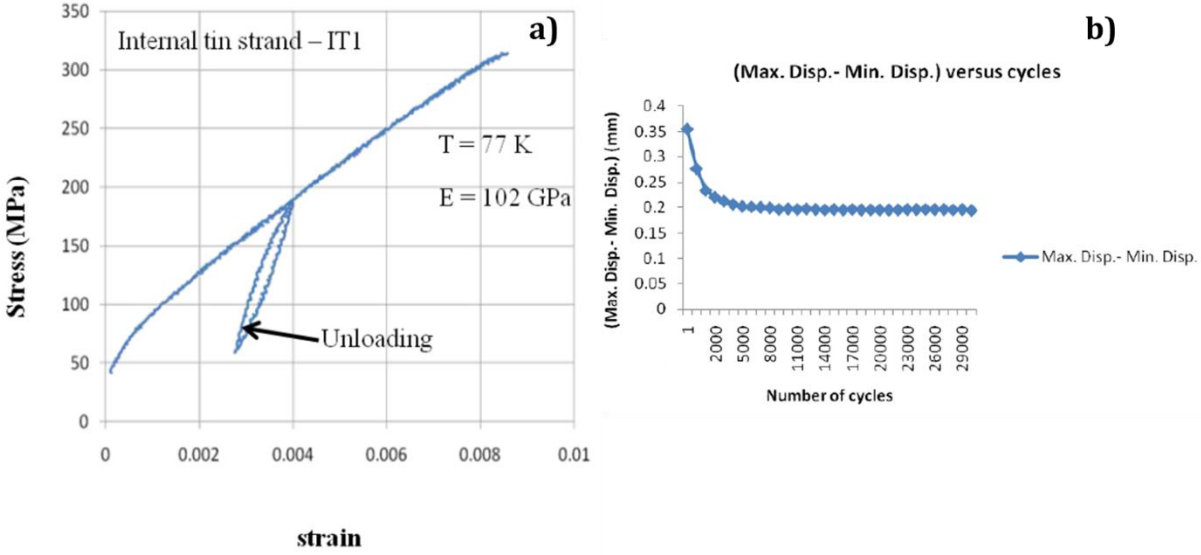

Figure II.1.8. a) Strain-stress characteristic of an IT-wire with unloading to measure the Young's modulus; b) difference between the maximum and minimum displacement as a function of the cycles (Sheth 2011).

The cycling shows a progressive hardening of the sample due to the plasticization of the matrix of the composite, with a stabilization of the phenomenon around 10000 cycles. The strand does not break even after 30000 cycles.

This is the only study, based on the author's knowledge, presented in literature investigating the cyclic behavior of Nb_3Sn wires for a mechanical tensile characterization. One objective of this Ph.D. work is to reproduce and enrich the mechanical qualification of cyclic loadings of Nb_3Sn strands, and extend the scientific knowledge about this topic. On the other hand, one of the challenges of this Ph.D. is to provide an experimental protocol to test the wires in compression since the real mechanical loads sustained by the wire induce compressive stresses. In particular, a full characterization of the same wire both in traction and in compression for hundreds of cycles would permit more precise comparisons and understanding of its mechanical behavior.

II.1.3 Post-processing procedure

The main results concern the strain-stress curves and there are two different methods to calculate them depending on what has to be studied. In particular, the results can refer either to the true stress and strain or to the engineering stress and strain.

The true stress σ_{true} is defined as the longitudinal applied force F over the instantaneous cross-sectional area of the sample S, while the true strain ε_{true} is the deformation with respect to initial gauge length dl over the instantaneous gauge length l of the extensometer:

$$\begin{cases} \varepsilon_{true} = \dfrac{l - l_0}{l} \\ \sigma_{true} = \dfrac{F}{S} \end{cases}. \tag{II. 1}$$

These definitions take into account all the instantaneous modifications occurring to the sample in the gauge length zone. However, in some cases it is preferable to simply calculate the corresponding engineering values, which consider only the initial state (l_0, S_0) of the sample:

$$\begin{cases} \varepsilon_{eng} = \dfrac{l - l_0}{l_0} \\ \sigma_{eng} = \dfrac{F}{S_0} \end{cases}, \tag{II. 2}$$

obtaining in this way an easier and quicker estimation of the strain and the stress.

Generally, in the linear elastic domain the difference between the engineering and true stress/strain is very small, but in the domain of the large transformations it could not be true anymore. Hence, for the plasticity study, it is better to use the true stress/strain values and they can be calculated as a function of the engineering ones assuming that the plastic regime is characterized by a constant volume of the sample $S_0 \cdot l_0 = S \cdot l$:

$$\begin{cases} \varepsilon_{true} = \ln(1+\varepsilon_{eng}) \\ \sigma_{true} = \dfrac{F}{S} = \sigma_{eng}(1+\varepsilon_{eng}) \end{cases} \quad \text{(II. 3)}$$

and these are the formula that are used to plot all the following results.

One important parameter to be measured is the modulus of elasticity. However, for this kind of wires, specific recommendations are given by (Osamura 2008) since the initial part of the strain-stress plot is strongly affected by the sample manipulation, the clamping method, the initial bending of the sample and the recovery of the eventual misalignment of the clamps. This difference usually disappears for the larger solicitations. The elasticity modulus is thus calculated on the linear part of the unloadings through the method of the linear regression. The coefficients for the regression β_0, β_1 are simply given by solving the following system:

$$\begin{bmatrix} y_1 \\ \vdots \\ y_n \end{bmatrix} = \begin{bmatrix} 1 & x_1 \\ \vdots & \vdots \\ 1 & x_n \end{bmatrix} \begin{bmatrix} \beta_0 \\ \beta_1 \end{bmatrix} \rightarrow \Upsilon = \mathrm{X} \cdot \mathrm{B} \rightarrow B = \frac{\mathrm{X}}{\Upsilon}, \quad \text{(II. 4)}$$

where y_i and x_i are the experimental values of respectively the stress and the strain. The quality of the interpolation is given by the coefficient of determination R^2 calculated as:

$$R^2 = 1 - \frac{\sum_i (y_i - \hat{y}_i)^2}{\sum_i (y_i - \bar{y})^2}, \quad \text{(II. 5)}$$

where $\hat{y}_i$ are the calculated values and $\bar{y}$ is the mean value of the experimental data.

The modulus of elasticity can evolve with cycles, so it is important to calculate it within the first +0.15 % of strain.

II.1.4 Conclusion

The experimental data are an important tool for the study of the mechanical behavior of the composite wires, but also, they are largely used for the definition of material constitutive laws to be implemented in numerical codes. Even though, specific experimental protocols were defined based on several studies for the tensile behavior, the scientific literature is lacking in information about the compressive behavior of the superconducting wires, since due to the small diameter (<1mm) the critical load to avoid the bending of the strand is too much small. Moreover, only one study was found from the author on the tensile fatigue behavior. Hence, the experimental studies performed during this Ph.D. work aim to investigate the fatigue behavior of the Nb_3Sn wires for tensile and compressive solicitations at room and cryogenic temperature. In particular, the tensile tests are based on the work done by G. Lenoir with some adaptations, while for the compressive tests a specific experimental protocol has been developed on purpose. Finally, it is worth mentioning that the test range of these experimental activities is the

wire behavior at relatively high stresses values, so that the difference in initial slopes does not affect the final result and analysis as discussed by (Osamura 2008).

II.2 CHAPTER – TENSILE TESTS

In the prospect of numerical modelling, and in order to take one step further in the description of superconducting wires mechanical properties, it was decided to perform a series of test campaigns. They aimed at characterizing an ITER Nb_3Sn superconducting IT-strand chosen because of its use in a particularly rich experimental SULTAN campaign on the TFIO1 conductor sample.

This chapter presents the tensile tests performed on Nb_3Sn IT-strands. First, it was necessary to know the specific mechanical properties of the wire used for these activities. Second, the experimental protocol had to be defined and adapted to the tools available in the CEA laboratory. Therefore, the two main goals of these experiences are to validate the experimental protocol of the ITSCOTT campaign, see section II.2.1, and to analyze, section II.2.2, the cyclic behavior of the superconducting strands when hundreds of cycles are applied to the strand. Finally, the results are discussed in section II.2.3.

II.2.1 Experimental protocol

The experimental activities were performed both at CEA Paris-Saclay (LCSE Laboratory) and at CEA Cadarache (GAIM Laboratory). The tests at the LCSE Lab were useful to learn the experimental protocol to test the very brittle Nb_3Sn strands under tensile solicitations both at room temperature and at liquid nitrogen temperature. These preliminary tests allowed this Ph.D. project to develop the procedure used afterwards with the tensile machine at the GAIM Lab permitting more various and numerous tests. In particular, the GAIM tensile machine is very useful because it allows the performance of thousands of cycles. Even though the machine has been already used at RT for regular mechanical tests on large samples of steel, cooper, resins, etc…, several adaptations, during the Ph.D. work, were necessary for testing these specific brittle wires concerning the machine software program, the extensometer and the clamping system of the sample. The following paragraphs report the delicate sample preparation and the general machine setup used for the two Labs. A more detailed description of the specific setup used in each Lab is given in the next section II.2.2.

II.2.1.1 Sample preparation

The procedure developed by G. Lenoir (Lenoir 2017), and adapted to the Ph.D. experiences, foresees a preliminary preparation of the sample to develop the SCUTT

device, which is an intermediate component between the sample and the clamping jaws. It permits to handle the strand during the clamping phase without the occurrence of the filaments accidental damage.

Figure II.2.1 shows the design of the SCUTT setup with a steel chamfered tube and a soldered brass ball at each end of the strand.

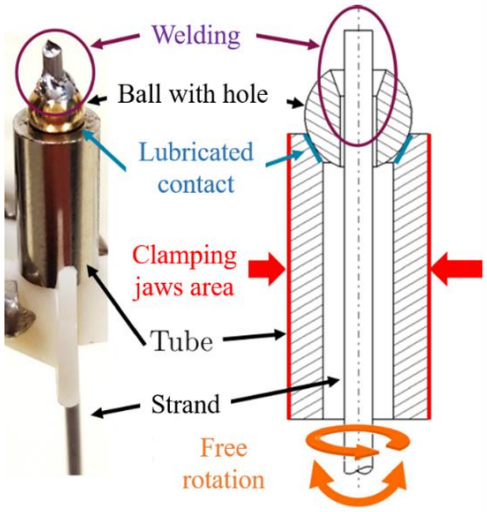

Figure II.2.1. SCUTT device schematical drawing (Lenoir 2017).

The main advantages of the use of the SCUTT setup are:

1. To minimize the bending stress thanks to the alignment of the strand with the clamping jaws;
2. To allow the transmission of the tensile stress, but also the rotation of the strand around its axis;
3. To limit the damage due to the strand handling during the clamping of the strand in the tensile machine;
4. To ensure the application of a uniaxial stress.

The preparation of the sample foresees the following steps and some of them are illustrated by Figure II.2.2:

1. To treat the strand surface by abrasion with sandpaper and orthophosphoric acid;
2. To tin the strand ends to help the metal grip during soldering (see Figure II.2.2a-b);
3. To solder one ball at one end (soldering temperature: ~300 °C);
4. To insert the tubes;
5. To solder the second ball at the other end (see Figure II.2.2c).

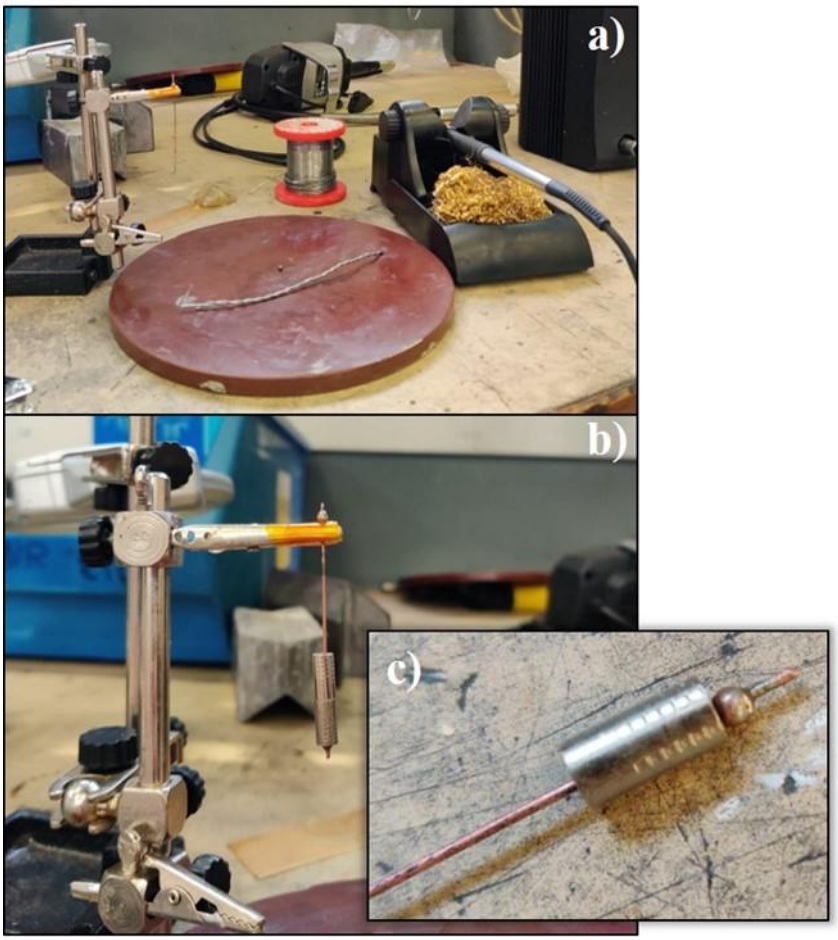

Figure II.2.2. SCUTT sample preparation at CEA.

Figure II.2.3 shows two final samples with the SCUTT device ready to be clamped into the tensile machine. The sample useful length L_0 to consider is the balls distance.

Figure II.2.3. Two IT-strands with the integrated SCUTT device.

II.2.1.2 Tensile test setup

When the sample is ready, it is clamped in the tensile machine by following the later steps:

1. The sample is first clamped into the upper jaw through the tube.
2. The moving crosshead is climbed to insert the second tube inside the lower jaw. It is important to clamp the tube by leaving some space between the ball and the tube, as shown in Figure II.2.4a). This step is needed in order not to apply additional stress to the strand during the placing of the extensometer on the strand.

3. The edges of the extensometer are glued to the strand Figure II.2.4b) with a drying time of 24 h. This step is very delicate since the orthogonality between the extensometer edges and the strand has to be ensured.
4. Finally, the contact between the lower tube and ball is made by means of the application of a pre-load.

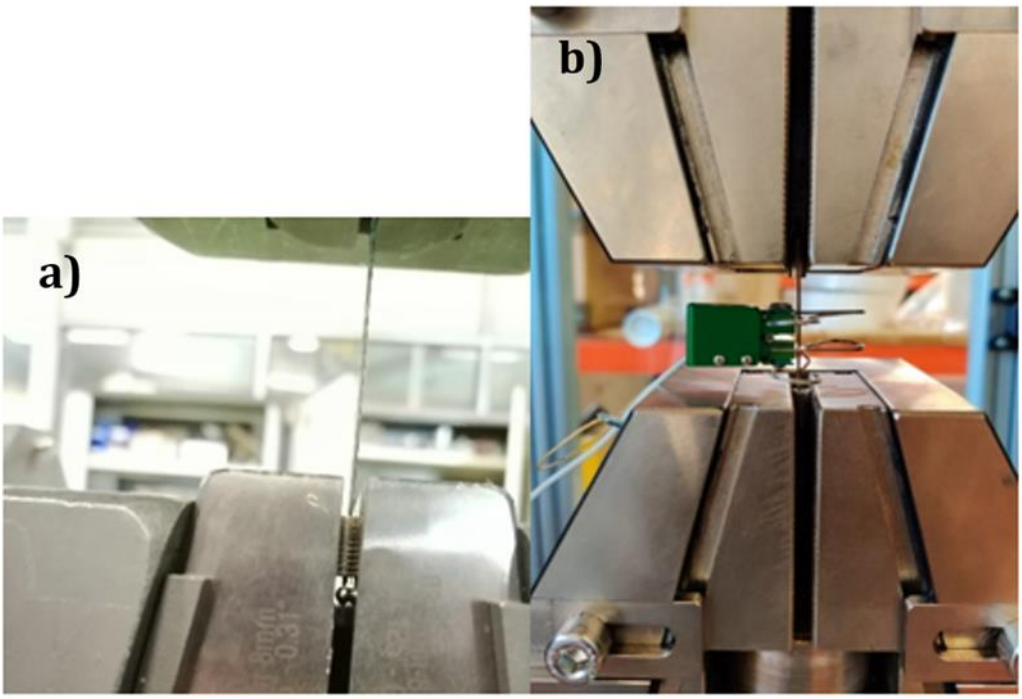

Figure II.2.4. a) The space left between the tube and the ball at the lower jaw; b) the final setup of the extensometer glued to the strand.

The same protocol is adopted for the cryogenic tests, the only difference is that the jaws, the strand and the extensometer are immersed in a liquid nitrogen bath. Moreover, a certain time is needed to have a uniform cooling down of the sample.

II.2.2 ITSCOTT campaign

The tensile tests campaign performed during this Ph.D. work was named ITSCOTT (*Internal Tin Superconductors Tensile Tests*) and includes all the tensile tests performed in the Ph.D. framework. Hence, this section presents the main tests that were performed in the two Labs, LCSE and GAIM, and describes the experimental setups and operating conditions adopted in the two specific cases. In particular, experimental protocols adopted in both Labs follow the main steps presented in the previous section, with some variations due to a different availability of the tools in the Labs. At the same time, the chosen levels of stress and strain to apply during the test refer to the ranges of strain usually studied in similar works. The work range of the superconducting wires goes from -1.5 % to 0.8 % of axial strain according to the results of simulations presented in part IV. However, the taking into account for the bending as well has an impact on the axial strain,

which can reach higher values. Hence, the tests aim to study the mechanical behavior within this range.

II.2.2.1 LCSE tests

Tanks to the collaboration with the LCSE Laboratory (CEA Paris-Saclay, building 192), it was possible to perform three tensile tests: one at room temperature (RT) and two tests at 77 K. The main goal was to learn the experimental procedure proposed by Gilles Lenoir to mechanically test strain-sensitive superconducting strands. Therefore, monotonous tensile tests with unloads were performed at RT and at 77 K. In the latter case, few tens of cycles were also performed as demonstration. However, the LCSE machine software is unfortunately not adapted to investigate higher numbers of cycles, which are representative of the fusion magnets operation.

1. LCSE room temperature tests

Tensile machine setup: The tensile machine is an electro-mechanical machine (INSTRON 5586), see Figure II.2.5. The sample is clamped with V-grooved jaws. The test is performed in displacement control by moving the crosshead in order to load the sample with a uniaxial strain and the force is measured by a specific load cell. An extensometer with knife-edges is glued on the sample to measure the strain. The reduced size of the extensometer limits the bending stress on the strand. Table II.2.1 reports the main information concerning the test tooling.

Table II.2.1. Summary of the main information of the LCSE tensile test at RT.

Load cell	MODEL: INSTRON 2525-818, CAPACITY: 2 kN
Test control	Displacement control
Extensometer	MODEL: INSTRON 2620-603, WEIGHT: 20 g, GAUGE LENGTH: 10 mm
Glue	Loctite 401

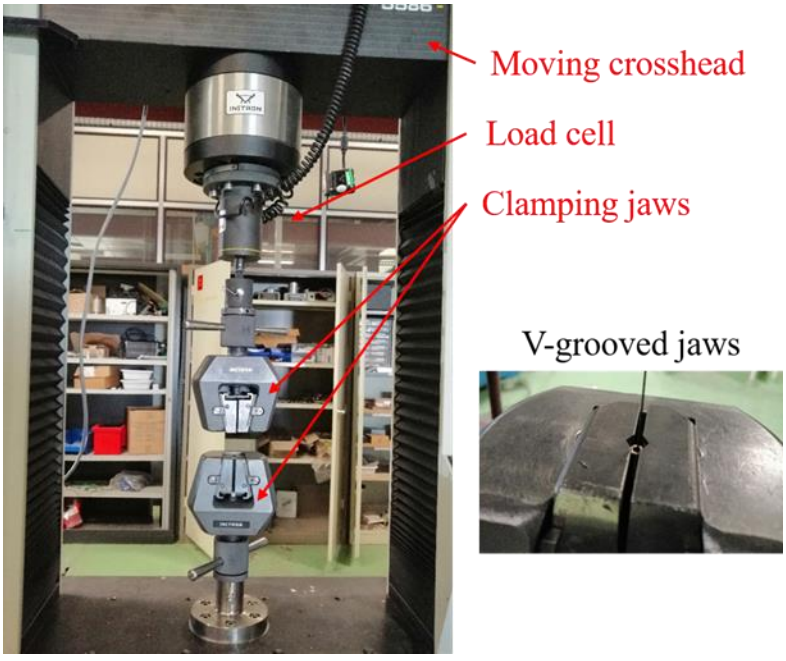

Figure II.2.5. INSTRON 5586 tensile machine and the V-grooved clamping jaws.

Operating conditions: Table II.2.2 summarizes the main settings and parameters of the test. The moving crosshead speed is given by the product between the sample useful length and the aimed strain rate of $v_{th} = 10^{-4}s^{-1}$. A pre-load of 2 N is a delicate and necessary step, especially with the SCUTT device, to guarantee the good contact between the ball and the tube at the sample extremities.

Table II.2.2. Summary of the main parameters of the LCSE tensile test at RT.

	TENSILE TEST RT
Sample length L_0 [mm]	74
Sample diameter ø [mm]	0.82
Test speed [mm/min]	0.444
Software pre-load [N]	2
Acquisition frequency [Hz]	10
Stages number	4
Number of cycles per stage	1
Rupture	Close to soldering

Figure II.2.6 shows the plot of the displacement performed by the crosshead during this test. In this case a monotonous axial tensile loading and four unloadings at different displacement steps are performed. The main goal was to characterize the specific wire used during the experimental activities of the Ph.D. work.

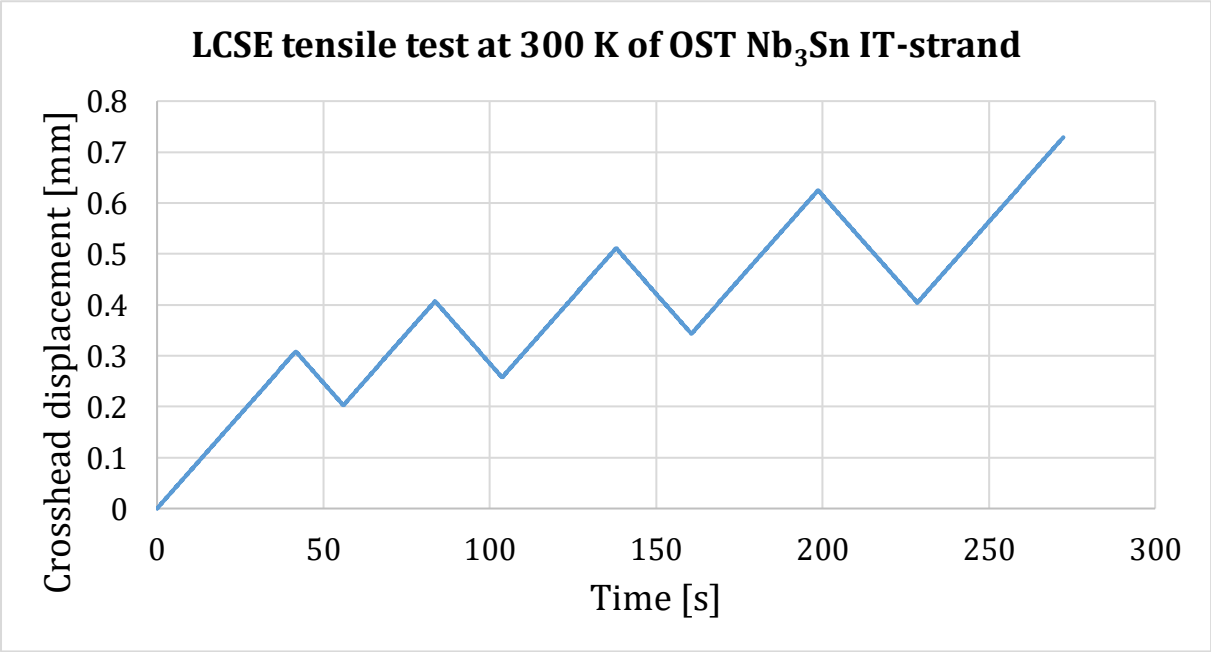

Figure II.2.6. Plot of the crosshead displacement performed during the test as a function of the time at 300 K.

Thanks to this experience, it was possible to learn a reliable method to test the Nb_3Sn wires laying, thus, the foundations for a consistent experimental campaign at GAIM Lab. The strain-stress curves, results and analyses of this test are presented in paragraph II.2.3.1.

2. LCSE cryogenic tests

Tensile machine setup: A specific cryostat is used at LCSE Lab to perform tensile tests at 77 K with liquid nitrogen (LN_2). The tensile machine is an electro-mechanical machine (INSTRON 5500R). A specific protocol foresees to glue the extensometer to the strand (Figure II.2.7a)) and then all the device including the jaws, the sample and the extensometer is inserted into the cryostat, Figure II.2.7b). Finally, the cryostat is filled with LN_2 and the test can start after the time for the cooling down stabilization. Table II.2.3 reports the main information about the test tooling.

Table II.2.3. Summary of the main information of the LCSE tensile test at 77 K.

Load cell	MODEL: INSTRON 2525-818, CAPACITY: 2 kN
Test control	Displacement control
Extensometer	MODEL: INSTRON 2620-603, WEIGHT: 20 g, GAUGE LENGTH: 10 mm
Glue	Loctite 3M DP 190
Cooling liquid	Liquid Nitrogen

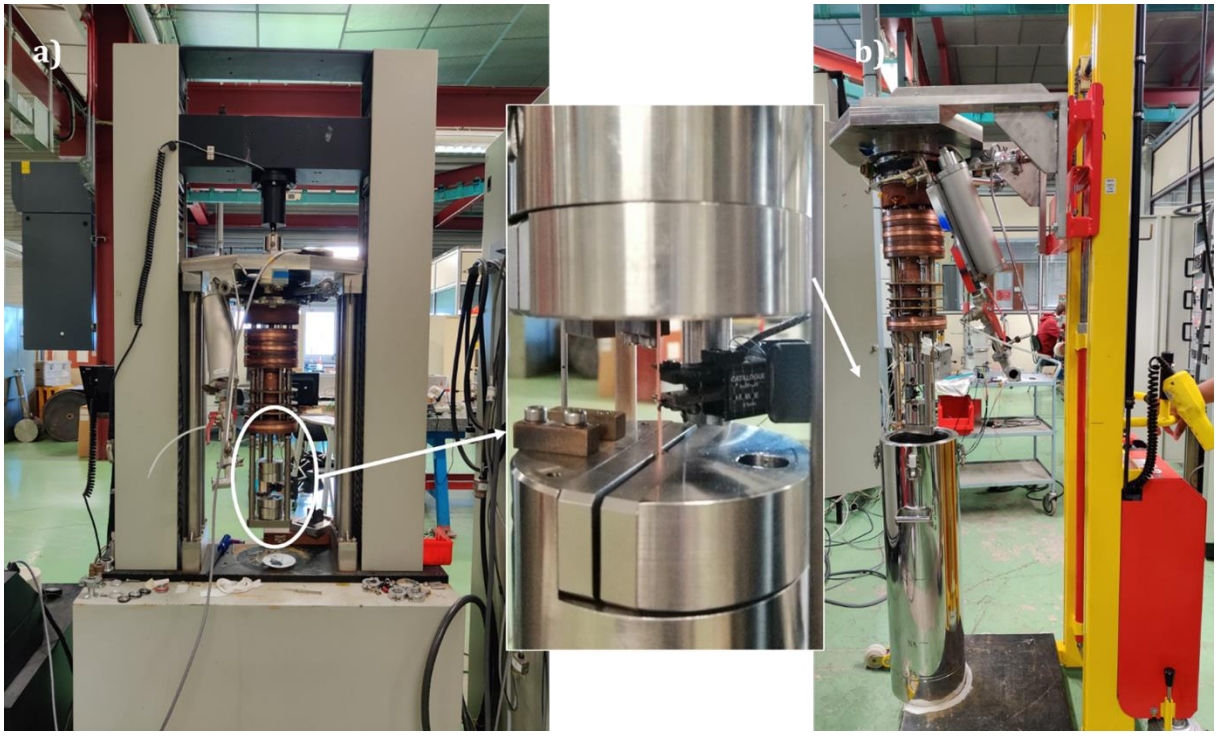

Figure II.2.7. a) INSTRON 5500R **t**ensile machine for cryogenic tests; b) insertion of the device with clamps, sample and extensometer into the cryostat.

Operating conditions: Table II.2.4. presents the main operating conditions. Differently from the previous test, this time the targets are force stages since several unloads are performed at the same stress value. In particular, the test program foresees a monotonous tensile curve with two unloads and 21 cycles load-unload 75-15 N.

Table II.2.4. Summary of the main parameters of the LCSE tensile test at 77 K.

	TENSILE TEST 77 K
Sample length L_0 [mm]	76
Sample diameter ø [mm]	0.82

Test speed [mm/s]	0.06		
Software pre-load [N]	5		
Acquisition frequency [Hz]	10		
Stages number	3		
Stress loads [N]	25	50	75
Stress unloads [N]	15	15	15
Number of cycles	1	1	21
Rupture	Close to soldering		

Figure II.2.8 reports the displacement control during the tensile test. The main purpose was to provide a reference curve for the wires at cryogenic temperature as well and for several cycles. Due to the limits of the tensile machine and software, it was not possible to perform more than 20 cycles. It was decided to work at an imposed effort of 75 N corresponding to 150 MPa to ensure a work range not over 0.5 % of strain. The results are discussed in paragraph II.2.3.2.

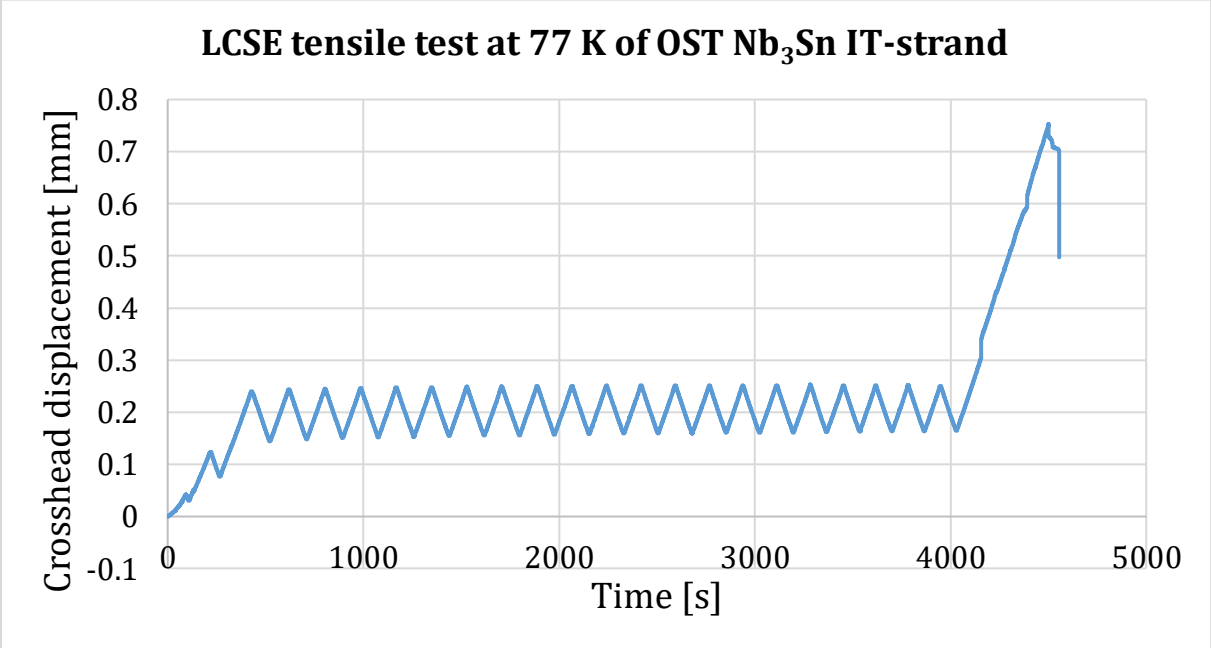

Figure II.2.8. Plot of the crosshead displacement performed during the tensile test at 77 K.

II.2.2.2 GAIM cyclic tests at RT

Tensile machine setup: The tensile machine is an electro-mechanical machine (INSTRON 1175) with a capacity of 100 kN, see Figure II.2.9a), but a more sensitive load cell is used. The extensometer and the test setup are shown in Figure II.2.9b). The sample is clamped thanks to specific tools (Figure II.2.9c)) that have been developed during the Ph.D. to assure the axial application of the tensile force (more details about the design are given in Annex B). Table II.2.5 provides the details of the test. The test is force controlled; the extensometer with V-knife edges, glued on the sample, measures the strain. The extensometer was selected and bought on purpose to satisfy the requirements of the ITSCOTT campaign.

Table II.2.5. Summary of the main information of the GAIM tensile test at RT.

Load cell	MODEL: INSTRON, CAPACITY: 1 kN
Test control	Force control
Extensometer	MODEL: EPSILON 3442-010M-010M-LT, WEIGHT: 8 g, GAUGE LENGTH: 6 mm
Glue	Loctite 409

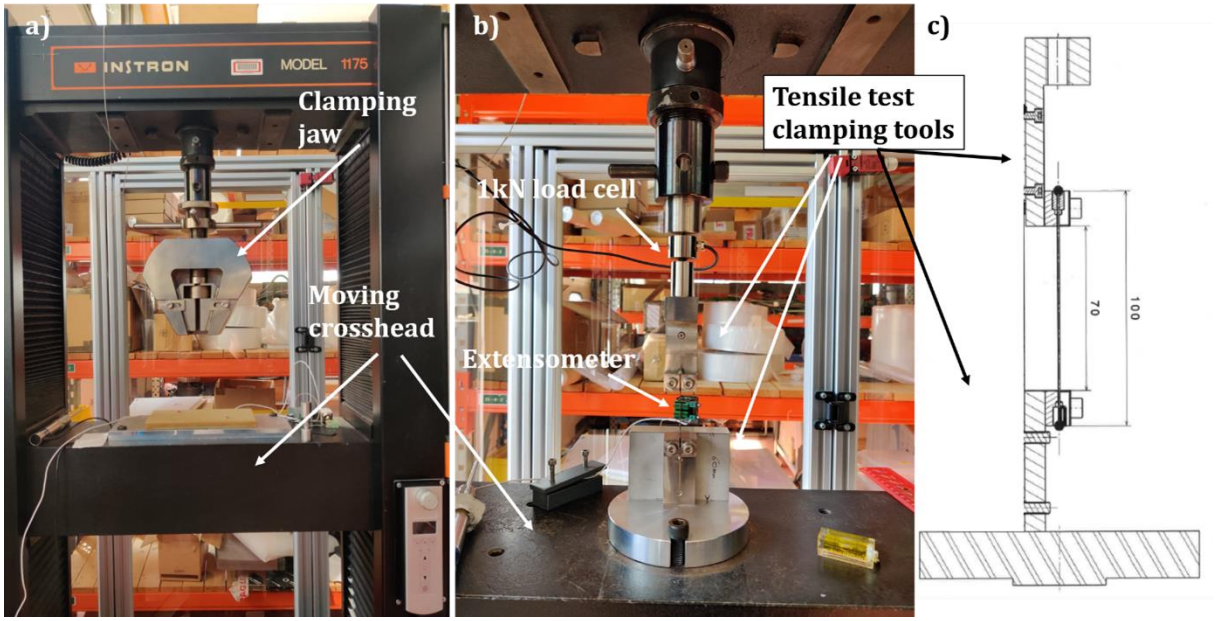

Figure II.2.9. a) Tensile machine; b) tensile tests setup; c) tensile clamping tools.

Operating conditions: Table II.2.6 summarizes the main operating conditions of the tensile test. The force is controlled by a proportional controller; hence the resulting force curve is proportional to the imposed signal. A set of parametric tests was performed to find the correct parameter (*control_force_coefficient*) to respect the imposed signal corresponding to a speed of 20N/s. This parameter is related to the response of the machine to a given solicitation and it should be adapted to the sample overall stiffness.

Table II.2.6. Summary of the main parameters of the GAIM tensile test at RT.

	TENSILE TEST RT		
Sample length L_0 [mm]	80		
Sample diameter ø [mm]	0.82		
Test speed [N/s]	20		
Control force coefficient	54		
Software pre-load [MPa]	2		
Pre-load speed [mm/s]	0.005		
Acquisition frequency [Hz]	5		
Stages number	3		
Stress loads [MPa]	50±2	100±2	150±2
Stress unloads [MPa]	30±2	30±2	30±2
Number of cycles	1	1	1000
Rupture	Close to soldering		

Figure II.2.10 plots the force that was applied during the test. Only 50 loads-unloads cycles at 75 N (150 MPa) are here shown.

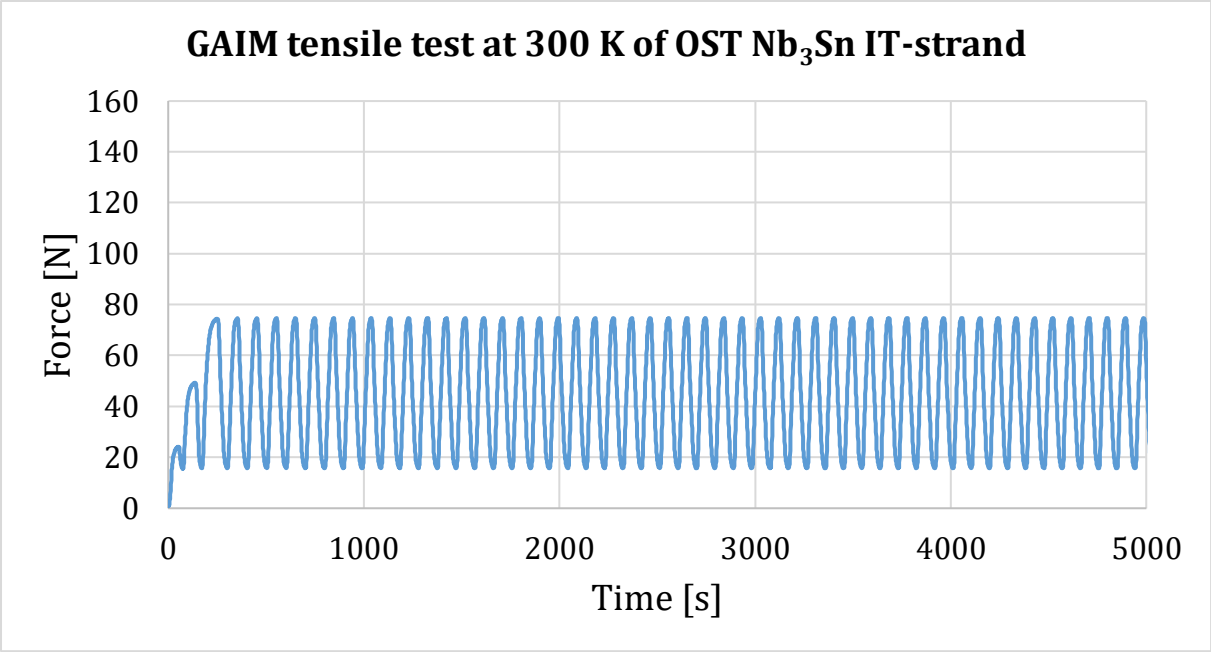

Figure II.2.10. Plot of the applied force to the sample during the tensile test at 300 K.

The GAIM software and machine allowed the performance of 1000 cycles at RT, after validation of the experimental method by comparison with the LCSE results. The next step was to develop and perform cryogenic tests.

II.2.2.3 GAIM cryogenic tests

Tensile machine setup: The tensile machine is the same, but this time the clamping tools are immersed in a LN_2 bath. A picture of the box designed during this Ph.D. (CAD drawings examples are shown in Annex B) is shown in Figure II.2.11. The insulating resin G-10 is used on the top of the clamping line and on the bottom of the box to insulate the machine from the cold temperature. Moreover, the glue used for the extensometer has to be able to work at cryogenic temperatures and for the purpose an epoxy adhesive was used. Table II.2.7 illustrates the main information about the tools adopted for the GAIM cryogenic tests.

Table II.2.7. Summary of the main information of the GAIM tensile test at 77 K.

Load cell	1 kN
Test control	Force control
Extensometer	MODEL: EPSILON 3442-010M-010M-LT, WEIGHT: 8 g, GAUGE LENGTH: 6 mm
Glue	Loctite Ablestik 286
Cooling liquid	Liquid Nitrogen

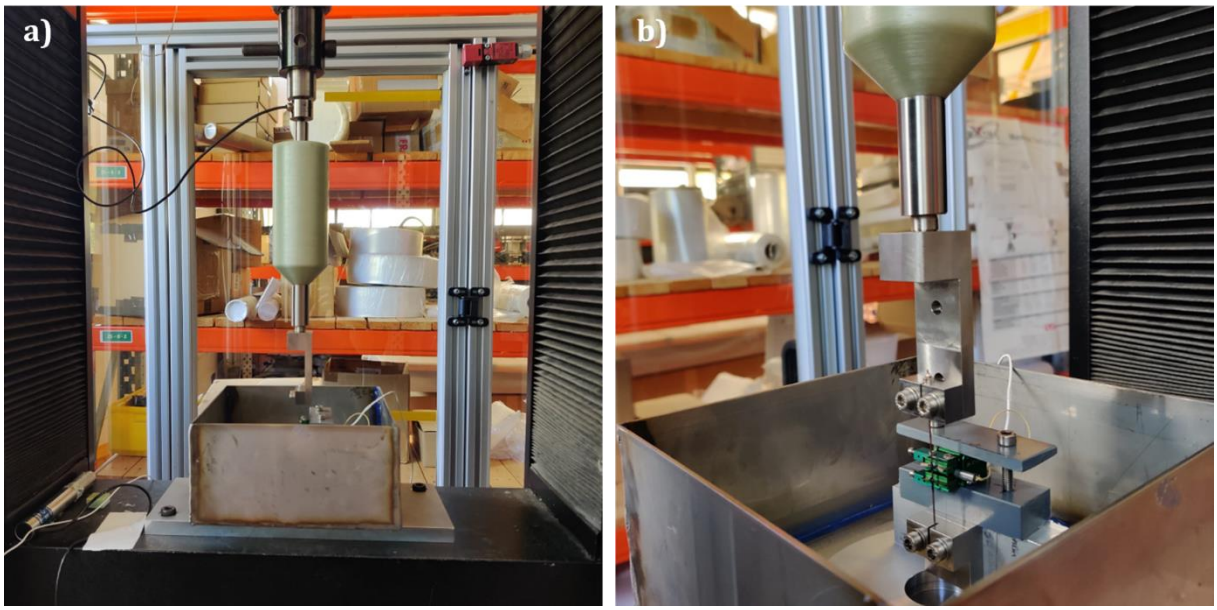

Figure II.2.11. a) Overview of the cryogenic tests setup; b) detail from the inside of the box.

Operating conditions: Table II.2.8 summarizes the main operating parameters. The test sequence at the cryogenic temperature is the same one than at RT, however during the test the operator needs to keep refilling the LN_2 containment box since LN_2 evaporates very quickly.

Table II.2.8. Summary of the main parameters of the GAIM tensile test at 77 K.

	TENSILE TEST 77 K		
Sample length L_0 [mm]	60		
Sample diameter ø [mm]	0.82		
Test speed [N/s]	20		
Control force coefficient	54		
Software pre-load [MPa]	2±1		
Pre-load speed [mm/s]	0.005		
Acquisition frequency [Hz]	5		
Stages number	3		
Stress loads [MPa]	50±2	100±2	150±2
Stress unloads [MPa]	30±2	30±2	30±2
Number of cycles	1	1	1000
Rupture	Close to soldering		

Figure II.2.12 shows the applied force during the cryogenic test and the first 50 load-unload cycles at 75 N, corresponding to a stress of 150 MPa.

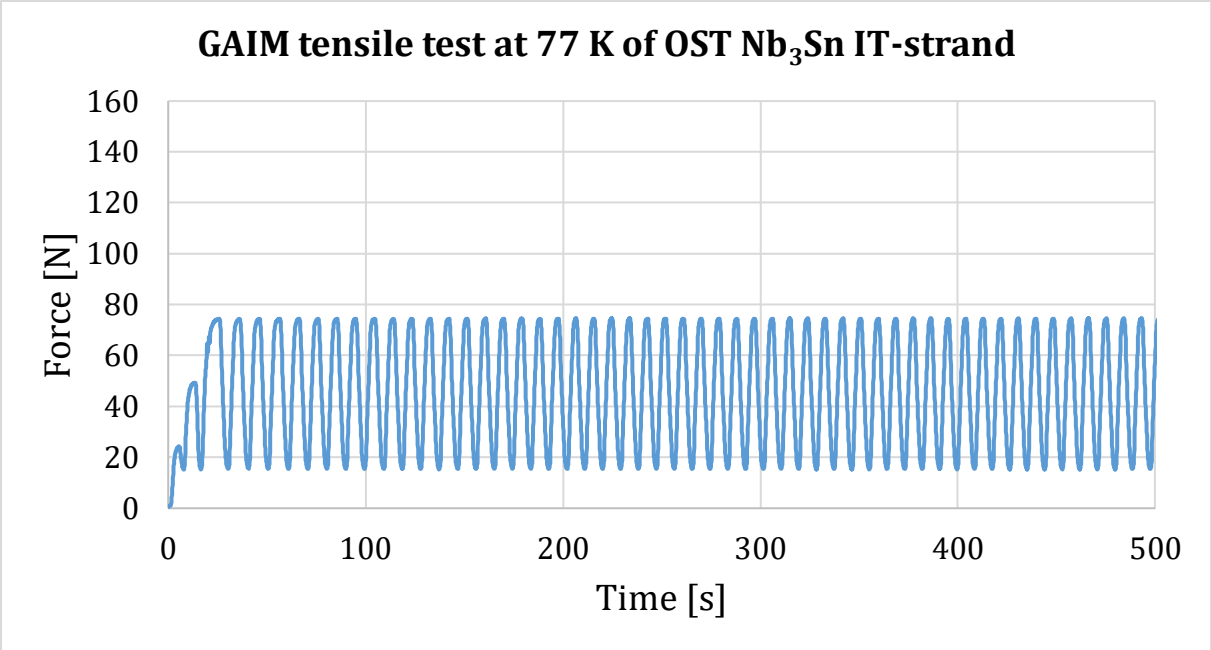

Figure II.2.12. Plot of the applied force to the sample during the tensile test at 77 K.

II.2.3 Results discussion

II.2.3.1 RT tensile results

Figure II.2.13 compares the strain-stress characteristics obtained in the two Labs at RT. Only one test was performed at LCSE Lab and the two more relevant tests performed at GAIM Lab are here reported.

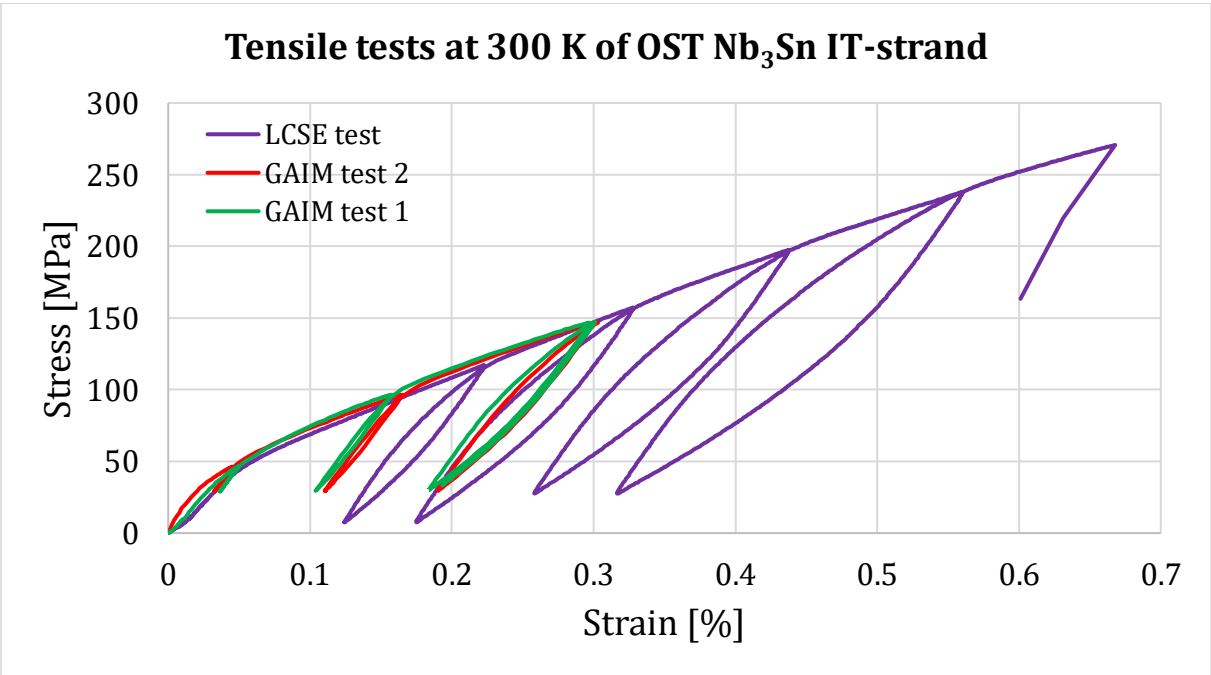

Figure II.2.13. Comparison of the strain-stress plots of the OST G 01EX0571A01C strand tensile test at 300 K.

The software test program of the tensile machine and the tooling to perform the tests in the two Labs are quite different, as explained in paragraphs II.2.2.1 and II.2.2.2.

However, the accordance in the resulting envelopes of the tests shows that the experimental protocol and adaptation devices, that have been developed until now during this Ph.D. work to perform the tensile tests on brittle Nb_3Sn wires at the GAIM Lab, produce consistent results. The initial slopes of the plots are slightly different, probably due to the manipulation of the sample and/or an initial bending, which is the reason why (Osamura 2008) recommends measuring the elasticity modulus on unloading curves. Moreover, the ratio between the initial elasticity modulus E_0 and the one calculated on the first unloading at 150 MPa E_u belongs to the 0.7-1.3 range as recommended in II.1.2.1 to can consider the test validated.

Once the procedure was validated, several load-unload cycles were performed at a set stress to study the behavior of the Nb_3Sn wire when thousands of cycles are applied. Figure II.2.14 presents the result and after the thousandth cycle (in red), the test continues until rupture of the sample.

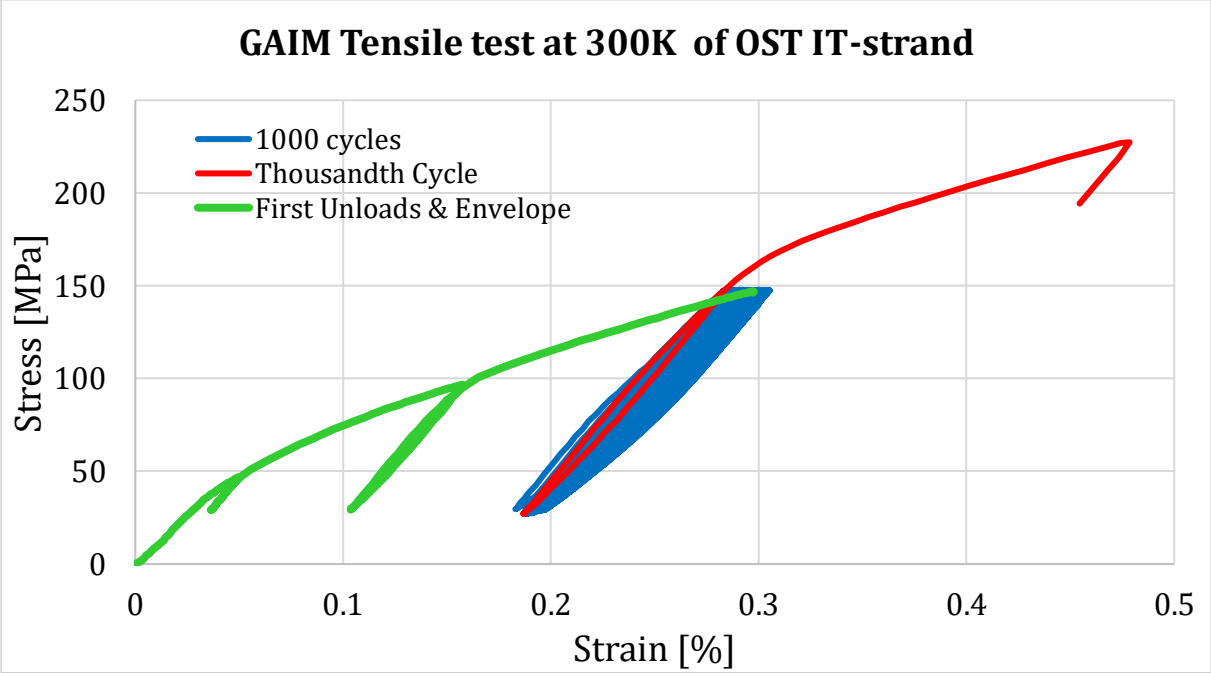

Figure II.2.14. Strain-stress plot of the OST G 01EX0571A01C strand tensile test 1 at 300 K performed at the GAIM Lab.

Figure II.2.15 and Figure II.2.16 report the evolution of the modulus of elasticity for the tensile tests at RT for both Labs. As already anticipated, the initial slope is affected by the setting-up and the sample initial state, so the analyses of the elasticity moduli are done on the unloading curves. The two tests at GAIM Lab exhibit a similar behavior. The elasticity modulus within 0.15 % of strain is between 133 MPa and 135 MPa, in accordance with the 135 MPa found by (Bajas 2011), even if it is not the same wire.

The elasticity modulus increases with the applied tensile load because of the composite nature of the wire: the twisted filaments stretch and tend to become parallel.

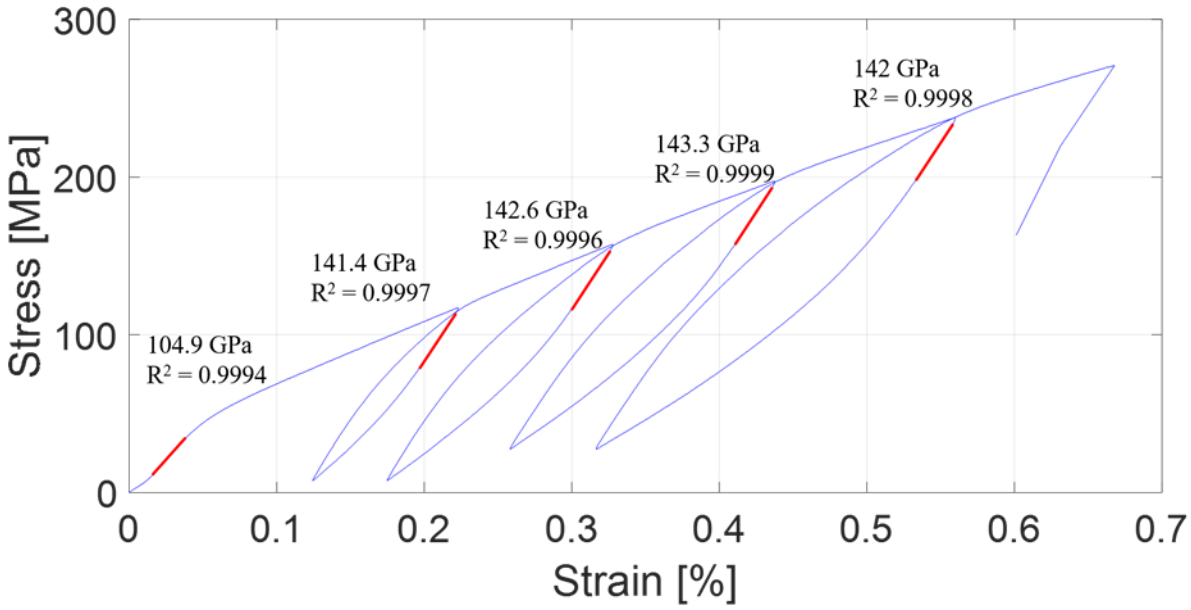

Figure II.2.15. Elasticity modulus evaluation of the LCSE tensile test at RT.

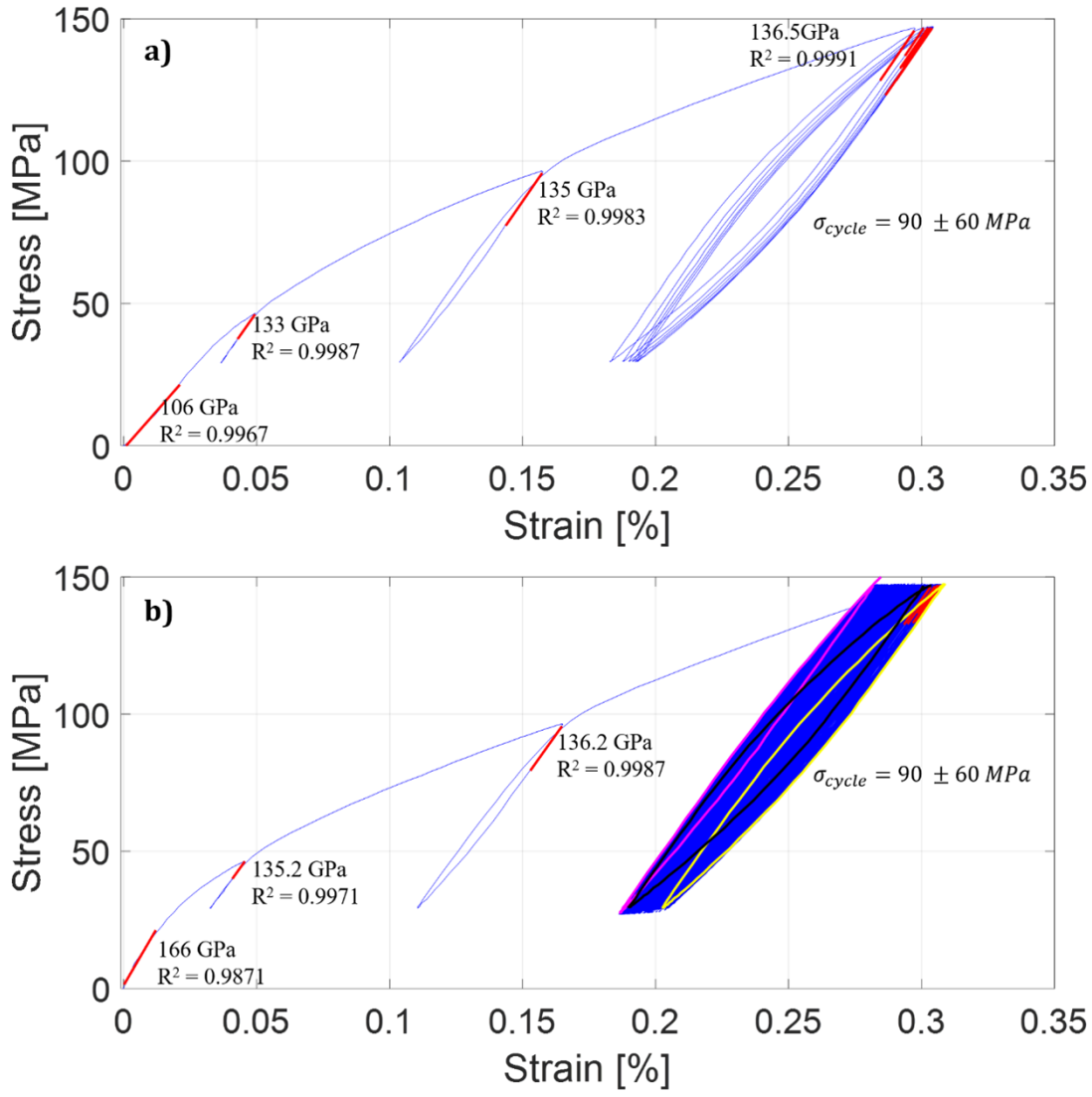

Figure II.2.16. Elasticity modulus evaluation of the GAIM tensile test at RT a) for test 1 and b) test 2.

Figure II.2.17a) reports the evolution of the strain as a function of the time during cycling for the first 30 cycles. Figure II.2.17b) shows the complete evolution of the peak strain with cycles and the average value of strain. The first strain upper peak corresponds to 0.298 % and it reaches its maximum at 0.305 % after 13 cycles. After it starts decreasing until 0.284 % after 1000 cycles. Figure II.2.17c) reports the difference between the maximum and minimum peaks. This plot presents a behavior like the one found by (Sheth 2011), the difference between the maximum and minimum peaks decreases with cycles with an initial more accentuated slope. (Sheth 2011) shows that this behavior tends to stabilize around 10000 cycles at 77K. The Ph.D. tests do not show a stabilization of the phenomenon, probably due to the smaller number of cycles.

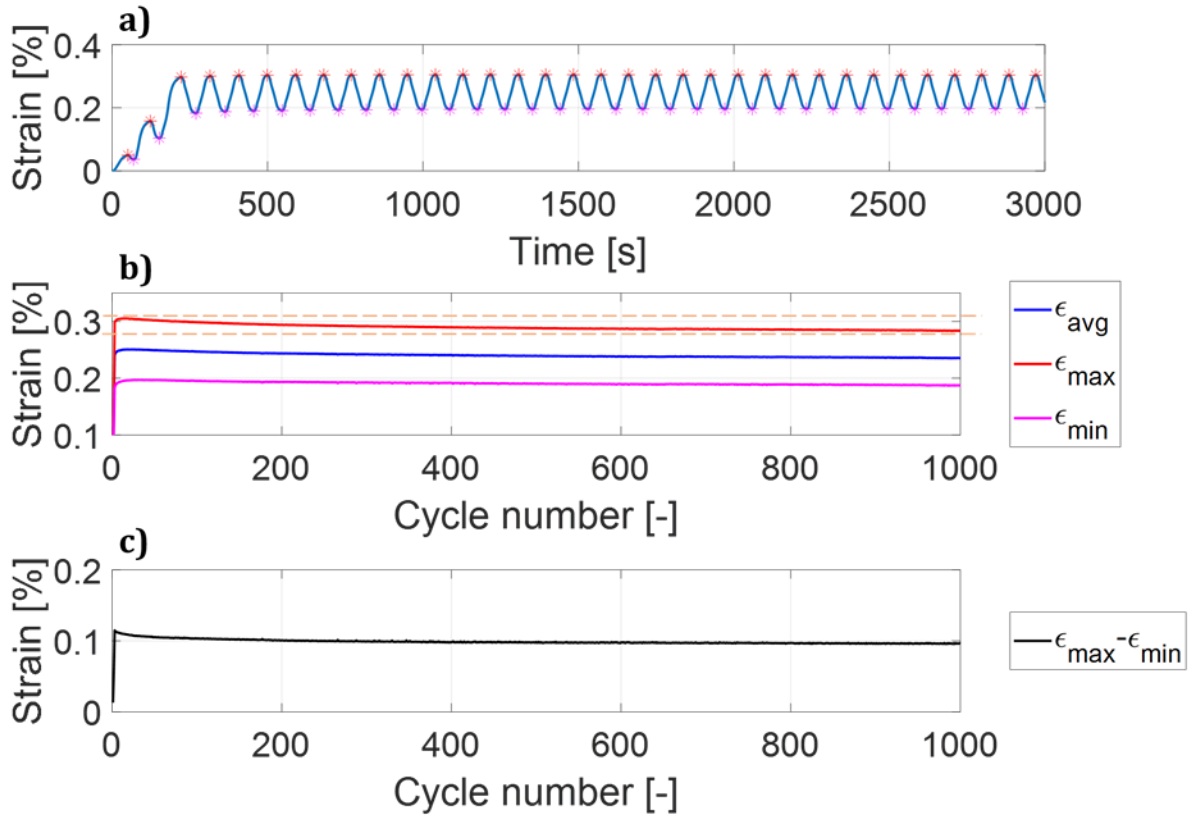

Figure II.2.17. a) Plot of the strain for the first 30 cycles versus the time for GAIM test 1 at RT, b) evolution of the max, min and mean values of the strain with cycles, c) difference between the max and min strains with cycling.

However, what (Sheth 2011) could not see with the plot of the difference between the max and min displacements (see Figure II.1.8) is this change of behavior after the first cycles. According to (Bajas 2011) during the first 15 cycles, there is an accumulation of the irreversible plastic strain. The same effect is observed in the present study for the first cycles, but then a progressive hardening, probably due to the plasticization of the matrix as explained by (Sheth 2011), predominates and the global effect is the decrease of the average strain. The explanation for this behavior is difficult due to the composite structure of the wire. Therefore, there is both a material and structure answer to the tensile solicitation. In order to identify the two contributions, a numerical model of the wire

considering the interactions between the composite components is recommended. Figure II.2.18 shows the accumulation of the irreversible plastic strain on the stress-strain characteristic. The difference between the first cycle (black) and the 13th cycle (yellow) corresponds to a $\Delta\varepsilon$ of +0.0077 %, while from the 13th cycle to the thousandth cycle (pink) there is a variation of $\Delta\varepsilon$ = -0.0217 %.

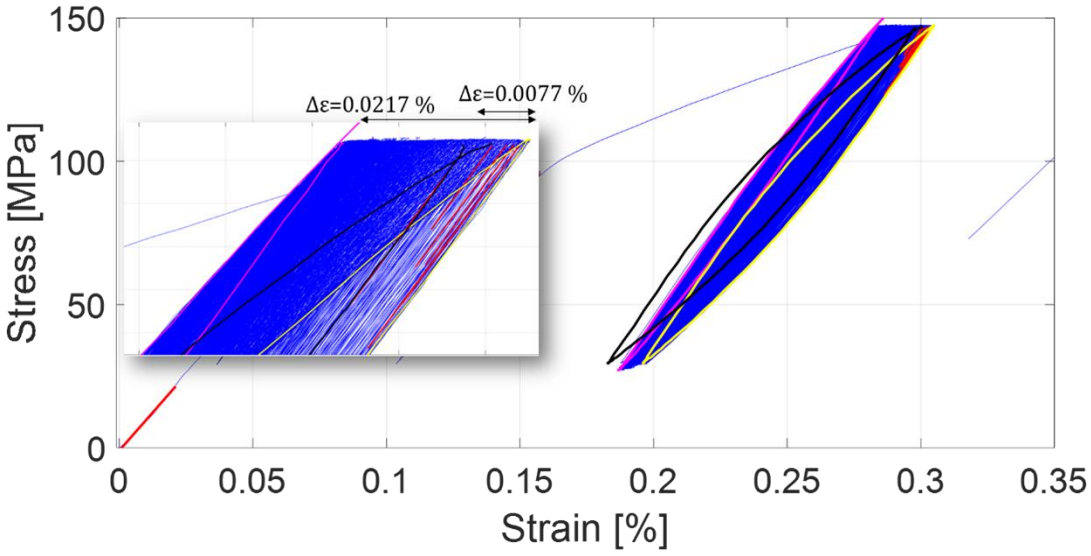

Figure II.2.18. Strain-stress characteristics of the GAIM tensile test 1 with focus on the plastic deformation accumulation with cycling.

These tests reveal a two-steps dynamic evolution of the composite behavior made of STEP 1 [~1 → 15 cycles]: accumulation of plastic strain and STEP 2 [>15 cycles]: kinetical hardening. More investigations are recommended to understand its impact on the global cable electrical behavior with cycling.

Figure II.2.19 shows the evolution of the elasticity moduli with cycling, illustrating the global increase of the axial stiffness of the wire.

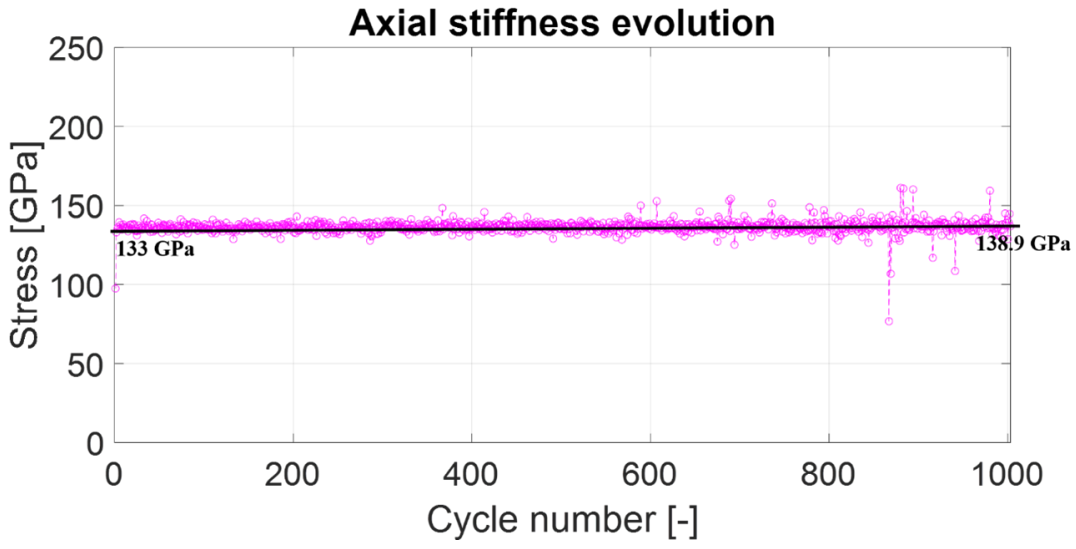

Figure II.2.19. Axial stiffness evolution with cycles for the GAIM tensile test 1 at RT.

The average experimental kinetical hardening of the strand under this cyclic loading can be approximated by the linear relation:

$$E_N(N_{cycles}) = E_u + 0.0024N_{cycles}[\%], \quad \text{(II. 6)}$$

where E_u is the elasticity modulus on the first unloading at 150 MPa corresponding to 136.5 GPa.

Table II.2.9 summarizes the main mechanical parameters of the characterization of the wire performed at the GAIM Lab.

Table II.2.9. Summary of the main mechanical parameters of the GAIM tensile tests at RT.

	TEST 1	TEST 2
Elasticity modulus (50 MPa unload)	133 GPa	135.2 GPa
Elasticity modulus (150 MPa 1000th unload)	138.9 GPa	139 GPa
E_0/E_u ratio	0.78	1.21
Strain peak at 150 MPa 1st cycle	0.298 %	0.301 %
Strain peak after 13 cycles	0.305 %	0.309 %
Strain peak after 1000 cycles	0.284 %	0.282 %

II.2.3.2 Cryogenic tensile results

As shown in Figure II.1.4 (Van den Eijnden 2005), the impact of the temperature on the stress-strain characteristics is not expected to be too much relevant. However, the tests performed at the LCSE Lab showed more impact of the temperature on the result, as illustrated in Figure II.2.20.

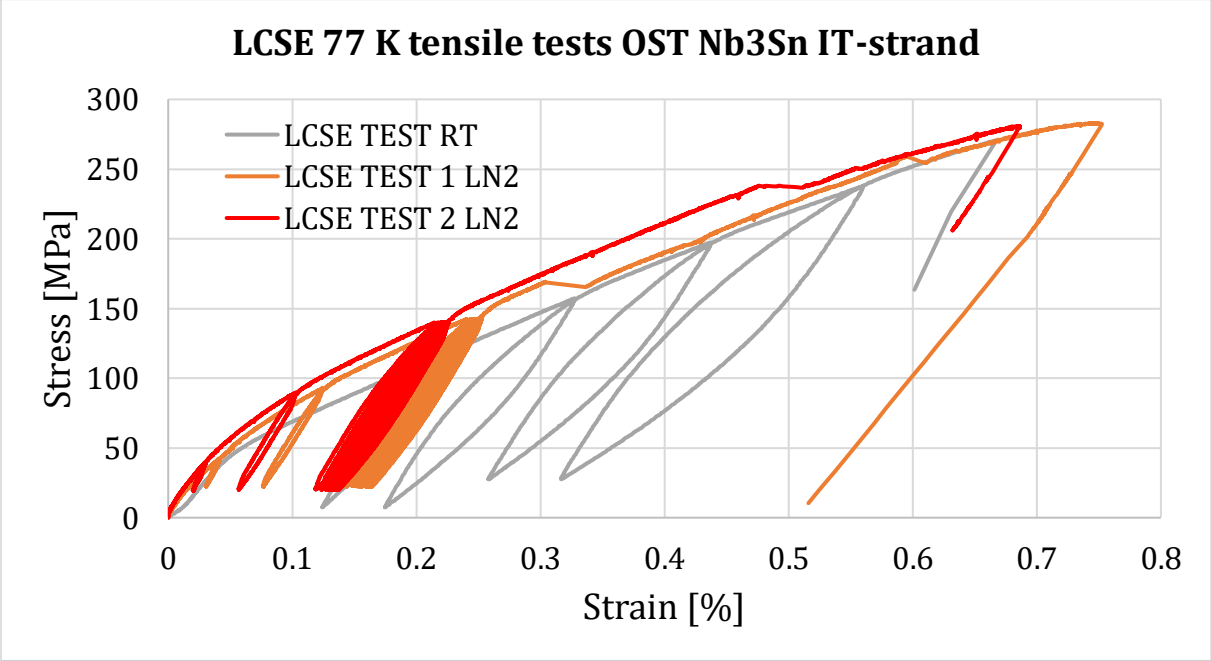

Figure II.2.20. Strain-stress plot of the OST G 01EX0571A01C strand tensile test at 77 K performed at the LCSE Lab and comparison with the RT test.

The envelop discontinuity in the cryogenic tests is due to local ungluing of the extensometer during the test.

In this case, it was possible to perform only 21 cycles at 150 MPa. Hence, it was possible to observe the first strain accumulation phenomenon of $\Delta\varepsilon$ = 0.01 %, but not the second probably due to the limited number of cycles. The temperature increases the global stiffness of the wire compared to RT. This could explain why the plastic deformation reaches its peak for a lower number of cycles at RT, while at 77 K after 20 cycles the plastic strain seems to keep accumulating. However, a similar phenomenon as the one observed at RT during cycling is still expected according to the results of (Sheth 2011). This is why a major effort was produced to adapt the GAIM tensile machine to cryogenic tests in open LN_2-bath conditions. Hence, it was important to evaluate the cyclic behavior of the wire at 77 K as well under higher numbers of cycles.

Figure II.2.21 reports two GAIM attempts and compares them to the LCSE test 2 at LN_2 temperature and to the GAIM RT test envelop. The first attempt (GAIM TEST 1) gives a result that superposes to the RT result because of the non-optimal temperature control during the test. In fact, the box was filled with LN_2 at the beginning of the test and the nitrogen level decreased during the test affecting the measurement. During the second attempt (GAIM TEST 2), the level was maintained to keep the sample constantly immersed for all the duration of the test. This attempt seems in good accordance with the one obtained by the LCSE cryogenic tests, except for the initial part of the curve.

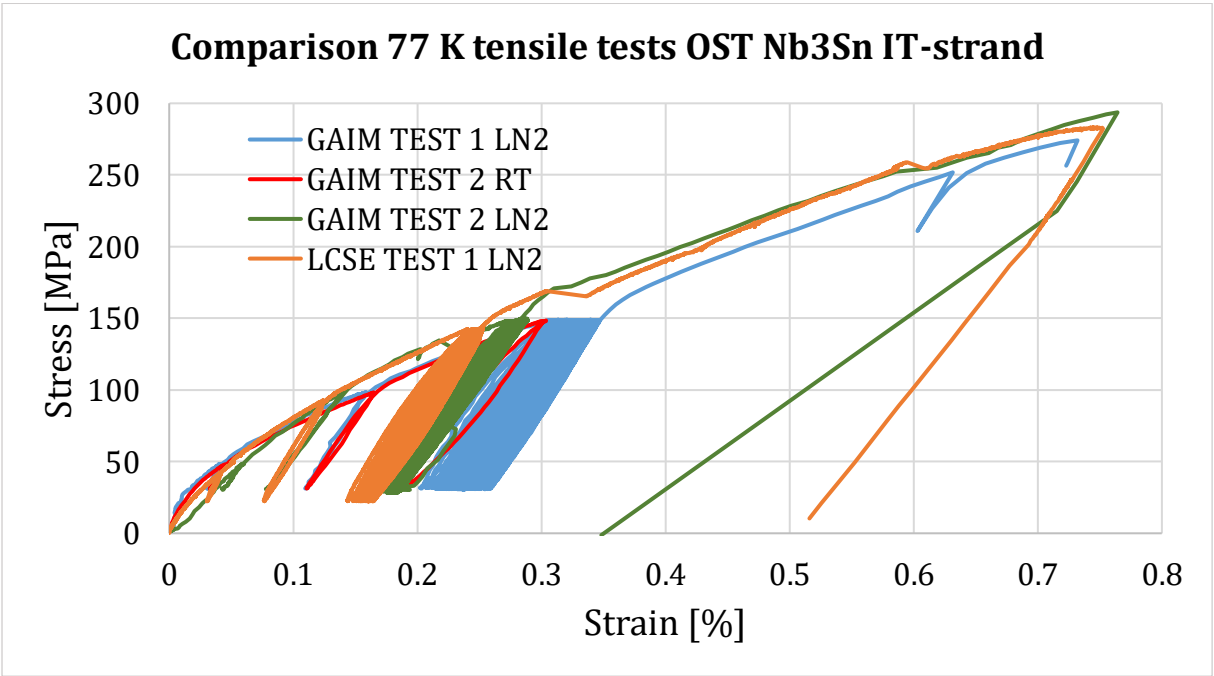

Figure II.2.21. Strain-stress plot of the OST G 01EX0571A01C strand tensile test at 77 K performed at the GAIM and LCSE Labs and comparison with the GAIM RT test.

Figure II.2.22 reports the evolution of the strain with the cycles. According to the strain accumulation of the LCSE LN_2 tests, after 21 cycles an irreversible plastic strain of 0.01 % is observed. There is a discontinuity at the 760th cycle due to the temperature control. After 750 cycles, there is an accumulation of strain of 0.012 % and again the

decrease of the maximum and minimum strains difference is visible. However, it is still not possible to see the two accumulation phenomena characterizing the test at RT. At the same time, the major accumulation of strain happens within the first 20 cycles and then the deformation speed decreases. An inversion of the behavior is expected after more cycles as for the RT tests. Hence, a further investigation at cryogenic temperature is recommended.

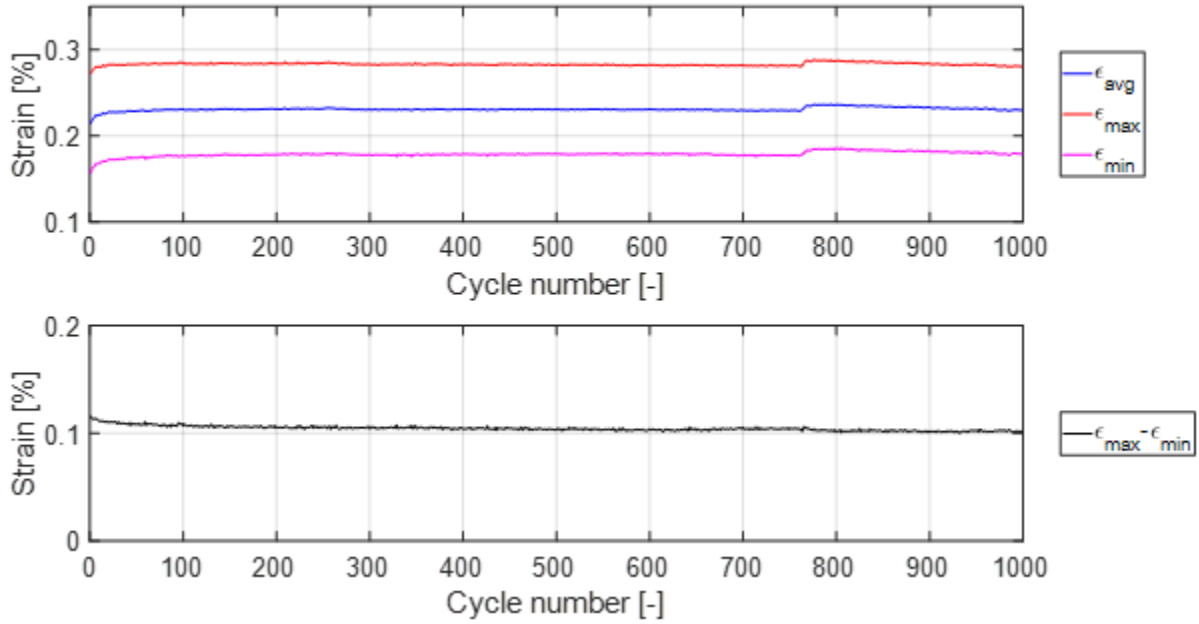

Figure II.2.22. Evolution of the max, min and mean values of the strain with cycles and difference between the max and min strains with cycling at 77 K.

Figure II.2.23 reports the identification of the elasticity moduli for the GAIM test 2 at 77 K. The values are lower than the ones found at RT, but these results should be analyzed with some precautions since temperature control and gluing are extremely difficult for this type of tests for both the LCSE and GAIM Labs. Additional studies are thus recommended for cross-checks and statistics, as well as to improve the reliability of the cryogenic tests in the box and the quality of the chosen glue.

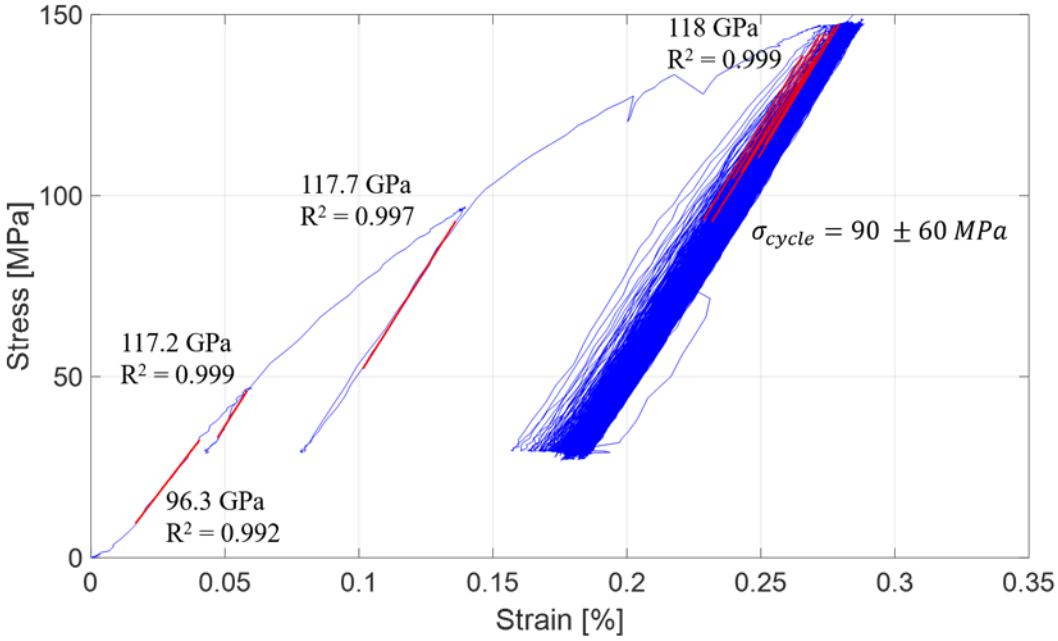

Figure II.2.23. Elasticity modulus assessment of the GAIM tensile test at 77 K for test 2.

Figure II.2.24 plots the evolution of elasticity moduli with cycling and according to all the previous tests, the effect of the cycles is a small increase of the elasticity modulus.

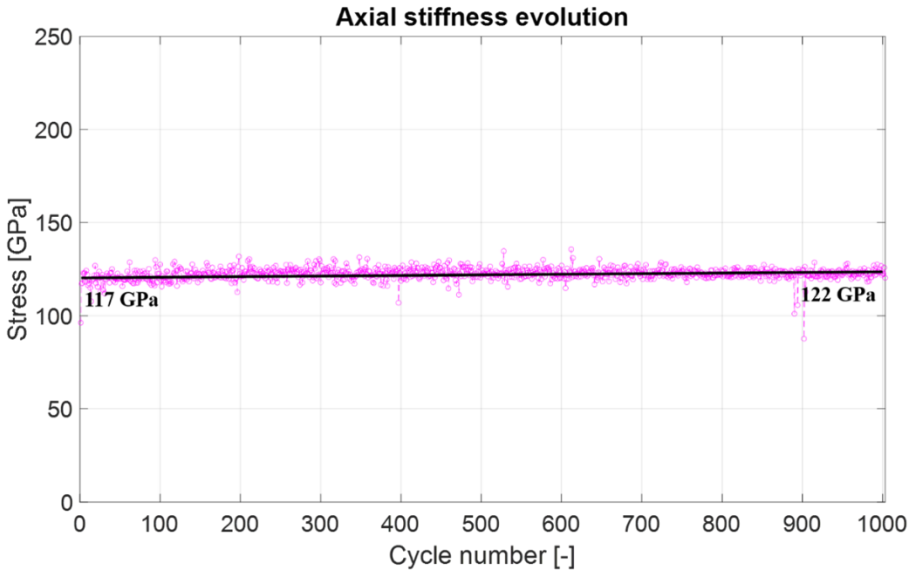

Figure II.2.24. Axial stiffness evolution with cycles for the GAIM tensile test 2 at 77 K.

Even though, the experimental protocol adopted for the 77 K tests at the GAIM Lab is still under improvement, the preliminary results show a reasonable behavior with cycling, consistent with trends established in tensile tests, although with an apparent lower modulus of which the measurement could be affected by the boiling liquid nitrogen.

II.2.4 Conclusion

These experimental activities allowed a deep analysis and a full mechanical characterization, more detailed than the studies presented in literature, of the Nb_3Sn IT-wires for hundreds of cycles. The work highlighted two phenomena at RT associated with the plastic deformation of the wire. In particular, a two-steps dynamic evolution of the strain was highlighted. This characterization enriches the description of the mechanical behavior of superconducting composites submitted to fatigue loading in traction.

The tests performed at cryogenic temperature need further improvements, but the cyclic behavior of the strain provides results in reasonable agreement with what was found by (Sheth 2011).

For all the tests, a progressive increase of the elasticity modulus has been observed, thus highlighting a change in the mechanical properties of the wire with cycles.

It is worth noting already that the range of accumulated strain (~0.02% after 1000 cycles) is relevant to a change in the current carrying capability. The typical change of effective strain in a TF sample after 1000 cycles is in the range 0.02%-0.05% (Breschi 2011), although the applied load during the uniaxial tests is quite higher than what is expected in strands inside a cable. In the end, the effects observed during the experimental campaigns should be confirmed, and integrated, if possible, in further developments of the strands mechanical constitutive laws. Furthermore, these phenomena should also be confirmed in compressive cyclic loadings, which is treated in the next section.

II.3 CHAPTER – COMPRESSIVE TESTS

This chapter presents the compressive tests performed on the reference Nb_3Sn IT-strand. Before illustrating the several steps that compose the protocol, it is important to explain why it is necessary to create and adopt a specific experimental protocol. Section I.2.3 shows how the cables inside the jacket work in compression during the machine operation due to the cooling down at the operating temperature of 4.2 K. Hence, as previously mentioned, it is important to have the material constitutive laws for the Nb_3Sn wires in the compressive domain. However, the small diameter of the wire makes the longitudinal compressive solicitation impossible without the occurrence of buckling/bending of the wire. Differently from the tensile tests presented in chapter II.2, in this case a completely new experimental protocol was developed in order to provide an insight into the compressive behavior of the superconducting wires. The main goals of this experimental activity are to develop an experimental protocol to test Nb_3Sn strands under compressive solicitations, to compare the compressive behavior to the tensile one and to identify any potential phenomenon specific to the compressive behavior. Section II.3.1 presents the new compressive protocol, section II.3.2 reports the experimental campaign and section II.3.3 analyzes and discusses the main results.

II.3.1 EPSIC protocol

This section presents the new experimental protocol named EPSIC (*Experimental Protocol to measure Strands In Compression*) that was entirely developed during this Ph.D. program. Paragraph II.3.1.1 illustrates the studies performed to design this very specific compressive test sample. Then, the protocol describes the full preparation and test procedure from the manufacture (paragraph II.3.1.2) to the test setup and execution (paragraph II.3.1.3).

II.3.1.1 EPSIC sample design

The main idea behind the design of the EPSIC sample is to design and test a bundle of compacted parallel wires instead of a single wire, deducing the compressive law of the single strand by scaling the results to the single wire cross-section.

In fact, the bundle of wires has a lower tendency to bend than the single wire for a given applied compressive axial stress. To demonstrate this behavior, it is possible to calculate the *Euler's critical load* N_c, which is the compressive load over which a further

load suddenly deflects laterally the straight sample (Desai 2018). The calculation is based on several assumptions: the sample is straight, axially loaded, perfectly elastic, homogeneous, isotropic, its cross-section is uniform and the length is very large if compared to the cross-sectional surface. Finally, the shortening of the sample due to the compression is neglected. The formula, taken from (Desai 2018), is:

$$N_c = \frac{\pi^2 EI}{l_{eff}^2}, \tag{II. 7}$$

where E is the Young's modulus, I is the momentum of inertia, and l_{eff} is the effective length of the sample. The minimum momentum of inertia for a beam is given by:

$$I = \frac{\pi {D_{sample}}^4}{64}. \tag{II. 8}$$

For the studied cases, the ends are considered fixed and so l_{eff} is equal to half of the initial length of the sample l_0. Considering all the assumptions, this load is calculated for the bundle of wires and for the single wire in order to have a qualitative comparison of the critical loads for the two cases. Table II.3.1 summarizes the parameters that were considered for the calculation, the modulus of elasticity is taken from the tensile tests at RT of the previous chapter and the same initial length is taken for the comparison. The diameter of the bundle is taken around 9 mm (corresponding to the final design of a typical bundle of 130 wires after compaction).

Table II.3.1. Parameters to calculate the Euler's critical load for the bundle and the single strand.

	E [MPa]	L_0 [m]	l_{eff} [m]	D_{sample} [m]	I [m⁴]	N_c [N]	σ_c [MPa]
Bundle	133	0.02	0.01	0.009	$3.22 \cdot 10^{-10}$	4227	66
Strand	133	0.02	0.01	0.00082	$2.22 \cdot 10^{-14}$	0.29	0.55

The result shows that for the same material (same modulus of elasticity) and same length, the critical load significantly increases for the bundle, since it is proportional to the fourth power of the sample diameter. Even if it would be possible to reduce the initial length of the single wire during the application of the compressive stress, there is a great difficulty associated with the correct application of a uniaxial load on a single strand, as well as measuring the displacement on a very small length. The EPSIC sample and protocol permit to avoid such difficulties.

II.3.1.2 EPSIC sample manufacture

The manufacture of the EPSIC bundle takes almost one month and the numerous steps characterizing it are summarized in Table II.3.2. In the framework of this Ph.D. project, 19 EPSIC samples were manufactured in 4 batches. The manufacture steps aim at sintering the wires during heat treatment into one bulk cylinder to avoid buckling during axial compression. This is achieved through a RT radial compaction before heat treatment

to form the Nb_3Sn phase. In the following paragraphs a deeper description of the manufacture steps is given.

The first step (STEP I in Table II.3.2) is to wind the unreacted strands thanks to a specific mechanical support, paying attention to keep the strands straight and parallel. In this phase, the strands have a 0.01 mm thick Chromium plating typical of the ITER TF Nb_3Sn strands. Hence, the second step implies the removal of the Chromium plating, via chemical reaction with hydrochloric acid *HCl*, to maximize the Cu-Cu sintering during heat treatment (STEP II in Table II.3.2).

In order to compact the strands, the bundle is inserted into a stainless-steel tube and then compacted by the use of am hydraulic cramping machine (STEP IV in Table II.3.2). This step is repeated as many times as needed (usually 2 times) to achieve the maximum compaction needed to remove voids as shown by the polished cross-sections of Figure II.3.1.

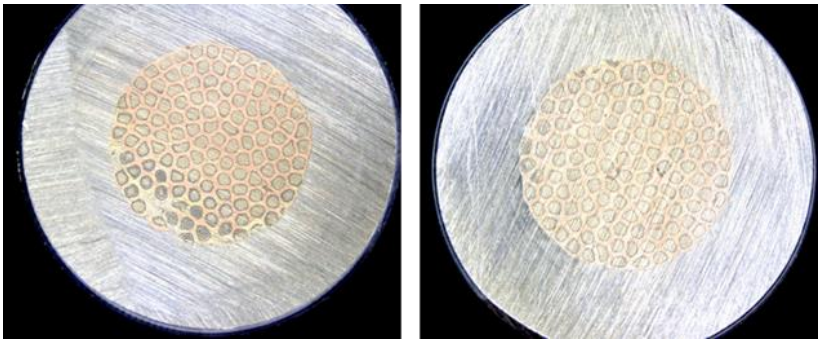

Figure II.3.1. Polished surfaces of an EPSIC sample ends observed with microscope.

Moreover, before inserting the strands into the stainless-steel tubes, the bundle is wrapped with a 0.01 mm thin steel wrapping to avoid sticking between the strands and the steel tube after HT (STEP III in Table II.3.2). Once the bundle is ready, its ends are TIG-welded to avoid Tin-leaking (STEP V in Table II.3.2) and then it can be thermally treated following the adequate temperature sequence and protocol explained in Annex A (STEP VI in Table II.3.2). The heat treatment creates the superconducting Nb_3Sn phase. At the same time the high temperatures, the long HT time and the high bundle mechanical compaction drastically increase the strands sintering.

A final machining of the sample is needed for opening of the central zone of the steel tube so as to expose the strands bundle for the mechanical testing (STEP VII and STEP VIII in Table II.3.2). The external steel wrapping is also helpful to protect the brittle strands during the removal of the steel tube and it will be kept during the whole test.

Table II.3.2. EPSIC sample manufacture procedure.

STEP I – Strands winding	Winding of the Cr-plated Nb_3Sn IT-strands.	
STEP II – Cr-plating removal	Removal of the Cr-plating with an HCl chemical treatment.	
STEP III – Bundle pre-compaction + Wrapping	Use of mechanical clamps to tighten the bundle and reduce the diameter. Bundle wrapping with a steel wrapping.	 
STEP IV – Tube + Compaction	Insertion of the bundle in a double SS tube and compaction with the cramping machine.	 
STEP V – Ends welding	TIG welding of the bundle ends.	
STEP VI – Heat treatment	20 days long heat treatment at 650 °C.	
STEP VII – Cut and polishing	The sample radially machined until the nominal dimensions, and a polishing of the ends is done for analysis of the cross-section.	

STEP VIII – SS tube machining	Machining of the bundle to open the sample test-zone.	

It is very important for a successful manufacture to respect each of these steps. Numerous samples were needed to fine-tune this specific procedure, with trials and errors sometimes leading to un-testable bundles. Figure II.3.2b) reports two failed samples for two different modes of buckling. For both cases, the problem was a non-optimal manufacture of the bundles: the sample on the left was characterized by a too long test-zone, about 40 mm (see paragraph II.3.1.1, which details subsequent decrease of the critical load), and the sample on the right was improperly opened during the stainless-steel tube removal procedure in the central zone (some strands were cut, despite the presence of the steel wrapping). Moreover, in both cases, the global compaction of the sample left some visible voids. Figure II.3.2a) shows a typical successful EPSIC sample, where the nominal diameter is the one allowing the absence of visible voids.

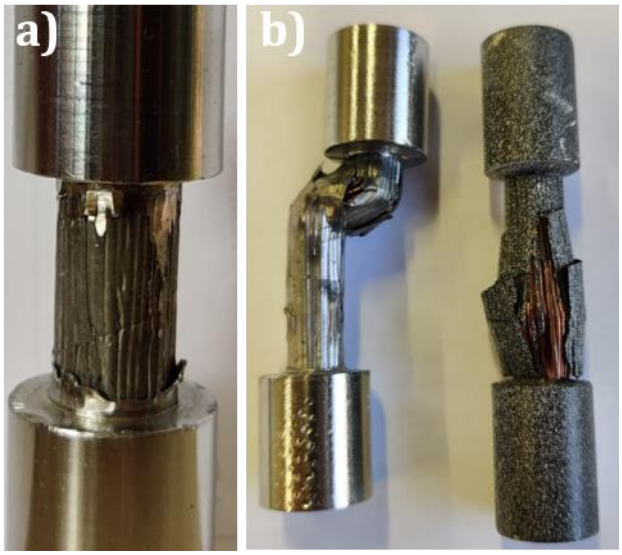

Figure II.3.2. a) Typical successful EPSIC sample, b) two failed samples during the compressive tests.

The final nominal diameter of the bundle depends on the compaction and on the number of wires. It is defined by visual examination and delicate metrology of the sample. When the sample is voids-free, the nominal diameter is considered achieved. Moreover, each batch of samples may have a different number of wires, hence the nominal diameter varies in a range of 9-10 mm.

II.3.1.3 EPSIC compressive tests setup

The setup of the tests is an important phase of the experimental protocol and it is as important as the sample manufacture for an optimal result. It is extremely important to guarantee as much as possible a uniform uniaxial application of the compressive stress.

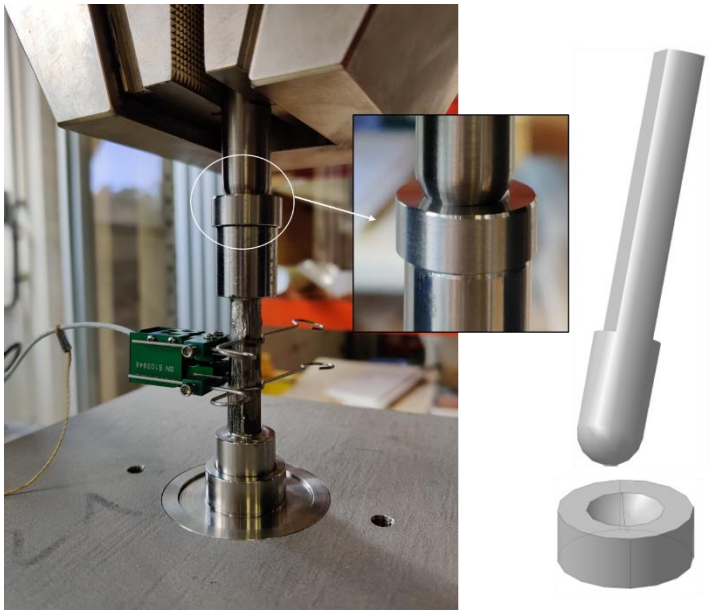

Figure II.3.3. Setup of the EPSIC compressive tests.

Figure II.3.3 shows the generic setup that was developed and manufactured during this Ph.D. work to perform this kind of tests. The top of the sample is not directly clamped into the jaw. The load is transferred through a specific intermediate component (on the right of Figure II.3.3). The spherical contact assures the homogenous transmission of the compressive force even in case of small misalignment of the sample with the machine axis. Considering the complex manufacture process and subsequent imperfect sample geometry, it was deemed necessary to include such an alignment-recovery intermediate piece.

II.3.2 EPSIC compressive tests campaign

The compressive EPSIC experimental activities were performed both at the LMA Laboratory of the CNRS Institute (LMA Laboratory) and at the CEA Cadarache (GAIM Laboratory). The collaboration with LMA Lab was very helpful to develop the method and the tools to test the EPSIC samples in compression. Thanks to these preliminary tests, it was possible during this Ph.D. project to develop the required tools (presented in Annex B) and setups that were then used to adapt the GAIM machine. This step ultimately led to more numerous and successful test campaigns at GAIM Lab to investigate the cyclic behavior similar to the ITSCOTT tensile campaign.

II.3.2.1 LMA preliminary compressive test campaign

Tensile machine setup: The machine is a hydraulic testing machine (MTS 322 *Test Frame*) fed by a 100 l/min hydraulic control unit at a maximal pressure of 210 bar. The measurement of deformation is handled by an optical extensometer. Pictures of the specimens are captured during testing by a camera. The pictures are then analyzed with the direct image correlation GOM ARAMIS 6.5 software: two points are chosen on the surface of the sample and the differential displacement between them is used to estimate

the deformation of the specimen. Table II.3.3 summarizes the main features of the LMA test, while Figure II.3.4 illustrates the setup for the compressive tests at the LMA Lab.

Table II.3.3. Summary of the main information of the LMA compressive test at RT.

Load cell	CAPACITY: 100 kN
Test control	Force control
Extensometer	PCO.edge sCMOS camera equipped with 5.5-megapixel sensor

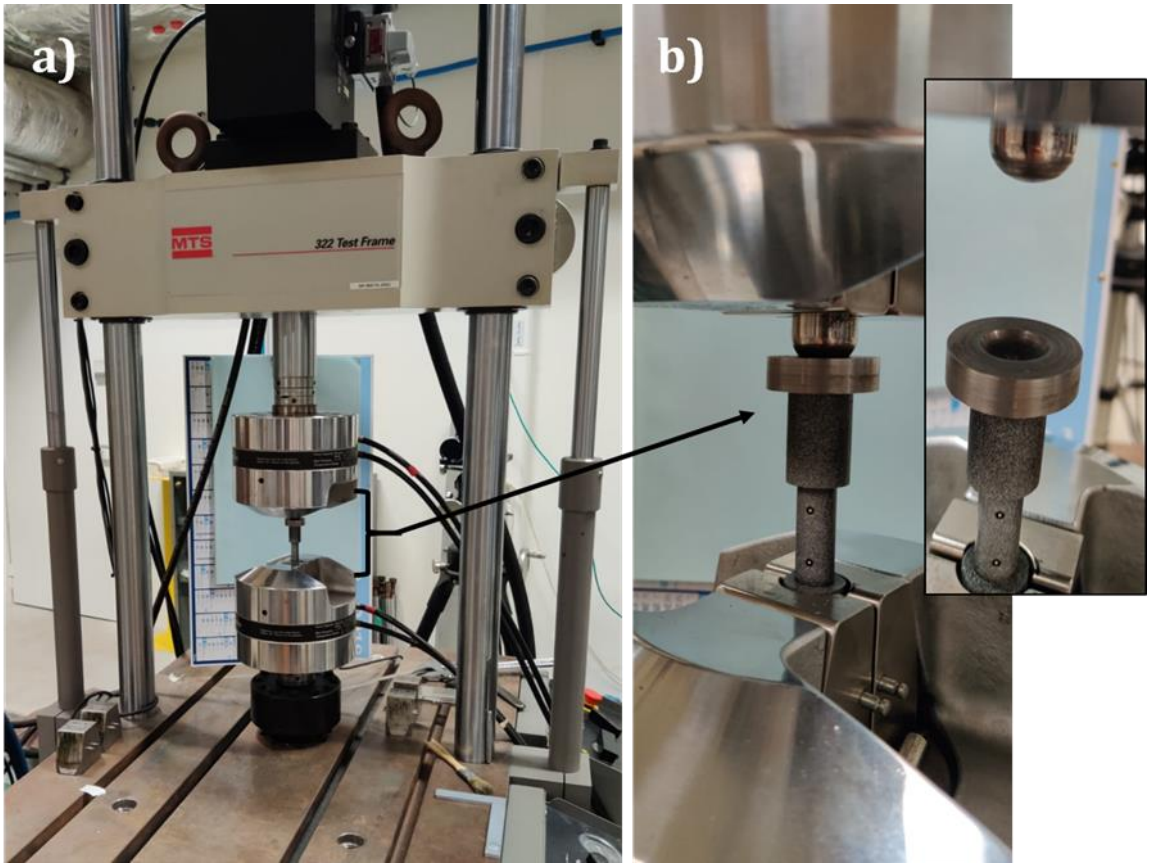

Figure II.3.4. a) Tests setup at the LMA Lab, b) focus on the top and bottom ends of the sample, with spherical contact intermediate piece.

Operating conditions: The operating conditions are summarized in Table II.3.4. The EPSIC bundle of wires has a diameter of 10 mm and a 100 N pre-load is manually applied.

Table II.3.4. Summary of the main parameters of the LMA compressive test at RT.

	COMPRESSIVE TEST RT		
Sample length L_0 [mm]	34		
Sample diameter ø [mm]	10		
Test speed [N/min]	10000		
Software pre-load [N]	100		
Acquisition frequency [Hz]	0.5		
Stages number	3		
Force loads [N]	50000	10000	15000
Force unloads [N]	200	200	200
Number of cycles	1	1	15

Figure II.3.5 reports the applied force during the test.

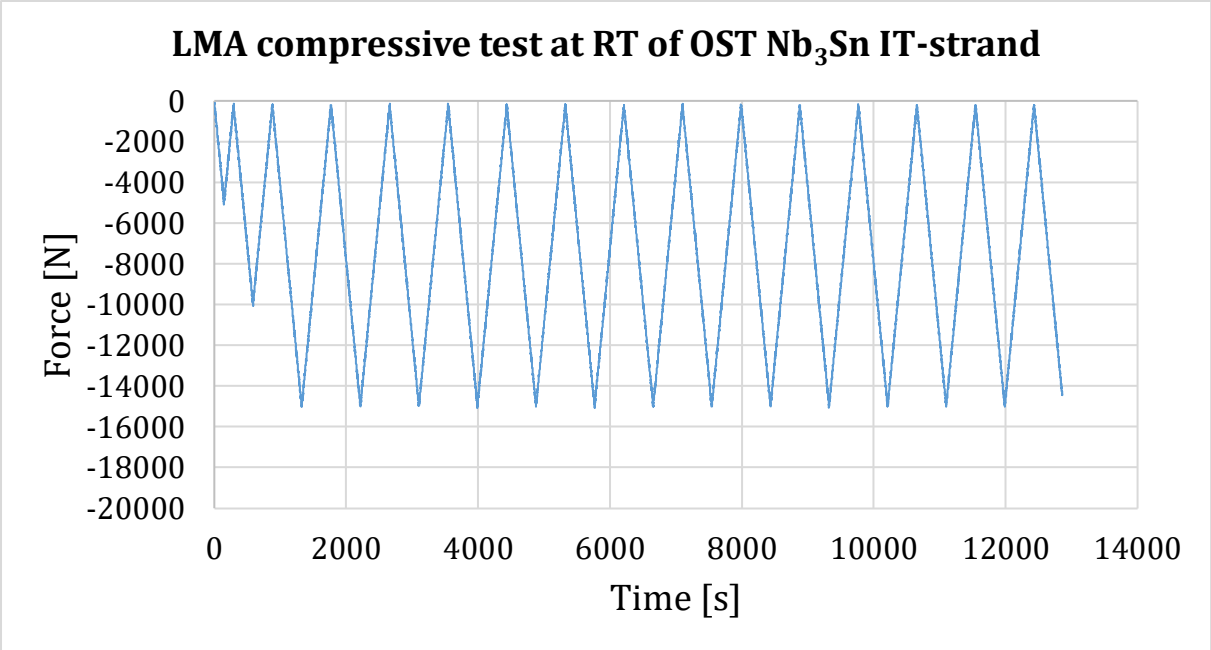

Figure II.3.5. Plot of the applied force to the EPSIC sample during the LMA compressive test at 300 K.

The sample of this test bended after 14 cycles, so the data are not directly exploitable. However, the test was very useful to validate the testing process and to design the required tools to perform cyclic compressive tests at GAIM Lab.

II.3.2.2 GAIM compressive tests campaign: cyclic behavior

Tensile machine setup: The machine is the same as the one for the tensile tests of Figure II.2.9a). The GAIM test setup is the one illustrated by Figure II.3.3. The test is performed by force control. The extensometer presented in paragraph II.2.2.2 measures the strain directly on the sample, but this time with standard knife-edges and clamps. The extensometer knifes and clamps are also glued to the sample. Table II.3.5 reports the main setup information.

Table II.3.5. Summary of the main information of the GAIM compressive test at RT.

Load cell	CAPACITY: 100 kN
Test control	Force control
Extensometer	MODEL: EPSILON 3442-010M-010M-LT, WEIGHT: 8 g, GAUGE LENGTH: 6 mm
Glue	Loctite 409

Operating conditions: The test is force-driven and so a *control_force_coefficient* of 195 was found after several test to respect the speed of 1500 N/s. Table II.3.6 summarizes the main characteristics of the compressive test.

Table II.3.6. Summary of the main parameters of the GAIM compressive test at RT.

	COMPRESSIVE TEST RT
Sample length L_0 [mm]	20
Sample diameter ø [mm]	10
Test speed [N/s]	1500
Control force coefficient	195
Software pre-load [MPa]	20±5

Pre-load speed [mm/s]	0.005		
Acquisition frequency [Hz]	5		
Stages number	3		
Stress loads [MPa]	50±2	100±2	150±2
Stress unloads [MPa]	30±2	30±2	30±2
Number of cycles	1	1	230

Figure II.3.6 plots the force that is applied during the test and only 21 loads-unloads cycles are here shown, at 150 MPa corresponding to 9300 N,.

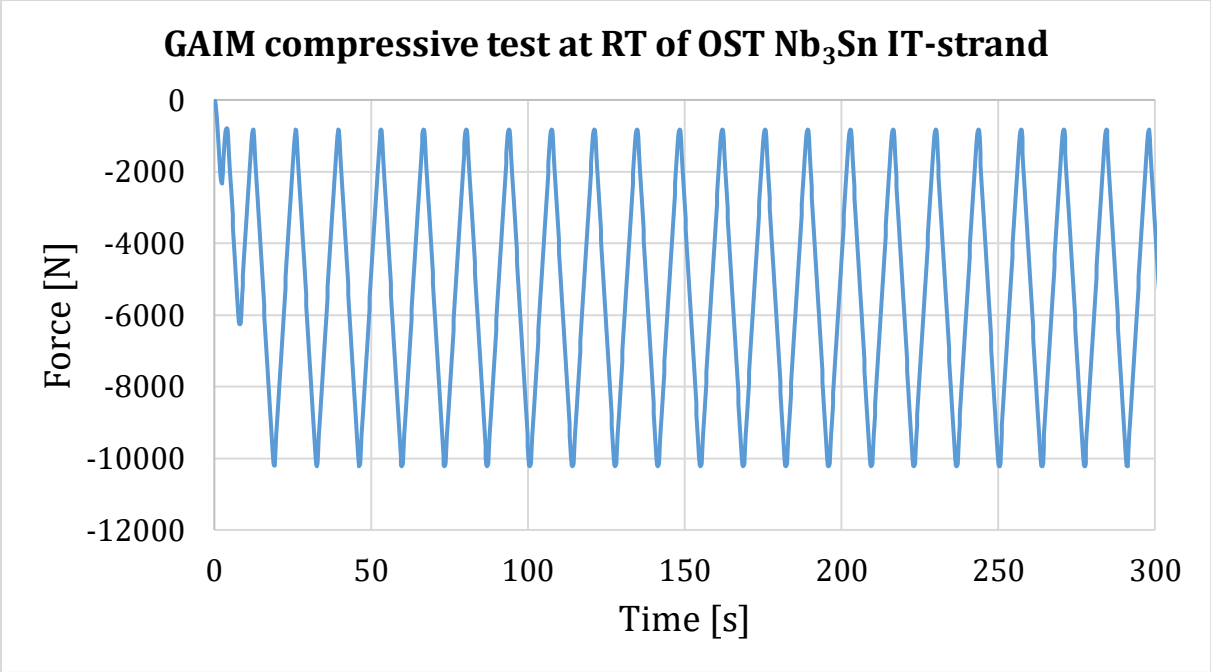

Figure II.3.6. Plot of the applied force to the EPSIC sample during the GAIM compressive test at 300 K.

Several difficulties were overcome to perform this kind of tests. Many of them are related to the manufacture and the opening of the test-zone. Moreover, even though the tensile machine software had to be updated and tuned several times in order to perform such a long cyclic test, the full 1000 cycles test could not be completed in compression. The software has tendency to bug during cycling, phenomenon that did not occur for the tensile cycling. However, the results presented in next section show that this approach is promising.

II.3.3 Results discussion

Figure II.3.7 and Figure II.3.8 report the stress-strain characteristics of the EPSIC compressive test performed at LMA Lab and GAIM Lab respectively.

As aforementioned, the sample tested at LMA Lab had buckling issue due to improper opening of the test-zone, hence a direct comparison with the result obtained at GAIM Lab is not appropriate. However, thanks to the LMA test it was possible to validate the experimental protocol concerning the test procedure, since the stresses seem to be homogeneously applied.

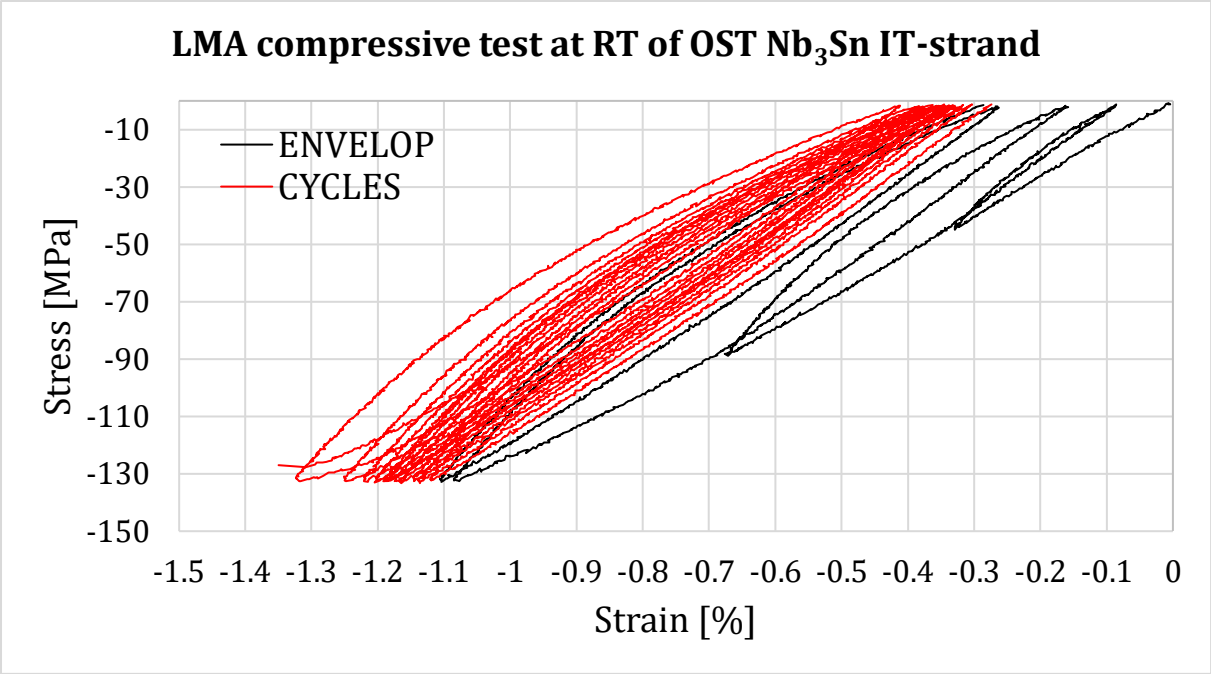

Figure II.3.7. Strain-stress plot of the OST G 01EX0571A01C strands compressive test at 300 K performed at the LMA Lab.

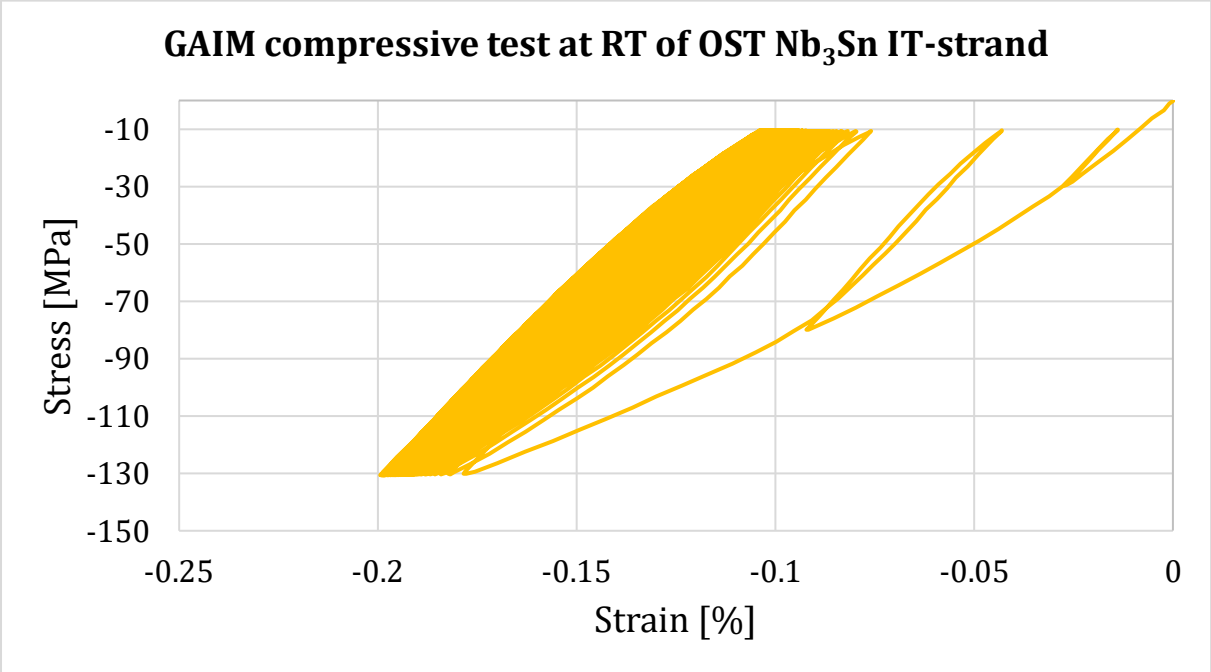

Figure II.3.8. Strain-stress plot of the OST G 01EX0571A01C strands compressive test at 300 K performed at the GAIM Lab.

Figure II.3.9 shows a direct comparison between the tensile and the compressive results, where the compressive plot was switched to positive strains and stresses. Both curves are plot at net of the pre-load. The contribution of the bundle steel wrapping is neglected since the force applied to it (~3 N at 200 MPa) is 5 times lower than the bundle wires force (~15 N at 200 MPa).

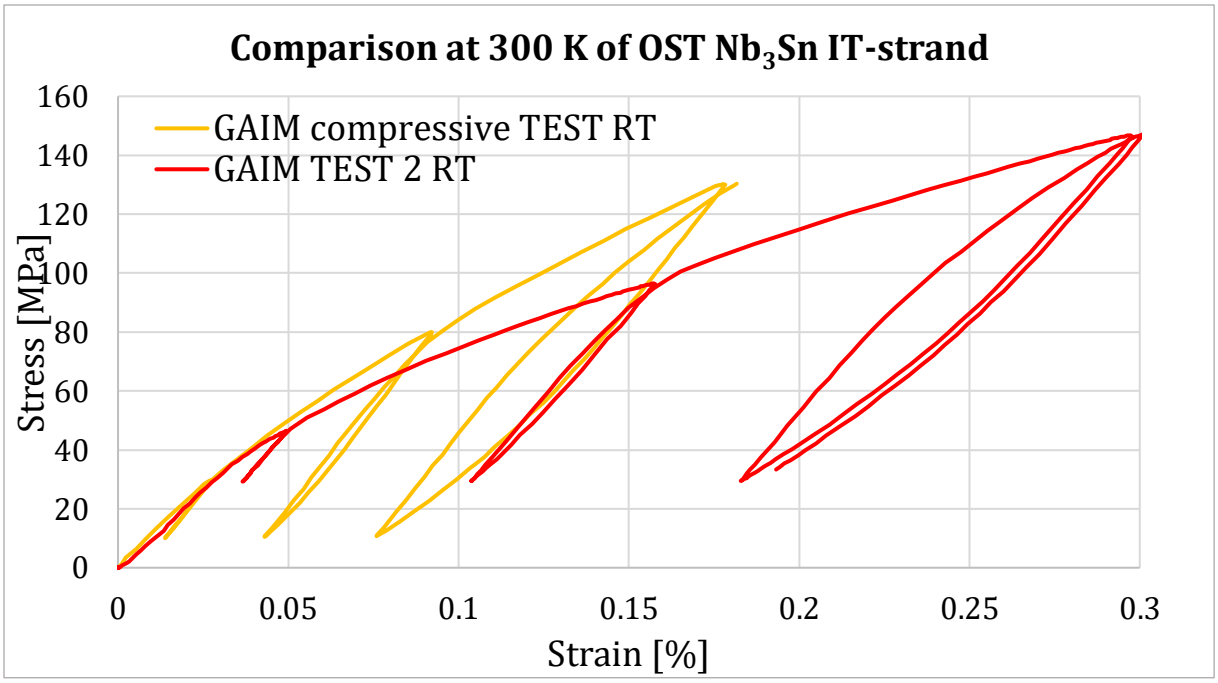

Figure II.3.9 Comparison between the tensile in red and the compressive in yellow GAIM tests at RT. The compressive test has opposite signs of the axes.

The compressive behavior is stiffer than the tensile one, this could be due to the pre-load that the bundle undergoes during the cool-down from the HT and RT. The annealed copper composing the composite wires plasticizes and so, differently from the tensile test, the copper has already reached its yield strain/stress when the sample is tested. The two plots are relatively close for the lower strains, but the behavior changes for the higher loads range. This is probably because at lower stresses the bundle answer is driven by the structure phenomena, while at greater stresses it is probably the material answer. Therefore, a first attempt of explanation suggests that the observed tensile behavior is more characterized by structure phenomena, while the compressive behavior seems to present a real material behavior.

Figure II.3.10 presents the cyclic behavior and the elasticity moduli evolution. Even though the first modulus should not be used for quantitative analyses, it is interesting to notice that the slope is very close to the test 1 of ITSCOTT campaign. This result validates the mechanical compressive behavior. However, the global rigidity of the sample is greater than the tensile one. In this case, a major Ratcheting effect, corresponding to $\Delta\varepsilon$ = 0.02 %, is observed during cycling that does not stabilize after 230 cycles. At the same time, the elasticity modulus does not increase with cycles, but it is constant. This effect with the plastic strain cumulation reveal the presence of the Rochet effect in compression with cycles.

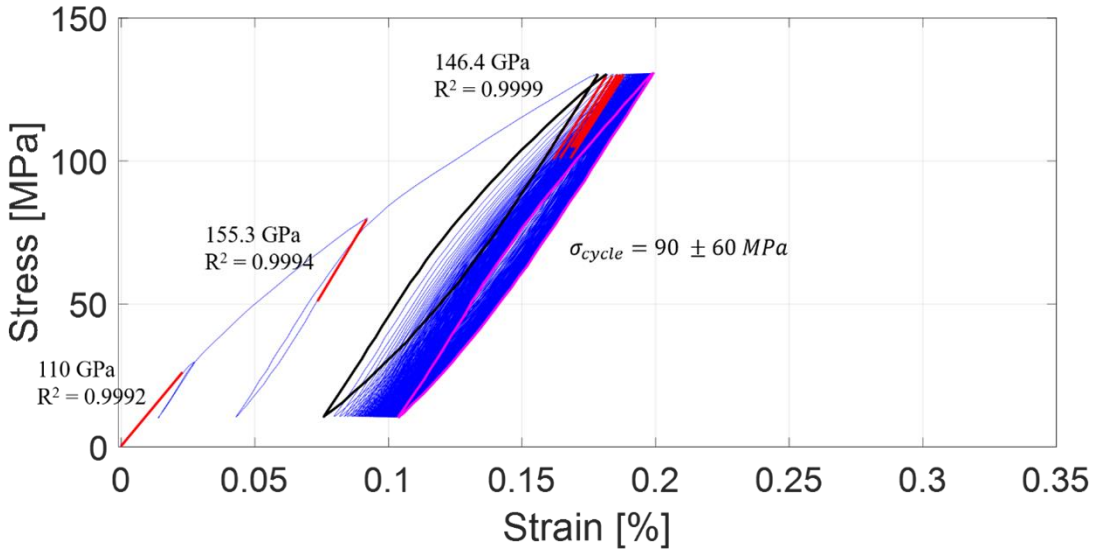

Figure II.3.10. Elasticity modulus evaluation of the GAIM EPSIC compressive test at 300 K with opposite signs of the scales.

Figure II.3.11 reports the evolution of the strains with the cycles. The difference between the two peaks strains decreases from 0.125 % to 0.0956 % for the compressive test. For the tensile test 1 the same decrease is obtained in 1000 cycles. In fact, the initial difference is 0.115 % and after 1000 cycles decreases down to 0.0958 %. This means that a global plasticization occurs in both cases due to the copper matrix. However, in compression there is not a two-steps behavior, and the behavior is more similar to a Rochet effect, since the average strain keeps increasing with cycles and the elasticity modulus is constant.

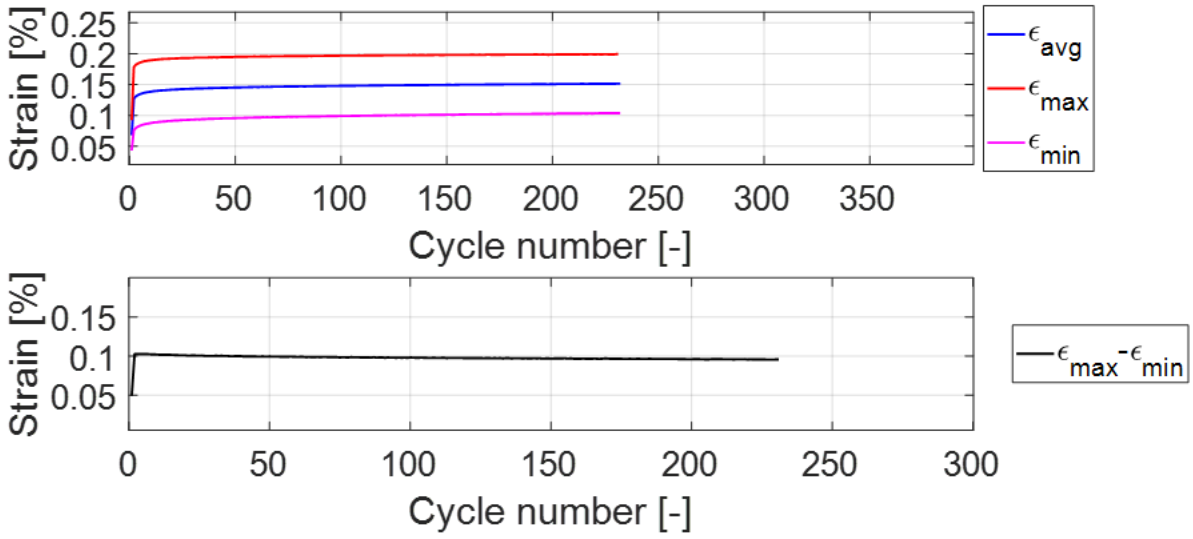

Figure II.3.11. Evolution of the max, min and mean values of the strain with cycles and difference between the max and min strains with cycling in compression at 300 K.

II.3.4 Conclusion

In the framework of the Ph.D. project a completely new experimental protocol was developed to test under compression very brittle and small superconducting wires. The first results, if compared to the tensile behavior, show a reasonable behavior, considering the present limited knowledge about this topic.

The envelope of the compressive curve is quite different from the tensile one, with a trend that implies a more rigid behavior probably due to the HT. The elastic modulus measured on unloading curves is about 25% higher than in tension. The cyclic behavior is quite different, with a visible Ratcheting effect (cumulative compressive strain) of about 0.02 % in 230 cycles. Differently from traction, the effect is only cumulative.

The order of magnitude of the cumulative strain is relatively high and it would induce a decrease of current carrying capability not negligible. Nevertheless, as mentioned for the tensile test, the level of stress in the test is relatively high compared to what is expected in a cable and the effect should not have direct consequences on electrical properties.

III. THIRD PART – Nb_3Sn CICC ELECTROMECHANICAL MODELLING

LIST OF SYMBOLS

A_{Cu}	$[mm^2]$	Cu surface
A_{fil}	$[mm^2]$	Filamentary surface
A_{Non-Cu}	$[mm^2]$	non-Cu surface
A_s	$[mm^2]$	strand surface
B	$[T]$	Magnetic field
B_{ave}	$[T]$	Average magnetic field
$cos\,\vartheta$	$[-]$	Mean twist angle
E	$[-]$-$[\%]$	Green-Lagrange strain tensor
E_0, E_c	$[V/m]$	Critical electric field
f	$[N]$	External forces
F, F_L	$[N]$	Lorentz force
g	$[-]$	Directors
I_c	$[A]$	Critical current
I_{Ccable}	$[A]$	Cable critical current
I_{Cs}	$[A]$	Strand critical current
I_{op}	$[A]$	Operating current
I_p	$[A]$	Operating petal current
J	$[A/mm^2]$	Current density
J_c	$[A/mm^2]$	Critical current density
Jc_{Non-Cu}	$[A/mm^2]$	non-Cu critical current density
k	$[-]$	Penalty coefficient (contact stiffness)
L	$[mm]$	Length
N, n	$[-]$	Numerical step(s)
N_{strand}	$[-]$	Strands number
n	$[-]$	n-value
$\hat{n}$	$[-]$	Normal versor
R	$[mm]$	Radius
R_{fil}	$[mm]$	Filamentary radius
R_m	$[mm]$	MULTIFIL radius
R_s	$[mm]$	Strand radius
S	$[mm^2]$	Cross-sectional area
t	$[s]$	Time
T	$[K]$	Temperature
T_{cs}	$[K]$	Temperature of current sharing
u	$[mm]$	Displacement of particle position
v	$[mm]$	Virtual displacement
x	$[mm]$	Particle placement
ε	$[-]$-$[\%]$	Strain

ε_{app}	*[-]-[%]*	Longitudinal applied strain
ε_{ax}	*[-]-[%]*	Axial strain
ε_{eff}	*[-]-[%]*	Effective strain
ε_{extra}	*[-]-[%]*	Extra strain due to Lorentz force levels
ε_{out}	*[-]-[%]*	Boundary strain
ε_{th}	*[-]-[%]*	Thermal strain
ξ	*[-]*	Material particle
ξ_1, ξ_2, ξ_3	*[mm]*	Material particle coordinates
σ	*[MPa]*	Stress tensor
Ω_R	*[mm³]*	Beam volume
χ	*[-]*	Cu-non-Cu volume ratio

III.1 CHAPTER – STATE OF THE ART

In the superconducting community, there are many models dealing with CIC conductors, either analytical or numerical. Depending on the goal, some models aim to reproduce only the cable geometry, others the mechanical state of the cable, sometimes up to the electrical performance, and some of them even treat the thermohydraulic stability of the cable. This chapter provides an overview of the models and studies that aim to investigate the mechanical behavior of the CICCs, and that were considered to be the most suitable for the topic of this dissertation.

III.1.1 Electro-mechanical analytical models

The scale-up of the electrical performance (T_{cs}, *n-value*) from wire to conductor reveals the difficulty to describe the complex nature of the multi-strand conductor by a simple scaling law (equations (I.1) and (I.3)). In order to have a simple fit of the conductor performance, during operation or during SULTAN testing, the smeared models for electrical performances, and the fully bonded models for mechanical estimation of the conductor strain are approaches that have been largely used so far. These analytical models have sometimes been coupled to try to predict expected properties of a cable from its strands properties.

In the framework of SULTAN campaigns on the ITER conductors as well as for inserts and model coils, one of the easiest ways to try to predict the strain in the conductor has been the fully bonded model (FBM). For example (Mitchell 2003) and (Decool 2008) used the FBM to calculate the thermal strain that the cable undergoes inside the jacket due to the differential thermal contraction between jacket and cable. These examples show the use of the FBM for two different purposes: (Mitchell 2003) aims to find a strain to deduce electrical parameters of the tested conductors, while (Decool 2008) provides a mechanical investigation of the thermal strain on the tested conductors. The limit of this model is that it cannot describe adequately the mechanical information related to some cable characteristics, like for example the electrical contacts, compaction or twist pitches of the considered conductor, that (Bessette 2014) demonstrated to have a large impact on the macroscopic behavior of the cable.

The smeared models are based on the use of the strand scaling law to represent the full conductor performance. Therefore, they make use of a single value for the

conductor strain when the real cable experiences a complex strain map. This model has also been developed to consider the extra strain due to the EM force to be added to the thermal strain. This extra strain is a function of the EM load and it comes from a linear fit of the effective strain found from the T_{cs} experimental measurements at different levels of IB load: $\varepsilon_{extra} = -\gamma IB_{ave}$ from (Ciazynski 2007) where I is the current and B_{ave} is the average transverse magnetic field in the cross-section of the conductor.

Another type of smeared model has been proposed to represent the irreversible degradation of the cable performances with EM cycling. This one is not based on strain estimation (or smearing), but for a constant strain ε_{th}, it defines the remaining unbroken superconducting area as α. The conductor current carrying capacity is then simply scaled from the strand scaling law $I_c(B,T,\varepsilon_{th})$ by: $I_{Ccable}=\alpha N_{strand} I_c(B,T,\varepsilon_{th})$, where N_{strand} is the number of superconducting strands in the cable.

Other works focused on the development of analytical models to consider the effect of the bending on the strain, as for example in (Mitchell 2002), (Nijhuis 2006) and (Ciazynski 2010), with final goal the assessment of the impact of bending on the cable/wire electrical performance.

All these models have their specific field of application, especially when it comes to quick assessment or comparison of the performance. These methods are quick and simple, and can help extrapolating to other operating conditions, but in no way they can help understanding the mechanical phenomena happening inside the cable. In fact, numerical models should help tune and improve such models so that they are more representative of the cable real behavior.

III.1.2 Mechanical numerical models

The numerical models are usually focused either on the modelling of the superconducting wire or on the macroscopic mechanical behavior of the cable. Moreover, the numerical methods for the wires material constitutive laws identification have often as final goal to support the cables simulations. Therefore, the effort of the scientific community is usually made on these two purposes.

III.1.2.1 Composite Nb_3Sn wire structure mechanical modelling

N. Mitchell largely worked on the mechanical representation of Nb_3Sn wires structure developing an elastoplastic one dimensional finite element model to predict the internal stresses of Nb_3Sn wires during the cable life. (Mitchell 2005b) and (Mitchell 2005c) present the FE Ansys approach to simulate the response of the Nb_3Sn wire to a thermal loading, for example the cool-down (CD), and the strain state inside the composite wire. Mitchell's work provided an important data base of the Nb_3Sn strain-stress curves that is still largely used for the material constitutive laws, based on a power law relation, in several models.

Other works propose homogenized models for the description of the mechanical wire behavior. Two examples of the most relevant works are (Boso 2013) and (Lenoir 2019).

III.1.2.2 Nb_3Sn CICCs mechanical models

(Mitchell 2005a) proposes a simple mechanical model of CICC cable under operating transverse magnetic loadings relying on simplified assumptions of square/rectangular shape and idealized cable with uniformly distributed loads in the strands. Successively, (Nijhuis 2008), (Nijhuis 2006) present the Transverse ElectroMagnetic Load OPtimization (TEMLOP) based on (Mitchell 2005a)'s mechanical model. The schematical representation of the initial cable geometry is reported in Figure III.1.1 taken from (Nijhuis 2006).

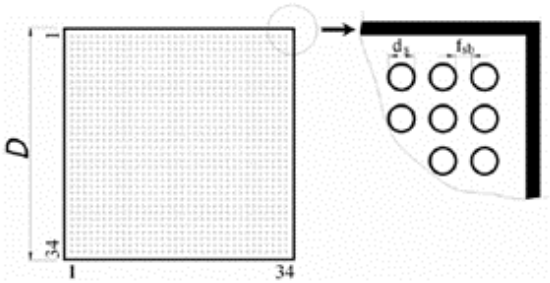

Figure III.1.1. a) Idealized cable geometry with squared cross-section in TEMLOP (Nijhuis 2006),

TEMLOP aims to assess the bending strain due to EM loadings and provides the T_{cs} of the cable. This study proposes a long twist pitch CICC with low void fraction (VF) as solution for the TF CICC design to prevent degradation.

(Miyagi 2012) and (Qin 2010) are examples of work aiming to reproduce the cable geometry. The first one focuses on the identification of wires positions inside the cable, and the second one on the full cable stages modelling.

(Qin 2011) developed a mechanical model to predict local strain/stress and contact forces in a multi-staged cabled CICC using the wire rope theory. However, the geometry is still quite idealized (see Figure III.1.2) and the thermal strain is given as an input variable.

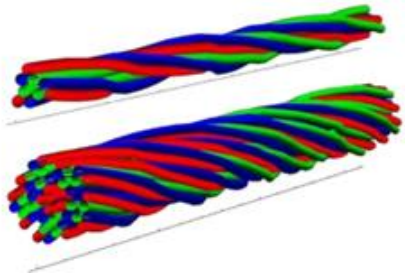

Figure III.1.2. Ideal petal geometry of (Qin 2011)'s modelling.

(Wang 2016) proposed a 3D numerical model by Abaqus of the IT-wire considering the filaments twist. The same team works on the mechanical behavior of CICCs with Abaqus (Li 2013).

(Yue 2018) simulates the CICCs behavior based on a simplified geometry as reported in Figure III.1.3. The study concludes that the main responsible for T_{cs} degradation is a progressive axial compression applied to the cable. Here, the thermal strain is an input parameter as well.

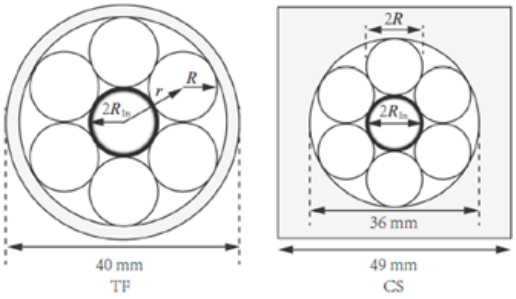

Figure III.1.3. CICCs geometries simulated by (Yue 2018).

(Gao 2019), (Gao 2020) present a mechanical model for CICC aiming to assess the cable stiffness and the contacts behavior. However, these models present idealized geometries at reduced scale and there is no simulation of the impact of the operating loadings.

III.1.2.3 MULTIFIL mechanical code

The approach used in this Ph.D. is based on the use of a finite elements simulations code called MULTIFIL (MULTIFIL-aments) developed by D. Durville (ECS, France). In the past, the code was adapted to the simulation of fusion cables during H. Bajas' Ph.D. Bajas' work provided to the fusion community a tool that gives access to local strain maps on the strands inside the conductor when thermal and EM loadings are applied (Bajas 2010). His work was extremely exploited by several researchers to deduce important information on the cable mechanical behavior, on the strands local strain state inside the cable and on the impact of CICC design parameters with specific case studies on ITER CICCs. Here a list of the major works done in the past based on MULTIFIL (Torre 2011), (Bajas 2012), (Breschi 2012b), (Torre 2013), (Torre 2014), (Breschi 2015), (Xue 2020). Bajas' work was so important for the community that similar approaches were later developed inspired to MULTIFIL code, like for example (Du 2021).

However, the final state of the code in 2011 left plenty of open issues that required in depth modification of the overall modelling approach. In particular, an adequate treatment of boundary conditions, cable-jacket equilibrium and electromagnetic loading were necessary. This code was deemed very promising but further improvements were needed in order to reach a more representative and predictive tool. The extensive work done on the core of the code for the fusion application is a major part of this Ph.D. work,

and it is detailed in chapter III.2. Figure III.1.4 reports the evolution timeline of the MULTIFIL fusion cables model in the last ten years, where the Ph.D. contribution is related to the developments in years 2019-2021.

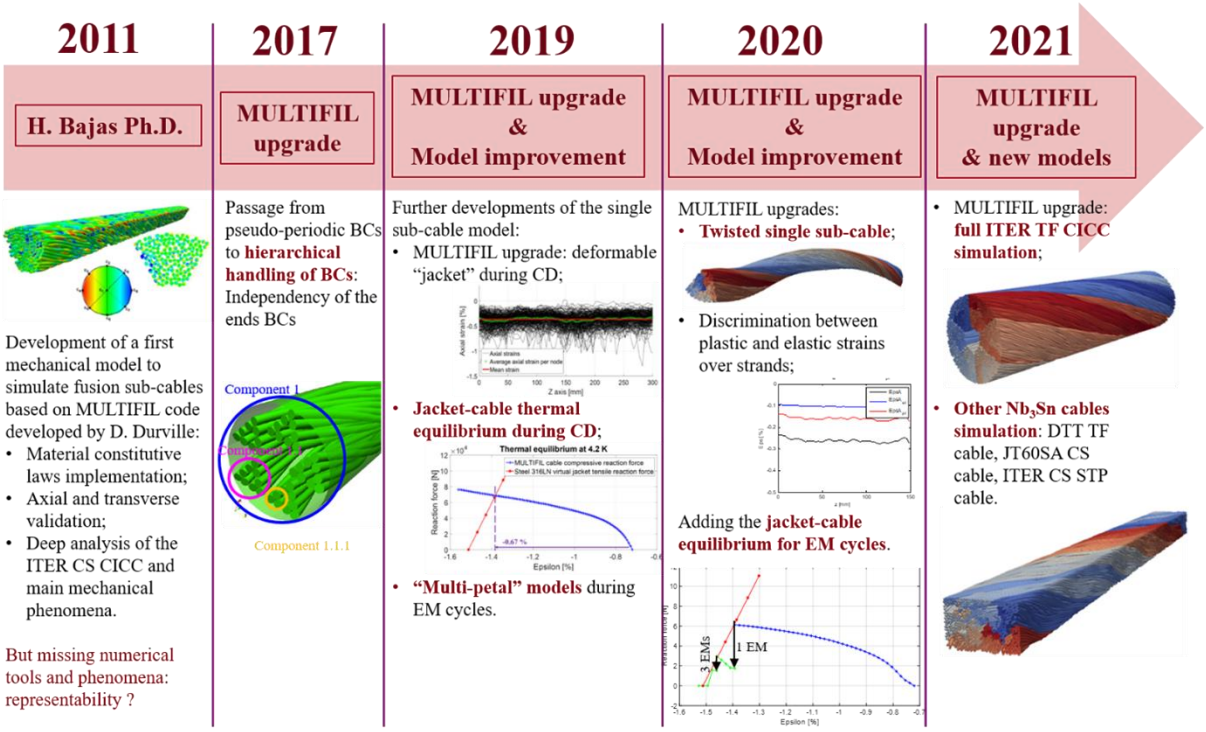

Figure III.1.4. Timeline of MUTLFIL evolution for fusion cables.

III.1.3 Conclusion

The state of the art on CICCs modelling highlights some difficulties concerning the mechanical simulations. First, the inability to provide the local strain state for a complex full-scale cable geometry, and thus to reproduce the macroscopic mechanical phenomena occurring inside the cable under loadings. Second, the capacity to predict the wires trajectories, as result of the manufacture process and operating loads. Finally, all the numerical models usually consider the thermal strain as an input variable. The former MULTIFIL code partially covered these issues, since it was able to assess the impact of the thermal and EM loadings on the wires trajectories and local strains. However, there were still modeling limits and drawbacks to the initial version of this code.

This is why the mechanical modelling during this PhD work was based on the MULTIFIL code developed at ECS during Bajas' PhD in 2010-2012. Since then, the core of the code had been extensively modified, in particular in terms of boundary conditions definition. The improvements made to the MUTIFIL fusion cable model in the Ph.D. framework, described in next chapter, focus on three main aspects: integration of the new code-core for fusion cable study, upgrade of boundary conditions while scaling-up to full cable model and development of a standardized numerical protocol to simulate CICC cables. In particular, the simulation protocol foresees an analytical-numerical coupling

developed during this Ph.D. work and that can be seen as an improvement of the FBM thanks to integration of the cable's mechanical behavior modelled by MULTIFIL code.

III.2 CHAPTER – MECHANICAL MODELLING OF CICCs WITH MULTIFIL

The mechanical model used in this Ph.D. dissertation for fusion cables simulation relies on the mechanical code MULTIFIL. This chapter presents the numerical approach of the code, as well as several upgrades developed during this Ph.D. project. Each of them aims at obtaining a more representative and tentatively predictive model in terms of cable mechanical behavior and performance. This is handled by the scale-up from strand mechanical reaction to macroscopic behavior, permitting the identification of driving phenomena at the strand scale. Section III.2.1 illustrates the physics and the models of MULTIFIL and so the starting point of this work, while sections III.2.2 and III.2.3 present the many changes that were implemented with respect to H. Bajas' MULTIFIL model (Bajas 2011) thanks to the presented Ph.D. thesis.

III.2.1 Finite elements simulations code MULTIFIL

The physics treated in MULTIFIL is based on the mechanical modelling of beams with deformable sections for large transformations developed by D. Durville (Durville 1998). This choice relies on the need to simulate the mechanical behavior of a large number of metallic fibers or wires that interact by frictional and contact forces.

III.2.1.1 The enriched beam model

The transverse behavior of the wires is important for the representability of the transverse stiffness of the wires, like the torsional and flexural rigidities, inside the cable. Hence, MULTIFIL considers a beam model with an enriched kinematics using nine degrees of freedom as opposite to the classical beam models with rigid sections considering six degrees to describe the section kinematics. The enriched kinematics uses two directors of the cross-section that can vary in norm and angle to describe the deformations of the transverse sections. The main advantages with respect to the beam model with rigid sections are an easier mathematical treatment of the sections displacements/rotations and the adequate description of the section deformations (like for example the Poisson's effect) in the beam model, very useful in the framework of the metallic cables where geometrical precision is required.

The beam sections kinematics is described by directors, which are no orthonormal, so there is no particular constraints and they are variable in norm and angle. First, a reference configuration is considered for the beam that occupies the volume Ω_R described by a cylinder of length L and radius R:

$$\Omega_R = \{\boldsymbol{\xi} \in \mathbb{R}^3 | \xi_1^2 + \xi_2^2 \leq R^2, 0 \leq \xi_3 \leq L\}, \quad \text{(III. 1)}$$

so that a beam section is identified by the curvilinear abscissa ξ_3, while a given particle $\boldsymbol{\xi}$ of the section is defined by the transverse coordinates (ξ_1, ξ_2).

In the general approach of the works (Green Albert Edward Naghdi 1974), the beam is seen like a line which points $(0, 0, \xi_3)$ are represented by directors describing the material deformation around and so in all the volume of the beam. A given point of the beam can be described by an infinitive family of directors:

$$\boldsymbol{x}(\xi_1, \xi_2, \xi_3, t) = \boldsymbol{x_0}(\xi_3, t) + \sum_{N=1}^{\infty} \xi_{\alpha_1} \xi_{\alpha_2} \cdots \xi_{\alpha_N} \boldsymbol{g}_{\alpha_1, \alpha_2, \cdots, \alpha_N}(\xi_3, t), \alpha_1, \cdots, \alpha_N = 1,2 ; \quad \text{(III. 2)}$$

where the vectors $\boldsymbol{g}_{\alpha_1, \alpha_2, \cdots, \alpha_N}$ are the directors and they represent the deformation modes of the section as a polynomial expansion with respect to the transverse coordinates (ξ_1, ξ_2).

In the MULTIFIL approach, the kinematical model of the beam with deformable sections foresees a first order polynomial expansion of the placement $\boldsymbol{x}(\xi)$ of the generic particle $\boldsymbol{\xi}$ at the time t with respect to the transverse coordinates (ξ_1, ξ_2):

$$\boldsymbol{x}(\xi_1, \xi_2, \xi_3, t) = \boldsymbol{x_0}(\xi_3, t) + \xi_1 \frac{\partial \boldsymbol{x}}{\partial \xi_1}(\xi_3, t) + \xi_2 \frac{\partial \boldsymbol{x}}{\partial \xi_2}(\xi_3, t) + o(\xi_1, \xi_2) \quad \text{(III. 3)}$$

$$\boldsymbol{x}(\boldsymbol{\xi}, t) = \boldsymbol{x_0}(\xi_3, t) + \xi_\alpha \boldsymbol{g}_\alpha(\xi_3, t), with\ \alpha = 1,2. \quad \text{(III. 4)}$$

Therefore, the position of each particle $\boldsymbol{\xi}$ is defined by three kinematical vectors, which are the position of the center of the section $\boldsymbol{x_0}(\xi_3, t)$ and two section directors $\boldsymbol{g}_\alpha(\xi_3, t)$ corresponding to the first derivative of the position $\partial \boldsymbol{x} / \partial \xi_\alpha$. This linear description of the particle position allows to have planar sections in all the configurations, but the absence of assumptions on the directors makes the sections deform following the directors variations.

In the presented kinematical model, the displacement of the material particle $\boldsymbol{u}(\boldsymbol{\xi}, t)$ is also a linear function of the transverse coordinates:

$$\boldsymbol{u}(\boldsymbol{\xi}, t) = \boldsymbol{x}(\boldsymbol{\xi}, t) - \boldsymbol{x}(\boldsymbol{\xi}, 0) = \boldsymbol{x_0}(\xi_3, t) - \boldsymbol{x_0}(\xi_3, 0) + \xi_\alpha \big((\boldsymbol{g}_\alpha(\xi_3, t) - \boldsymbol{g}_\alpha(\xi_3, 0)) \big) \quad \text{(III. 5)}$$

$$\boldsymbol{u}(\boldsymbol{\xi}, t) = \boldsymbol{u_0}(\xi_3, t) + \xi_\alpha \boldsymbol{h}_\alpha(\xi_3, t), with\ \alpha = 1,2 ; \quad \text{(III. 6)}$$

where $\boldsymbol{u_0}(\xi_3, t)$ describes the displacement of the cross-section center, and $\boldsymbol{h}_\alpha(\xi_3, t)$ are the variations of the section vectors.

Figure III.2.1 reports a schematic drawing of the beams interactions on the left and the evolution of the displacement field from a configuration to another at time t.

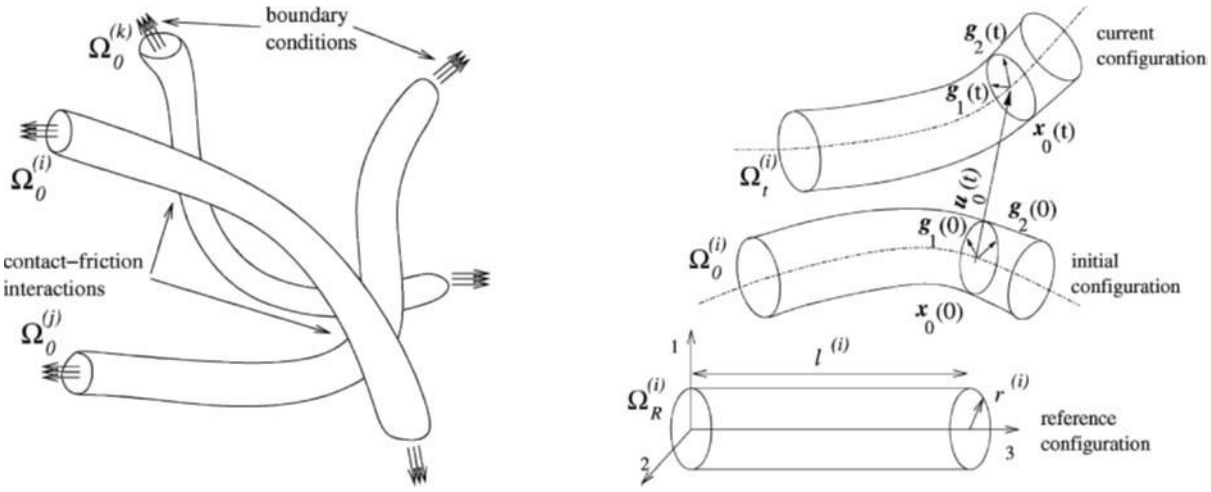

Figure III.2.1. Beams configurations and interactions described in MULTIFIL (Durville 1998).

The main advantage of this model with respect to the classical beam model with rigid sections is that no constraint needs to be put on the kinematical fields so that the displacement fields and their variations are of the same kind. This approach simplifies the formulation of the principle of virtual work in large transformations presented in next paragraph (Durville 1998).

III.2.1.2 The mechanical problem

The mechanical equilibrium of an assembly of beams is defined by the following strong formulation:

$$\begin{cases} -div\boldsymbol{\sigma} = 0 \\ \boldsymbol{\sigma} \cdot \hat{\boldsymbol{n}} = \overline{R_{J\to\iota}}\left(\xi^{(i)}, t\right) \\ \boldsymbol{\sigma} \cdot \hat{\boldsymbol{n}} = \boldsymbol{f} \end{cases}. \tag{III.7}$$

The physical problem formalized by equation (III.7) considers null the divergence of the *Cauchy stress tensor* $\boldsymbol{\sigma}$ and the boundary conditions, defined at the boundary surfaces Γ_t, foresee frictional-contact interactions $\overline{R_{J\to\iota}}$ between beams and external forces $\boldsymbol{f}$.

The differential equation (III.7) is solved in its variational formulation represented by the virtual work formulation:

$$\int_{\Omega_t^{(i)}} \boldsymbol{\sigma} : \frac{D\boldsymbol{v}}{D\boldsymbol{u}} d\Omega_t^{(i)} - \int_{\Gamma_{c,t}^{(i,j)}} \overline{R_{J\to\iota}}\left(\xi^{(i)}, t\right) \cdot \boldsymbol{v}\, d\Gamma_t^{(i)} = \int_{\Gamma_{f,t}^{(i,j)}} \boldsymbol{f} \cdot \boldsymbol{v}\, d\Gamma_t^{(i)}. \tag{III.8}$$

Equation (III.8) permits to find, for a beam, the kinematical admissible displacement $\bar{u}$ so that for all corresponding virtual displacements $\bar{v}$ the virtual work of the internal forces (left terms of the equality) balances the virtual work of the external ones (right terms of the equality). For an assembly of N beams, it becomes:

$$\sum_{i=1}^{N} \int_{\Omega_t^{(i)}} \boldsymbol{\sigma} : \frac{D\bar{v}}{D\bar{u}} d\Omega_t^{(i)} = \sum_{i=1}^{N} \sum_{j=i+1}^{N} \int_{\Gamma_{c,t}^{(i,j)}} \overline{R_{J\to\iota}}\left(\xi^{(i)}, t\right) \cdot \bar{v}\, d\Gamma_t^{(i)} + \sum_{i=1}^{N} \int_{\Gamma_{f,t}^{(i,j)}} \bar{f} \cdot \bar{v}\, d\Gamma_t^{(i)}. \quad \text{(III. 9)}$$

Equation (III.9) constitutes a non-linear equation that can be numerically solved by finite element method with the Newton-Raphson implicit scheme of resolution.

III.2.1.3 The frictional-contact model

The contacts are detected at some discrete locations due to the finite elements description of the beam. At these locations it is necessary to geometrically detect the contacts if they occur. More details about the geometrical detection of the contacts are given in (Bajas 2011). Once the contacts are detected, a mechanical description is needed. Both the normal and the tangential behavior is defined.

The normal behavior of the contact relies on the penalty method. To prevent the discontinuity of the normal contact stiffness in the transition between contact and non-contact status, a regularization of the linear contact reaction for small penetrations with a quadratic function is implemented. Moreover, the penalty (contact stiffness) coefficient k is not fixed, but it is adapted for each contact zone not to exceed the maximum allowed penetration. Figure III.2.2 reports the regularized penetration model for the normal contact force, where g is the penetration depth and g_{rg} is the penetration depth under which a quadratic model is considered to describe the normal contact force as a function of the penetration depth.

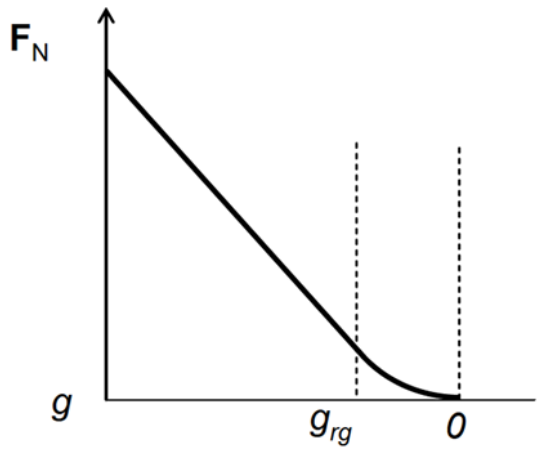

Figure III.2.2. Regularized penetration model (Bajas 2011).

For the tangential behavior of the contact, a friction model is used. In particular, for small relative displacements between beams, an initial reversible elastic tangential

displacement is allowed based on the regularized Coulomb model. When the maximum allowed reversible tangential displacement is reached the tangential force is fixed. Figure III.2.3 reports the maximum reversible tangential force allowed at the maximum reversible tangential displacement u_{rev}^{T} and defined as a function of the friction coefficient.

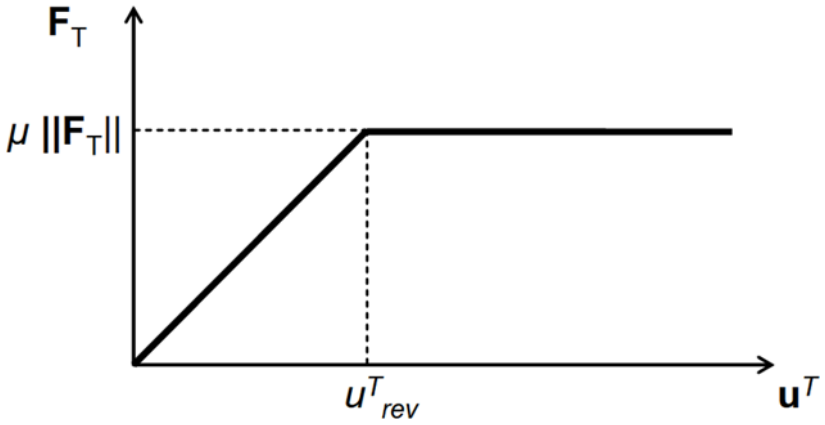

Figure III.2.3. Regularized Coulomb model for the tangential description of the contact (Bajas 2011).

III.2.1.4 Rheological model

The term related to the internal forces in equations (III.8-9) is related to the *Green-Lagrange strain tensor* ***E*** describing the strain field in all directions. A consequence of the beam kinematics described by equation (III.5) is that the terms of the Green-Lagrange strain tensor do not have the same polynomial degree with respect to the transverse coordinates. Only the constant terms of the strain tensor with respect to the section coordinates can be described by a 3D tensor, while for higher terms of the strain tensor expansion some components are null. Therefore, a classical 3D Hooke's law can be used only for the constant terms in the section.

Moreover, it is assumed that only the longitudinal components of the strain tensor are affected by the plastic deformation of the beam. The elastoplastic behavior is limited to the relation between the longitudinal stress σ and longitudinal strain ε based on a mono-dimensional model $\sigma=f(\varepsilon)$, where f is a unique non-linear function that fits the experimental curves presented in (Bajas 2011). Therefore, homogenized characteristics in the longitudinal direction have been considered and for more details one may refer to (Bajas 2011).

III.2.1.5 Boundary conditions

The current version of MULTIFIL, used during this Ph.D. work, is an upgraded version with respect to the one used in Bajas' Ph.D. thesis, in particular concerning the handling of the boundary conditions.

In the previous version, the code used pseudo-periodic boundary conditions that coupled by penalty method the displacements of each strand end to the displacements of

the two nearest ends of strands located at the opposite side of the sample. This modeling caused a perturbation in the obtained solution at both ends of the sample, which was highly dependent on the penalty coefficients chosen to ensure these pseudo-periodic conditions. In the new version, boundary conditions are prescribed independently at both ends following a hierarchical structure in accordance with the multi-stage layout of the fusion cables (Riccioli 2019).

Figure III.2.4 reports a conceptual scheme of the hierarchical structure of the boundary conditions definition in MUTLTIFIL referring to a generic cable. Thanks to this structure, it is possible to prescribe proper boundary conditions to sub-cables belonging to different levels of the hierarchy, thus greatly reducing boundary effects.

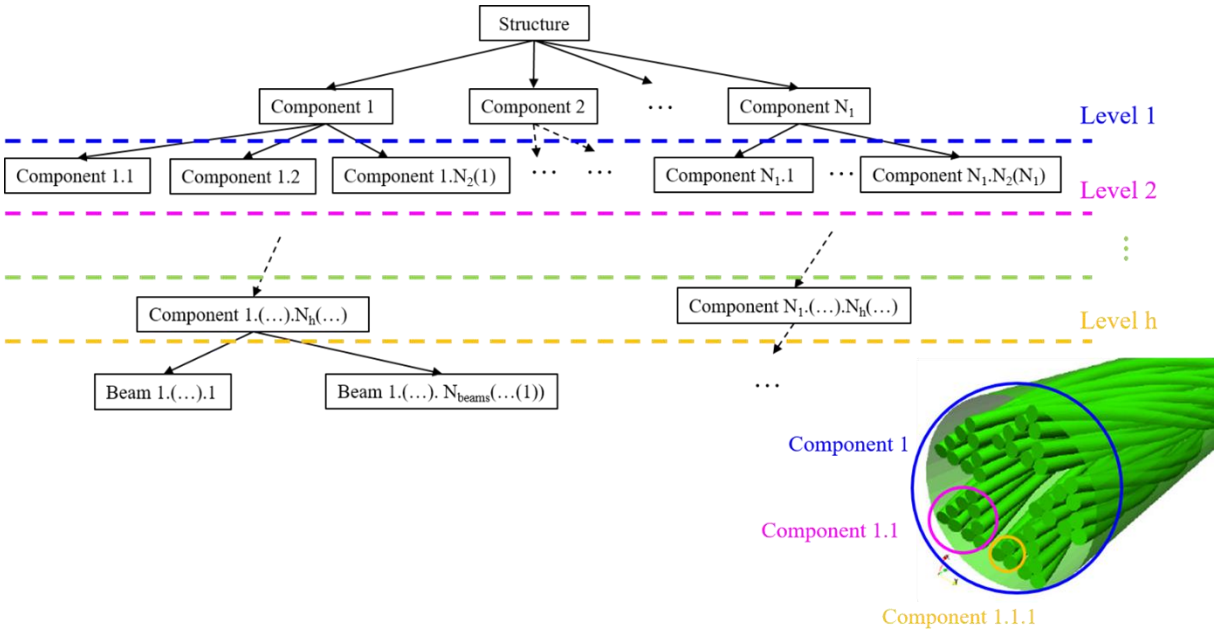

Figure III.2.4. Hierarchical structure of the boundary conditions in MULTIFIL for a generic cable.

Moreover, average conditions, formulated for both displacements and rotations, can be prescribed to the ends of all the sub-components of a sub-cable with respect to the coordinate system integral with the parent component. For a better understanding of the definition of the average conditions, an example is proposed in Figure III.2.5 and Figure III.2.6 for the translation and rotation conditions respectively.

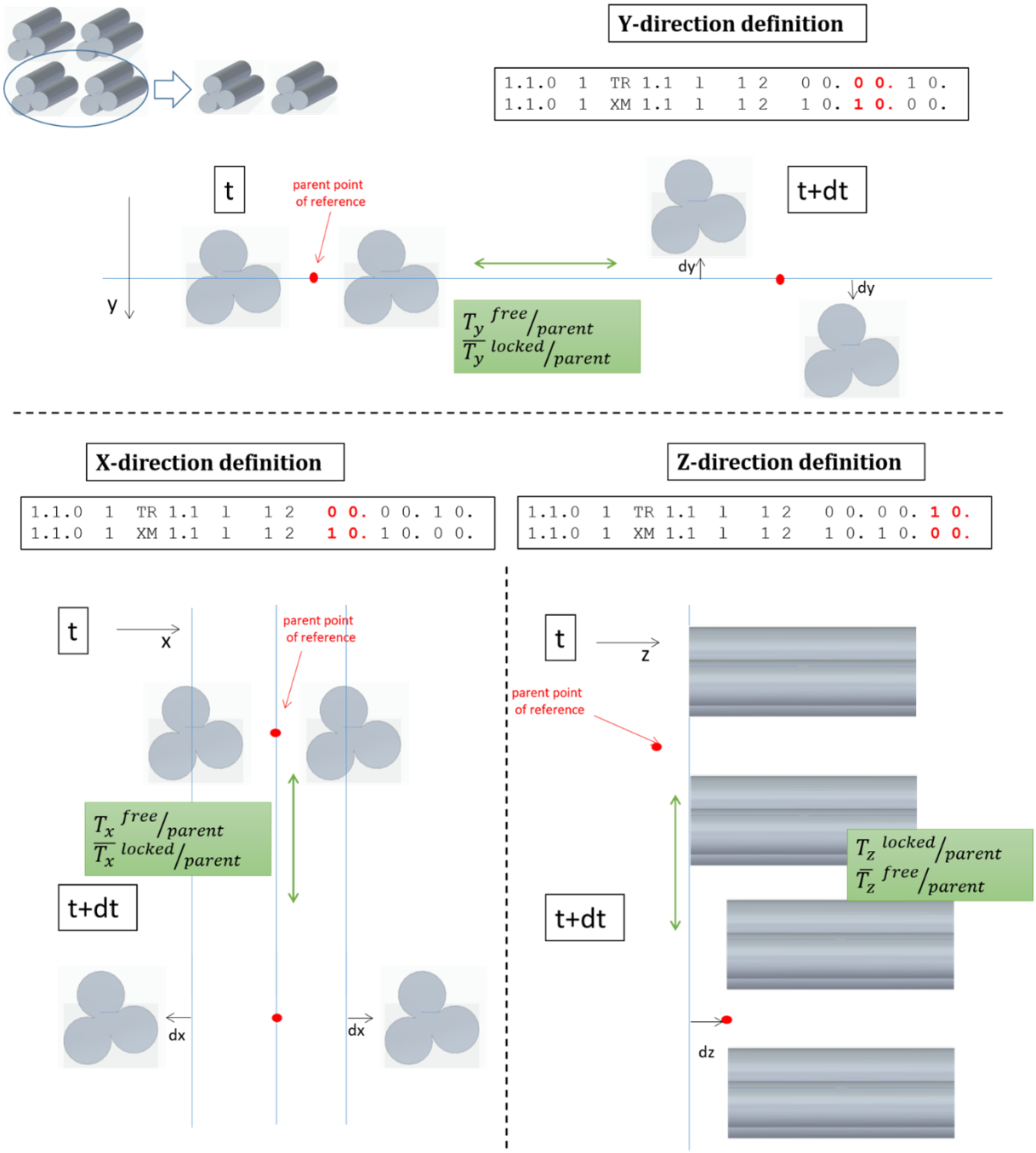

Figure III.2.5. Example of the average boundary conditions definition for the translation.

The symbol *TR* refers to the punctual translation, while *XM* refers to the average translation of the considered hierarchical level. In particular, the condition (0 0.) sets a free condition for a given direction, while (1 0.) imposes a locked condition. Hence, the condition in the y-direction means that the translation of the single components is free with respect to the parent, but the average global y-translation of the level is locked. In this example, for the z-direction, it is the opposite: the single components are locked and the average z-translation is set free. An example is also given for the rotations in Figure III.2.6, where *RM* refers to the average rotation of the level and *RO* to the rotation of each component of that level.

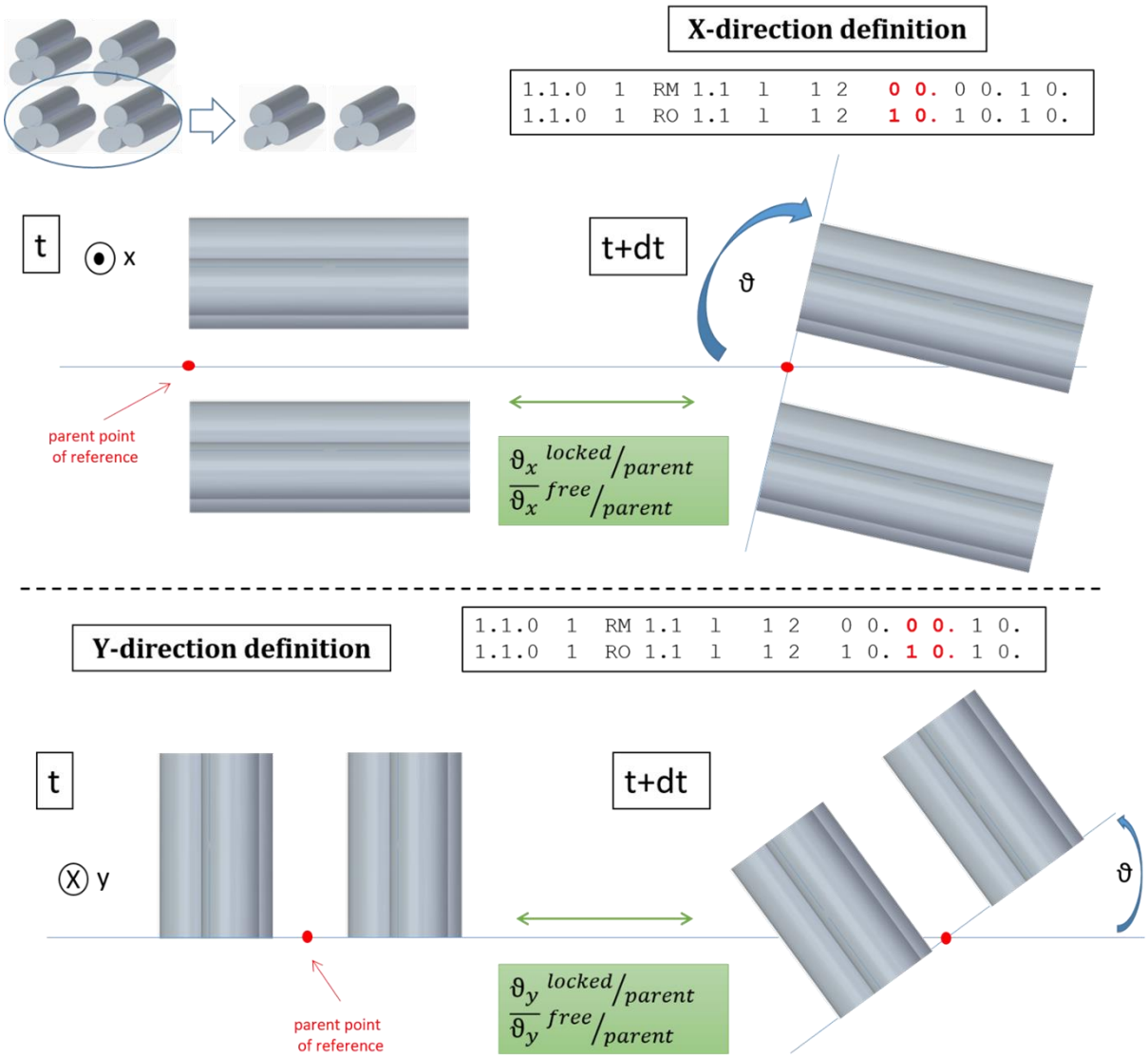

Figure III.2.6. Example of the average boundary conditions definition for the rotation.

This combination of hierarchical handling and average conditions at each level allows both a rearrangement of the ends of strands to accommodate to the various applied loadings, and a sufficient control of displacements at different levels to avoid untwisting effects. Perturbations observed in the results at the ends of the cable are much more limited with the new version (Riccioli 2019). Part of this Ph.D. work has been dedicated to the definition of the adequate set of hierarchical BCs to be applied to fusion CICC model for a correct simulation of the case study.

III.2.2 MULTIFIL upgrades

During the Ph.D. program, three main upgrades were performed in collaboration with the developer of the code D. Durville to improve fusion cables simulation. More details about the specific steps of the simulation are presented in chapter III.3. Here an overview of the main changes that contribute to the model reliability is presented.

III.2.2.1 Deformable tools

The set of beams simulated by MULTIFIL can represent the assembly of wires belonging to a cabling stage, or sub-cable, of a conductor. This assembly has to shaped into the desired final geometry, defined by the cable design. MULTIFIL disposes of a set of particular rigid tools, which are analytical surfaces interacting by frictional-contact forces with the wires, that shape the assembly during all the loading sequence and can be treated as specific boundary conditions (an illustration of these surfaces is given by Figure III.2.11). One of the most important improvements that needed to be done concerns the interaction rigid tools-cable. The first case studies proposed by (Riccioli 2019) present for the first time the issue illustrated in Figure III.2.7. The plot of the local axial strains on the wires, which is the strain on the wire axis as a function of the longitudinal coordinate of the cable, shows a highly non-homogenous distribution when the cable undergoes a compressive load during the cool-down simulation from 650 °C to –268.65 °C.

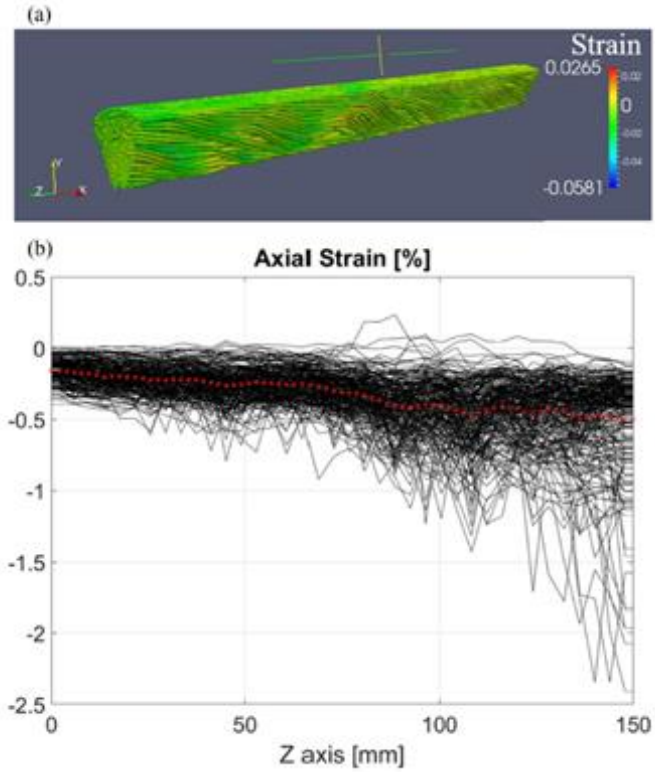

Figure III.2.7. Non-homogenous distribution of the axial strain over the axis of the simulated cable for a global applied axial compression of –0.84 % due to the frictional interaction forces between the rigid tools and the simulated cable (Riccioli 2019).

This phenomenon occurs during the cool-down simulation, which implies an incremental axial displacement applied to one end of the cable, while this is constrained inside the set of analytical surfaces, and the other end is fixed. The longitudinal surfaces acting as rigid obstacles interact with the strands through frictional contact, keeping the shape of the assembly of wires into the desired geometry. It was found that the aforementioned problem during the application of longitudinal compressive/tensile

forces to the cable is due to assuming as non-deformable the surfaces defining the rigid tools around the cable. Under these assumptions, the relative displacements between strands and the obstacles during, for example, compression is greater at the cable end submitted to the applied displacement than at the opposite end, which in turn results in a decreasing average value of the axial load along the cable (see Figure III.2.7b)). To overcome this artefact, the work presented in (Riccioli 2019) set at zero the friction coefficient between strands and the rigid surfaces to allow a more homogenous axial load distribution. Although it did work, the result is not entirely satisfactory, since frictionless contacts increase dramatically the buckling phenomena.

To cope with this issue while keeping friction as part of the contact modelling, it was introduced a correction that simulates an artificial deformation of the analytical surface: a correction was applied to the calculation of relative displacements between the nodes on the strands and their corresponding contact points on the obstacles. Instead of considering the contact nodes fixed, their displacement is proportional in the longitudinal direction to the axial deformation prescribed at the cable ends. Frictional effects between the strands and the surfaces are then fully taken into account in the cool-down simulations, thus preventing local buckling (Riccioli 2020). Figure III.2.8 reports schematic drawings helping to understand the implemented change.

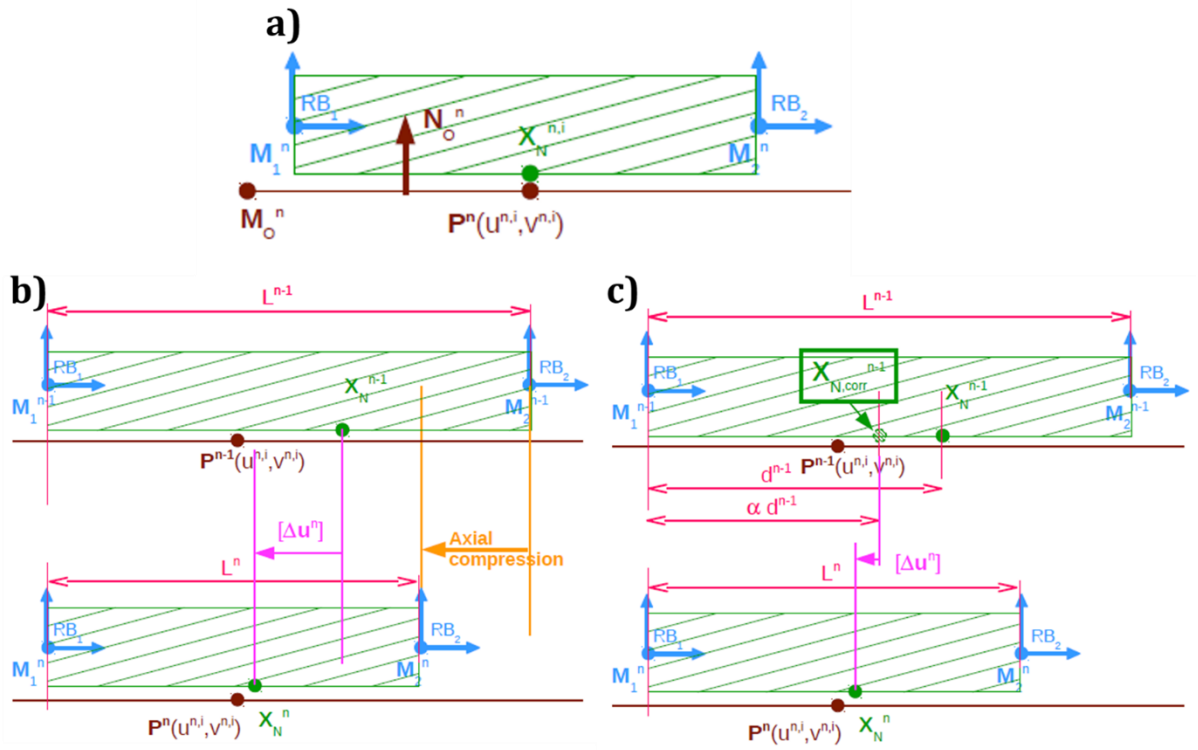

Figure III.2.8. a) Definition of the strand node *N* and its projection $P^n(U^{n,i},V^{n,i})$ on the rigid obstacle, b) increment of the relative displacement calculation without the correction, c) increment of the relative displacement calculation with the correction.

Figure III.2.8a) represents the projection $P^n(U^{n,i},V^{n,i})$ on the obstacle O of a strand node N located in $X_N^{n,i}$ at iteration i for an imposed increment n in the longitudinal direction. Before the correction (Figure III.2.8b)), for a given axial compression, the corresponding increment of relative displacement between the node N and the obstacle O is given by $\Delta u_N^n = X_N^n - X_N^{n-1}$. The correction acts on the previous location of the strand node N to consider an artificial deformation of the rigid tool with imposed displacement, as shown in Figure III.2.8c) to avoid the frictional interactions between the cable and the rigid tools. Hence the increment of relative displacement is now defined by $\Delta u_N^n = X_N^n - X_{N,corr}^{n-1}$, where $X_{N,corr}^{n-1}$ is the corrected position of the strand node N taking into account the applied axial contraction $\alpha = L^n/L^{n-1}$. In fact, the correct position is found by imposing the condition:

$$\left\| X_{N,corr}^{n-1} - M_1^{n-1} \right\| = \alpha \| X_N^{n-1} - M_1^{n-1} \|. \qquad \text{(III. 10)}$$

A more realistic strain distribution is now computed by the code during overall axial loading, as shown in Figure III.2.9 for a global axial compression of –0.84 % applied to the cable.

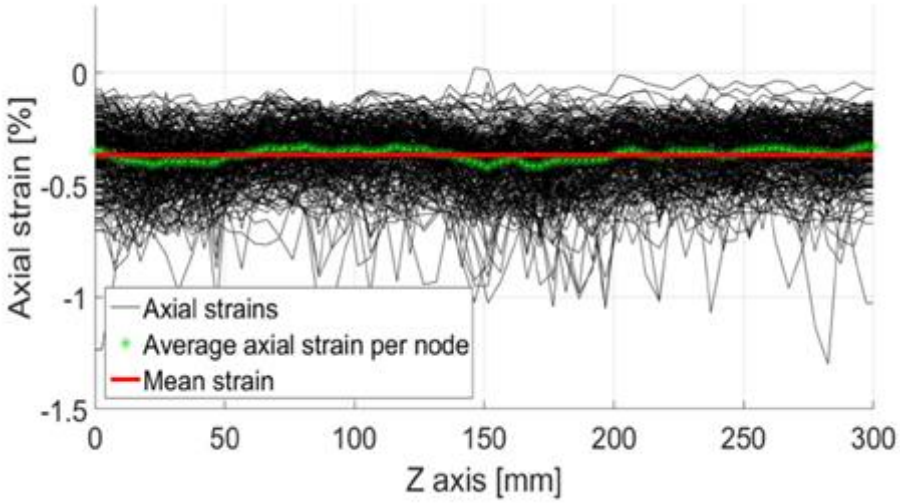

Figure III.2.9. Homogenous axial strain plot over the cable length for a global applied axial compression of –0.84 % (Riccioli 2020).

Figure III.2.10a) reports the qualitative comparison between the application of a compressive strain on a 300 mm long sample without and with the deformable tools upgrade. A quantitative comparison is also presented in Figure III.2.10b) where the probability density function for the strains is plotted for both cases. With and without deformable tools the distributions are compared to the normal distribution to illustrate the overall better compliance of the model using deformable tools.

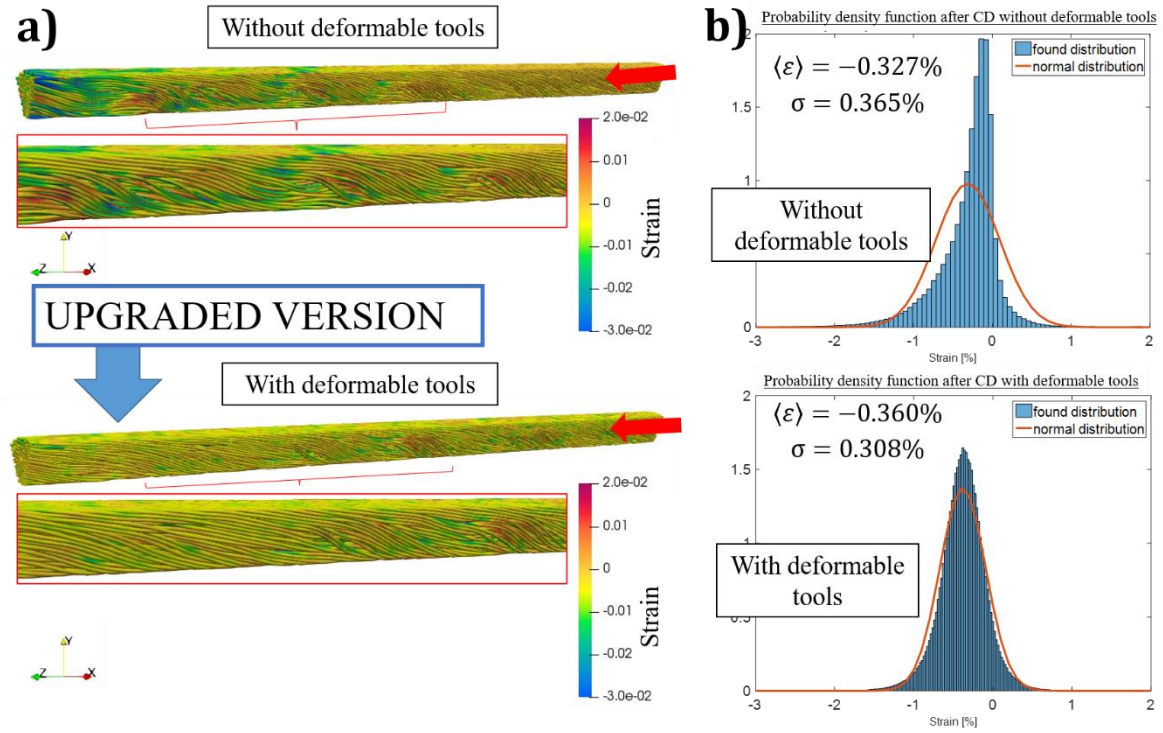

Figure III.2.10. a) Qualitative illustration of the more homogenous distribution of the strain map after the application of longitudinal displacement on one end of the cable thanks to the deformable tools upgrade; b) quantitative illustration of the more homogenous distribution of the strain distribution after the application of longitudinal displacement on one end of the cable thanks to the deformable tools upgrade.

Thanks to this new set of longitudinal deformable tools, it is now possible to use MULTIFIL for the study of the cool-down behavior with a very high degree of representability. In particular, since the cool-down is the first step of the modelled operating sequence, it is probable that previous calculations were greatly biased by this initial step. Longitudinal and transversal reaction forces of the cable for a given applied load can now be analyzed, since the frictional interactions between strands and obstacles do not affect the mechanical behavior of the cable anymore. This upgrade opens the way to new and critical analyses as the study of the rigidity of the modelled cable, the study of the longitudinal equilibrium between cable and jacket and unbiased studies of the strain maps.

III.2.2.2 Helical boundary conditions

The rigid analytical surfaces can be cylinders or planes, as shown in Figure III.2.11. By moving these rigid tools, the cable can be compacted from a theoretical shape of multi-twisted helical trajectories to the final compacted cable or sub-cable. This is called the shaping step of the MULTIFIL modelling sequence.

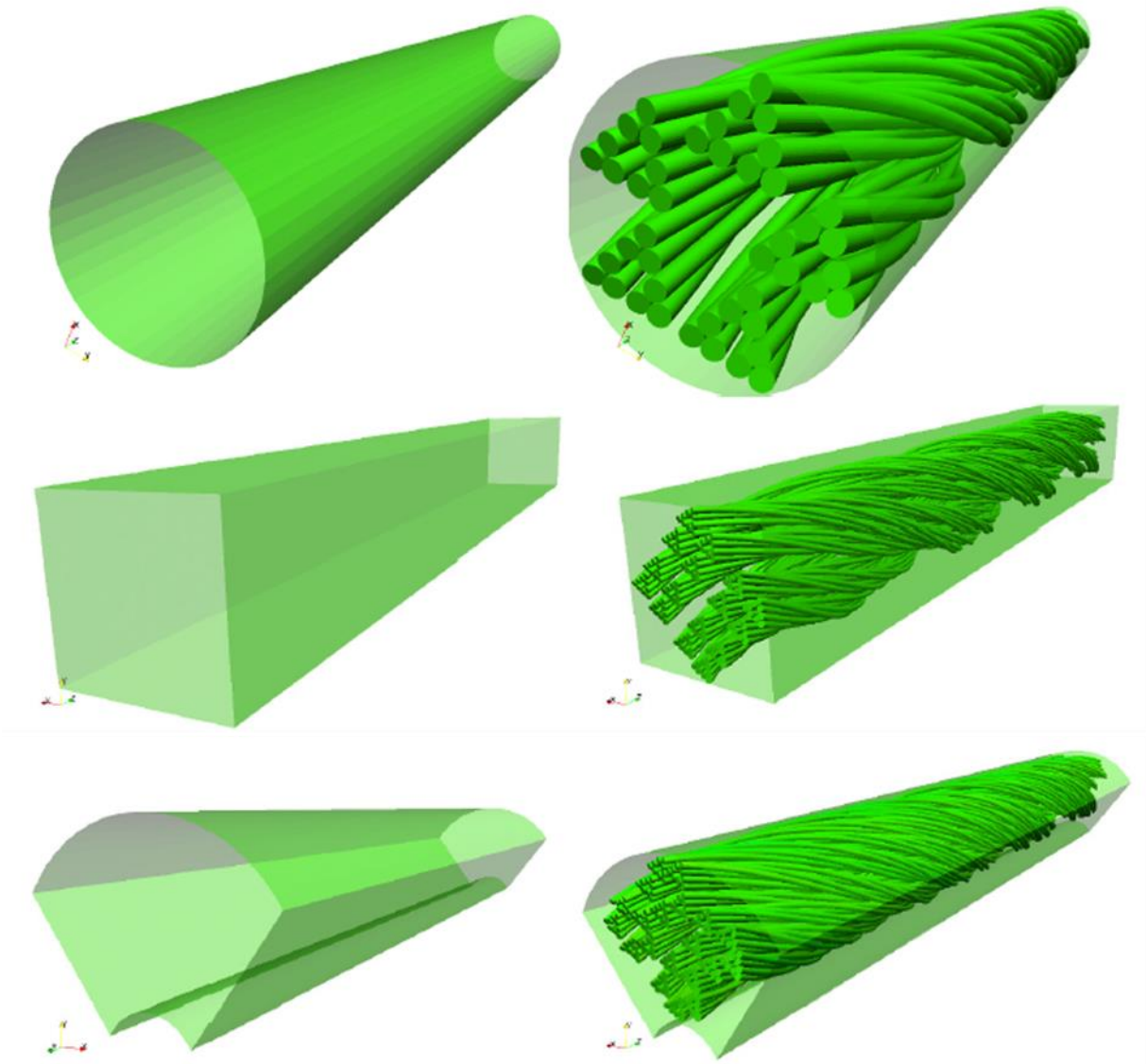

Figure III.2.11. Different shapes of the wires assembly simulated by MULTIFIL thanks to the rigid tools (Bajas 2011).

The former model developed by (Bajas 2011) allowed the simulation of one of the six sub-cables, also called "petal", referring for example to the ITER CS CICC (Bajas 2010). Moreover, the petal was untwisted, which is quite a critical difference with real cables. This limit was related to several modelling restrictions. First, 10 years ago the boundary conditions in MULTIFIL did not follow a hierarchical structure as presented in paragraph III.2.1.5; hence, at that time it was unthinkable to apply the previous approach to a full cable model. Second, the presence of the wrapping in real conductors among the petals suggested the idea that the sub-cables had to be kept separated, so a simple additional twisting of the petals was not possible. Finally, the simulation needed to handle several hundreds of wires instead of a few hundreds, hence there would be drastic increase of the computation time.

Thanks to the new system of BCs a scaling-up of the model was deemed possible. However, the first step was to code an analytical helical plane representing the presence

of the wrapping and to add another stage to the hierarchical structure of the cable. This work was done during this Ph.D. thesis as here presented.

Figure III.2.12 reports the parametrization of a generic helical plane and the main parameters to be defined are:

- Origin $\boldsymbol{O}$;
- Orthonormal reference system (D_1,D_2,D_3): D_1,D_2 transverse directions, D_3 longitudinal direction;
- Axial length L;
- Starting point in the orthoradial direction a_1;
- Ending point in the orthoradial direction a_2;
- Helix period p;
- Helix initial angle ϑ_0.

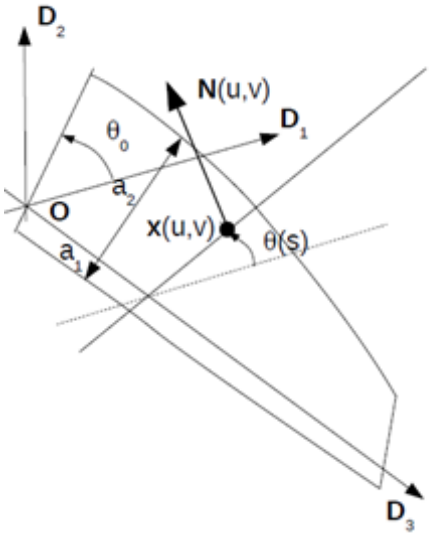

Figure III.2.12. Parametrization of a helical surface.

The position of a generic point on this surface $\boldsymbol{x}(u,v)$ is given by:

$$\boldsymbol{x}(u,v) = \boldsymbol{O} + u\boldsymbol{D}_3 + v\boldsymbol{d}_\vartheta(u). \tag{III. 11}$$

In equation (III.11) $\boldsymbol{d}_\vartheta(u)$ represents the orthoradial direction defined as $\boldsymbol{d}_\vartheta(u) = \cos\vartheta(u)\,\boldsymbol{D}_1 + \sin\vartheta(u)\,\boldsymbol{D}_2$, u and v are respectively the longitudinal and orthoradial components of the position and $\vartheta(u) = \vartheta_0 + u(2\pi/p)$ is the angle defining the rotation of the surface. The tangent and normal vectors to the surface are defined as follow:

$$\frac{\partial \boldsymbol{x}}{\partial u} = \boldsymbol{D}_3 + \frac{2\pi}{p} v(-\sin\vartheta(u)\,\boldsymbol{D}_1 + \cos\vartheta(u)\,\boldsymbol{D}_2), \tag{III. 12}$$

$$\frac{\partial \boldsymbol{x}}{\partial v} = \cos\vartheta(u)\,\boldsymbol{D}_1 + \sin\vartheta(u)\,\boldsymbol{D}_2, \tag{III. 13}$$

$$\boldsymbol{N}(u,v) = \cos\vartheta(u)\,\boldsymbol{D}_2 - \sin\vartheta(u)\,\boldsymbol{D}_1 - \frac{2\pi}{p}v\boldsymbol{D}_3. \tag{III. 14}$$

Finally, for the adequate integration of these helical planes in MULTIFIL, the normal projection of a point $\boldsymbol{P}$ on the helical surface has to be defined and it has to respect the following conditions:

$$\begin{cases} c_u(u_P, v_P) = \big(\boldsymbol{x}(u_P, v_P) - \boldsymbol{P}, \partial_u \boldsymbol{x}(u_P, v_P)\big) = 0 \\ c_v(u_P, v_P) = \big(\boldsymbol{x}(u_P, v_P) - \boldsymbol{P}, \partial_v \boldsymbol{x}(u_P, v_P)\big) = 0 \\ 0 \le u_P \le L \\ a_1 \le v_P \le a_2 \end{cases}. \tag{III. 15}$$

Differently from the other analytical surfaces, the projection of a point on the helical surface cannot be determined in a direct way. A Newton algorithm had to be introduced to compute numerically this projection, important for the determination of the contact points between the wires and the surface. Defining the first tentative solution as $({u_P}^0, {v_P}^0)$, the correction $\big(\delta {u_P}^{i+1}, \delta {v_P}^{i+1}\big)$ to the solution at the *i+1* iteration is given by:

$$\begin{bmatrix} \delta {u_P}^{i+1} \\ \delta {v_P}^{i+1} \end{bmatrix} = -\begin{bmatrix} \partial_u c_u\big({u_P}^i, {v_P}^i\big) & \partial_v c_u\big({u_P}^i, {v_P}^i\big) \\ \partial_u c_v\big({u_P}^i, {v_P}^i\big) & \partial_v c_v\big({u_P}^i, {v_P}^i\big) \end{bmatrix}^{-1} \begin{bmatrix} c_u\big({u_P}^i, {v_P}^i\big) \\ c_v\big({u_P}^i, {v_P}^i\big) \end{bmatrix}, \tag{III. 16}$$

where the components of the system are defined as follow:

$$\begin{aligned} \partial_u c_u(u,v) &= \big(\partial_u \boldsymbol{x}(u,v), \partial_u \boldsymbol{x}(u,v)\big) - \big(\boldsymbol{P}, {\partial^2}_{uu}\boldsymbol{x}(u,v)\big) \\ \partial_v c_u(u,v) &= \big(\partial_v \boldsymbol{x}(u,v), \partial_u \boldsymbol{x}(u,v)\big) - \big(\boldsymbol{P}, {\partial^2}_{uv}\boldsymbol{x}(u,v)\big) \\ \partial_u c_v(u,v) &= \big(\partial_u \boldsymbol{x}(u,v), \partial_v \boldsymbol{x}(u,v)\big) - \big(\boldsymbol{P}, {\partial^2}_{uv}\boldsymbol{x}(u,v)\big) \\ \partial_v c_v(u,v) &= \big(\partial_v \boldsymbol{x}(u,v), \partial_v \boldsymbol{x}(u,v)\big) - \big(\boldsymbol{P}, {\partial^2}_{vv}\boldsymbol{x}(u,v)\big) \end{aligned} \tag{III. 17}$$

$$\begin{aligned} {\partial^2}_{uu}\boldsymbol{x}(u,v) &= \left(\frac{2\pi}{p}\right)^2 v(-\cos\vartheta(u)\,\boldsymbol{D}_1 - \sin\vartheta(u)\,\boldsymbol{D}_2) \\ {\partial^2}_{uv}\boldsymbol{x}(u,v) &= \frac{2\pi}{p}(-\sin\vartheta(u)\,\boldsymbol{D}_1 + \cos\vartheta(u)\,\boldsymbol{D}_2) \\ {\partial^2}_{vv}\boldsymbol{x}(u,v)) &= 0 \end{aligned}. \tag{III. 18}$$

Once the new helical analytical surfaces were coded in the core of MULTIFIL, it was necessary to introduce an additional stage in the hierarchy, representing the twisting of the petals in the cable hierarchical description. This hierarchical level is not like the others because it has to consider the presence of a virtual wrapping separating the petals. A specific command was thus introduced in the code (*PETAL_HELIX*) to consider the presence of this particular level, which follows a specific helix. Therefore, the main information about the helix representing this level has to be defined, like the radius, the initial angle and twist pitch.

Hence, this approach, involving helical rigid tools and the additional twisting stage in the cabling, is only necessary when the simulated cable is characterized by a structure

of petals physically separated by a steel wrapping, like for the ITER CS and TF conductors. Nevertheless, it should be noted that this is a fundamental addition to the capacity of the code since it might be used in the future to fine-tune the shaping process of any multi-staged cable. In particular, for a better modelling of the real cabling process of a cable, one might want to pre-compact individual sub-stages using this helical tool, even if wrappings are not foreseen. Figure III.2.13 shows the helical rigid tool and last stage twisted petal successfully implemented in MUTLIFIL. Although it permits twisted single-petal models with limited size and computation time, it obviously opens the way for full cable models.

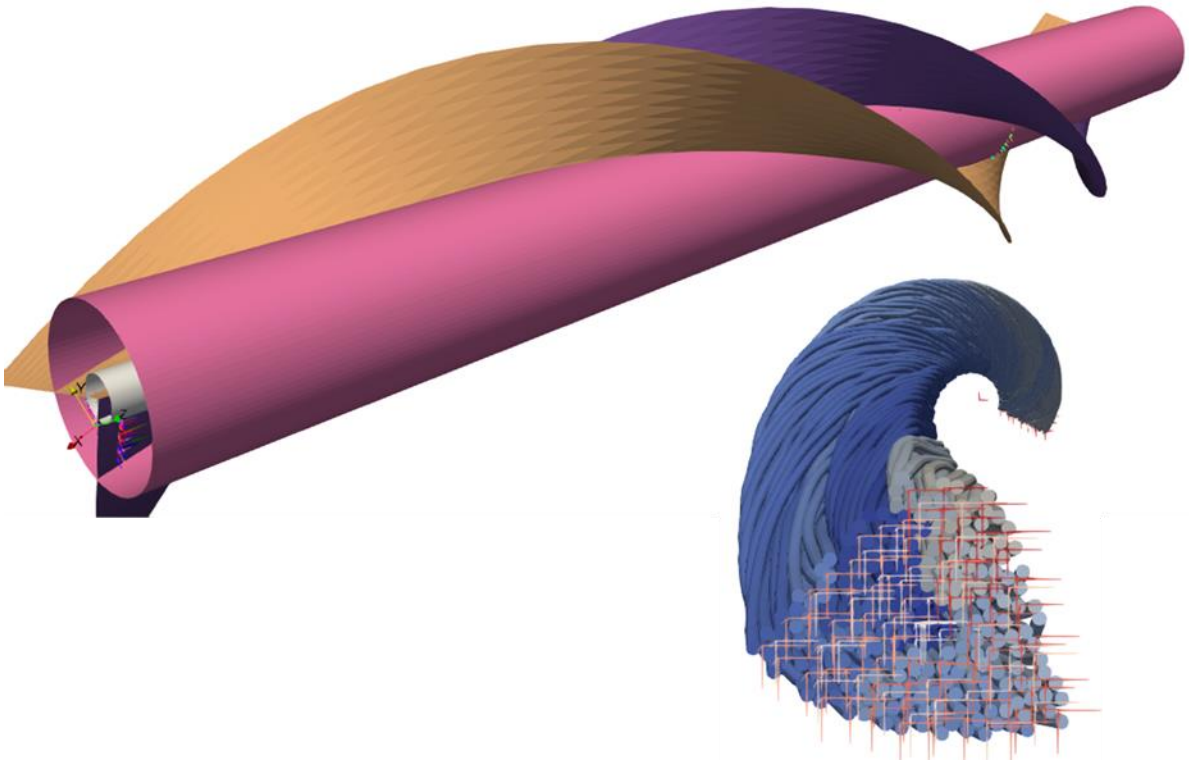

Figure III.2.13. Illustration of the helical analytical surfaces and of the twisted petal implemented in MULTIFIL.

III.2.2.3 Full cable model

Once the helical rigid tools and twisted stage features were implemented, the way to the full cable model was paved. The main difficulty in this case was related to the new hierarchical structure and so to the adequate handling of the components in each stage.

A new object called *PETAL* was defined and implemented in the core of the code, so that full cable needs to specify the number of these components, their twist pitch and their helix radius. At the same time, helical surfaces have to be defined as described in the previous paragraph, and these surfaces are in the same number as the *PETAL* components. Figure III.2.14 reports an example of the full cable model with sub-cables/petals separated by a wrapping.

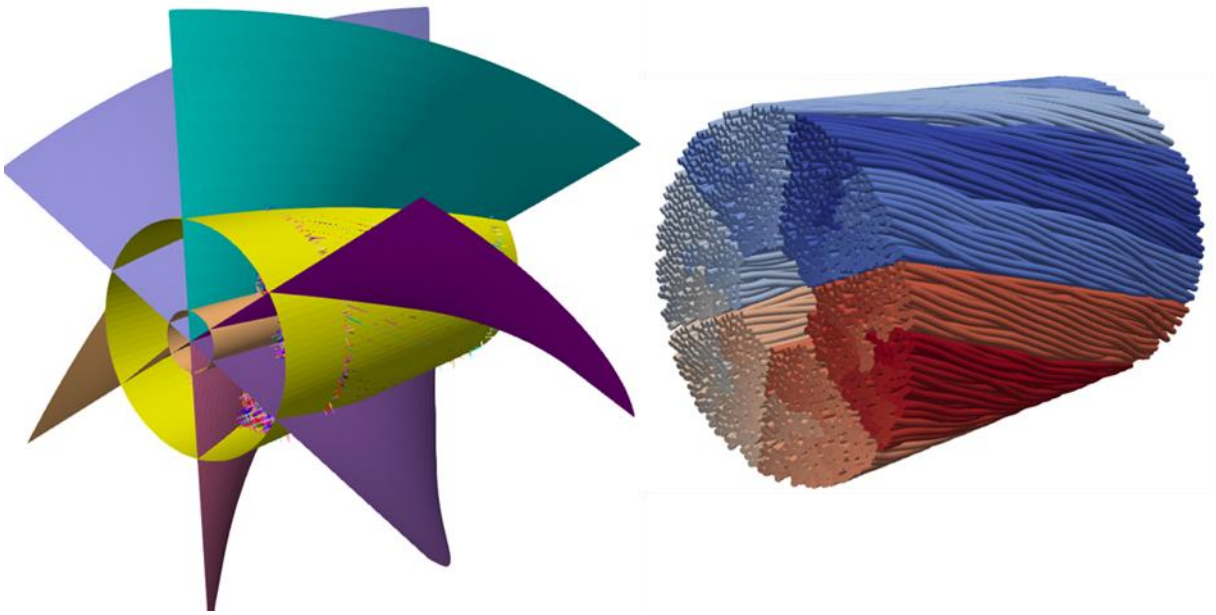

Figure III.2.14. Full cable model implementation in MULTIFIL code.

This final scale-up of the code permitted a completely new simulation approach, giving access to new information about macroscopic mechanical phenomena occurring at the cable scale that were near impossible to understand using the single petal/sub-cable model.

Even though this section shows the final result of the scale-up from petal to full cable, a huge effort was also invested in the development of a more reliable single petal model. This was of course due to timescale in the development of the full cable model which required almost two years during which single petal models were investigated. The other reason is related to the large difference in computing time between the sub-cable and full cable models. It was deemed important to develop a reliable sub-scale model of a cable that could still be a useful tool for quicker analyses. Part IV presents the main studies that were performed using both the petal and full cable models, each of them with their most relevant results.

III.2.3 Analytical-Numerical coupling for additional physics

This section presents two major improvements of the modelling, where analytical approaches have been coupled to the numerical model in order to represent adequately specific physical behaviors. Both improvements were developed with the goal to improve the petal model, but the first one was also applied to the full cable model.

III.2.3.1 Jacket-cable equilibrium implementation

As anticipated in paragraph III.2.1.5, the new hierarchical structure of the BCs gives an easier access to the longitudinal reaction effort of the simulated cable. This important feature allows the consideration of the presence of the conductor jacket even

if only simulated by rigid analytical tools that have no mechanical properties or material constitutive law. The rigid analytical surfaces act as shaping obstacles for the wires assembly and can thus be considered as boundary conditions. In real cables the jacket is a structural material extremely important for the global jacket-cable equilibrium occurring in fusion cables, in particular when simulating the effect of the thermal loadings due to cool-down (CD) and warm-up-cool-down (WUCD). Indeed, this equilibrium is defined by the thermo-mechanical properties of the involved materials, in particular by their differential thermal expansion. For a detailed simulation of the cable strain state, the equilibrium state of the cable due to its interaction with the jacket has to be known. The previous works presented in chapter III.1, MULTIFIL included, considered this equilibrium state as an input parameter, coming from literature. (Mitchell 2005b), for example, talks about a differential contraction between the cable and the jacket of –0.8 %, based on material properties and fully bonded analytical models, but since the cable longitudinal rigidity cannot be assessed once inside the jacket, this assumption is near-impossible to verify.

The method presented here can be applied to any code simulating the mechanical state of a cable and its overall longitudinal reaction force. The cable-jacket equilibrium is based on an extension of the well-known fully bonded model and it compares the reaction force of a virtual analytical jacket of known cross-section to the reaction force of the simulated cable, as shown in Figure III.2.15 for a generic case. The reaction force is extracted from MULTIFIL computation at cable's extremities (BC), and corresponds to the longitudinal force acting on the cable for a given applied strain. The plot shows a typical case of progressive compression of the superconducting cable by the jacket from its initial freestanding thermal strain ($\varepsilon_{thcable}$) and the corresponding traction of the stainless steel (SS) jacket from its freestanding thermal strain (ε_{thSS}). The freestanding thermal strains are related to the different coefficient of thermal expansion of the two materials from heat treatment (HT) temperature (650 °C) to cryogenic temperature (Mitchell 2005b). The intersection of the curves provides the equilibrium between the two mechanical entities, one simulated by MULTIFIL and the other analytically modelled by simple elastic behavior with Young Modulus E^{SS}.

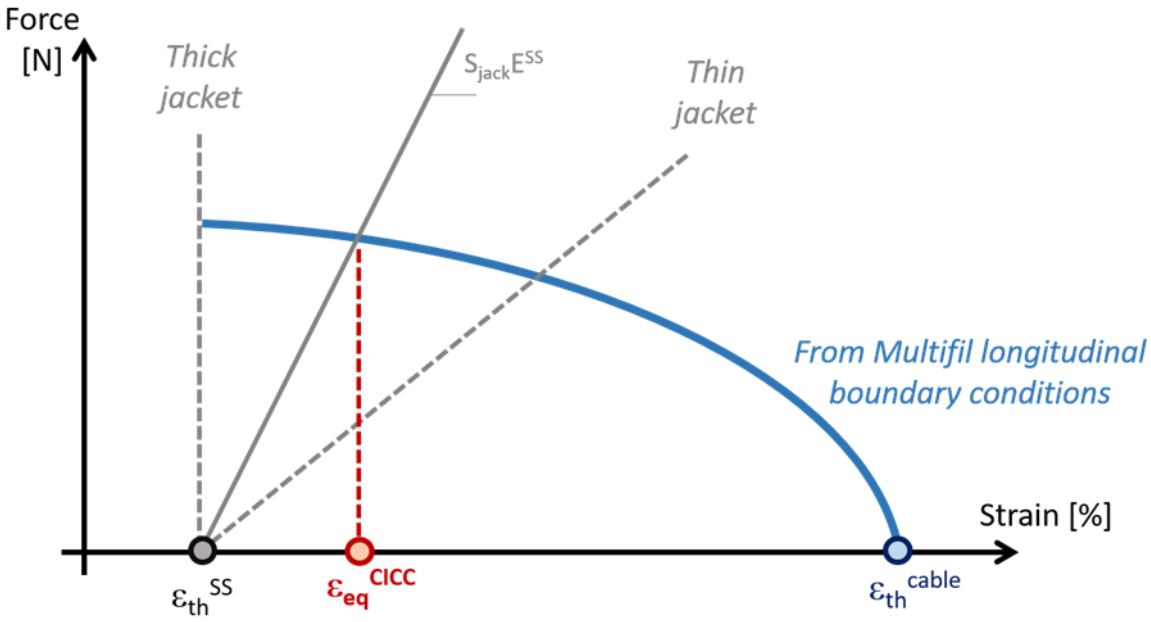

Figure III.2.15. Virtual analytical steel jacket and MULTIFIL cable.

The same approach is used when a WUCD is simulated, and in this case another equilibrium point is defined for the warm-up temperature (300K), as in Figure III.2.16.

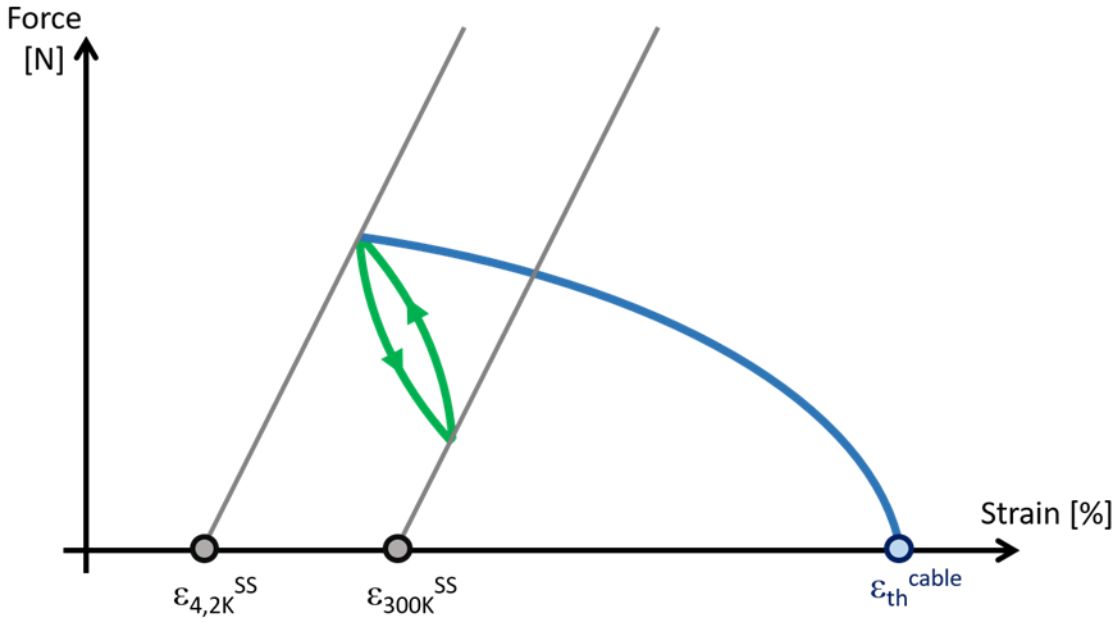

Figure III.2.16. Virtual analytical steel jacket at 4.2 K and 300 K and MULTIFIL cable.

Also, since the cable reaction force changes when other thermal and electromagnetic (EM) loadings are applied, the apparent longitudinal rigidity of the cable changes as well and a new equilibrium needs to be found after each variation in rigidity, see Figure III.2.17. In particular, a gradual softening of the cable was identified during EM cycling which tends to shift the cable-jacket equilibrium towards the compressive side.

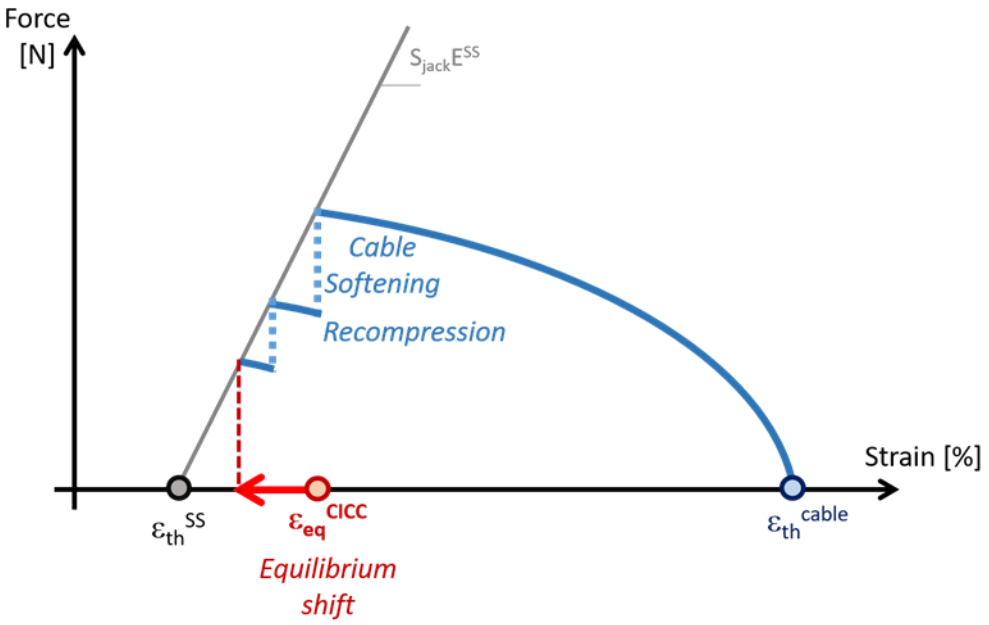

Figure III.2.17. Equilibrium point between the virtual analytical steel jacket at 4.2 K and MULTIFIL cable after each electromagnetic loading simulation.

This last point allows some interesting considerations: the application of EM cycles triggers a macroscopic softening of the cable, related to plasticization and release of frictional contacts. Hence, the equilibrium tends to shift towards the thermal equilibrium point of the jacket at its freestanding thermal strain, the cable's rigidity becomes negligible after a certain number of cycles (typically 5-10 cycles). This point will be discussed in detail in part IV, since it is one of the major results obtained thanks to this Ph.D. work.

III.2.3.2 Multipetal analytical model

One of the limitations of the sub-cable model is the missing information of the over-load due to the cumulative body force in other petals. When the electromagnetic loading is applied, it is important to consider the cumulative effect of the Lorentz force of the other petals on the simulated one. The former MULTIFIL single petal model did not represent the cumulative load of adjacent petals on the studied petal, which seemed like a major deviation from reality. An analytical multipetal model was developed in order to include this over-load as boundary conditions when simulating an electromagnetic loading on a single petal. Figure III.2.18 reports a schematic drawing of the presented strategy for the petal on the bottom of the cable cross-section.

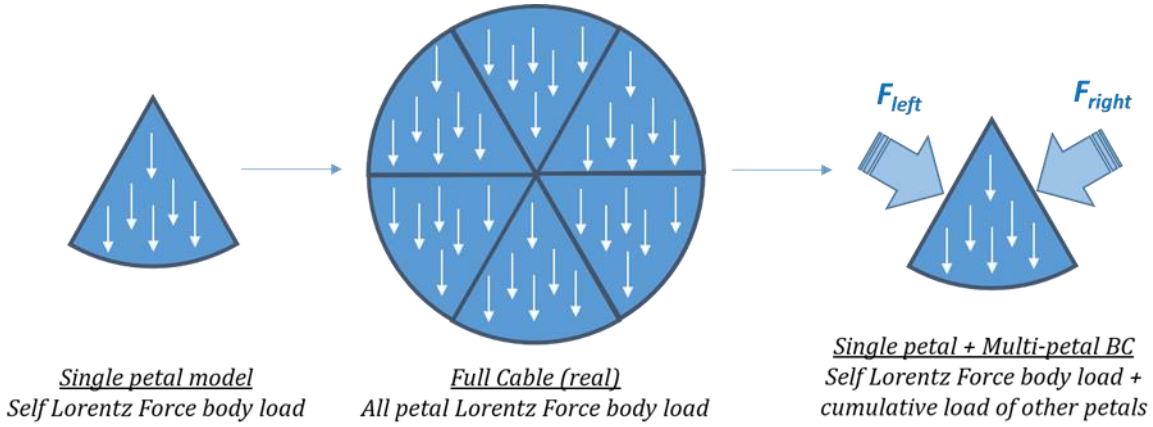

Figure III.2.18. Schematic drawing of the cumulative Lorentz forces to be taken into account in the petal model through specific BCs.

The aim of these multipetal analytical models is to identify the appropriate boundary conditions to be applied during the EM cycle simulation of one petal properly accounting for the loads applied by the other petals on the analyzed one. Two models, reported in Figure III.2.19, have been developed, namely the rigid model (RM) and the fluid model (FM). In both models, the geometry is ideal and current and magnetic field are assumed uniform.

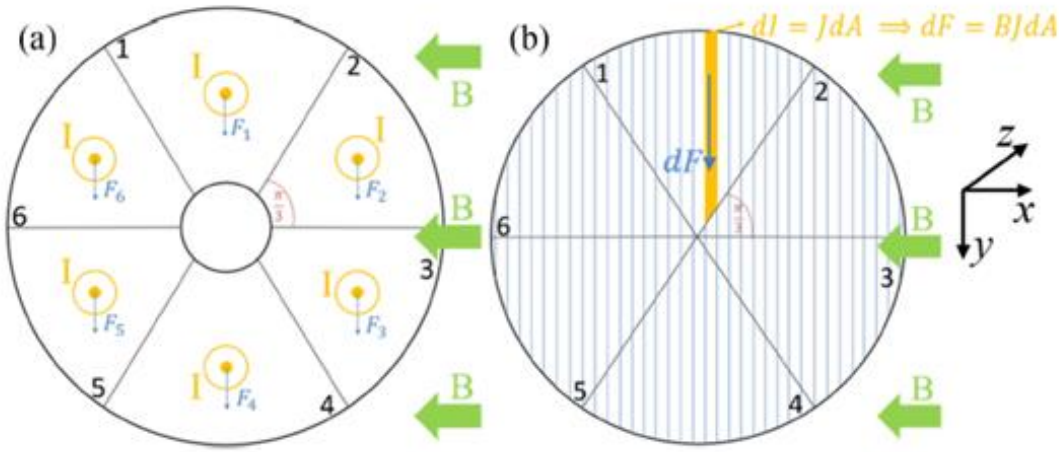

Figure III.2.19. a) Full cable rigid analytical model for the EM loading and b) full cable fluid analytical model for EM loading (Riccioli 2020).

In the RM, the cable is composed of six petals interacting with each other like rigid bodies. The Lorentz force of each petal is applied at the petal center and the cumulated Lorentz force is transmitted to the other petals at the petals' interfaces, as illustrated in Figure III.2.20.

Reaction forces:

$F_{j4} = F_4 + F_{34} = F_4 + F_3 + F_2 + F_1 = 4 \cdot I_p B$

$F_{j3} = F_3 + F_2 + F_1 = 3 \cdot I_p B$

$F_{j5} = F_5 + F_6 + F_1 = 3 \cdot I_p B$

$F_{j2} = F_1 = I_p B$

$F_{j6} = F_1 = I_p B$

Interaction forces:

$F_{12} = F_{21} = F_1 = I_p B$

$F_{32} = F_{23} = F_2 + F_1 = 2 \cdot I_p B$

$F_{34} = F_{43} = F_3 + F_2 + F_1 = 3 \cdot I_p B$

$F_{54} = F_{45} = F_5 + F_6 + F_1 = 3 \cdot I_p B$

$F_{56} = F_{65} = F_6 + F_1 = 2 \cdot I_p B$

$F_{16} = F_{61} = F_1 = I_p B$

Petal forces:

$F_1 = F_2 = F_3 = F_4 = F_5 = F_6 = I_p B$

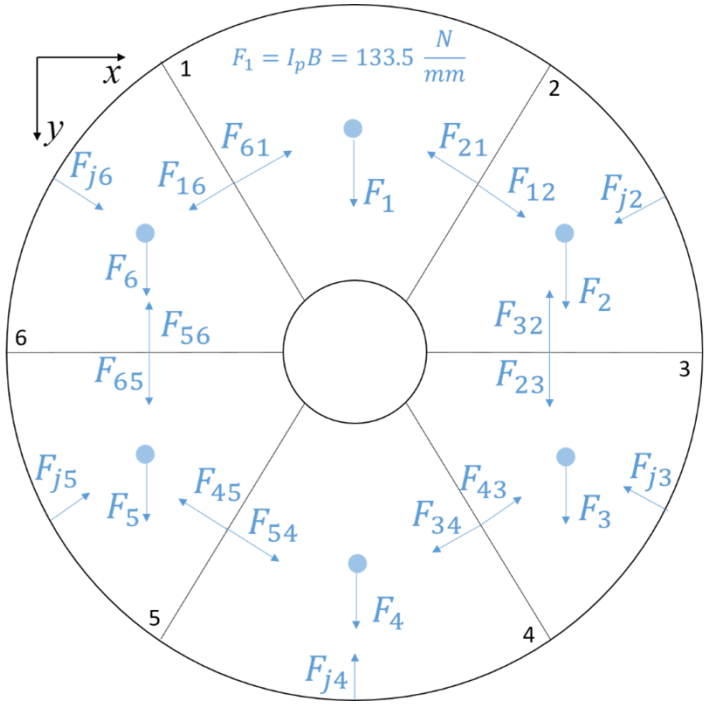

Figure III.2.20. Forces acting in the cable according to the RM assumptions.

In the FM, the cable is described as a single entity, and is discretized into small and independent columnar elements, each subjected to a cumulative EM force *dF* integrated over the height of the element. The Lorenz force is unidirectional and acts similarly to a hydrostatic pressure; only the contribution to the Lorentz force of the elements located upon the studied petal is taken into account. The equilibrium forces are illustrated in Figure III.2.21.

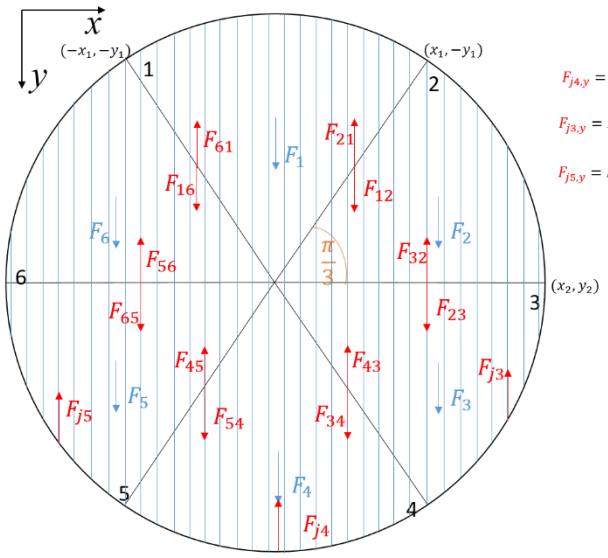

Reaction forces:

$F_{j4,y} = F_4 + F_{34} + F_{54} = BJ\frac{\pi}{6}R_{ext}^2 + 2\left(BJ\frac{\pi}{12}R_{ext}^2 + BJ\sqrt{3}x_1^2\right) = \left(2 + \frac{3\sqrt{3}}{\pi}\right)\left(BJ\frac{\pi}{6}R_{ext}^2\right)$

$F_{j3,y} = F_3 + F_{23} - F_{43} = BJ\frac{\pi}{6}R_{ext}^2 + BJ\frac{\pi}{4}R_{ext}^2 - BJ\frac{\pi}{12}R_{ext}^2 - BJ\sqrt{3}x_1^2 = \left(2 - \frac{3\sqrt{3}}{2\pi}\right)\left(BJ\frac{\pi}{6}R_{ext}^2\right)$

$F_{j5,y} = F_5 - F_{45} + F_{65} = BJ\frac{\pi}{6}R_{ext}^2 - BJ\frac{\pi}{12}R_{ext}^2 - BJ\sqrt{3}x_1^2 + BJ\frac{\pi}{4}R_{ext}^2 = \left(2 - \frac{3\sqrt{3}}{2\pi}\right)\left(BJ\frac{\pi}{6}R_{ext}^2\right)$

Interaction forces:

$F_{12} = F_{21} = BJ\frac{\pi}{12}R_{ext}^2 = \frac{1}{2}\left(BJ\frac{\pi}{6}R_{ext}^2\right)$

$F_{32} = F_{23} = BJ\frac{\pi}{4}R_{ext}^2 = \frac{3}{2}\left(BJ\frac{\pi}{6}R_{ext}^2\right)$

$F_{34} = F_{43} = BJ\frac{\pi}{12}R_{ext}^2 + BJ\sqrt{3}x_1^2 = \left(\frac{1}{2} + \frac{3\sqrt{3}}{2\pi}\right)\left(BJ\frac{\pi}{6}R_{ext}^2\right)$

$F_{54} = F_{45} = BJ\frac{\pi}{12}R_{ext}^2 + BJ\sqrt{3}x_1^2 = \left(\frac{1}{2} + \frac{3\sqrt{3}}{2\pi}\right)\left(BJ\frac{\pi}{6}R_{ext}^2\right)$

$F_{56} = F_{65} = BJ\frac{\pi}{4}R_{ext}^2 = \frac{3}{2}\left(BJ\frac{\pi}{6}R_{ext}^2\right)$

$F_{16} = F_{61} = F_1 = BJ\frac{\pi}{12}R_{ext}^2 = \frac{1}{2}\left(BJ\frac{\pi}{6}R_{ext}^2\right)$

Petal forces:

$F_1 = F_2 = F_3 = F_4 = F_5 = F_6 = BJ\frac{\pi}{6}R_{ext}^2$

Figure III.2.21. Forces acting in the cable according to the FM assumptions.

These two models do not give exactly the same results, since the force distributions are slightly different. To choose which one is more relevant to a given cable, it is reasonable to assume that the rigid bodies of the RM better represent the behavior of a cable with highly compacted and stiff petals, characterized by a strong mechanical bonding between strands. The FM seems instead more relevant to study a loose cable with less compaction. In general, the two models represent ideal limit cases; the behavior of a real cable should be included between these limits.

The models have been implemented in MULTIFIL for the study of the petal number 4 (bottom petal when the body load is from top to bottom) in Figure III.2.19. To implement them, the idea is to move the plane surfaces of the petal in MULTIFIL until the stresses acting on them reach the values prescribed by the analytical models, thus corresponding to the accumulated load due to the other petals. For example, for the ITER TF model, each petal is subjected to a Lorentz force of 133.5 N/mm (at 68 kA under 11.78 T background field); the analytical models prescribe the application on the flat surface of each petal of 400 N/mm and 177 N/mm, for the RM and the FM respectively. To reach these forces on the rigid tools, a study of the transverse rigidity of the cable is done through the application of an increasing load on the lateral planes of the petal. The plots in Figure III.2.22 show that the surfaces have to displace from their initial design position by 0.249 mm for the RM and 0.376 mm for the FM. This coupled analytical-numerical modelling process depends on the cable rigidity, and thus on the cable model. Nevertheless, it can be extrapolated to any cable design by adding this specific step of transverse rigidity definition.

The Figure III.2.22 shows also the direction of the surface displacements for both models. The direction of the displacement changes depending on the model: in the RM the force is transmitted from petal to petal along the direction orthogonal to their interfaces, while in the FM the force is transmitted along the same direction as the Lorentz force. To simulate the unloading phase of the EM cycle, the planes are moved back to their original position for both models.

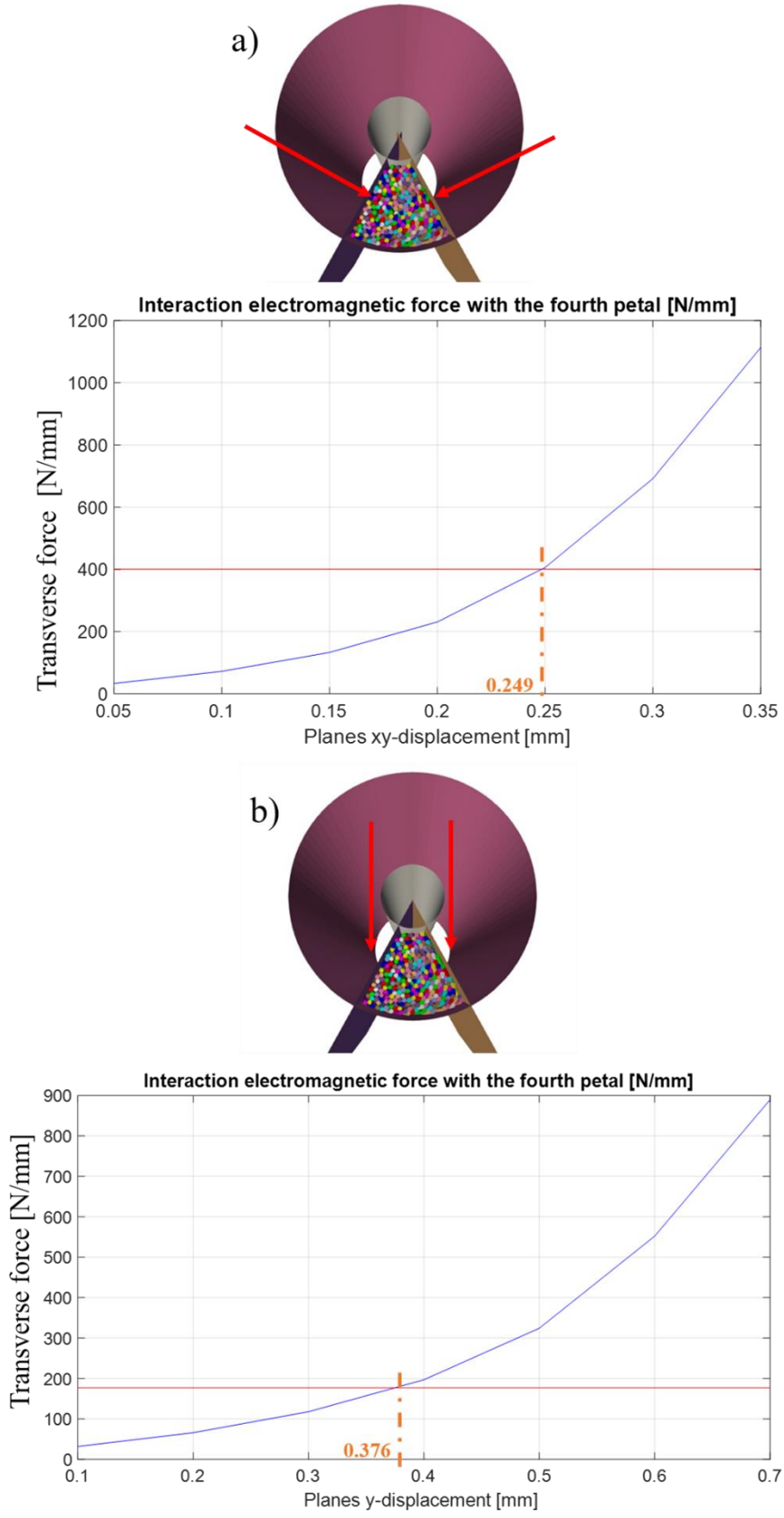

Figure III.2.22. (a) Implementation of the RM in MULTIFIL and (b) implementation of the FM in MULTIFIL.

III.2.4 Conclusion

The main contribution of this work to the fusion cables modelling relies on new upgrades of the code itself in collaboration with the developer of the code D. Durville, but also on the development of analytical models in support to the numerical modelling, like for example the equilibrium jacket-cable. Thanks to these improvements, this Ph.D. was able to provide more reliable and important results on the mechanical behavior of the fusion cables. Next chapter provides the details of how the various steps of a fusion cable lifecycle are simulated, considering all the upgrades described in this chapter.

III.3 CHAPTER – FUSION CABLES MULTIFIL SIMULATION PROTOCOL

The different upgrades and improvements, introduced in the previous chapter, allowed the definition of a specific numerical protocol to simulate the main phases of a fusion Nb_3Sn cable life. The protocol foresees several numerical steps alternated with analytical studies to support and provide parameters to the numerical simulations.

The following sections describe the handling of each step of the protocol reported in Figure III.3.1.

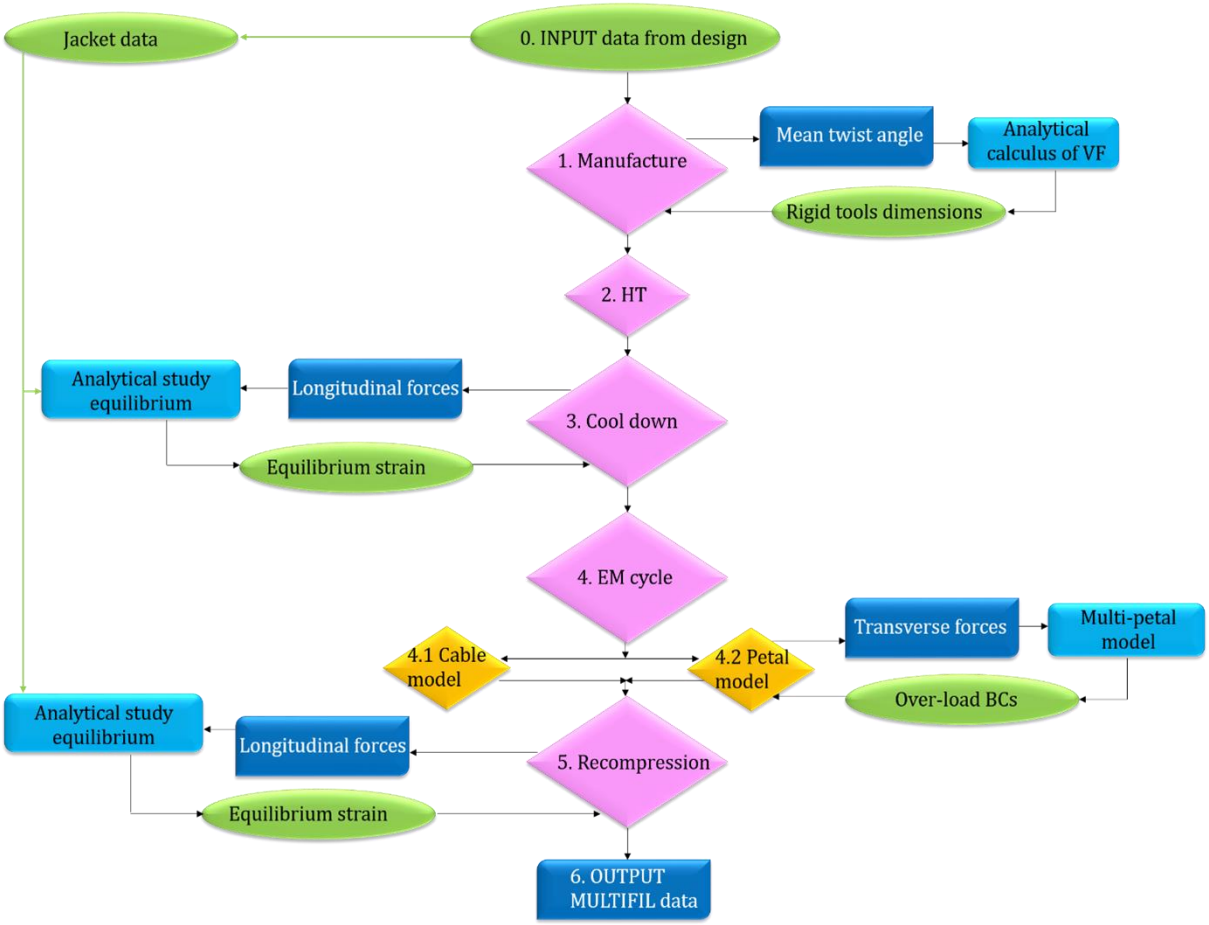

Figure III.3.1. Numerical protocol of the fusion cable simulation with MULTIFIL code.

III.3.1 Numerical protocol - STEP 1: Manufacture

The first phase of the conductor life to be simulated is the manufacture. So first, the design geometry of the cable has to be defined, like the cabling stages number and sub-elements, the twist pitches and the void fraction (VF). From this, the code computes the initial theoretical multi-twisted helical trajectories of the wires, which are then compacted into the final design shape using rigid tools. The compaction is one of the most delicate phases of the whole simulation, because the code can easily diverge. In particular, a different strategy is used depending on the final shape of the cable and if the model relies on the full cable or petal model. Each case is here presented and recommendations for a successful manufacture simulation are given. Although the methods and pieces of advice given here are specific to MULTIFIL simulations, other codes might encounter similar numerical instabilities that might be treated in the same way.

III.3.1.1 Straight single petal model

The single petal model is shaped thanks to two planes and two cylinders if the conductor design foresees a cooling channel and wrappings, as shown in Figure III.3.2.

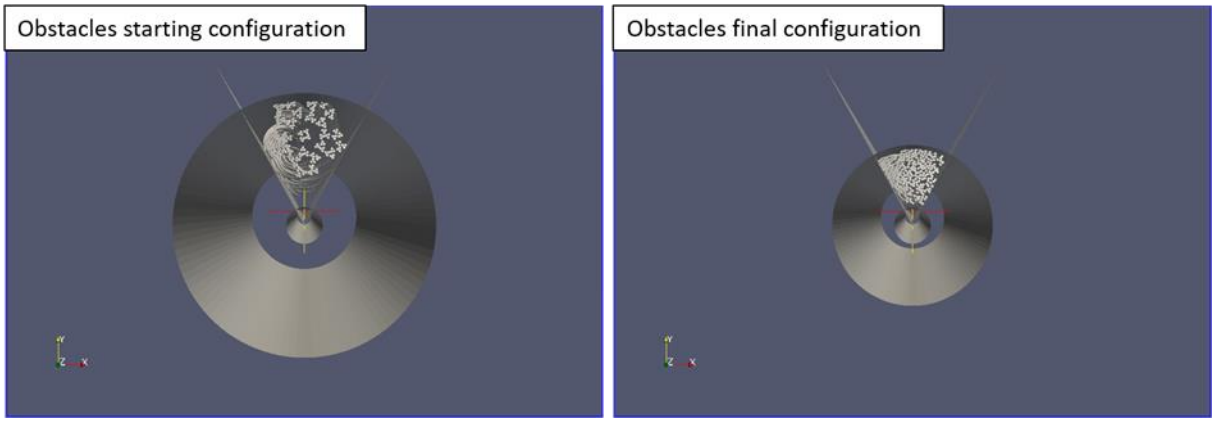

Figure III.3.2. Straight single petal model compaction simulation.

The central channel is set to the real spiral diameter, the planes have an angle corresponding to the design one (here 60 degrees), while the external cylinder is bigger than the real final jacket diameter. This initial diameter is chosen according to the initial wires assembly theoretical diameter, and then it is progressively reduced according to the reduction factor (*reduct_factor*) until its design value, by following the recursive formula:

$$S_{tool}^{n+1} = (1 - reduct\_factor) S_{tool}^{n}. \quad \text{(III. 19)}$$

The *reduct_factor* is extremely important for the convergence. At the beginning of the compaction, the contacts between the rigid tools and the wires have to be created. This phase is delicate and a small *reduct_factor* of about 0.01 is used. After few numerical steps it can be increased until 0.02 or even 0.04. Moreover, in order to facilitate the convergence at the beginning a little interpenetration of about a wire radius between the

tools and the cable is necessary, while the BCs lock most of the degrees of freedom of the hierarchical levels to impede untwisting of the stages.

The final cylinder radius R_{ext} is slightly different from the design one, in order to have a simulated cable with the design VF, because MULTIFIL does not take into account the cable external wrappings. Hence, when the cylinder diameter achieves the real cable dimension, the mean twist angle $\cos\vartheta$ is calculated based on the MULTIFIL trajectories and so the VF is found using the following formula, where R_{wire} and R_{spiral} are the wire and spiral radius respectively:

$$VF = \frac{\pi R_{ext}^2 - \pi R_{spiral}^2 - \frac{N_{wires}\pi R_{wire}^2}{\cos\vartheta}}{\pi R_{ext}^2 - \pi R_{spiral}^2}. \qquad \text{(III. 20)}$$

The equation (III.20) provides the diameter of the MUTLIFIL cable as a function of the design VF. Figure III.3.3 reports a schematic drawing on the calculation of the twist angle and the set of equations (III.21) provides the average twist angle.

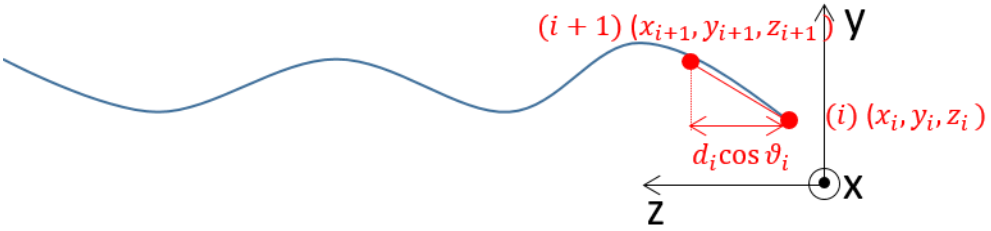

Figure III.3.3. Calculation of the local twist angle referring to two nodes on a generic wire trajectory.

$$\begin{aligned} \cos\vartheta_i &= \frac{z_{i+1}-z_i}{d_i} = \frac{z_{i+1}-z_i}{\sqrt{(x_{i+1}-x_i)^2+(y_{i+1}-y_i)^2+(z_{i+1}-z_i)^2}} \\ \langle\cos\vartheta\rangle_k &= \frac{1}{L_{strand}}\sum_{i=1}^{n_{nodes,strand}-1}\Delta L_i\cos\vartheta_i \\ \langle\cos\vartheta\rangle &= \frac{1}{n_{strands}}\sum_{k=1}^{n_{strands}}\langle\cos\vartheta\rangle_k \end{aligned} \qquad \text{(III. 21)}$$

Another consideration to prevent the simulation from diverging is the correct use of the average BCs exposed in paragraph III.2.1.5. The recommendation is to start with an almost completely locked configuration and then to release progressively translations and rotations of sub-stages hierarchical levels while keeping an overall cable average locked configuration.

III.3.1.2 Twisted single petal model

To shape a single petal with a helical trajectory, the previous observations are still applicable. At the same time, a further model fine-tuning has to be done. For the straight petal, during shaping, only the outer cylinder moves by reducing its diameter. In this case, it is necessary to start with larger helix radius and twist pitch with respect to the final

configuration. The protocol starts with a longer petal twist pitch (twice longer than the nominal one) of the rigid tools and of the helical petal and then decreases during the compaction. The twisting of the petal is driven by the helical planes, so that when decreasing their twist pitch, the wires in the petal assembly follow it. This simultaneous compaction and twist of the petal is crucial in order to obtain representative trajectories and avoid buckling issues. Figure III.3.4 shows the difference of simple compaction versus coupled compaction-twisting procedure.

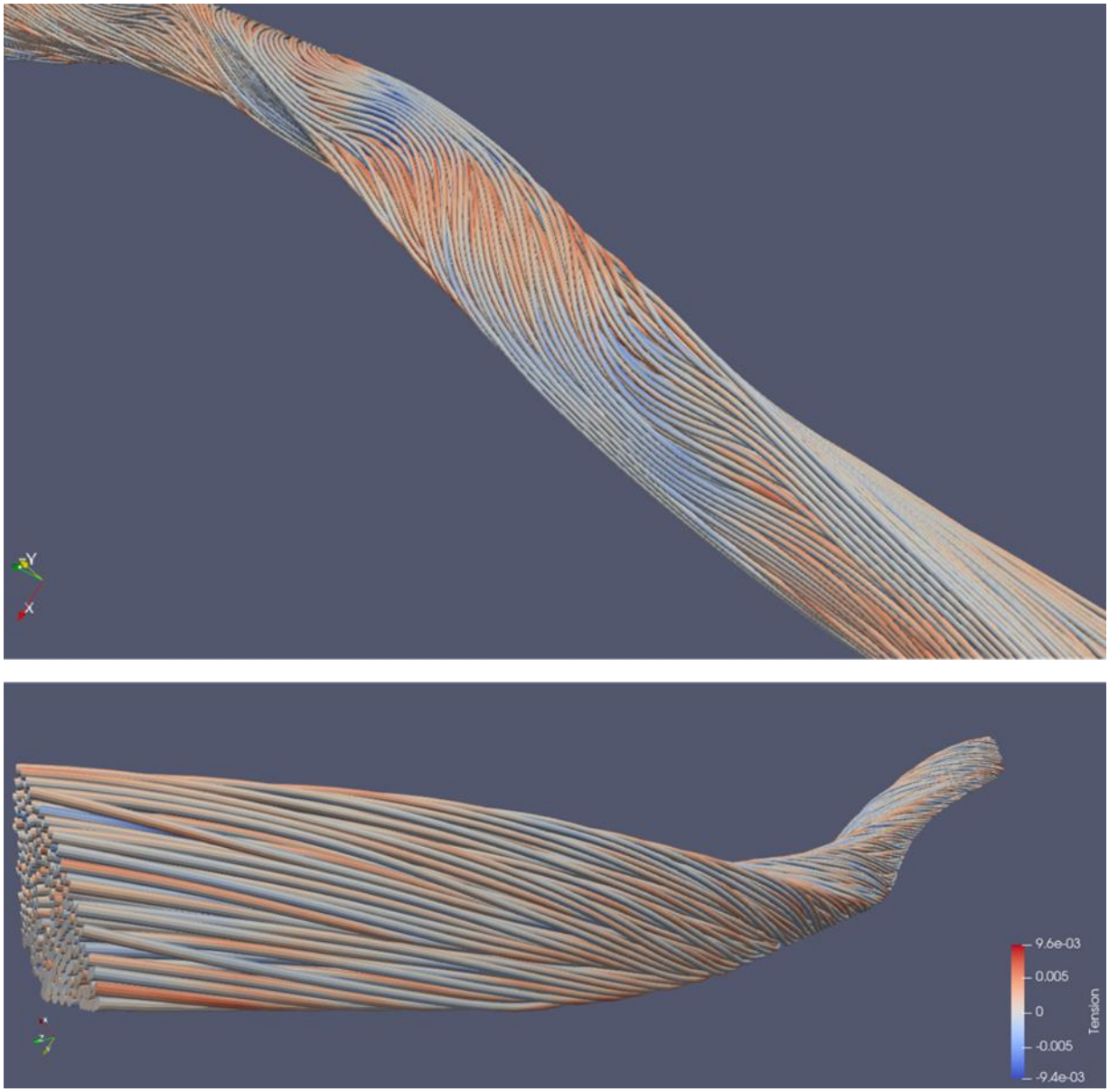

Figure III.3.4. Comparison of strain maps between the case of a simple reduction of the radius and of the planes angle (top figure) and the case of the reduction of the helix twist pitch (bottom figure).

The coupled compaction-twisting procedure involving a variable twist pitch of the helical rigid tools is needed to prevent the buckling on the extrados side of the helical petal due to the reduction of the helix radius during the outer cylinder compaction. The result aims at having an extension of the extrados strands with respect to the intrados strands.

Figure III.3.4 illustrates a more homogenous distribution of the wires on the bottom with the twist pitch reduction method.

Finally, in order to avoid detwisting of the wires during the helix twist pitch reduction, a global rotation is applied to the petal around the z-axis through the BCs that opposes to the rotation of the petal due to the variation of the twist pitch and assessed by:

$$\Delta\vartheta_z = \frac{360\,L}{N}\left(\frac{1}{TP_2} - \frac{1}{TP_1}\right), \qquad \text{(III. 22)}$$

where L is the length of the cable/petal, N is the number of steps needed to achieve the nominal helix twist pitch, while TP_1 and TP_2 are the initial and final helix twist pitches respectively.

III.3.1.3 Full cable model

The modelling of a full cable model depends on the internal cable separators. If wrapping is present between petals, the numerical protocol to be used is based on the twisted petal method, with the helix twist pitch dynamic reduction that applies to all the helical planes. However, if the cable does not have segregated petals (no wrappings), then the modelling approach to be used is based on the single straight petal without the lateral planes, taking into account a central channel if foreseen, as shown in Figure III.3.5 for the example of JT-60SA CS conductor, before and after compaction.

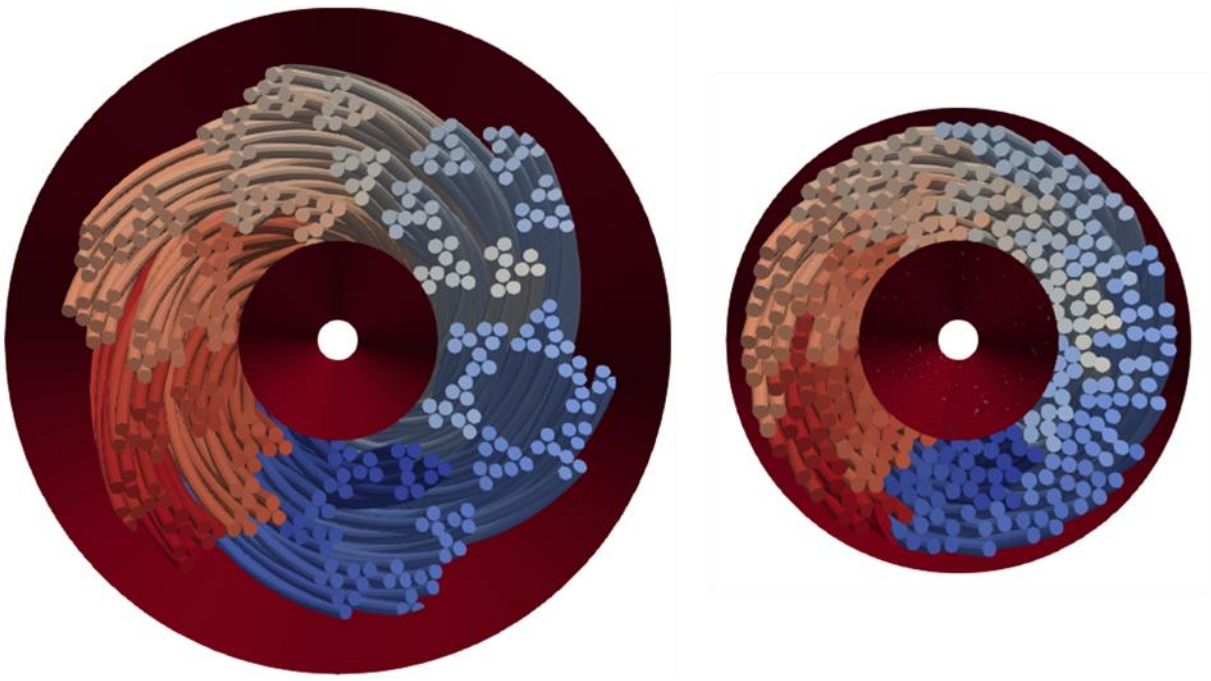

Figure III.3.5. Full cable model compaction without wrappings, example of JT-60SA CS conductor.

If the final cross-section is rectangular or square, the compaction occurs by means of a progressive displacement of the plane rigid tools imposed through the BCs. For convergence matters, some of the previous recommendations are still true, like the need for small initial interpenetration between wires and rigid tools (about a wire radius) and

for a gradual releasing of the BCs of the hierarchical levels. An example of rectangular compaction, relevant of JT-60SA TF conductor, is given in Figure III.3.6.

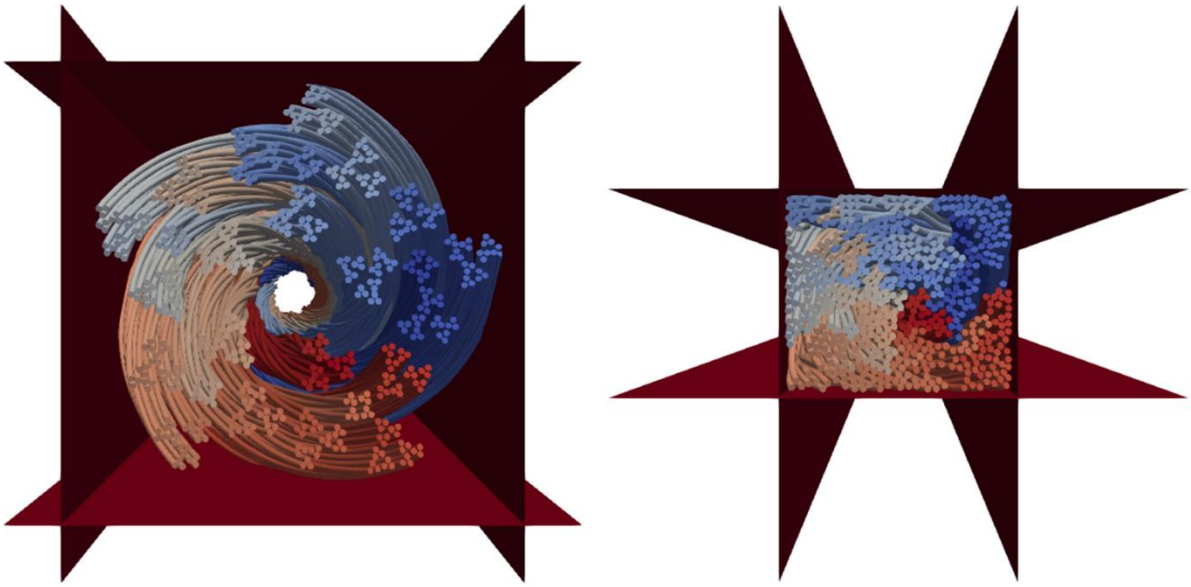

Figure III.3.6. Full cable model compaction without wrappings and square section.

Even for the square geometry, the final dimensions (base L and height h) are not exactly the ones as for the design, but they are found in order to have the design VF:

$$VF = \frac{Lh - \frac{N_{wires}\pi R_{wire}^2}{\cos\vartheta}}{Lh}. \quad \text{(III. 23)}$$

III.3.2 Numerical protocol - STEPS 2-3: HT and thermal loadings

III.3.2.1 Heat treatment

After the manufacture (shaping) simulation, the *wind & react* cables are thermally treated to create the superconducting phase. In MULTIFIL this phase is simulated by resetting the local stresses generated during the shaping phase to consider the annealing of the material occurring during the HT (Bajas 2011).

III.3.2.2 Cool-down

Once the HT is complete; a typical Nb_3Sn conductor is at 650 °C and it cools down to RT and then down to cryogenic temperature, typically 4.5 K for ITER Nb_3Sn CICC. In MULTIFIL after the HT phase, the cable is axially compressed to simulate the thermal differential contraction between cable and stainless-steel jacket by moving one end of the cable, when the other is fixed. The total longitudinal strain applied to the cable will be called in the following sections *applied strain* ε_{app}. As anticipated in paragraph III.2.3.1,

the final ε_{app} is determined using the analytical equilibrium between the jacket and the cable. This method considers the mismatch between theoretical stainless steel jacket thermal contraction and Nb_3Sn (material thermo-mechanical properties from (Mitchell 2005b)), so that the tensile load from the jacket (analytical) and the compressive load from the cable (MULTIFIL simulation) are equal at equilibrium strain. To find the equilibrium strain some recommendations are here reported. The starting point of the curves corresponds to the freestanding thermal contraction of materials from HT temperature to 4.2 K (taken from (Mitchell 2005b)). For example, when considering Nb_3Sn and a stainless steel independently, the initial thermal contraction mismatch at 4.2 K between the two materials is –0.79 % as shown in Figure III.3.7.

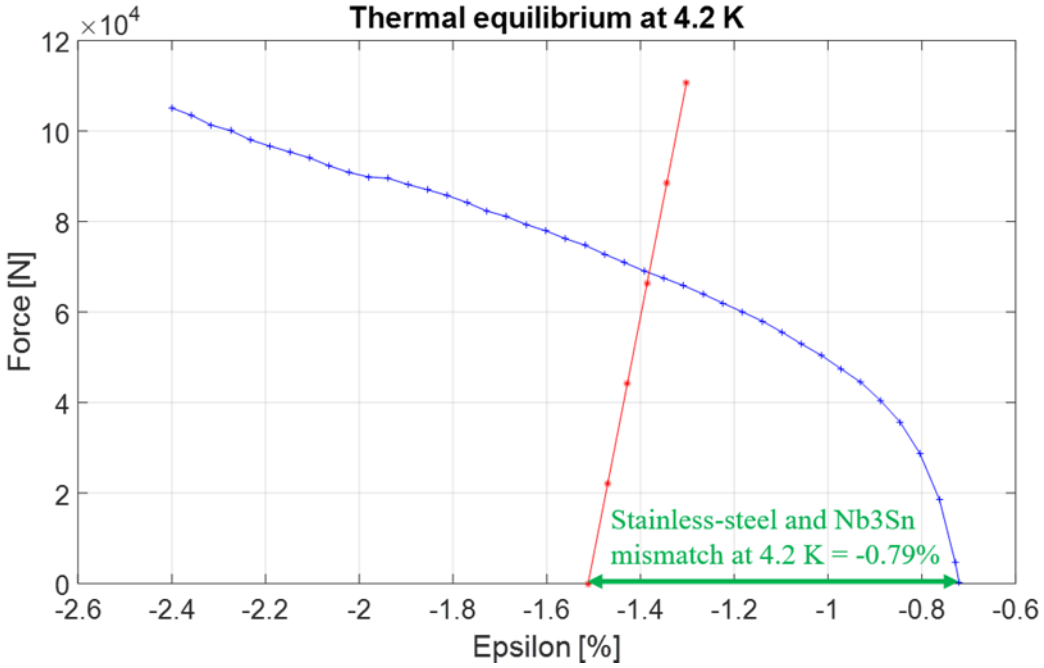

Figure III.3.7. Initial mismatch at 4.2 K due to the different thermal contraction between the SS jacket and the Nb_3Sn cable.

It is worth to be mentioned that a SULTAN configuration is here considered, since the thermal equilibrium is provided by the only presence of the jacket and the cable. In real coils, the reaction force of the jacket is supposed to be a vertical line because of the mechanical support offered by the magnet steel structure.

As explained in paragraph III.2.3.1 the same method is used when a WUCD is simulated. In this case, the jacket tensile curve and the new equilibrium at 300 K or at 80 K have to be found.

III.3.3 Numerical protocol - STEPS 4-5: EM cycles (+recompression)

After the CD simulation, the electromagnetic loadings can be applied. MULTIFIL allows the application of a Lorentz force orthogonal to the wires trajectories uniformly

distributed over the cable length, so it is usually expressed in N/mm. Typically, for an ITER TF cable in SULTAN with 68 kA and 10.78 T and homogenous current distribution among strands, the EM load is about 0.89 N/mm on each superconducting strand.

For the single petal model, this simulation step is more complex than for the full cable model since the over-load due to the presence of the other petals has to be considered. Following the general method presented in paragraph III.2.3.2, before applying the EM forces, the BCs to consider the over-load have to be found. Therefore, an EM cycle at 0 N/mm force is performed while the planes are moved according to the RM or FM. This step permits to define the global displacement to impose during the EM cycle simulation to have a global effort on the planes corresponding to the one associated to the around petals. Once the multipetal displacement contribution is found, the real EM cycle can be performed with both the application of the Lorentz force by MULTIFIL and the planes displacement. For the full cable model this step is of course not necessary.

As anticipated in paragraph III.2.3.1, the jacket-cable equilibrium is a physical condition that should be maintained during all the main loadings simulation steps. This is why after the EM loading, the longitudinal reaction force of the cable is compared to the virtual jacket reaction load, and an axial recompression is eventually performed to account for the softening of the cable. This additional step is called *recompression* and it is needed for all models and designs.

III.3.4 Conclusion

This chapter presented the numerical protocol, elaborated in the framework of this Ph.D. project, to which a MULTIFIL user may refer for the correct simulation of typical fusion cables. The protocol foresees several numerical steps, intermediate analytical steps supporting the numerical modelling as well as specific steps to simulate either sub-cables or full cables.

III.4 CHAPTER – COUPLING WITH ELECTROMAGNETIC MODELS

MULTIFIL provides the local strain map over the strands trajectories in a simulated cable as output information. The major goal of the Ph.D. thesis was to improve the mechanical simulation of the fusion cables for a better understanding of the macroscopic mechanical phenomena. Nevertheless, the evaluation of the impact of such mechanical behavior on the electrical properties of the cable is of the major interest for the cable designer or user. This chapter presents the main tools that were used to couple the MULTIFIL mechanical results to electrical models. Section III.4.1 presents analytical models and section III.4.2 a numerical approach.

III.4.1 Analytical models

III.4.1.1 HRL and LRL models

In order to predict the critical current I_c of a cable, two analytical models are used for finding the redistribution of the injected current inside the cable as a function of the simulated strain distribution (Riccioli 2019). The two models represent two limiting cases: the Low Resistivity Limit (LRL) model and the High Resistivity Limit (HRL) model. They are extrapolated from the so-called Ekin models used for strands under bending conditions. In the LRL model the current can completely redistribute among strands, since the interstrand transverse electrical resistivity is considered null. This implies a constant electric field in each cable cross-section. In the HRL model, an infinitive resistivity impedes the redistribution of strand current, which is, hence, forced to keep flowing in the same wire.

Among the assumptions, both models consider a constant *n-value* and neglect the strands bending, taking only into account for the axial strain provided by MULTIFIL. Although it might seem an extensive simplification, it is justified if the intra-strand redistribution is deemed possible, as the case with low resistivity matrix and long filament twist pitches. Nevertheless, bending will be introduced later when considering fracture inside the strands in the analysis.

In the traditional LRL model, the electric field is constant in each cable cross-section defined by the z coordinate. Thus, the current carrying capacity of each cable cross-section can be calculated as:

$$I_{ca}(z) = \sum_k I_{ck}(z)\,, \qquad with\ locally\ I_{ck}(z) = I_{ck}\big(B(z), T(z), \varepsilon(z)\big). \tag{III. 24}$$

Then, for this longitudinal distribution of $I_{ca}(z)$, one computes the equivalent cable critical current I_{caLRL} by finding the current at which the average electric field on the cable volume is E_c. The application of the superconductor power law for the single value I_{caLRL} and for the distribution $I_{ca}(z)$ leads to:

$$E_c \left(\frac{I_{op}}{I_{caLRL}}\right)^n = \int \frac{E_c}{L}\left(\frac{I_{op}}{I_{ca}(z)}\right)^n dz\,. \tag{III. 25}$$

One can see that this equation is valid for any transport current I_{op} that can be simplified if *n-value* is considered constant. The equivalent critical current for the full cable in LRL assumption I_{caLRL} can thus be extracted:

$$I_{ca_{LRL}} = \sqrt[n]{\frac{L}{\int_0^L \left(\frac{1}{I_{ca}(z)}\right)^n dz}}. \tag{III. 26}$$

This formula gives an equivalent critical current in LRL mode, but it can also, for example, provide a T_{csLRL} value by finding by dichotomy the temperature at which I_{caLRL} reaches the design transport current

For the HRL model, the current flowing in each wire is constant. For each wire of longitudinal distribution $I_{ck}(z)$ developing an average electric field E_c, the equivalent critical current of each wire I_{ck} is calculated through:

$$I_{ck} = \sqrt[n]{\frac{L}{\int_0^L \left(\frac{1}{I_{ck}(z)}\right)^n dz}}. \tag{III. 27}$$

In the HRL model, the total cable equivalent critical current is found by summing each strand I_{ck}:

$$I_{ca_{HRL}} = \sum_k I_{ck}\,. \tag{III. 28}$$

These two simplified models were implemented in MATLAB routines and provide I_c or T_{cs} boundaries for a preliminary evaluation of the electrical performance of the cable.

III.4.1.2 Multi-stages model

The aforementioned models can be generalized when the internal structure of the cable is known. Indeed, one can consider that LRL (free redistribution) is legitimate up to the triplet stage because of almost constant contact between the strands, while HRL should be applied between triplets. On the other hand, one might want to consider LRL inside a petal while keeping petals insulated from each other due to the presence of stainless-steel wrappings. The generalized multi-stage model permits to extend HRL (or LRL) to any of the cabling stages composing the cable. Of course, it does not change the fact that redistributions are either free or impeded, but it permits to give an idea of the level of redistribution needed to transport a given current. For a given multi-stage cable, $I_{c_{LRL}}^{k}$ defines the limiting case critical current for which LRL is considered up to stage k, while HRL is considered above stage k.

For the cabling stage k, N_g is the number of cabling stages and $N_b(k)$ is the number of superconducting wires in stage k. The multi-stage critical current $I_{c_{LRL}}^{k}$ is given by the set of equations (III.29):

$$\begin{cases} I_{cj}^{k}(z) = \sum_{i=1}^{N_b(z)} I_{ci}(z) & LRL\ treatment\ of\ all\ strands\ in\ each\ substage\ of\ level\ k \\ I_{cj}^{k} = K\left(I_{cj}^{k}(z)\right) & Equivalent\ critical\ current\ of\ each\ substage\ of\ level\ k \\ I_{c_{LRL}}^{k} = \sum_{j=1}^{N_g} I_{cj}^{k} & HRL\ treatment\ of\ substages\ of\ level\ k\ (between\ themselves) \end{cases} . \quad \text{(III. 29)}$$

For any $I_c(z)$ longitudinal distribution (strand or strand assembly), let K be the function that calculates the equivalent critical current over the length L:

$$I_{c_{eq}} = \sqrt[n]{\frac{L}{\int_0^L \left(\frac{1}{I_c\left(B(z), T_{cs}, \varepsilon(z)\right)}\right)^n dz}} = K\left(I_c(z)\right). \quad \text{(III. 30)}$$

Since this model generalizes HRL and LRL traditional models, it gives as expected $I_{c_{LRL}}^{1} = I_{c_{HRL}}$ and $I_{c_{LRL}}^{6} = I_{c_{LRL}}$ if referring to the ITER TF CICC structure. Thanks to this approach is possible to probe, for a given cable configuration, what level of redistribution is needed to carry a given transport current.

III.4.2 Numerical model with THELMA code

The *Thermal-Hydraulic-Electro-Magnetic* (THELMA) code was originally developed jointly by Politecnico di Torino (for the thermo-hydraulic part), University of Bologna (for the electromagnetic model of the conductor) and University of Udine (for the electromagnetic modeling of the joint) (Ciotti 2006). It was developed in order to analyze the thermohydraulic and electrodynamic transients in superconducting cables. In the

framework of this Ph.D. work, only the electromagnetic part of the code, which underwent several developments since its initial version, has been used (Breschi 2008). The weak coupling with the MULTIFIL code has been realized by implementing in the THELMA code the strain maps computed with the mechanical MULTIFIL code, so as to compute a numerical value of the T_{cs}.

The code splits the cable into *N_ce* cable elements (*CE*) that can correspond to single strands or groups of strands. The unknowns of the problem are the current values in each *CE*. In general, the current in each *CE* is assumed to be uniformly distributed in its cross-section and it is a function of a spatial coordinate ζ, which corresponds to the curvilinear coordinate of the cable axis (see Figure III.4.1). However, for the coupling with MULTIFIL, a different model was considered, which is explained in (Breschi 2012b). In this model, the CEs correspond to strands, but the current is not assumed uniform in the strand cross section. Instead, the strand is split into 8 sectors to which a given value of strain is attributed, that is derived from the MULTIFIL computation. The 8 sectors are assumed in parallel, so that the electric field is the same for all sectors. The relation between the total current in the strand (which is the unknown of the THELMA model) and this unique value of electric field is derived by computing the local current redistribution between the 8 sectors in parallel.

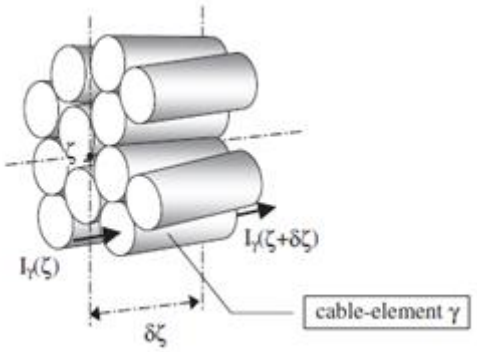

Figure III.4.1. Illustration of the spatial coordinate ζ for the *CE* when it represents a strand. (Ciotti 2006)

MULTIFIL provides nine values of strain per node for all the strands. In particular, one value corresponds to the value on the axis while the other eight values are computed on the periphery as shown in Figure III.4.2. More precisely, MULTIFIL provides the outer strains at a radius corresponding to 0.90825 times the radius of the wire, hence the values have to be corrected to be taken at the wire radius.

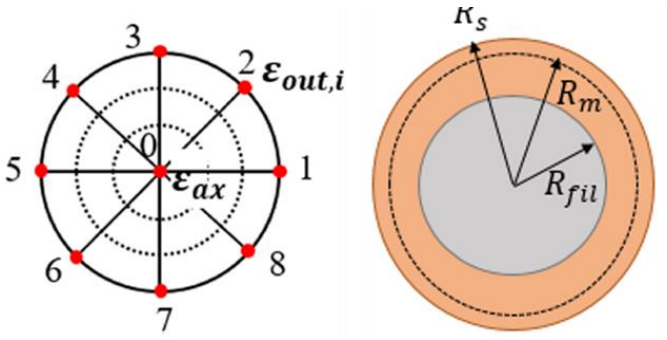

Figure III.4.2. MULTIFIL OUTPUT strains location on the wire cross-section.

The work (Breschi 2012b) already coupled THELMA with MULTIFIL by considering two different methods to account for the strain distribution in the THELMA strand cross-section. The first method assumes a uniform strain distribution on the cross-section and equals to the strain on the strand axis. The second one divides the cross-section into 8 sectors and a value of the strain is associated to each sector. In this second case, two models were considered. One model directly associates the outer value of strain to the whole sector, while the other associates to each sector an average value between the strain on the axis and the one on the periphery, assuming a linear variation of the strain with the radius.

In the present work, a different approach was used to couple the codes. This method associates to each sector of the wire cross-section an effective strain computed by integration of the critical current density over the filamentary section as a function of the strain, which varies linearly with the radius. Hence, in this work the strain varies linearly with radius over the cross-section as shown:

$$\varepsilon(r) = \varepsilon_{ax} + r\frac{\varepsilon_m - \varepsilon_{ax}}{R_m}. \tag{III.31}$$

The radius varies from the axis to the strand radius R_s, passing through the MULTIFIL radius R_m. To find the effective strain ε_{eff}, the critical current density has to be integrated for each sector i=1,…,8:

$$\begin{cases} \int_{A_{fil,i}} Jc_{Non-Cu}\big(B,T,\varepsilon_i(r)\big)dA = Ic_{s,i} \\ with\ \varepsilon_i(r) = \varepsilon_{ax} + r\dfrac{\varepsilon_{m,i} - \varepsilon_{ax}}{R_m} \end{cases}. \tag{III.32}$$

The filamentary area A_{fil} does not carry all the current and strand area A_s is given by the sum between the copper area A_{Cu} and the Non-Cu area A_{Non-Cu}. The ratio between these two areas gives the Cu/non-Cu volume ratio χ. Therefore, equation (III.32) can be rewritten as:

$$\langle Jc_{Non-Cu}\rangle = \frac{1}{A_{Non-Cu}}\int_{A_{Non-Cu}} Jc_{Non-Cu}dA \Rightarrow Ic_{Non-Cu} = \langle Jc_{Non-Cu}\rangle \frac{A_s}{1+\chi}. \quad \text{(III. 33)}$$

The present dissertation focuses on the OST IT-wires for which the Non-Cu area can be completely considered inside the filamentary area. Therefore:

$$\begin{cases} \int_{A_{fil}} Jc_{Non-Cu}dA = Ic_s \\ A_{fil} = A_{Non-Cu} \end{cases} \Rightarrow \pi {R_{fil}}^2 = \frac{\pi {R_s}^2}{1+\chi} \Longrightarrow R_{fil} = \frac{R_s}{\sqrt{1+\chi}}. \quad \text{(III. 34)}$$

Once the critical current is found for each sector *i*, the effective strain $\varepsilon_{eff,i}$ is found by the following expression: $Ic_{s,i} = Ic(B, T, \varepsilon_{eff,i})$.

The scaling law used for the calculations is the one in the plot reported in Figure III.4.3. An average peak field of 11 T was considered and the critical current limits of –1% and 0.8 % in terms of strain. (Dylla 2016) shows that the filaments completely fracture when a 0.8 % tensile strain is applied, therefore a pessimistic situation is here considered.

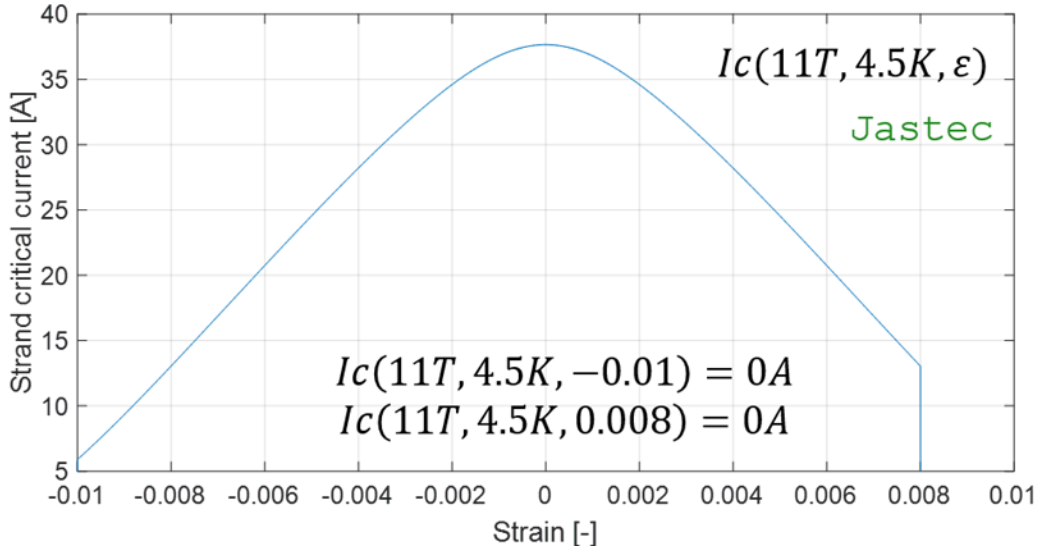

Figure III.4.3. Jastec ITER scaling law used for the MULTIFIL-THELMA data coupling.

The result of such integration provides for each sector of each wire an effective strain, which is included in the range from the strain on the axis and the strain on the filamentary radius, as shown in Figure III.4.4.

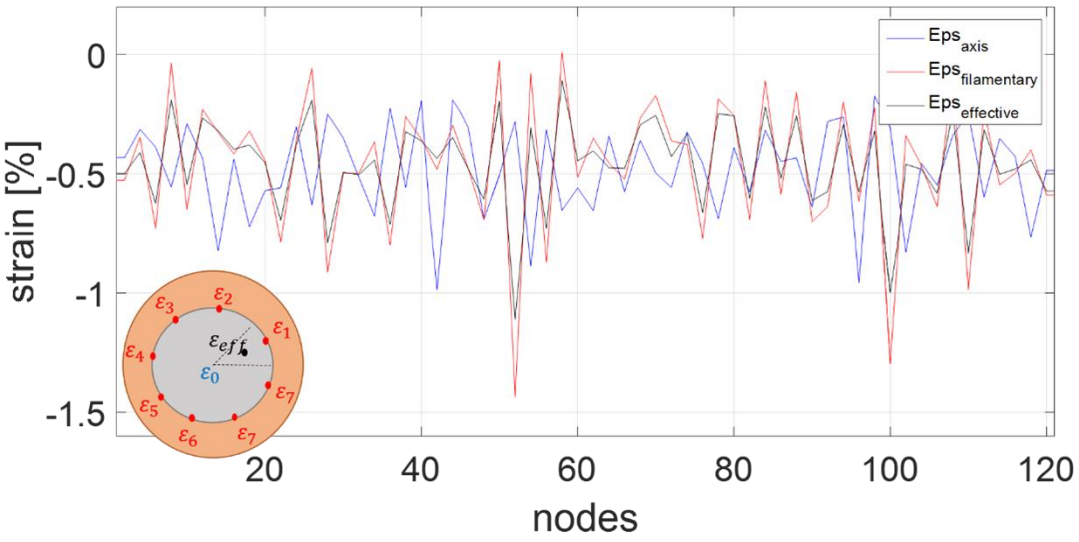

Figure III.4.4. Effective, axial and peripheral strains plot.

Moreover, specific MATLAB routines have been developed to provide to THELMA the coordinates and the corresponding strain values.

III.4.3 Conclusion

The numerical and analytical assessment of critical current and current sharing temperature is an important information for the evaluation of the conductor performance. This chapter introduced the tools that were used during this Ph.D. work to see the impact of the mechanical state on the electrical parameters.

Part IV of the dissertation presents the studies performed by applying this protocol and the promising results that were obtained.

IV. FOURTH PART – SIMULATIONS & ANALYSES

LIST OF SYMBOLS

A_{fHRL}	$[mm^2]$	Broken filamentary area with HRL current distribution
A_{fLRL}	$[mm^2]$	Broken filamentary area with LRL current distribution
B	$[T]$	Magnetic field
$cos\vartheta$	$[-]$	Mean twist angle
Cu	$[-]$	Copper
Cr	$[-]$	Chrome
d_{str}	$[mm]$	Strand diameter
E_0	$[MPa]$	Young's modulus at 0.2 % unloading
$Fract/m$	$[-]$	Fractures number per meter
$Fract/m/cycle$	$[-]$	Fractures number per meter and cycle
F_z	$[N]$	Longitudinal reaction force
Nb_3Sn	$[-]$	Niobium-three-Tin
N_{nodes}	$[-]$	Nodes number
N_{str}, N_s	$[-]$	Strands number
r_s	$[mm]$	Strand radius
R_f	$[mm]$	Filamentary radius
S_{cable}	$[mm^2]$	Annular cross-sectional surface of cable
$S_{strands}$	$[mm^2]$	Strand cross-sectional surface
T	$[K]$	Temperature
T_c	$[K]$	Critical temperature
T_{cs}	$[K]$	Temperature of current sharing
V_{tot}	$[m^3]$	Total volume
V_{str}	$[m^3]$	Strand volume
y_{lim}	$[mm]$	Y limit along the y-axis on the strand cross-section
α	$[-]$	Remaining unbroken superconducting area ratio
α,β,γ	$[-]$	Fitting parameters
ε	$[-]$-$[\%]$	Strain
ε_a, ε_{ax}, $EpsA$	$[-]$-$[\%]$	Axial strain
ε_{ap}	$[-]$-$[\%]$	Applied strain
ε_{ax}^{el}, ε_{el}, $EpsA_{el}$	$[-]$-$[\%]$	Elastic strain on strand axis
ε_{ax}^{pl}, ε_{pl}, $EpsA_{pl}$	$[-]$-$[\%]$	Plastic strain on strand axis
ε_b	$[-]$-$[\%]$	Bending strain
ε_{irr}	$[-]$-$[\%]$	Irreversible strain
σ_z	$[MPa]$	Longitudinal stress
η^{pl}, $EtaPl$	$[-]$	Plasticity ratio
γ^b, $GammaB$	$[-]$	Bending ratio
$\emptyset$	$[°]$	Angle

IV.1 CHAPTER – STANDARDIZED POST-PROCESSING PROTOCOL MUNDA

Since MULTIFIL applied to fusion cables has reached a state of development where a more rich and various set of test cases can be modelled and analyzed, it was necessary to rationalize the analysis process defining categories and levels. Hence, an analysis protocol, called MUNDA (*MUltifil Numerical Dataset Analysis*), was developed during the Ph.D. program to extract useful indicators and parameters both quantitative and qualitative that can be used for a rather wide range of objectives:

1. Numerical or experimental cross-checks / comparisons;
2. Code Validation;
3. Definition of mechanical or geometrical trends;
4. Definition of electrical models inputs for physics coupling;
5. Standardized comparison of different conductors' models.

The list of the categories of information that can be extracted from MULTIFIL datasets, as direct or indirect data, are:

1. GEOM : Geometrical information / direct;
2. STRAIN : Local strain maps / direct;
3. C-LOAD : Contact loads / direct;
4. FRACT : Fracture / indirect;
5. ELEC : Electrical performance extrapolation / indirect.

The following sections provide a detailed description of the post-processing analysis that can be performed through the MUNDA protocol, defining all the parameters that are mentioned in the chapters of part IV. The here illustrated steps refer to the example of the ITER TF full cable model.

IV.1.1 Geometrical analysis step: GEOM

The geometry is usually analyzed after the shaping step of the simulation. Table IV.1.1 reports the main studies that are performed in the GEOM category of MUNDA.

Table IV.1.1 MUNDA steps for the geometrical analysis of the cables.

Analysis	*Short description*	*Type of analysis*

GEOM	-XSec	Plot of strands position in a cross-section. Identification of petals.	Direct	Qualitative
	-XSecCu	Plot of strands position in a cross-section. Identification of Cu and Nb_3Sn strands.	Direct	Qualitative
	-Traj3D	3D plot of strands trajectory	Direct	Qualitative
	-CosTP	Plot of the local *cos(θ)* value	Direct	Qualitative
	-CosTM	Cable average *cos(θ)* value	Direct	**Quantitative**
	-VFP	Plot of cable local void fraction	Direct	Qualitative
	-VFM	Cable average void fraction value	Direct	**Quantitative**
	-VFT	Cable angular distribution of local void fraction	Direct	Qualitative

The first two steps (-Xsec and -XsecCu) provide a direct and qualitative evaluation of the positioning of the superconducting and copper wires on a given cross-section. The first discriminates the position of the petals and permits to estimate the petals inter-penetration during shaping, and the second differentiates Nb_3Sn and Cu wires for a qualitative distribution of the copper content of the cable (example in Figure IV.1.1).

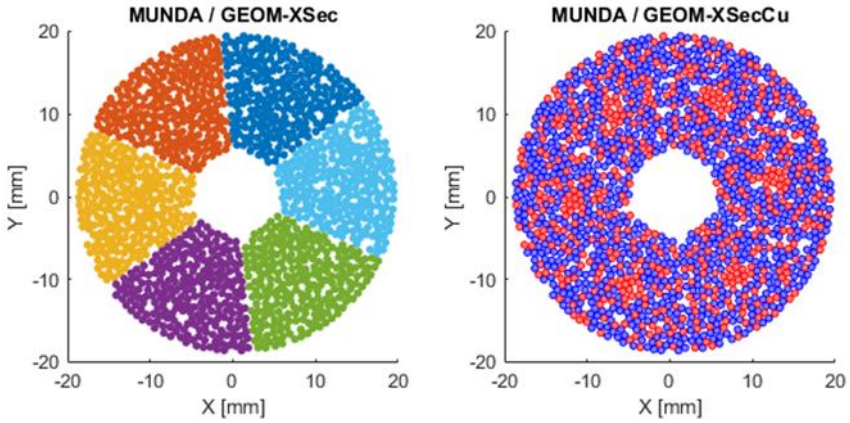

Figure IV.1.1. Petals and wires identification for the ITER TF CICC.

The third step (-Traj3D) provides a general view of the 3D trajectories, like the one in Figure IV.1.2.

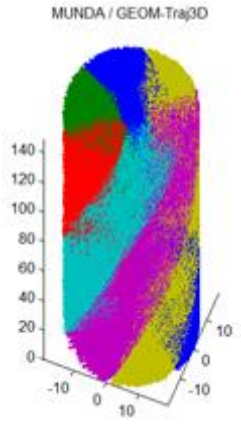

Figure IV.1.2. 3D trajectories of ITER TF CICC wires.

The fourth step (-CosTP) shows a local assessment of the twist angle (design parameter *cos(θ)*), averaged over the simulated cable length. This type of map is here called *cumulative polar map* (CPM) and it is used to understand the cross-sectional distribution of a parameter, permitting in particular to assess the impact of EM loads on this distribution. An example of CPM is reported in Figure IV.1.3. The fifth step (-CosTM) is simply the calculation of the average value of *cos(θ)* over the cable volume. The twist angle, defined as the angle between the strand trajectory and the cable axis, is an important indicator of the intertwining state of the wires inside a cable. Typically, the closer to 1, the more the wires are parallel to the longitudinal axis of the cable.

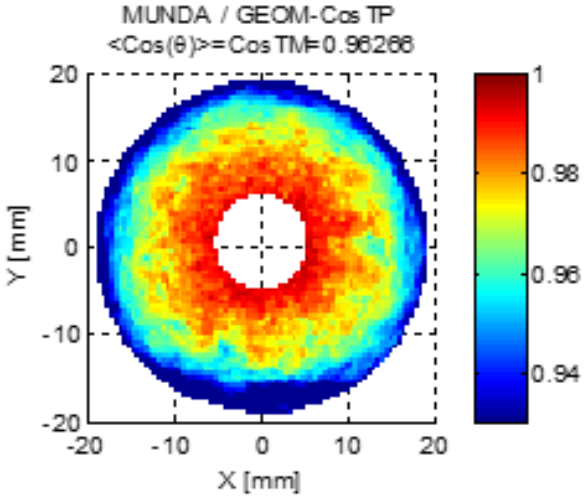

Figure IV.1.3.CPM of the twist angle for the ITER TF CICC.

The last three steps provide information on the local void fraction (VF) distribution inside the cable. On real cables, the VF is a global value that can be estimated from planimetry image analysis of the cable cross-section, but this method is usually imprecise since it relies on image thresholding. The most reliable method is based on weight and volume estimation: it calculates the volume of strands by weighting of the cable length (knowing the density of the strands and subtracting adequately the wrappings). Then, VF is calculated as $(V_{tot}-V_{str})/V_{tot}$. In case of dual-channel conductors, the void is usually calculated only in the annular domain. In a similar manner, the calculation of the local VF in the modelled CICC is based on a "volumetric assessment" of the numerical cable. The idea is to mesh the cross-section of the cable (x-y grid) and, for each mesh element, to calculate the volume of strands in the z-direction (cable longitudinal direction). This is done by counting the number of strands N_{str} located in the vicinity of the mesh element (distance of strand center to the mesh center below half of the strand diameter d_{str}) all along the N_{nodes} in the z-direction. Since this technique does not take into account the twist angle, the value obtained needs to be corrected by the average *cos(θ)*. Then, local void fraction can be deduced by:

$$VF_{loc} = \left(\frac{V_{tot} - V_{str}}{V_{tot}}\right) = \left(\frac{\pi\frac{d_{str}{}^2}{4}N_{nodes} - \left(\pi\frac{d_{str}{}^2}{4}N_{str}\right)/\langle\cos(\theta)\rangle}{\pi\frac{d_{str}{}^2}{4}N_{nodes}}\right) = \left(\frac{N_{nodes} - N_{str}/\langle cos\,(\theta)\rangle}{N_{nodes}}\right). \quad (IV.1)$$

It should be noted that this method is applicable to any trajectory defined by MULTIFIL or by any other means (geometrical code, tomography…). In equation (IV.1), a more precise assessment is made if the local *cos(θ)* is used instead of the average value *<cos(θ)>*, but this refinement has little impact on the VF map and was not included in the following analyses. An example of VF CPM is provided in Figure IV.1.4.

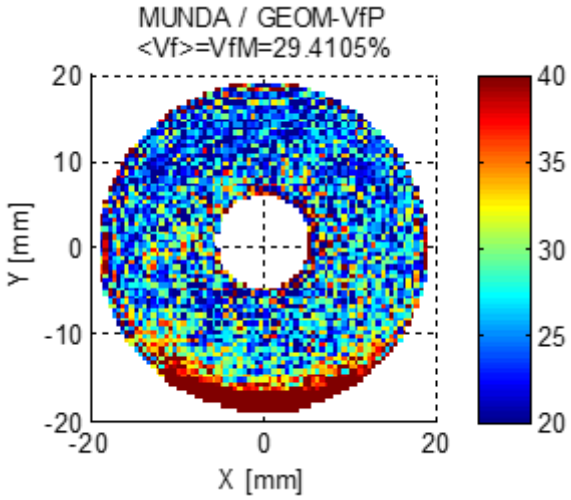

Figure IV.1.4. CPM of the local VF for the ITER TF CICC.

The analysis of local void fraction and its distribution in a numerical cable is of interest not only to cross-check design values, but it can also help to:

- See if the shape and design of the conductor (round, rectangular) permit a homogeneous distribution of the void;
- Assess the potential impact of loads on the void distribution;
- Check the gradual effect of cyclic loading on the void distribution;
- Compare with other VF estimates or measurements;
- Predict future cable VF.

IV.1.2 Mechanical analysis steps

IV.1.2.1 STRAIN

One of the main advantages of MULTIFIL simulations is the possibility to determine the local strain map over the strands in a complex configuration. As already explained in part III and illustrated by Figure III.4.2, the strain is calculated at 9 points on the strand cross-sectional surface and for each node of the wires, the axial strain ε_{ax} and the bending strain ε_b can be found. To determine the bending strain, the modulus of the

maximal outer value of strain in each cross-section has to be determined. The bending strain is then calculated as the difference between the maximum value on the cross-section and the value on the axis. Also, the outer value of strain is calculated at the filamentary radius found by equation (III.34). In this work, considering an OST IT-wire as the one presented in part II, the filamentary radius corresponds to 0.29 mm, since the Cu/non-Cu ratio is equal to 1 and the wire diameter is 0.82 mm.

In the framework of the Ph.D. work, the standardized output data of the code were refined to discriminate, at each calculation node, the elastic ε^{el} and plastic ε^{pl} components of the local strain. Thanks to this new data, it was possible to introduce a new mechanical indicator, the plasticity ratio η^{pl} defined as:

$$\eta^{pl} = \left| \frac{\langle \varepsilon_{ax}^{pl} \rangle}{\langle \varepsilon_{ax}^{el} \rangle} \right|, \tag{IV.2}$$

where $\langle \varepsilon_{ax}^{el} \rangle$ is the average elastic contribution to the strands axial strain and $\langle \varepsilon_{ax}^{pl} \rangle$ is the plastic one, i.e. $\langle \varepsilon_{ax} \rangle = \langle \varepsilon_{ax}^{pl} \rangle + \langle \varepsilon_{ax}^{el} \rangle$. The η^{pl} ratio allows one to study the level of plasticization of the cable. Moreover, another mechanical indicator introduced in the work (Riccioli 2021) is the bending ratio γ^b, given by

$$\gamma^b = \left| \frac{\langle \varepsilon_b \rangle}{\langle \varepsilon_{ax} \rangle} \right|. \tag{IV.3}$$

This parameter indicates weather the cable behaves more as a rigid bundle ($\gamma^b < 1$) or as a helical spring ($\gamma^b > 1$). In the first case, any longitudinal applied strain is converted mainly into axial strain, while in the second case it is converted into bending. These two indicators are defined to help understanding the mechanical status of the cable at various loading steps and to compare the different analyzed cables.

There is a large variety of studies and information that can be extracted from the local strain state, Table IV.1.2 reports the most relevant that were included in the standard MUNDA protocol.

Table IV.1.2. MUNDA steps for the mechanical analysis of the strain in the cables.

STRAIN	-EpsA	Averaged polar plot of axial strain	Direct	Qualitative
	-EpsAM	Average axial strain in the cable	Direct	**Quantitative**
	-EpsAel	Averaged polar plot of elastic axial strain	Direct	Qualitative
	-EpsAelM	Average elastic axial strain in the cable	Direct	**Quantitative**
	-EpsApl	Averaged polar plot of plastic axial strain	Direct	Qualitative
	-EpsAplM	Average plastic axial strain in the cable	Direct	**Quantitative**
	-EtaPl	Ratio of average plastic strain to average elastic strain	Direct	**Quantitative**
	-EpsB	Averaged polar plot of bending strain	Direct	Qualitative
	-EpsBM	Average Bending strain in the cable	Direct	**Quantitative**

	-GammaB	Ratio of average bending strain to average axial strain	Direct	**Quantitative**
	-Expo	EpsB(EpsA) plot of strands exposure to extreme tension or compression.	Direct	Qualitative

The cumulative polar maps can be plotted for all the aforementioned kinds of strain and a quantitative evaluation is provided by their average values. Examples of such maps are shown in Figure IV.2.6.

Finally, the curve of the ε_b as a function of the ε_{ax} provides a qualitative information on the exposure of the strands in the simulated cable to extreme tensile (above 0.2%) or compressive (below 1%) strains. Such a plot can indeed easily show and discriminate between cables with a high risk of fracture and another which is adequately protected by its compressive state. The example reported in Figure IV.1.5 shows two cable models results, only differentiated by a small parameter change (friction coefficient). The one on the left is clearly more exposed to fracture (above the green line) than its counterpart on the right.

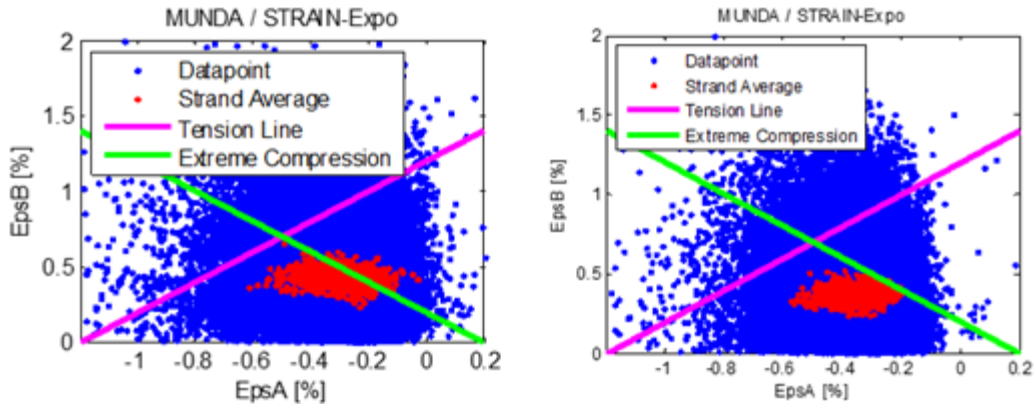

Figure IV.1.5. Axial strain-bending strain plots to assess the risk of filaments fracture exposure for two cables only differing for the friction coefficient.

IV.1.2.2 C-LOAD

The study of contacts between strands is important for both the strand current redistribution capacity as well as for the analysis of the AC losses, since they are directly linked to interstrand electrical resistances (Nijhuis 2004), (Yagotintsev 2019). This is why a quantitative and qualitative analyses of the contactsare included in the standard MUNDA protocol. Table IV.1.3 presents the information about the contacts analyses.

Table IV.1.3. MUNDA steps for the mechanical analysis of the contacts in the cables.

CLOAD	-CloadP	Averaged polar plot of perpendicular contact forces	Direct	Qualitative
	-CloadPM	Average perpendicular contact force	Direct	**Quantitative**
	-CloadT	Averaged polar plot of tangential contact forces	Direct	Qualitative
	-CloadTM	Average tangential contact force	Direct	**Quantitative**
	-Cwidth	Contact width distribution	Indirect	**Quantitative**

The tangential and normal forces characterizing the contacts are a direct information provided by MUTLIFIL output data. However, all normal contact forces below 5 N were ignored, since (Bajas 2011) showed that below 5N, the print on the wire (deflection) is small and to avoid a bias in the contacts distributions linked to low force "numerical contacts" that are generated by MULTIFIL but not relevant of a real cable. Figure IV.1.6a), from (Bajas 2011), shows a negligible depth of the print *d* for 5 N, while Figure IV.1.6b) provides an example of print on a Nb_3Sn wire under 25 N due to the pinching of the strands in contact and the depth is about 0.05mm.

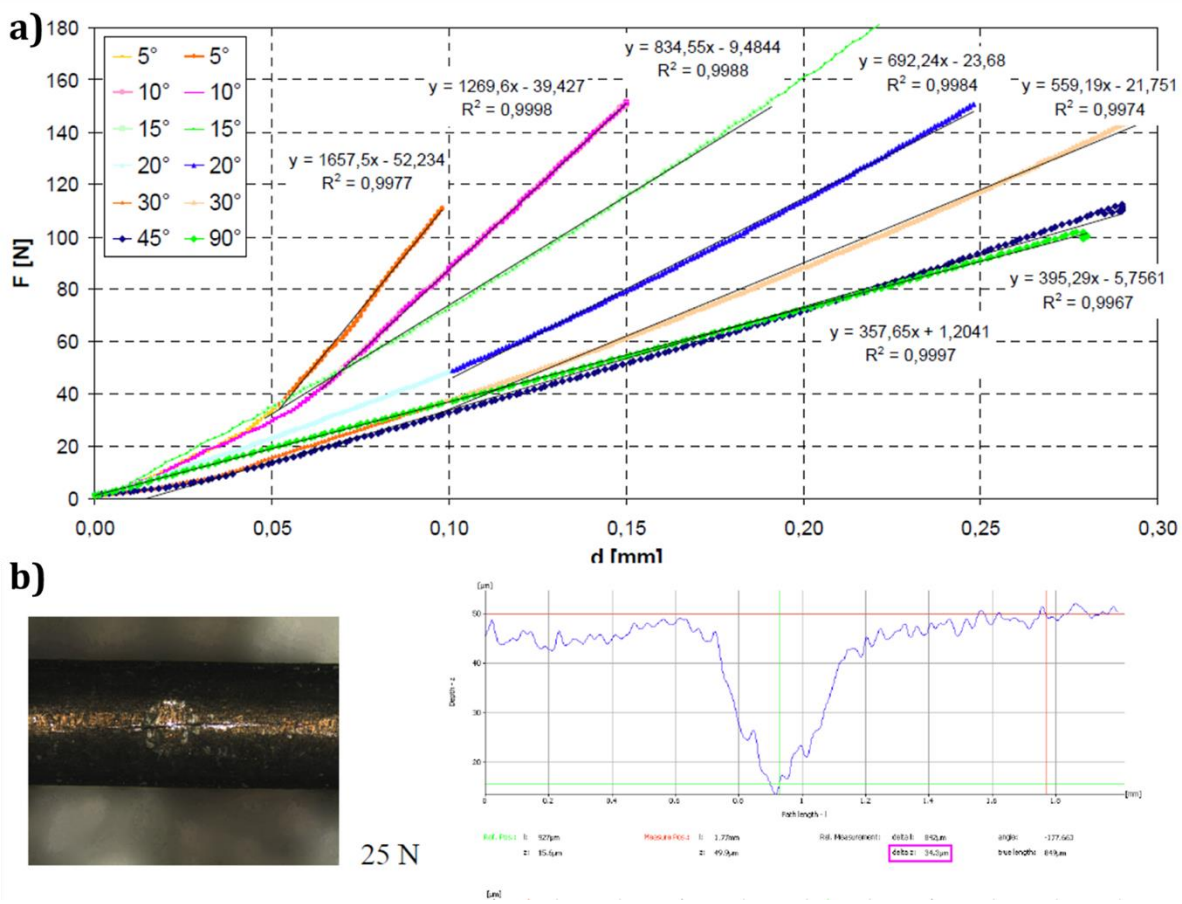

Figure IV.1.6. a) Correlation between the normal force and the print depth as a function of the wires crossing angle from (Bajas 2011). b) Left: print on a Nb_3Sn wire for a 25 N normal force. Right: measurement of the depth of the print by optical method.

The tangential contact force is a fraction of the normal one and in this case, it was decided to neglect the forces below 2 N. The cumulative polar plots are provided for these forces to highlight the zones with stringer contacts in the cables, an example is reported in Figure IV.1.7.

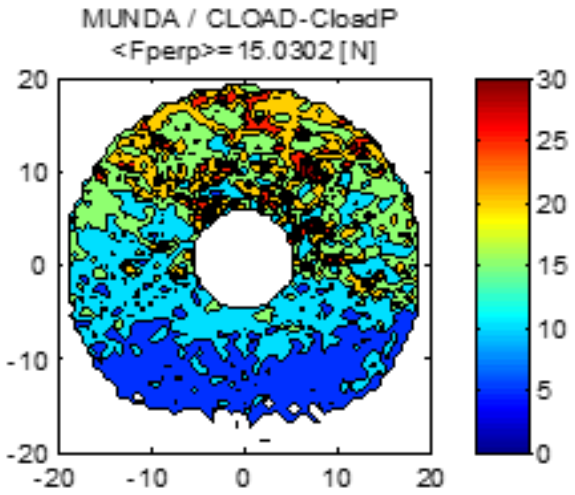

Figure IV.1.7. CPM of the normal contact forces for the ITER TF CICC at the electromagnetic peak.

Another important information about the contacts is their width distribution, since it is a data directly comparable with experimental analyses, like for example the micro-tomography presented in (Zani 2021). Differently from the contact forces, the contact widths are not a direct result from MULTIFIL. The calculation of contact widths in MULTIFIL datasets uses a mechanical criterion based on the crossing-strands experiments of (Bajas 2011). Using these experiments results, a general fit of the force-depth relation as a function of the crossing angle of the wires at the contact was deduced and plot in Figure IV.1.8.

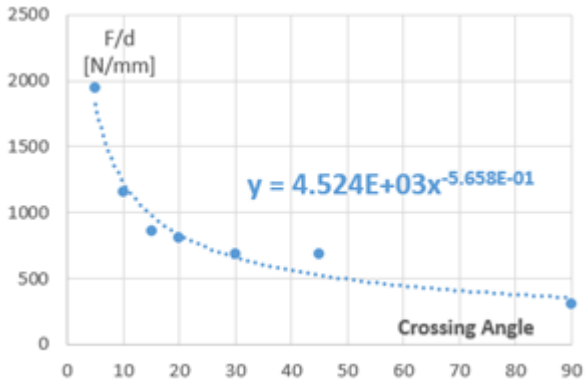

Figure IV.1.8. Normal contact force – print depth ratio as a function of the wires crossing angle at the contact point.

Then the width distribution can be plotted knowing from MULTIFIL the contact force and wires crossing angle for each contact.

IV.1.3 Electrical analysis step

IV.1.3.1 FRACT

The filaments fractures directly affect the current carrying capacity of the wires. MULTIFIL only represents the 1-D longitudinal beam behavior of the wire without the detailed information about the filaments. Therefore, in order to quantify the occurrence

of filaments breakage, two models are here proposed: LRL and HRL models, already proposed in section III.4.1 to define the inter-strand current redistribution and here applied to the filaments breakage (intra-strand).

The strain is supposed to vary linearly in the cross-section of the wire from $\varepsilon_a - \varepsilon_b$ to $\varepsilon_a + \varepsilon_b$. Thus, for a given irreversible strain ε_{irr}, one can define the limit coordinate y_{lim} at which $\varepsilon > \varepsilon_{irr}$ (in the local coordinate system of the wire where y is in the same direction as the bending):

$$y_{lim} = (\varepsilon_{irr} - \varepsilon_a)\frac{R_f}{\varepsilon_b}. \tag{IV.4}$$

Two different fractured filamentary areas can be identified, depending on the limiting case for current redistribution inside the strand, by the following set of equations:

$$\begin{aligned} Af_{LRL} &= \frac{{R_f}^2}{2}(\phi - \sin(\phi)) \\ Af_{HRL} &= \pi\left({R_f}^2 - {y_{lim}}^2\right) \end{aligned}. \tag{IV.5}$$

The equations assume that for the LRL model the fracture area has only local impact, and does not affect current carrying capacity of sections before or after the crack. The fractured surface is here limited to the Af_{LRL} illustrated in Figure IV.1.9 (right draw). On the contrary, the HRL model implies that the fractured area impedes current carrying in all filaments exposed to ε_{irr}, wherever in the strand that fracture happened. The fractured surface is here described as the crown of radius y_{lim}, since the current cannot redistribute in this model. Figure IV.1.9 report a schematic drawing of the fractured areas in the two models.

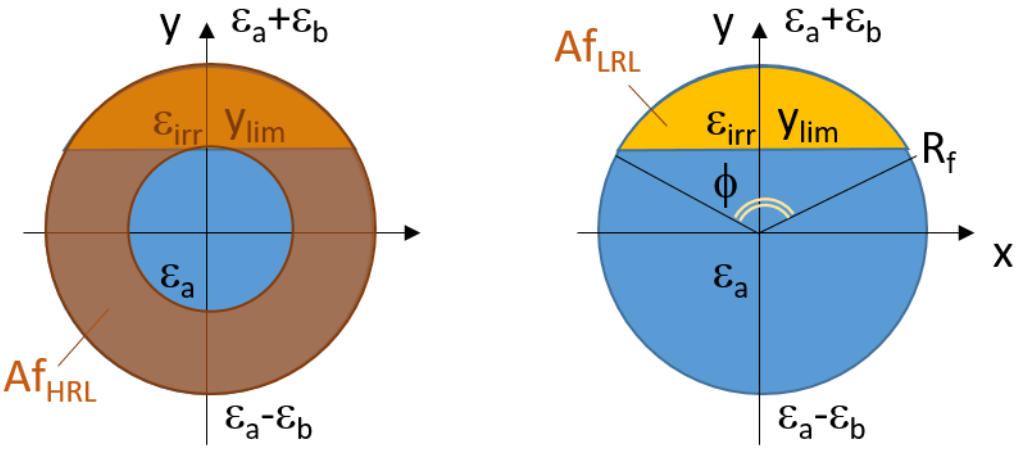

Figure IV.1.9. HRL and LRL filaments fracture models.

If α is the remaining valid superconducting surface, then the fractured surfaces ratio in the two models are:

$$\begin{aligned} 1-\alpha_{LRL} &= \frac{\frac{{R_f}^2}{2}(\phi-\sin(\phi))}{\pi {R_f}^2} \\ 1-\alpha_{HRL} &= \frac{\pi\left({R_f}^2-{y_{lim}}^2\right)}{\pi {R_f}^2} \end{aligned} . \quad \text{(IV. 6)}$$

The HRL fracture model gives a quite larger affected surface than LRL. The comparison of fractured area versus y_{lim} is shown in Figure IV.1.10 and gives an illustration of the difference between the two models.

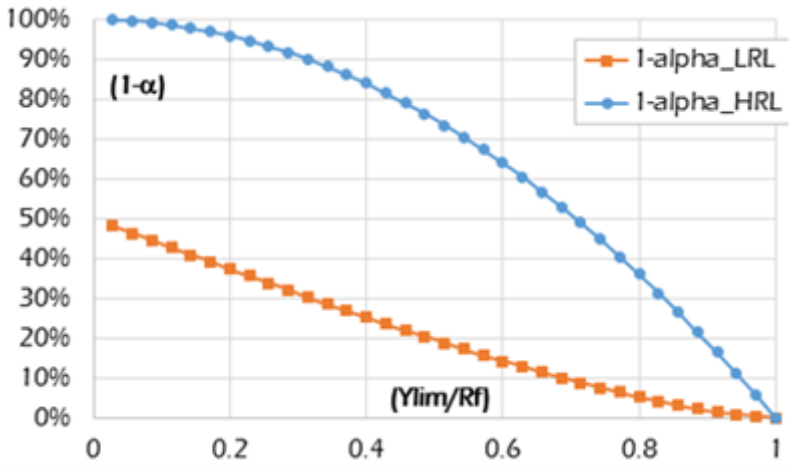

Figure IV.1.10. Assessment of the impact of the fracture model on the percentage of fractured filament area.

Although HRL model might seem like overly pessimistic, let recall that in the CPM, the average y_{lim} (not the maximum) along the z-direction is used in the equations above, which means that the strand is almost continuously broken at this level. In this sense, it is not that pessimistic to think that between two nodes (around 1-2 mm in z-direction), the current cannot be transferred adequately to neighboring filaments.

Usually, if not differently specified, the ε_{irr} is equal to 0.2 %. The study (Dylla 2016) shows that the strain-to-failure of the OST Nb_3Sn filaments follow a probability distribution and the 12 % of filaments fractures at 0.2 % of strain. So, to consider a 0.2 % of irreversible strain is a conservative assumption.

Table IV.1.4 provides the list of the main plots that can be found in the next chapters.

Table IV.1.4. MUNDA steps for the electrical analysis of the fractures in the cables.

FRACT	-FractLRLP	Polar plot of fractured cross-section fraction (in LRL assumption): $(1-\alpha_{LRL})$. Unfractured cross-section ratio is sometimes labelled α.	Indirect	Qualitative
	-FractLRLM	Average value of fractured cross-section fraction (in LRL assumption): $(1-\langle\alpha_{LRL}\rangle)$	Indirect	**Quantitative**

	-FractHRLP	Polar plot of fractured cross-section fraction (in HRL assumption): $(1-\alpha_{HRL})$. Unfractured cross-section ratio is sometimes labelled α.	Indirect	Qualitative
	-FractHRLM	Average value of fractured cross-section fraction (in HRL assumption): $(1-<\alpha_{HRL}>)$	Indirect	**Quantitative**

Figure IV.1.11 reports an example of CPM for the assessment of the fractures on the cross-sectional area after cool-down (CD).

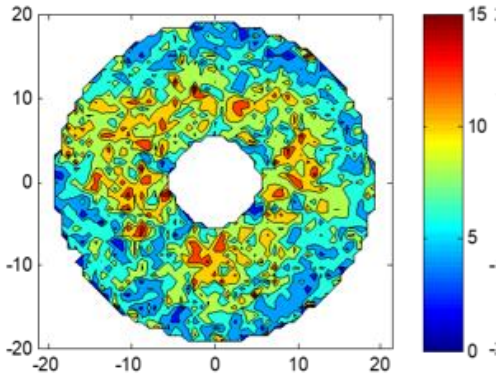

Figure IV.1.11. CPM of fractures for the ITER TF CICC after CD.

IV.1.3.2 ELEC

The last level of MUNDA couples the electrical analytical models presented in section III.4.1 to the MULTIFIL mechanical results for an indirect assessment of the critical current. The filament fractures rely on the HRL model, for the calculation of the critical current. Only the axial strain is considered, an average temperature of 6.5 K (close to a typical ITER TF SULTAN sample T_{cs} (Breschi 2017)) and an average magnetic field of 12 T are used for the calculation according to typical values of the ITER TF SULTAN campaigns (Breschi 2017).

Table IV.1.5. MUNDA steps for the electrical analysis of the critical current in the cables.

ELEC	-IcHRLStag	Limiting cases for I_c of the cable with insulated sub-stages (staged-HRL approach). Standard treatment of intra-strand breakage is HRL.	Indirect	**Quantitative**
	-IcMap-StrHRL	Polar cross-section plot of averaged I_c over z-direction. I_c is calculated at (*B,T,EpsA*), and intra-strand I_c is affected by standard HRL-Breakage.	Indirect	Qualitative
	-I/IcMap-StrHRL	Polar cross-section plot of averaged I/I_c over z-direction. I_c is calculated at (*B,T,EpsA*), and intra-strand I_c is affected by standard HRL-Breakage.	Indirect	Qualitative

The first level of MUNDA electrical analysis provides a definition of the critical current based on the multi-stages model presented in paragraph III.4.1.2. The parameter *IcHRLStag* represents the critical current of the cable considering that the groups of wires are insulated above a specific cabling stage. This parameter allows a qualitative comparison of the different need for redistributing current of the simulated cable.

Moreover, cumulative polar maps are proposed for the local critical current and the transport current to critical current ratio, assuming a homogeneous distribution of the transport current inside the cable.

In these plots, fracture is taken into account through the HRL model described above. These maps aim to evaluate the local critical current as a function of the local strain, highlighting the most critical zones inside the cable. An example is given in Figure IV.1.12 for the ITER TF CICC at the EM peak.

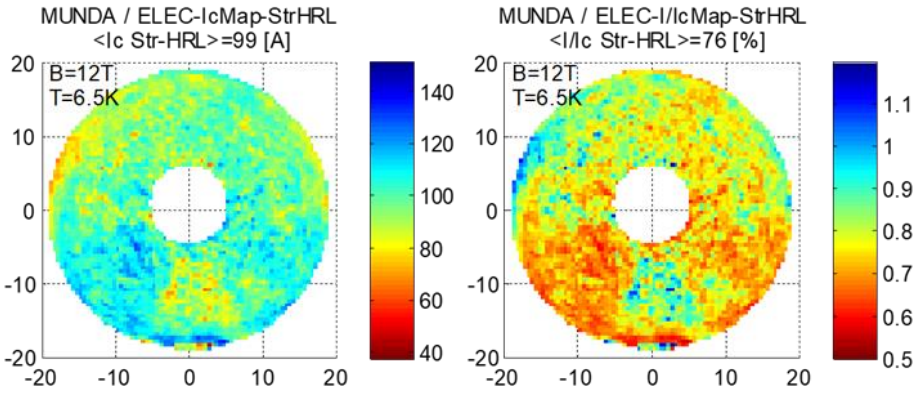

Figure IV.1.12. Left: CPM of critical current, right: CPM of transport current – critical current ratio.

IV.1.4 Conclusion

This chapter introduced key indicators and described the standard studies that were used to analyze the results of the simulations performed during this Ph.D. project. It should be noticed that in general, the cable case studies apply the full MUNDA protocol, but sometimes they skip some analyses if deemed unnecessary.

In particular, the Ph.D. investigation on fusion Nb_3Sn CICCs is based on two main kinds of study:

1. Phenomenological understanding of the macroscopic mechanical mechanisms affecting the global electrical performance degradation of the conductor;
2. Impact of the design parameters on the electromechanical behavior of the cable.

The first point is treated in chapter IV.2 by a deep analysis of the ITER TF single petal and full cable models. The second point is treated instead through parametric studies on the ITER TF single petal and full cable models and the analysis of other Nb_3Sn full cable models than the ITER TF CICC, respectively in chapters IV.3 and IV.4.

IV.2 CHAPTER – PHENOMENOLOGICAL STUDIES OF THE CYCLIC DEGRADATION

One of the main goals of this Ph.D. project was to provide a deep mechanical analysis of the ITER TF CICC and a possible explanation to the electrical degradation observed in SULTAN tests by means of the new model developed in part III. Section IV.2.1 presents the input parameters for the test cases simulations, section IV.2.2 presents the results of the single petal model and section IV.2.3 focuses on the full cable model.

IV.2.1 Test cases ITER TF input parameters

All the following studies refer to the operating conditions, or sometimes SULTAN tests conditions, of the ITER TF CICC and to its nominal design. Table IV.2.1 reports the main characteristics of the simulated models compared to the design ones.

Table IV.2.1. Main simulation parameters for the petal and full cable models compared to the ITER TF CICC design.

	ITER TF design	**Petal model**	**Full cable model**
Cabling layout	((2Nb_3Sn+1Cu)x3x5x5 +(3x4Cu))x6		
Central spiral diameter	10 mm		
Cable diameter	39.7 mm	38.44 mm	38.854 mm
Cr coated wire diameter	0.82 mm		
Wires number	1422	237	1422
Wires friction	[-]	0.1	0.1
Jacket outer diameter	43.7 mm		
Mean twist angle	0.97	0.988	0.967
Void fraction	29.7 %	29.7 %	29.8 %
Length	760 m in coil, 0.45 m high field in SULTAN	0.3 m	0.15 m
SULTAN conditions	(11.78 T, 68 kA)		

The cable dimensions differ, as explained in section III.3.1, from the simulated models to the real cable to consider the presence of the wrappings. The adding of the last twist pitch with the full cable model is fundamental to obtain the closest mean twist angle ($cos\,\vartheta$). Moreover, the simulated lengths are reduced for computational time reasons and the petal model refers to an ideal position inside the cable exposed to full EM load. Each simulation follows the numerical protocol exposed in chapter III.3.

Figure IV.2.1 reports the directions of the applied forces in the simulated petals with MULTIFIL: the Lorentz forces are perpendicular to the wires trajectories, while the thermal loading acts along the petal axis. The full cable model forces act along the same directions.

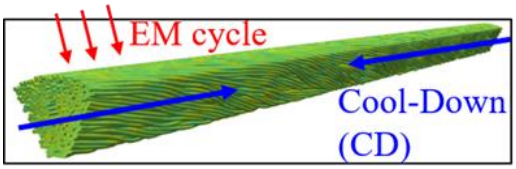

Figure IV.2.1. Forces direction in the simulated petal.

IV.2.2 Single petal model

Section III.2.3 explained the main reasons why it was necessary to have a reliable tool to simulate even the sub-scaled cable model. Thanks to the Ph.D. improvements on the model, it was possible to produce interesting results, which are presented in the following paragraphs.

IV.2.2.1 Mechanical results

Figure IV.2.2 reports the plot of the axial and bending strains after the CD simulation for all the nodes for each strand over the longitudinal axis of the petal.

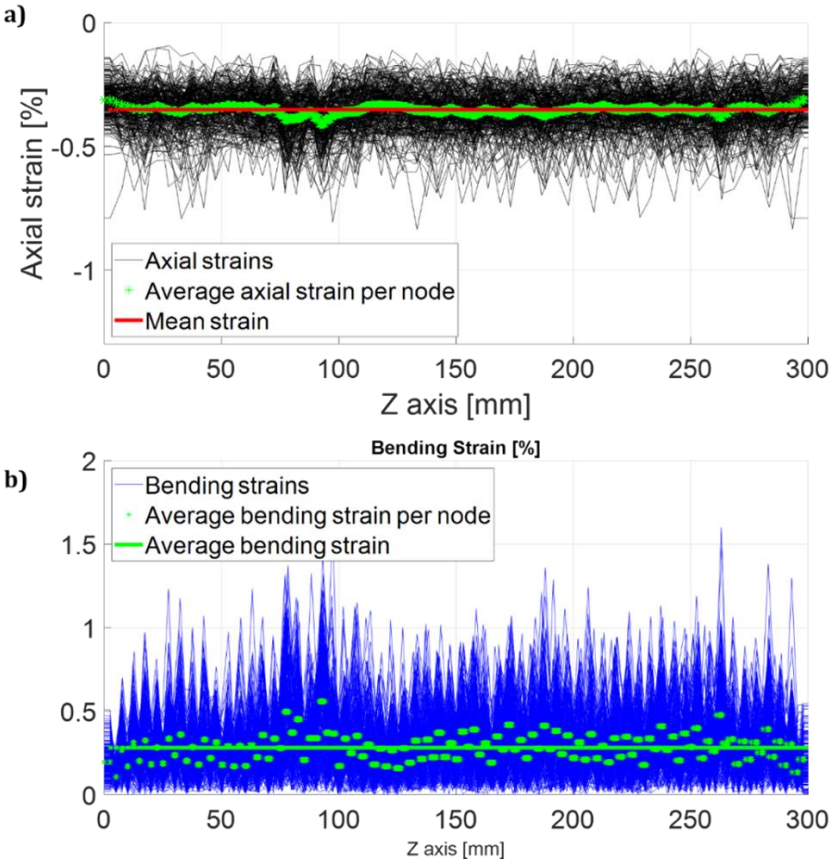

Figure IV.2.2. a) Axial strain plot over the longitudinal axis of the petal after CD; b) bending strain plot over the longitudinal axis of the petal after CD.

The plot shows that the range of the axial strain distribution is included between –0.1 % and –0.8 %. Some peaks exceed the maximal values of strain the material can withstand, which could lead to filament fractures. These maxima however represent rather localized peaks, as can be observed in Figure IV.2.2a), which shows the strain values on the axis of each strand (black line) and their average value among all strands at each node (red line). Figure IV.2.2b) presents the bending behavior highlighting a consistent flexional strain acting on the wires that translates in buckling, which is in accordance with what was observed for the Long Twist Pitch (LTP) configuration adopted for the TF cables. This phenomenon is in fact practically absent for conductors wound with Short Twist Pitches (STP), as shown in (Torre 2011).

Table IV.2.2 reports some of the parameters presented in chapter 0 for the CD and some EM cycles. The global average axial strain after the 1st EM cycle is consistence with the strain distributions determined in (Calzolaio 2013) through an indirect method based on T_c measurements for the EUTF7 sample tested in SULTAN. The values for the other tested samples vary in a range from –0.34 % to –0.42 %. However, the standard deviation of the distributions in (Calzolaio 2013) differs from the bending values that can be associated to the width of a strain distribution.

Table IV.2.2. Mechanical parameters of the nominal case petal model under the main loadings.

Loading	ε_{ap} [%]	ε_{ax} [%]	ε_b [%]	γ^b [-]	ε_{pl} [%]	ε_{el} [%]	η^{pl} [-]
CD	–0.638	–0.352	0.282	0.80	–0.247	–0.105	2.35
1st EM cycle	–0.059	–0.389	0.309	0.79	–0.394	0.0056	70.45
4th EM cycle	–0.0255	–0.398	0.331	0.83	–0.416	0.0185	22.5
7th EM cycle	–0.0085	–0.399	0.340	0.85	–0.420	0.020	21

Figure IV.2.3 reports typical strain values at each of the 8 outer locations and on the axis for a given strand after the cool-down simulation. As expected, the strain distribution at each cross-section is distributed around the value of the strain on the axis.

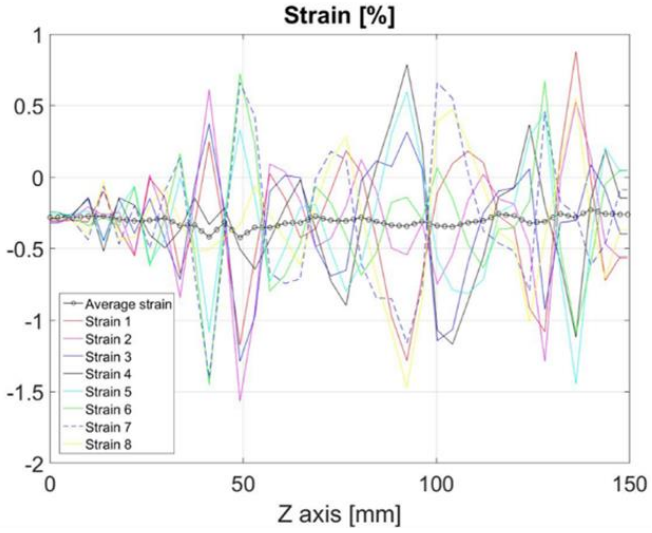

Figure IV.2.3. Strain distribution along the axis (black) and at the 8 surface locations (color) of one selected strand of the 300 mm long TF CICC petal modelled with MULTIFIL. The results refer to the CD simulation from 923 K to 4.5 K (Riccioli 2019).

As mentioned before, the plastic/elastic contributions to the total strain were analyzed during the present Ph.D. work. This step was fundamental in the understanding of unexpected behaviors as the one shown in Figure IV.2.4, where the axial strain before and after the EM cycle is almost the same. At first sight it would seem that the local effect of the EM loading only slightly affects the local strain map, but thanks to the analysis of the plastic strains, it was possible to highlight the real impact of the EM forces.

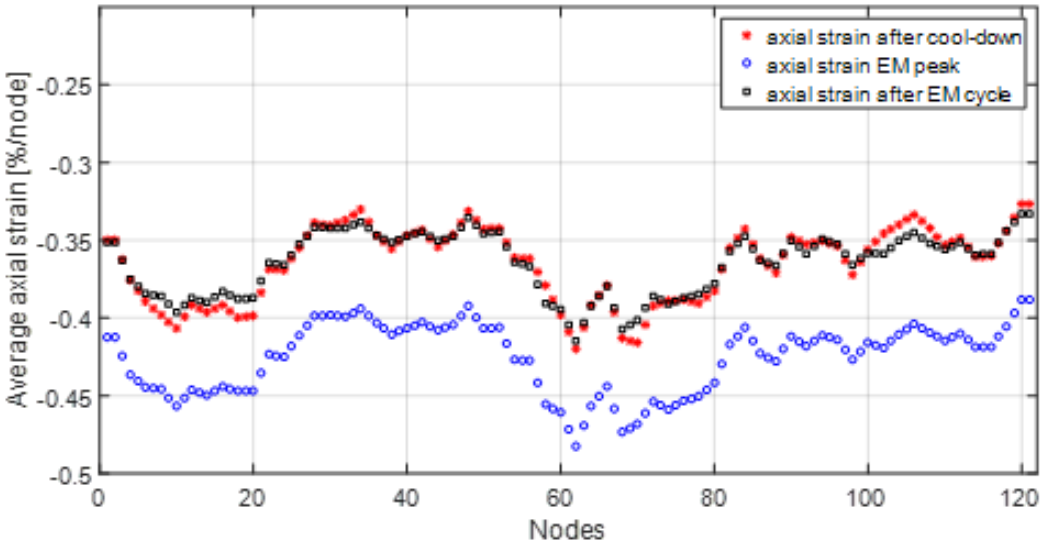

Figure IV.2.4. Plot of the average axial strain per node after CD (red), at the EM peak (blue) and after EM release (black) without recompression.

The information that is used as a method to evaluate the macroscopic behavior of the cable is the longitudinal reaction force F_z, which corresponds to the resultant force along the z-axis at the model extremities. This force can, for example, be used to obtain the macroscopic (homogenized) rigidity of the cable: the stress σ_z is calculated as F_z/S_{cable}, where S_{cable} is the cross-sectional surface of the annular part of the cable.

Figure IV.**2.5** reports the longitudinal reaction force of the petal when submitted to some loadings, in this specific case: one cool-down and three EM cycles. This plot corresponds to the study performed in (Riccioli 2021) for a slightly different petal test case than the one presented here. However, the reasoning reported below has a general validity.

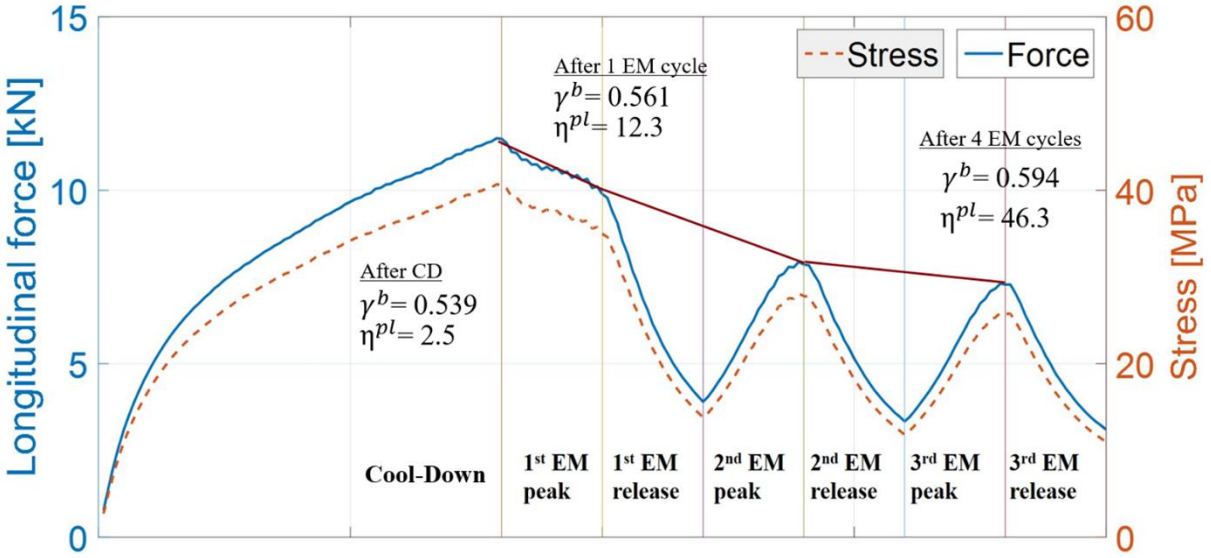

Figure IV.2.5. Longitudinal reaction force F_z and stress σ_z of the cable for the given sequence of loadings applied to the nominal case study (Riccioli 2021).

The longitudinal reaction force of the cable decreases during the application of the first EM load. Even though the average axial strain is almost the same (–0.45 %) after CD and after the first EM cycle, the plasticity ratio instead dramatically changes from 2.5 to 12.3. These results suggest that the major effect during the first EM cycle is the plasticization of the cable. Indeed, Figure IV.2.6 plots the axial strains discriminating the elastic and plastic contributions after CD and after the EM cycle. The axial strain plot highlights that the major effect of EM cycle is to release the elastic strain with a substantial compressive plasticization of the strands. This result is one of the major findings of the Ph.D. work: the effect of the EM cycles is a global softening of the cable through local plasticization of the strands.

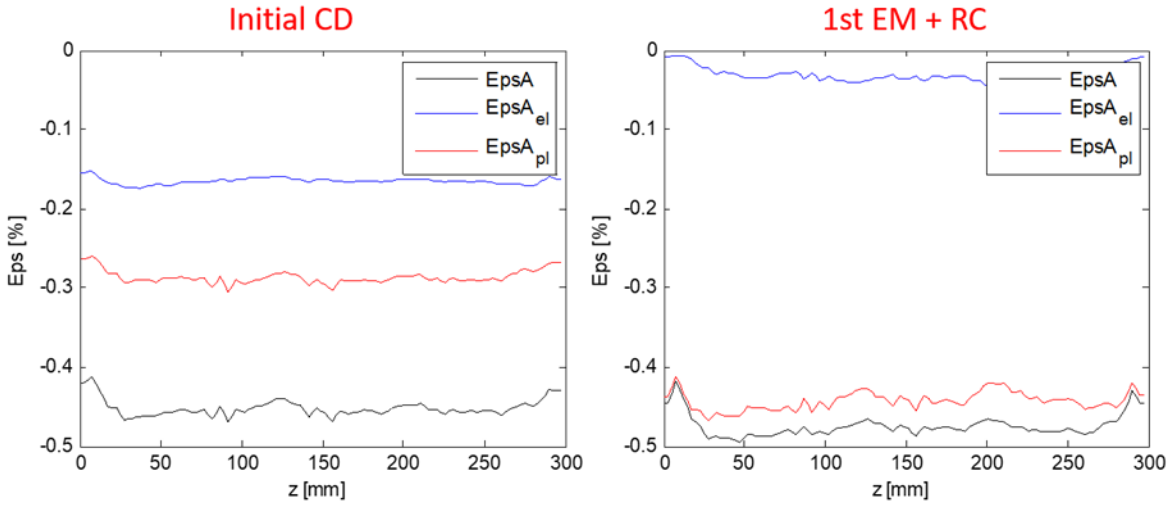

Figure IV.2.6. Plot of the average axial strain per node after CD (on the left), and after the EM cycle (on the right).

Since the longitudinal reaction force significantly decreases, it is reasonable to expect that a new equilibrium between the jacket and the cable is established. To reach

the new equilibrium, a recompression of the cable of –0.042 % is required with respect to the equilibrium found at the end of the CD. Therefore, since the cable is only slightly plasticized after the first CD, the first EM cycle results in a significant plasticization of the cable, as indicated by the η^{pl} value. A possible explanation to what is observed is that when the cable plasticizes, the jacket relaxes and gradually shifts towards its standalone thermal strain 4.2 K (~ –1.52 %). The initial equilibrium after CD is +0.18 % (tension) for the jacket and –0.61 % (compression) for the cable with respect to their standalone thermal strains at 4.2 K. This means that after CD the jacket has a "reserve" compressive strain of –0.18 % that applies to the cable during the EM cycling because of the cable's softening. The calculation shows that after ~100 EM cycles, the rest point of the jacket is reached, but the biggest change happens in the first few cycles. The progressive plasticization of the cable and corresponding relaxation of the jacket could be a possible explanation for the initial drop of the T_{cs} observed in several TF conductors (Breschi 2017).

The residual strain measurements along the jacket length on tested conductors are in good agreement with this theory. In particular, the SULTAN samples, after cycling, are cut in several points, the cable is extracted from the jacket, and the differential strain is measured (Decool 2008), (Hemmi 2012). All the studies show an almost null relaxation of the jacket in the high field zone (at full EM load), if compared to the low field zone, thus confirming that the cables are plasticized. An example of the results of this measurement is given in Figure IV.2.7 by (Hemmi 2012).

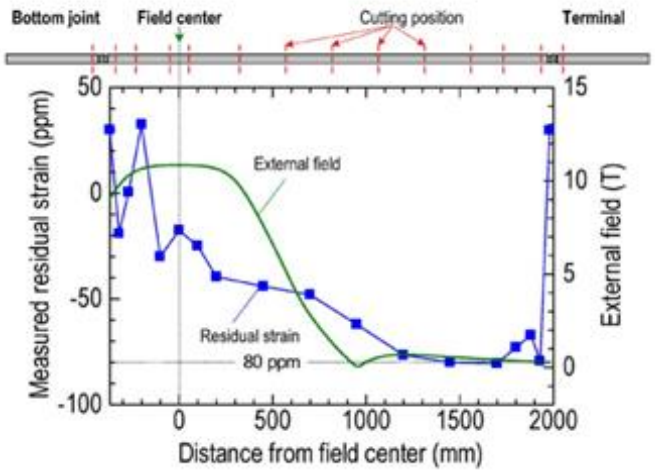

Figure IV.2.7. Residual strain on jacket after cutting JACS01 R sample at RT (Hemmi 2012).

IV.2.2.2 Electromagnetic results

An assessment of the T_{cs} was done by coupling the MULTIFIL results with the electromagnetic code THELMA and a comparison with the experimental results from (Breschi 2017) is proposed in Figure IV.2.8. In particular, three different transverse electrical resistances were tested as input parameter for the electromagnetic simulation:

$7 \cdot 10^8$ S/m^2, $7 \cdot 10^{11}$ S/m^2 (high conductance) and $7 \cdot 10^5$ S/m^2 (low conductance). A study of the AC losses is recommended to find the correct conductance that fits them and to be used in the simulation. As anticipated in paragraph III.4.2, the other assumptions of the model are: an average magnetic field set at 11 T according to the previous work (Breschi 2012b), filaments fracture at 0.8 %, LRL current redistribution between filaments.

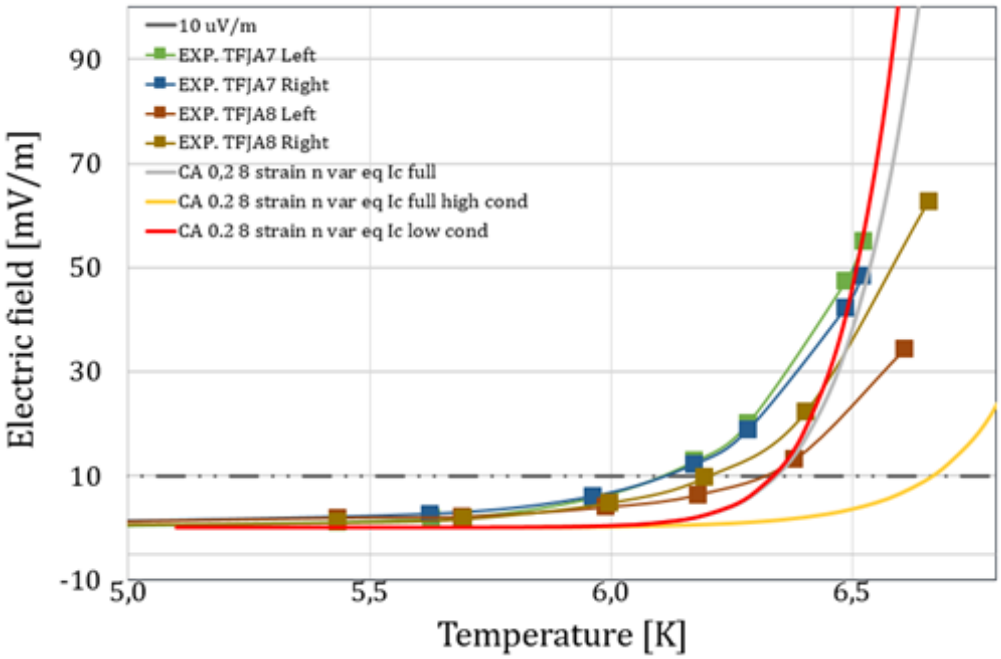

Figure IV.2.8. T_{cs} assessment with THELMA for three different conductance values.

The T_{cs} found by the petal model is quite close to the experimental measurements. Even though the EM model relies on assumptions that are recommended to be further investigated, the result achieved is already a great step with respect to the previous works (Breschi 2012b). The previous model of MULTIFIL needed to fit the THELMA output T_{cs} to find the correct thermal strain for the simulation of the CD. Thanks to the improvements on the model provided by this Ph.D. work, it is now possible to find consistent T_{cs} values without this additional free parameter.

Future works should focus on the assumptions considered in the THELMA model, like the use of a magnetic field map instead of the constant magnetic field, the correct conductance and the filaments fracture model.

IV.2.3 Full cable model

Even though the single petal model already unveiled the impact of the EM cycles on the mechanical behavior of a multi-twisted sub-cable, the scaling-up of the model was necessary for a complete analysis of the inter-petals phenomena as well as for the adequate description of cable behavior. The following paragraphs present the results and analyses for the full cable model, with a particular focus on the inter-petals behavior.

Nevertheless, some phenomena are similar to the ones observed for the single petal model and will not be detailed.

IV.2.3.1 Mechanical results

Figure IV.2.9 reports the plot of the axial and bending strains after the CD simulation for all the nodes for each strand over the longitudinal axis of the cable. For both the axial and bending strains, there is a larger spread with respect to the petals curves. This is the signature of a cable with a lot more bending, where the axial strain of the cool-down has been converted into flexion. The wires are thus closer to critical tensile strains and exposed to the risk of filaments fractures.

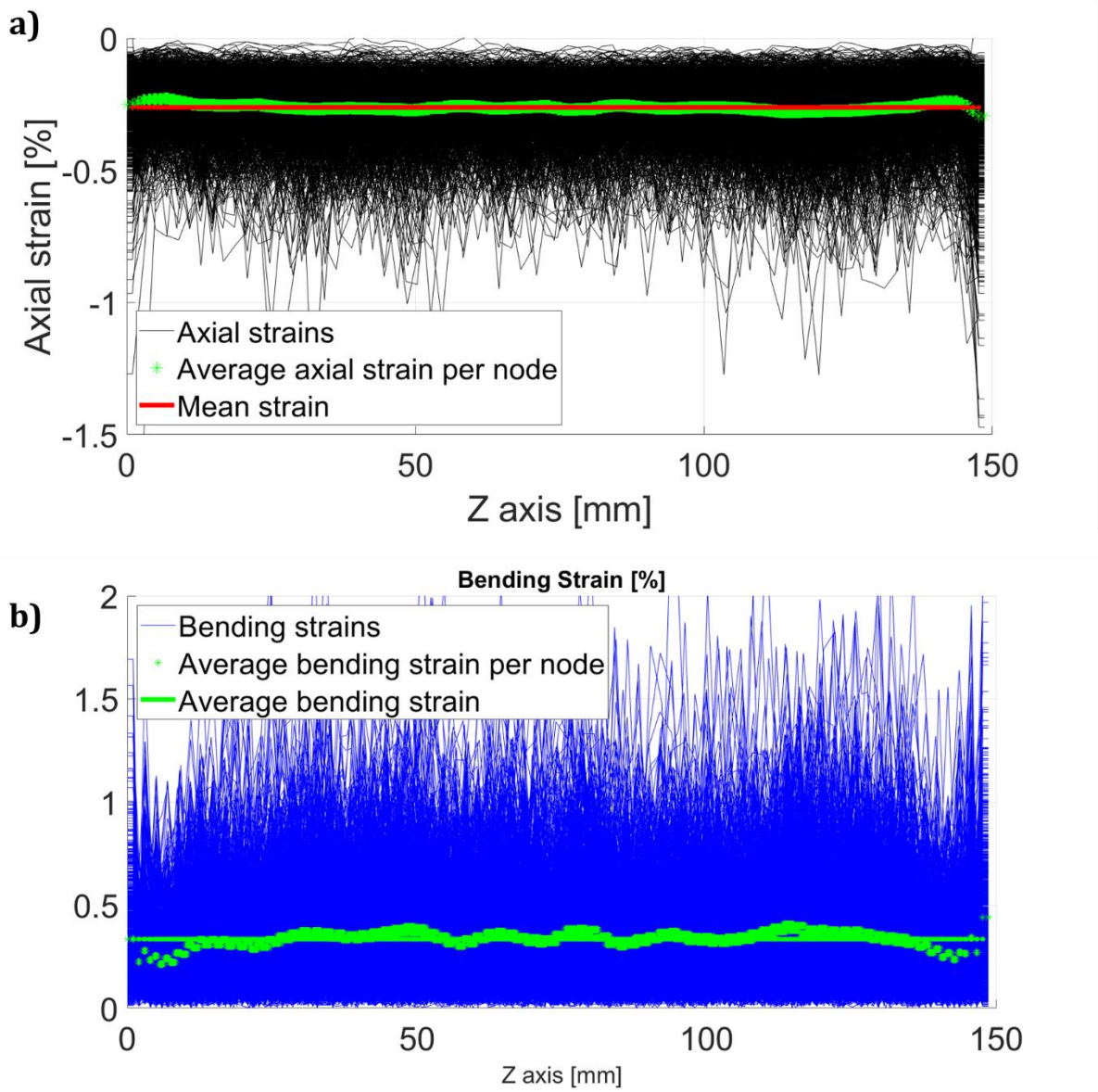

Figure IV.2.9. a) Axial strain plot over the longitudinal axis of the cable after CD; b) bending strain plot over the longitudinal axis of the cable after CD.

The analysis of the cable geometry at various loading steps is shown hereunder. The full cable model reveals the effect of the EM cycles on the wires displacement on the

low EM pressure side at full EM load, which is not detected by the petal model. Figure IV.2.10 qualitatively compares the geometry at the same z coordinate after CD, at the 1st EM peak (EMP), at the 1st EM release (EMR) and at the 5th EM peak (EMP5). In these figures, the EM load is vertical from bottom to top.

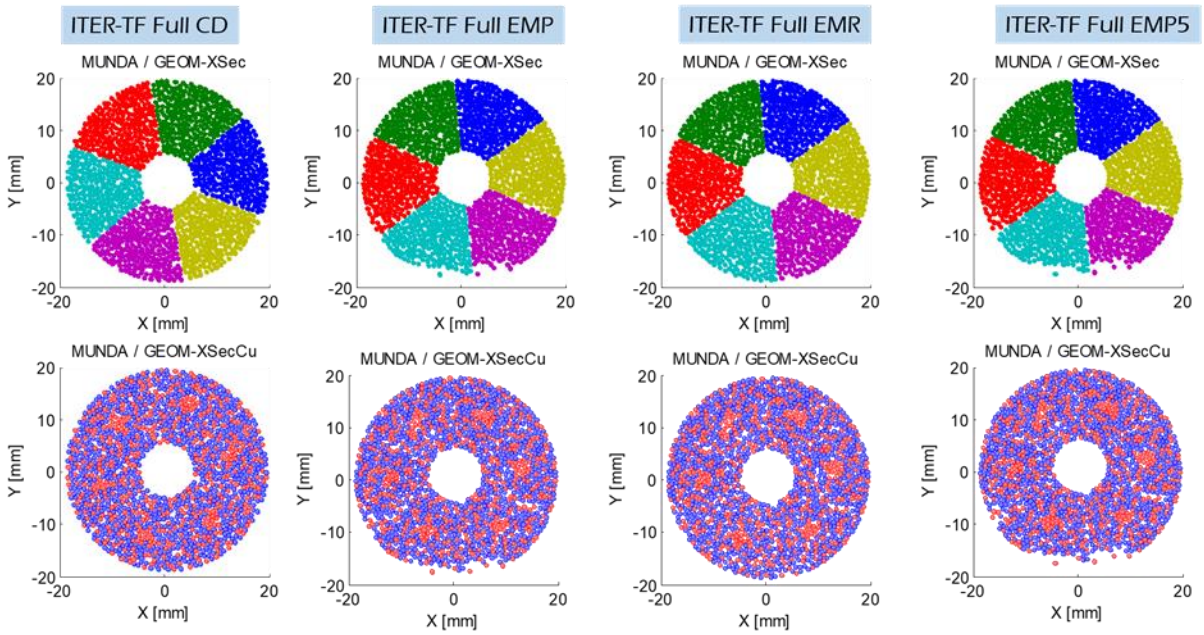

Figure IV.2.10. Qualitative assessment of the impact of the EM cycles on the cable geometry for a given cross-section at the center of the longitudinal direction (z=75 mm).

At full EM load, the wires displacement is significant (few diameters), and a gap opens on the low pressure side of the cable. Although the release of the EM load decreases this effect, some strands are plastically deformed and do not recover their initial position. A similar behavior was observed during destructive examination of the ITER CS CICCs tested sample JACS01 R (Hemmi 2012) reported in Figure IV.2.11.

Figure IV.2.11. Destructive examination of LTP CS conductors after cycling: visible displacement of the wires (Hemmi 2012).

This phenomenon is also visible using local void fraction CPM evolution illustrated in Figure IV.2.12. For an EM force applied in the positive y-axis direction (vertical direction), the low EM pressure zone is characterized by local drastic increase of the local VF in the low EM pressure side, and by a subsequent decrease, more gradual, of the VF in the high pressure side. This is not expected since the average value only marginally changes.

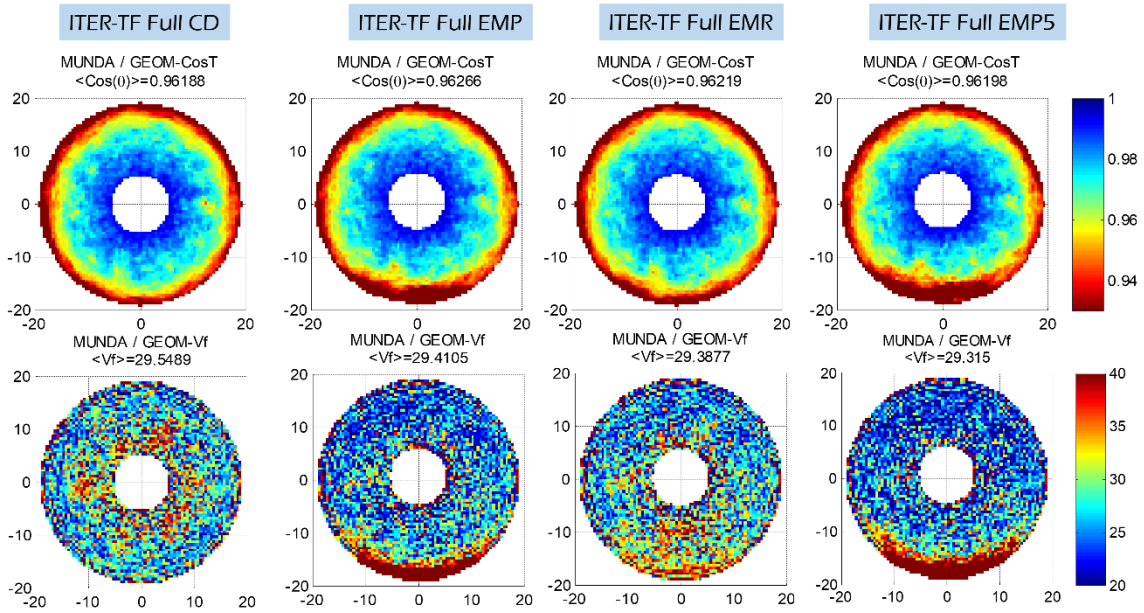

Figure IV.2.12. Qualitative assessment of the impact of the EM cycles on the local twist angle and void fraction with cumulative polar maps.

Figure IV.2.13 plots the void fraction, averaged on a radius over the longitudinal direction (cable axis), as a function of the angular (orthoradial) coordinate of the cable cross-section. These curves were investigated to better reveal the loss of symmetry of the cable due to the EM load and subsequent plastic deformation of the cross-section.

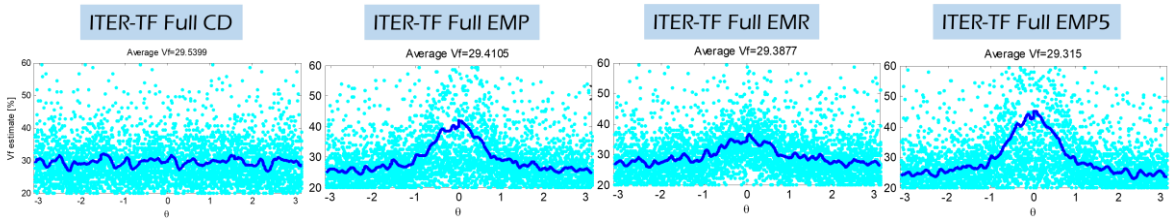

Figure IV.2.13. Impact of the EM cycles on the angular VF for a given cross-section at the center of the longitudinal direction (z=75 mm).

This angular distribution is in fact inspired by post-mortem macro-graphic analyses of cycled cables found by (Sanabria 2016). The comparison of these experimental results with the MULTIFL analysis are shown on the same plot (Figure 5 of (Sanabria 2016)) in Figure IV.2.14. Although the analyzed SULTAN sample was tested for more than one EM cycle while only one EM load is applied in the MULTIFIL model, the results are in very good agreement with the experimental image analysis.

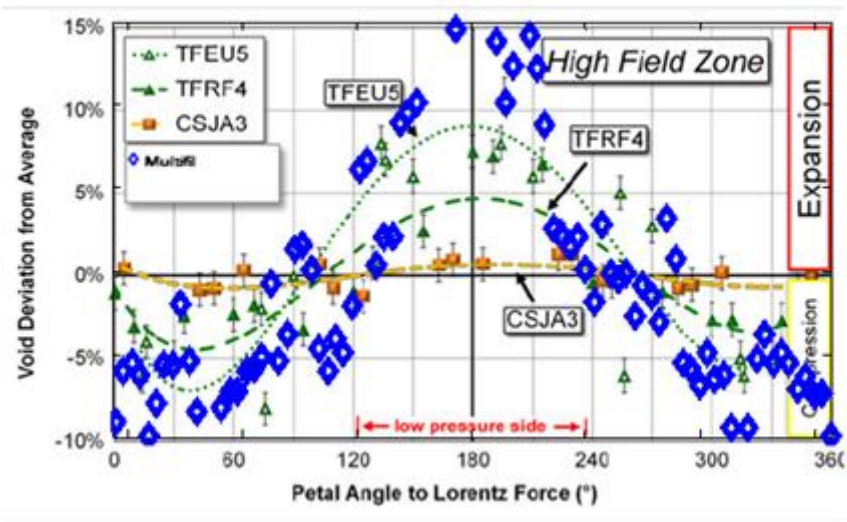

Figure IV.2.14. Comparison of the angular local void fraction between the (Sanabria 2016) plot and the MULTIFIL result.

Figure IV.2.12 also shows the cross-sectional distribution of the local twist angle and highlights a localized increase of the buckling in the low EM pressure zone corresponding to large displacements in this zone. This buckling was also observed experimentally on the low pressure side of conductors opened after test, as shown in Figure IV.2.15 by (Hemmi 2012).

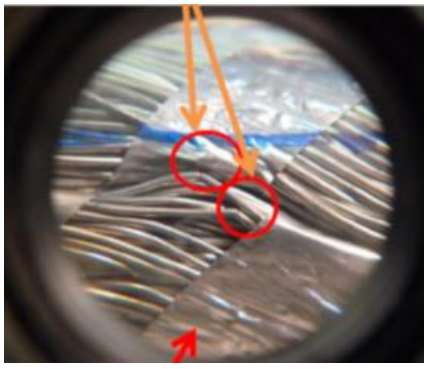

Figure IV.2.15. Destructive examination of LTP CS conductors after cycling: visible buckling of the wires in the high field zone (Hemmi 2012).

Table IV.2.3 reports the main mechanical indicators for the full cable model under the thermal and EM loadings.

Table IV.2.3. Mechanical parameters of the nominal case full cable model under the main loadings.

Loading	ε_{ap} [%]	ε_{ax} [%]	ε_b [%]	γ^b [-]	ε_{pl} [%]	ε_{el} [%]	η^{pl} [-]
CD	–0.672	–0.262	0.335	1.23	–0.177	–0.0847	2.09
1st EM cycle	–0.0676	–0.274	0.398	1.45	–0.282	0.0076	37.10
4th EM cycle	–0.0169	–0.276	0.439	1.59	–0.288	0.0185	24.41
5th EM cycle	–0.0169	–0.278	0.444	1.60	–0.290	0.0117	24.79

Differently from the petal model, the full cable seems looser both qualitatively (see strands displacements and buckling), as well as quantitatively with a smaller average axial strain (in absolute value) and a higher value of the bending strain. Since (Bessette

2014), there is a theory that a loose cable tends to degrade while a locked cable sustains the loadings better. This trend was one of the design solutions that drove the ITER-CS CICC design towards a more compacted configuration, solving the degradation issue. The former MULTIFIL studies by H. Bajas had only been able to model a single petal, which behaves quite differently from the full cable with a lot more potential exposure to fracture and associated gradual degradation of the performance.

Figure IV.2.16 reports the cumulative polar maps of axial (first column), elastic (second column) and plastic (third column) strains. After CD, all strains are relatively axisymmetric on the cross-section. The effect of the EM cycles is a progressive increase of compressive plastic strains in the high EM pressure side, breaching the initial symmetry. The color scale is the same for all plots showing that the elastic strain is marginal in the total axial strain, especially after EMP.

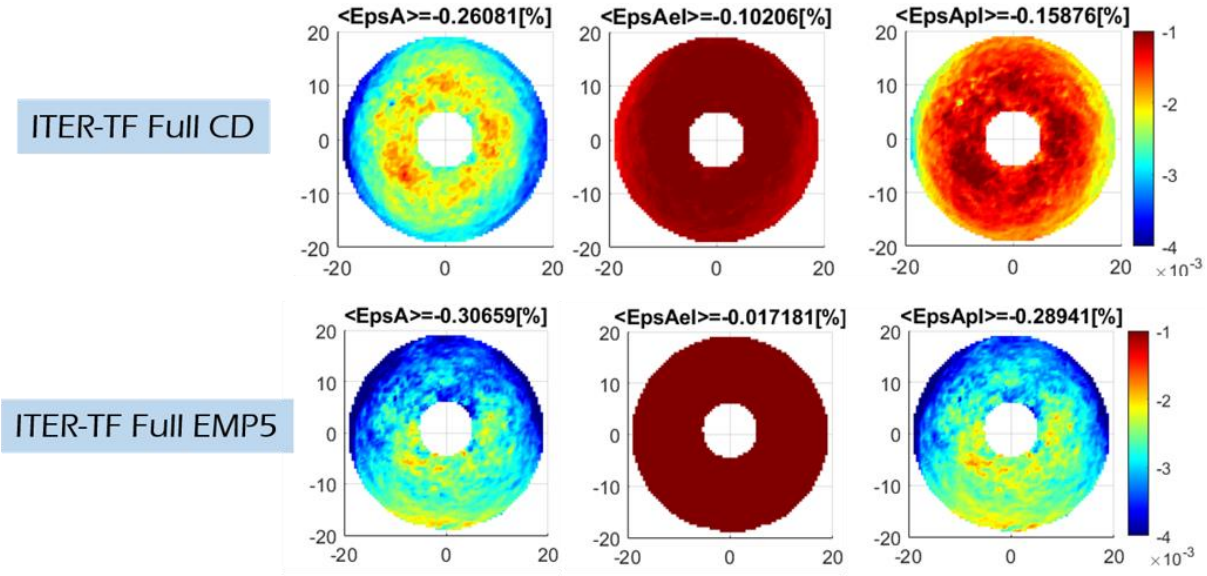

Figure IV.2.16. MUNDA strain assessment of the impact of the EM cycles on the axial, elastic and plastic strains with cumulative polar maps.

Figure IV.2.17 provides a zoom on the elastic strain after CD, at the EM peak and after EM releasing for a smaller color scale. It highlights a progressive releasing of the elastic strains in the low EM pressure side. As the cycles accumulate, there is a gradual diffusion of this release to the full cable.

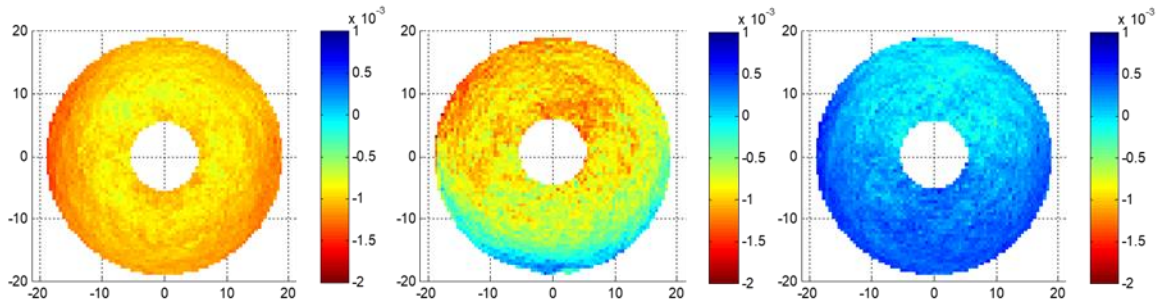

Figure IV.2.17. Cumulative polar elastic strain map after CD, at EM peak and after release of the 1st EM cycle.

Figure IV.2.18 shows the bending distribution and the exposure to compression and tension. The bending is relatively well distributed in the cable after CD, but it drastically increases with the EM cycles application, with a plastic permanent increase that is visible after EM release. The bending strain versus axial strain plots show the progressive exposure to the tensile strains due to the EM forces. As expected by the aforementioned strain distributions after CD, the EM force makes the full cable model qualitatively much more exposed (above green line) to fractures than the single petal model previously discussed.

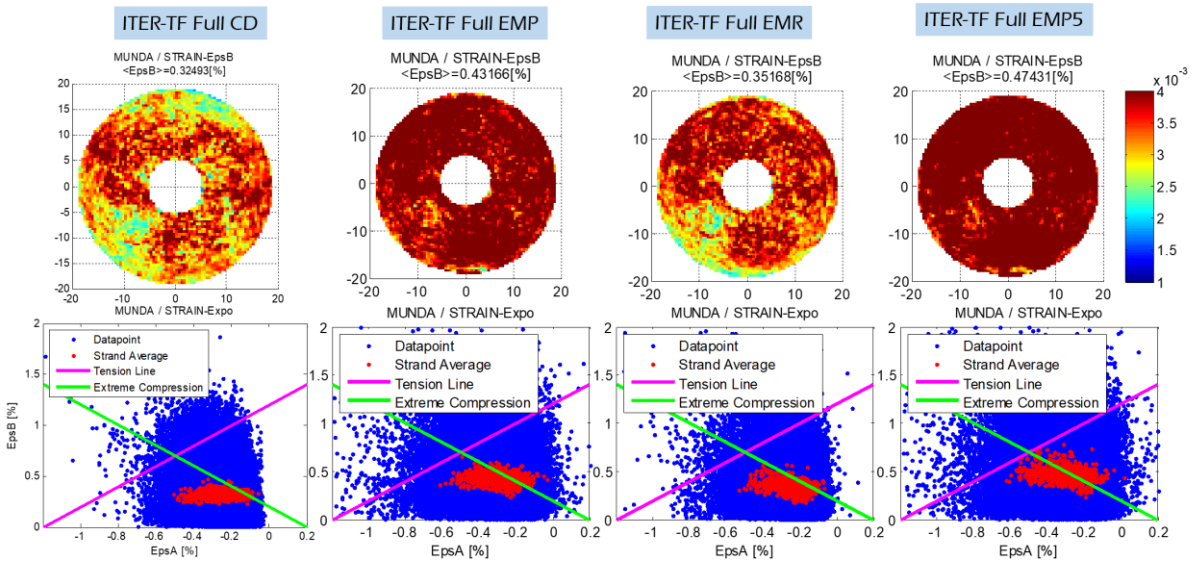

Figure IV.2.18. Cumulative polar map of the bending strain (first line) and exposure to extreme compression and tension after loadings (second line).

Figure IV.2.19 shows that the contact forces tend to decrease in the low EM pressure side of the cable, in accordance with the local void fraction maps in Figure IV.2.13. In addition, one can see that after EM release, a huge part of the initial contacts after cool-down have simply disappeared.

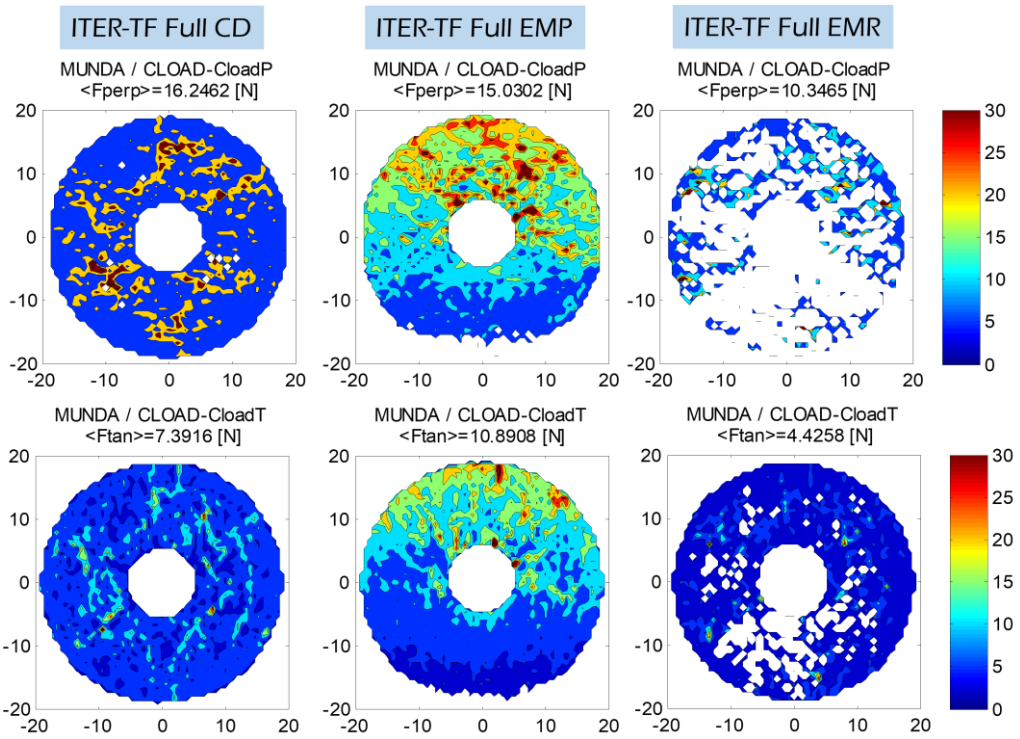

Figure IV.2.19. Cumulative polar map of the normal contact forces (first line) and the tangential contact forces (second line) after CD, at the EM peak and EM release.

This drastic drop in contact force amplitude and contact number is another phenomenon revealed by this Ph.D. study. It demonstrates that this cable design (ITER-TF) is not able to maintain good contacts between strands during its operating phase, thus lessening its current redistribution capacity. This is in complete accordance with the drastic decrease of AC losses in ITER TF cables after cycling (factor ~5-10 see Figure IV.2.20 from (Bessette 2014)), and can also be compared to direct measurements of inter-strand contact resistances by Twente (Nijhuis 2004).

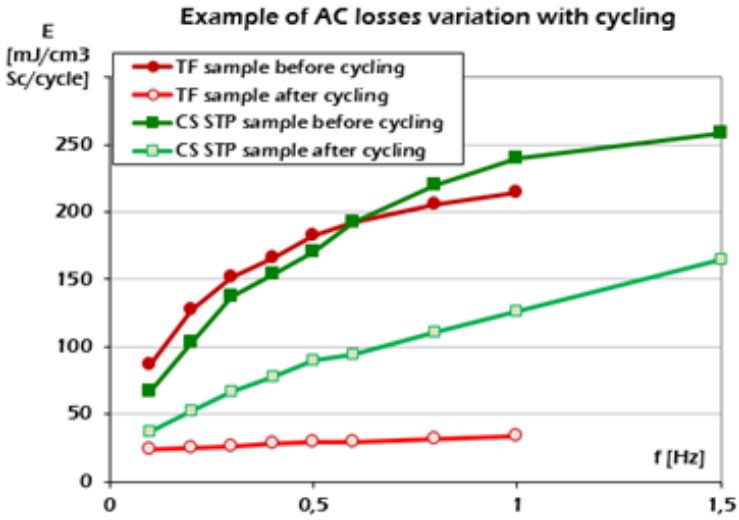

Figure IV.2.20. AC losses behavior before and after EM cycling of different conductor designs from (Bessette 2014).

Moreover, Figure IV.2.21 compares the strain distribution after CD of the ITER TF full cable model (FULL) with the single petal model (STRAIGHT).

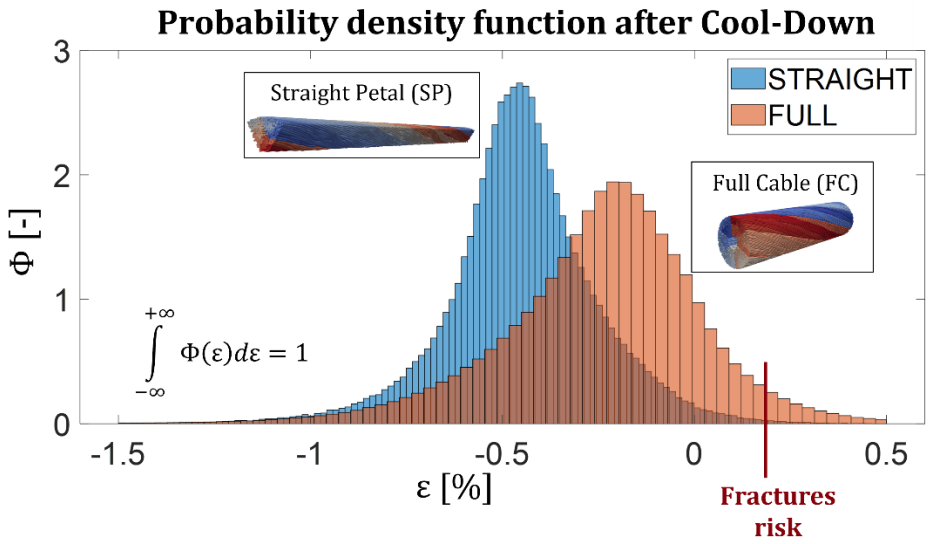

Figure IV.2.21. Strain distributions at the CD of the full cable and single petal models.

The comparison shows that even under the same design and numerical parameters, the full cable model appears looser than the petal model. The strain distribution is wider and less peaked. According to the strain plot of Figure IV.2.9 the wires are more exposed to the tensile strain and so to the risk of filaments fracture.

IV.2.3.2 Fracture analysis

Figure IV.2.22 compares the local fractured surface ratios of the wires with the HRL and LRL fracture models presented in paragraph IV.1.3.1.

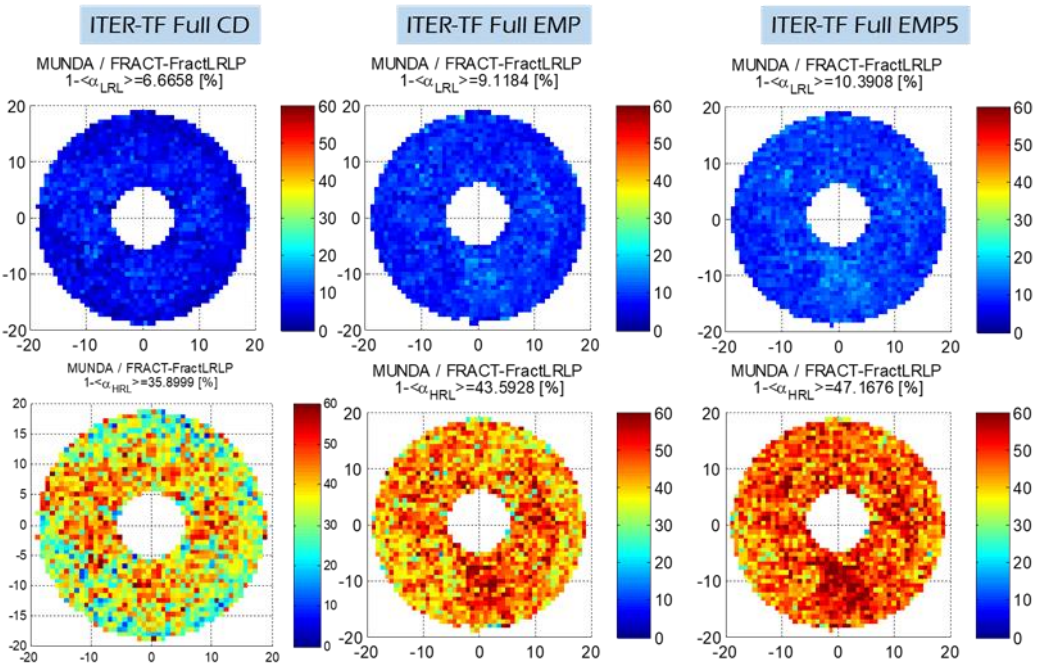

Figure IV.2.22. Cumulative polar maps of the fractured wires ratio with the LRL model (first line) and the HRL model (second line).

As expected, the fracture ratio increases with the application of the EM cycles, which increase the bending as previously showed even if a certain number of fractures is already present after CD. The models highlight a slight accumulation of the fractures in the low EM pressure side where the wires tend to have a large displacement. Figure IV.2.23 reports a zoom of the LRL fracture map to better see the most critical zones in the cable. However, inside MULTIFIL, there is no "history" of the fractured state which means that even if visually the fractured state seems less critical after release of the EM load, in reality, once fractured, the filaments stay broken.

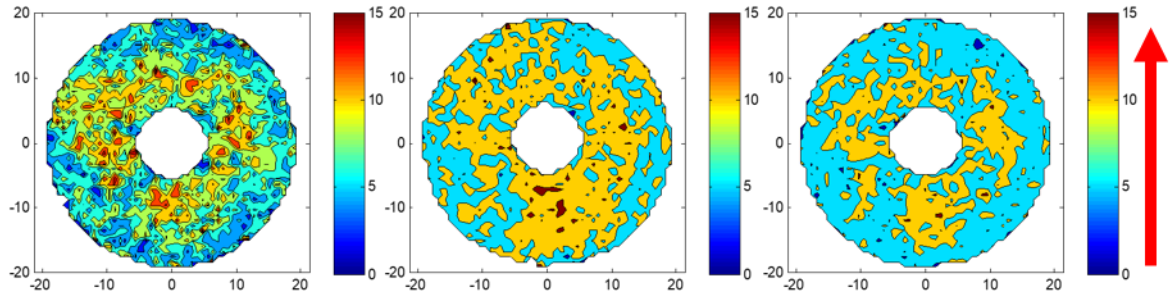

Figure IV.2.23. Cumulative polar map of fractured wires ratio after CD, at EM peak and after release of the 1st EM cycle with LRL fracture model.

Figure IV.2.24 assesses the evolution of cable current carrying capability. The average critical current decreases with the EM cycles and the map shows the most critical zones of the cable. The high compressive zone associated to the high EM pressure has less current carrying capability, but the low compressive side also shows some weak areas.

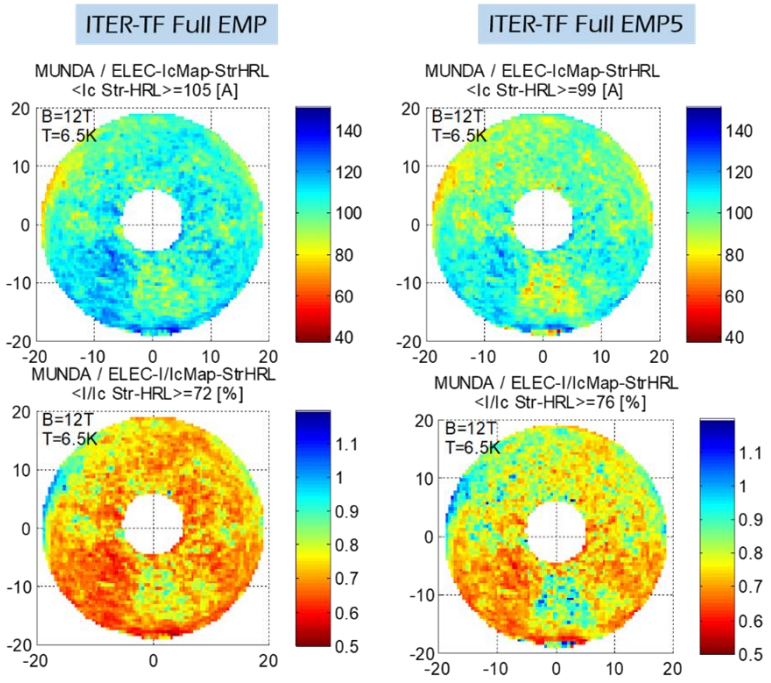

Figure IV.2.24. Cumulative polar maps of the critical current (first line) and the transport current/critical current ratio (second line).

Table IV.2.4 reports the results of the application of the multi-stages model. Each column corresponds to the cabling stage limit that defines the transition between the HRL and LRL models. For the wires belonging to the cabling stages below this limit the LRL model is assumed for the current redistribution between strands, while above this limit an HRL model is adopted.

Table IV.2.4. Multi-stages model applied to the full cable model.

		Cable LRL	*Petals HRL*	*3x3x5x5 HRL*	*3x3x5 HRL*	*3x3 HRL*	*wires HRL*
1st EMP	**Ic [kA]**	74.51	67.01	58.82	42.22	27.51	18.29
	I/Ic [%]	91	101	116	161	247	372
5th EMP	**Ic [kA]**	65.41	57.94	50.39	35.08	22.01	14.73
	I/Ic [%]	104	117	135	194	309	462

This kind of study, although only partially quantitative, shows that the need for current redistribution evolves as the cable is loaded. In this case, for a transport current of 68 kA, the multi-stages analysis shows that at the 1st EM peak, an intra petal redistribution of the current is sufficient to carry the nominal transport current. However, the progressive application of EM cycles shows that the cable would need inter-petal redistribution to keep carrying the transport current.

IV.2.4 Conclusion

The full cable model is more exposed to the tensile strains, and looser than the single petal model. If the latter is obviously more relevant of real cables, the single petal model provided guidance and useful insights at the sub-stage level.

The major effect of the EM cycles seems to be a progressive softening of the cable due to large plasticization and a substantial change of the jacket-cable equilibrium in a typical SULTAN test. This phenomenon can be compared qualitatively to the typical initial drop (first few cycles) of the T_{cs} observed in several TF conductors (Breschi 2017). In light of these results, this drop could be interpreted as an equilibrium shift between cable and jacket.

The full-scale model is recent and results have still to be confirmed, but preliminary analyses showed a good agreement with experimental studies and the model seems to be able to correctly describe typical behaviors of real TF CICCs.

IV.3 CHAPTER – CICCs MECHANICAL BEHAVIOR: DESIGN PARAMETERS

The main purpose of this chapter is to discuss the parametric study of the impact of the void fraction and of the inter-strands friction coefficient on the mechanical behavior of the cable. The baseline case study is characterized by a VF of 29.7 % and a friction coefficient between strands of 0.1. The following sections show the impact of the void fraction (section IV.3.1), while section IV.3.2 focuses on the strands friction coefficient.

IV.3.1 Impact of the VF

Five case studies were investigated with a VF of 27.8 %, 29.7 %, 32.7 %, 35.3 % and 36 % respectively. For all of them, a sequence of cool-down (CD) and one EM cycle with its recompression was applied.

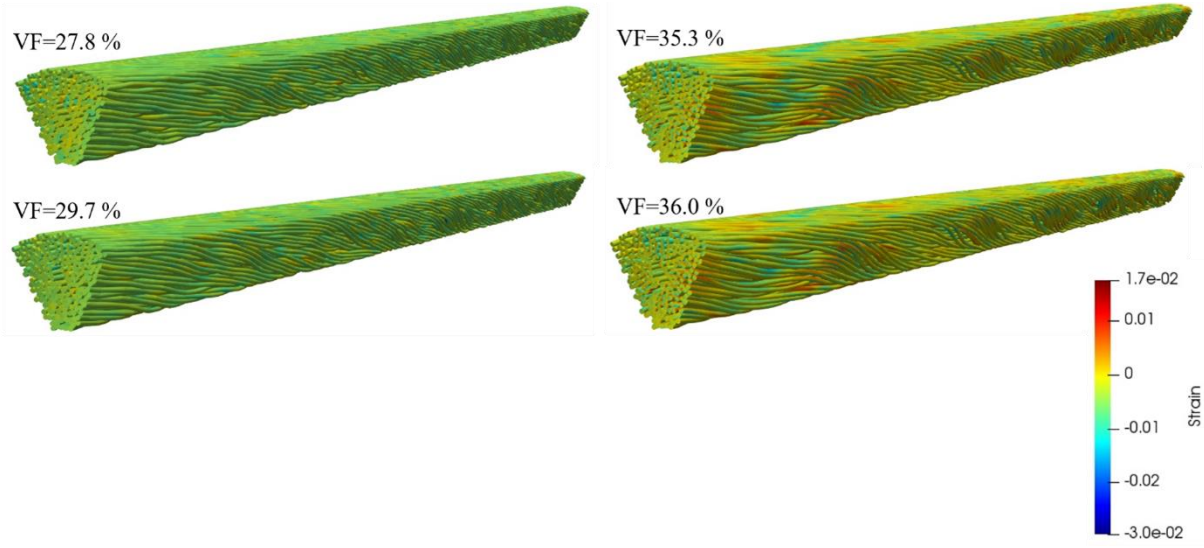

Figure IV.3.1. Qualitative assessment of the impact of the CD on the strain map for four different VFs.

The strain maps illustrated in the figure above show substantially more buckling for the less compacted cables, since the wires tend to bend more when the compressive CD occurs.

For the CD, the (ε, σ_z) mechanical characteristics was fitted by means of a fitting function where the linear part (Bajas 2011) represent the elastic behavior of the Nb_3Sn (Mitchell 2005b). The goal is to provide the mechanical properties of the homogenized

cable for future studies where the macroscopic behavior of the cable is required without simulating it. The fitting function for σ_z includes three parameters (α, β, γ):

$$\sigma_z = \alpha\left(1 - e^{-\beta\varepsilon}\right) + \gamma\varepsilon \ [MPa]. \quad \text{(IV. 7)}$$

Moreover, the Young's modulus E_0 is calculated via the method presented for the tensile tests in (Ilyin 2006) adapted here to the compressive stress $\sigma_{z,strands}$. The latter is defined as $F_z/S_{strands}$, where $S_{strands}$ is the cross-sectional surface of the strands $N_s {r_s}^2 \pi$ and F_z corresponds to the resultant force applied along the axis of the analyzed petal at its extremities, scaled to a full cable (factor 6). E_0 corresponds to the initial slope of the linear part of the unloading curve at –0.2 % of applied compressive strain (Ilyin 2006).

Table IV.3.1 reports the main mechanical indicators for each case study after CD and one EM cycle.

Table IV.3.1. Mechanical characterization of five case studies after CD and EM cycle (Riccioli 2021).

		VF=27.8%	*VF=29.7%*	*VF=32.7%*	*VF=35.3%*	*VF=36%*
CD	ε_{ap} [%]	–0.56	–0.61	–0.67	–0.7	–0.7
	ε_{ax} [%]	–0.49	–0.45	–0.31	–0.21	–0.19
	ε_b [%]	0.15	0.24	0.34	0.35	0.35
	γ^b [-]	0.30	0.54	1.09	1.68	1.82
	ε_{pl} [%]	–0.37	–0.32	–0.21	–0.13	–0.12
	ε_{el} [%]	–0.12	–0.13	–0.10	–0.077	–0.072
	η^{pl} [-]	2.9	2.5	2.0	1.8	1.7
	E_0 [GPa]	109	105	86.9	73.2	70.7
	α [MPa]	128.67	140.18	139.39	131.03	115.61
	β [MPa]	13.44	15.75	11.95	10.0501	10.00
	γ [MPa]	587.31	363.73	156.93	54.28	50.31
1st EM cycle	ε_{ap} [%]	–0.025	–0.042	–0.051	–0.042	–0.51
	ε_{ax} [%]	–0.51	–0.48	–0.32	–0.21	–0.20
	ε_b [%]	0.17	0.27	0.37	0.39	0.39
	γ^b [-]	0.33	0.56	1.16	1.85	1.98
	ε_{pl} [%]	–0.44	–0.44	–0.33	–0.22	–0.20
	ε_{el} [%]	–0.069	–0.036	0.0063	0.0021	0.003
	η^{pl} [-]	6.3	12.3	52	103	67

As expected, E_0 increases with decreasing VF. The same behavior is shown by the applied strain ε_{ap} during the CD to achieve the thermal equilibrium with the jacket at 4.5 K. As for the plasticity, the coefficient η^{pl} clearly indicates that it decreases with the VF. The CD affects more the η^{pl} of the less compacted cables that will be less subjected to the major plasticization due to the EM cycles. The γ^b values indicate that the bending phenomenon is predominant for the softer cables with higher VFs, as also confirmed by the strong buckling observed in Figure IV.3.1. Table IV.3.1 shows an inversion of the trend of γ^b between 29.7 % and 32.7 %, thus highlighting a change of the cable behavior that can be related to the transition between the locked and the loose regimes identified in (Bessette 2014). Figure IV.3.2 shows the same behavior in terms of the strain distribution. The distribution clearly switches from narrow and peaked to larger and wider for greater void fractions. In this study the nominal case is a locked cable; in real conductors this

threshold is expected at a lower VF since for the given twist pitches (*cosϑ* of 0.97), a VF of 29.7 % should correspond to a loose cable (Bessette 2014). It is however interesting to observe its qualitative detection and reproduction with the petal model. It is worth noticing that the results in Table IV.2.3 suggest that the scaling-up to the full cable model makes the simulated cable belong to the loose group as well as Figure IV.2.21.

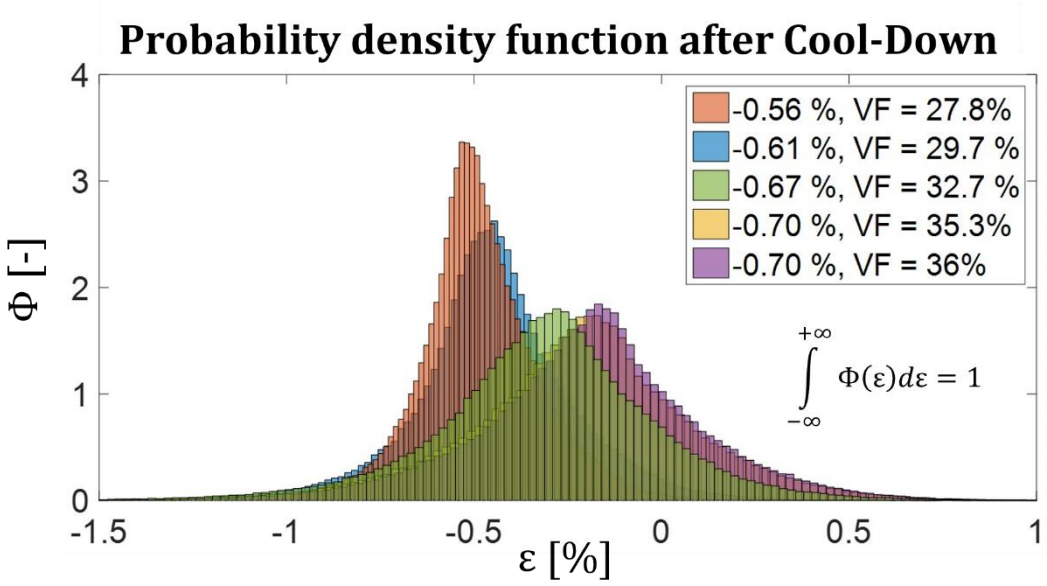

Figure IV.3.2. Strain distribution after CD as a function of the VF (Riccioli 2021).

Thanks to the fitting law, equation (IV.7), identified by the three parameters (α, β, γ) for each VF it is possible to propose a general law governing the longitudinal cable rigidity as a function of the VF to extrapolate the longitudinal stiffness for any VF. By fixing α and β at average values of 130 MPa and 12 MPa respectively, since their variation as a function of the VF was negligible, one can define the ad-hoc variation of γ as a function of VF as:

$$\gamma = 71644 \cdot VF^2 - 52208 \cdot VF + 9559\ [MPa]. \qquad \text{(IV. 8)}$$

Figure IV.3.3 reports the comparison of the (ε, σ_z) characteristics assessed by equations (IV.7) and (IV.8) respectively in Figure IV.3.3a) and Figure IV.3.3b). The fitted behavior is only very slightly different.

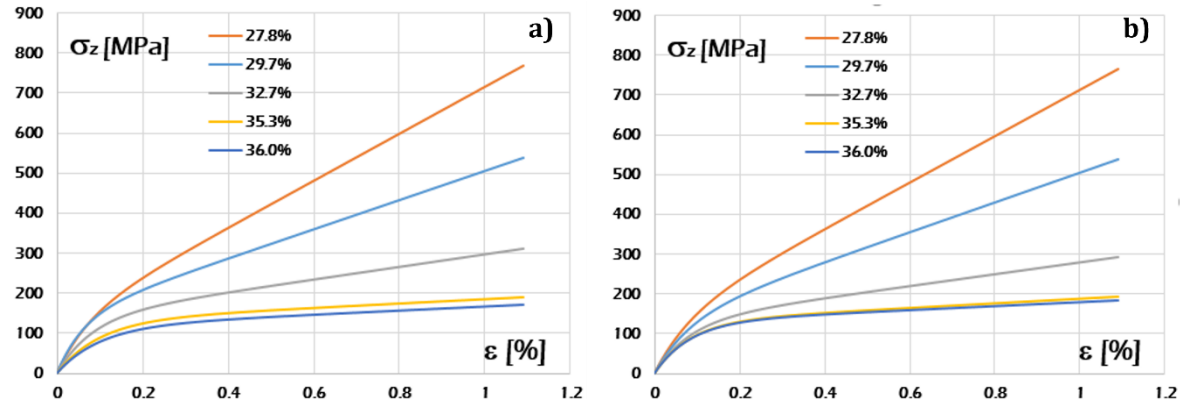

Figure IV.3.3. a) Longitudinal stiffness characterization for several VFs of simulated cables, b) longitudinal stiffness characterization for several VFs from linear fit.

Figure IV.3.4 reports the number of fractures per meter of conductor occurring at tensile strain with a filament breakage level set to +0.2 %. The counted fractures are studied after each loading and increase with the VF, highlighting also a transition from locked (less fracture) to loose behavior (more fracture). The impact of the EM cycles on the fractures increases with the VF as illustrated by the number of fractures per meter per cycle for two different VFs. At the same time the EM load increases in amplitude the fracture phenomenon.

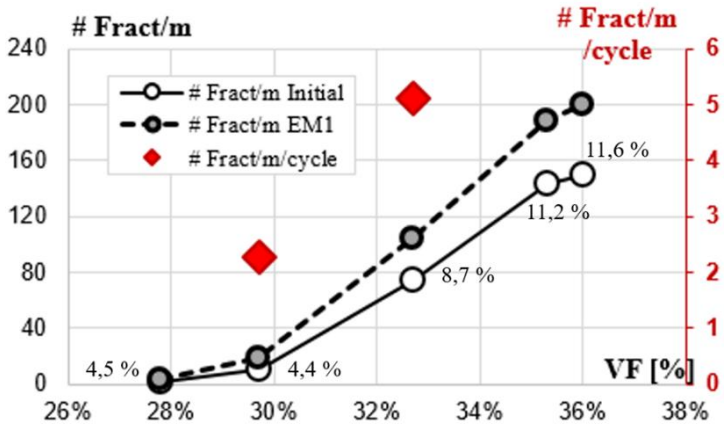

Figure IV.3.4. For each loading, variation of the number of fractures per meter as a function of the VFs (Riccioli 2021).

The contacts created during manufacture seem to have a lower electrical resistance, as mentioned by (Nijhuis 2004), and so the study of contacts (Yagotintsev 2019) is important for the analysis of the cable AC losses, since they directly affect the inter-strand resistances. Therefore, an assessment on the evolution of the number of strong contacts (created during manufacture) with loading is also provided. For this study, the contacts between wires belonging to the same triplet were neglected because they tended to bias the distribution with almost continuous and weak contact points (mostly numerical), as well as the contacts with copper wires that are considered negligible for current redistribution.

The plots in Figure IV.3.5 report the initial (after HT) and dynamic (CD/EM cycles) number of contacts per meter of strand. This study is focused on the contacts created during the manufacture of the cable, which underwent the initial compaction procedure (Yagotintsev 2019) and it aims to study how they evolve during the mechanical loadings. The most compacted cables are characterized by stronger and more resilient contacts, which tend to remain after mechanical solicitation.

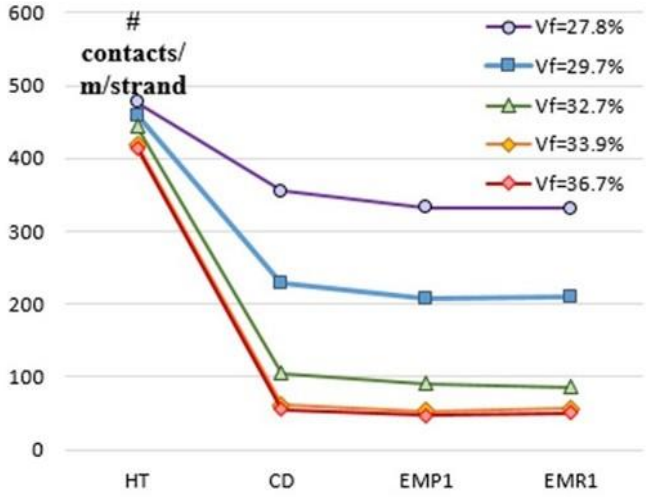

Figure IV.3.5. For each loading, variation of the contacts number per meter and per strand as a function of the VFs (Riccioli 2021).

It was observed also that the average normal contact force is greater for the lower VFs; the effect of the Lorentz force is an additional contact force that is significantly greater for the lower VF (see Figure IV.3.6).

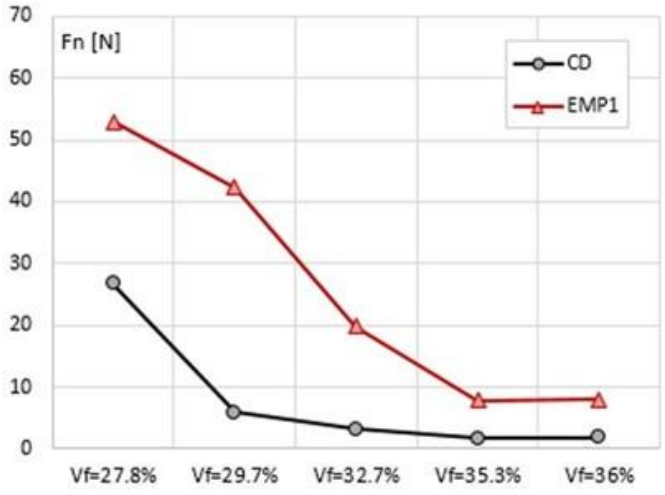

Figure IV.3.6. Impact of the VF on the average normal contact force.

Considering that the inter-strand conductance increases with decreasing the VF (Nijhuis 2005) and that it was experimentally observed an increase of the $n\tau$ value (initial slope of the AC losses plot) of 3 times from 36 % to 26 % of the VF (Chiletti 2020), all the

observations about the contacts are in accordance with AC losses evolution as a function of the compaction ratio, which gives confidence in the contact treatment of MULTIFIL.

To conclude the analysis on contacts, the curves in Figure IV.3.7 plot the contact width distributions for three different VFs.

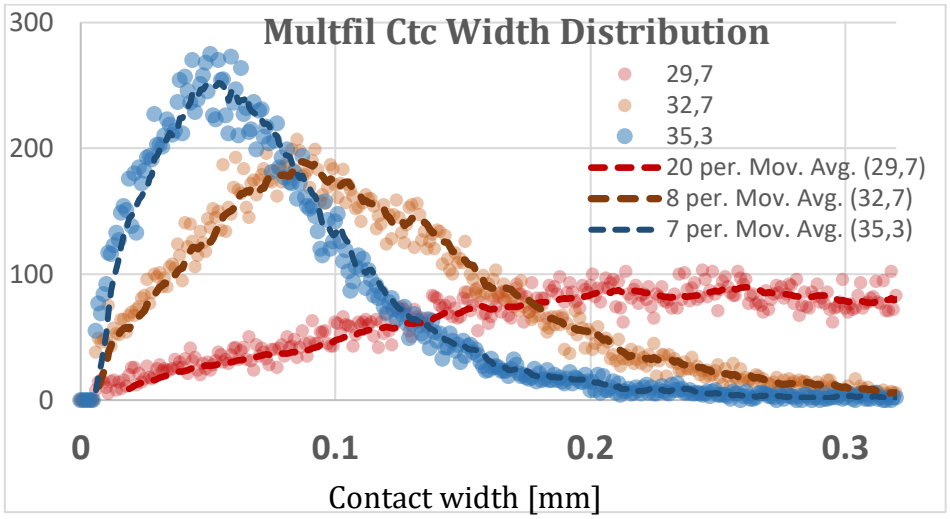

Figure IV.3.7. Contact width distributions as a function of the VF.

A similar distribution was plot in (Zani 2021) in the framework of experimental tomographic analysis of JT60SA TF conductors for different VFs. A preliminary analysis compared the average contact width after manufacture for a given cable as a function of the VF from the simulations to the tomography results. Even if the cable designs are quite different, the results in Figure IV.3.8 show consistent contact width for ITER TF petal model and JT-60SA TF cable. Additional studies of cables should indicate if this relation between contact width and void fraction is more general.

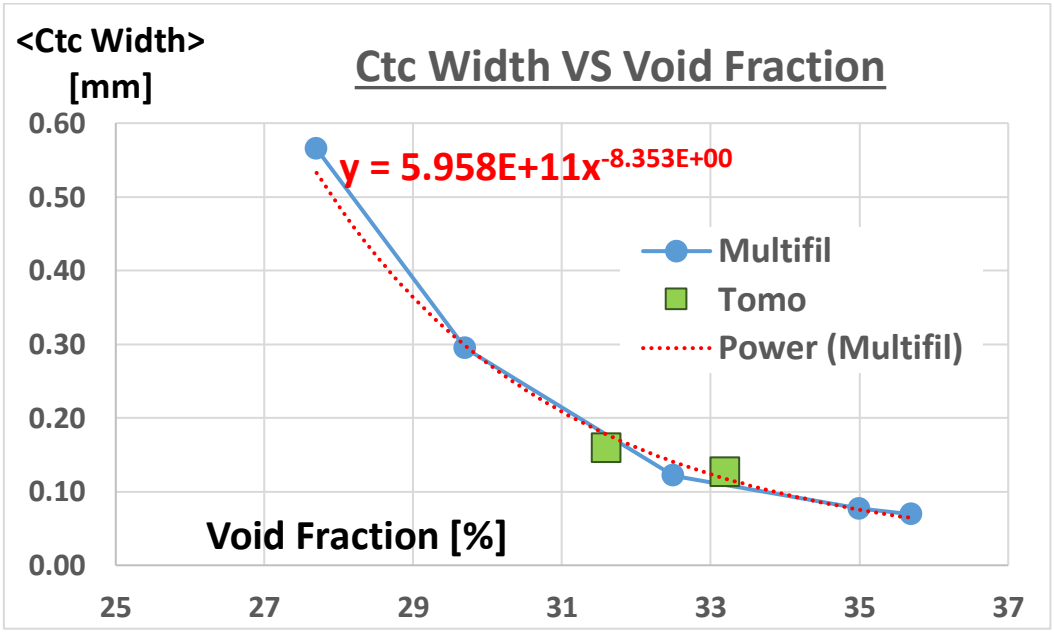

Figure IV.3.8. Comparison of the average contact width as a function of the VF between the JT60SA TF CICCs tomography and the ITER TF CICC simulations.

Figure IV.3.9 reports the assessment of T_{cs} by coupling THELMA with MUTLFIL.

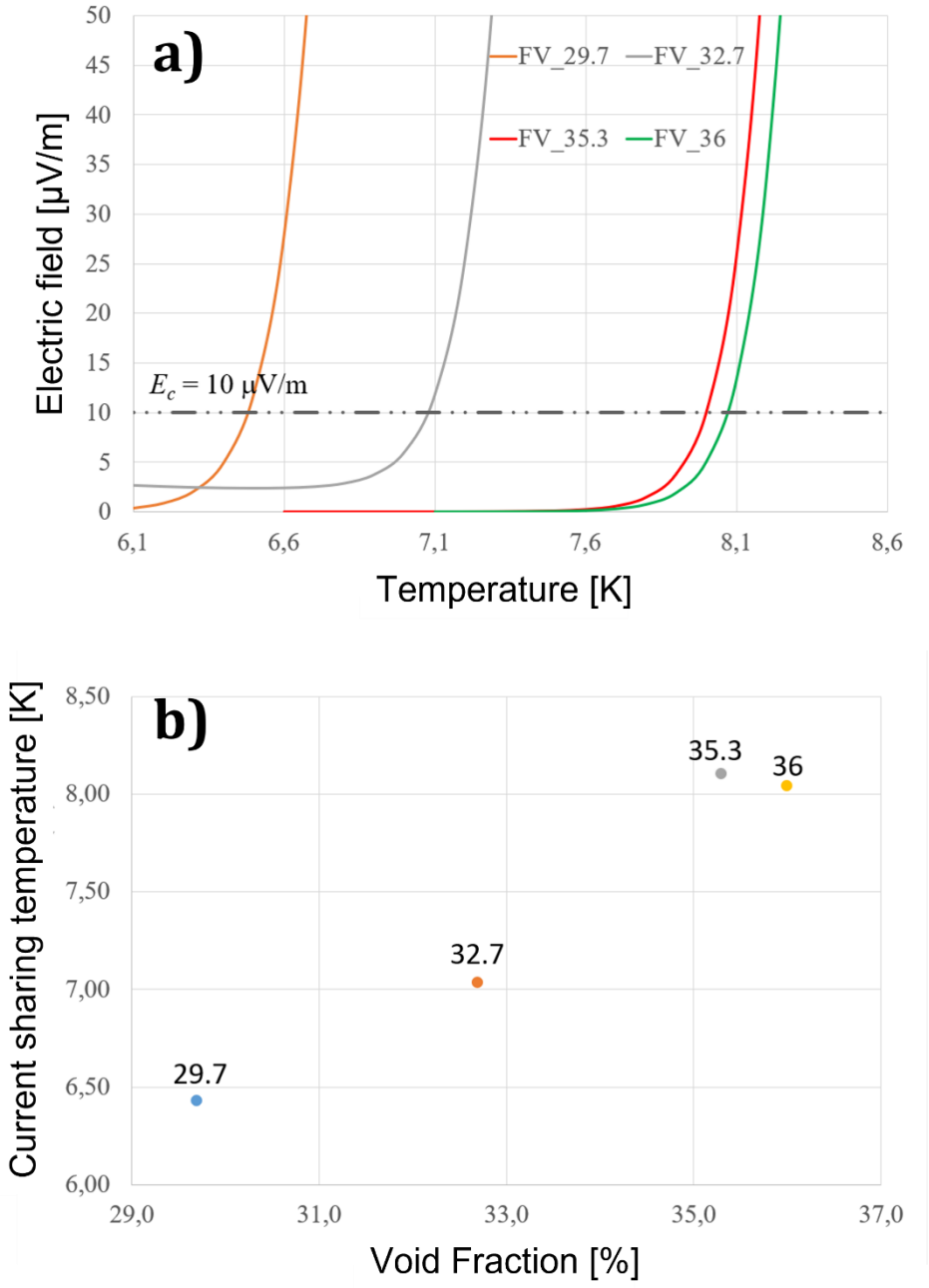

Figure IV.3.9. (T,E) characteristics (a) and T_{cs} (b) for different VFs.

The more compacted cables have a lower T_{cs} since the axial strain is higher. This means that they are more protected from tensile strain and so from the fracture risk. Therefore, an assessment of the T_{cs} with EM cycles is expected to show a more stable T_{cs} value for the most compacted cables (lower VF). Further studies are recommended.

IV.3.2 Impact of the friction coefficient

The SULTAN campaign to test the ITER TF conductors presented in (Breschi 2017) showed that the conductors manufactured by the Russian Federation did not degrade. A

possible explanation for this very interesting behavior was the higher roughness of the strands Chromium coating, which would increase the friction coefficient between strands and prevent them from slipping. The final cable behavior would be more locked by this additional roughness, and so more protected from filaments breakage. This section aims to investigate the results of the MULTFIL cable model to a variation of inter-strands friction coefficients.

IV.3.2.1 Single petal model

The CD was analyzed for different friction coefficients ranging from 0.1 to 0.9. Considering the nominal petal test case presented in Table IV.2.1, Figure IV.3.10a) presents the evolution of the number of fractures occurring on one meter length and b) the evolution of contacts after CD per meter of strand.

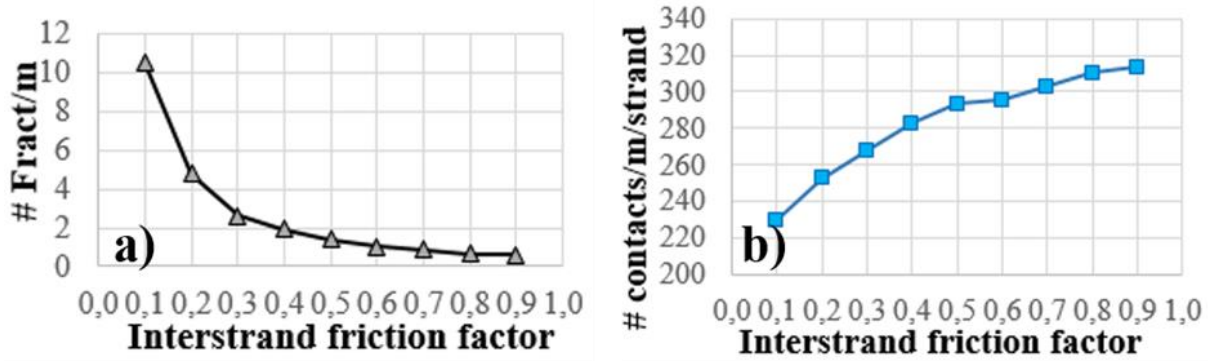

Figure IV.3.10. a) Variation of the number of fractures per meter as a function of friction coefficient after CD. b) Variation of the contacts number per meter and strand as a function of friction coefficient after CD (Riccioli 2021).

The analysis performed at the end of the CD confirms that as the friction coefficients increases, the fractures per meter decrease, and a threshold around 0.2-0.3 is observed. The plot in Figure IV.3.10b) refers to the number of contacts per meter and per strand and shows that higher friction coefficients make the cable preserve the strong contacts created during manufacturing.

Table IV.3.2 reports the results obtained for the friction coefficients 0.1, 0.2, 0.5, 0.7 and 0.9 after CD.

Table IV.3.2. Mechanical parameters for several friction coefficients after the CD.

	FC=0.1	*FC=0.2*	*FC=0.5*	*FC=0.7*	*FC=0.9*
ε_{ap} [%]	–0.61	–0.6	–0.59	–0.58	–0.57
ε_{ax} [%]	–0.45	–0.46	–0.47	–0.47	–0.47
ε_{b} [%]	0.24	0.22	0.19	0.17	0.16
γ^{b} [-]	0.54	0.47	0.39	0.37	0.35
ε_{pl} [%]	–0.32	–0.33	–0.34	–0.35	–0.35
ε_{el} [%]	–0.13	–0.13	–0.13	–0.12	–0.12
η^{pl} [-]	2.5	2.6	2.7	2.8	2.9
E_0 [GPa]	105	107	115	116	116
α [MPa]	140.18	121.1273	95.2338	91.0322	89.8284
β [MPa]	15.75	18.139	22.7317	23.5929	23.7675
γ [MPa]	363.73	432.9513	540.0393	575.146	596.1496

Figure IV.3.11 reports the effect of the FC on two different VFs. Therefore, this study detects a dependence between the cable longitudinal stiffness and the two parameters VF and FC. This can help designing a stiffer cable, less exposed to breakage and buckling.

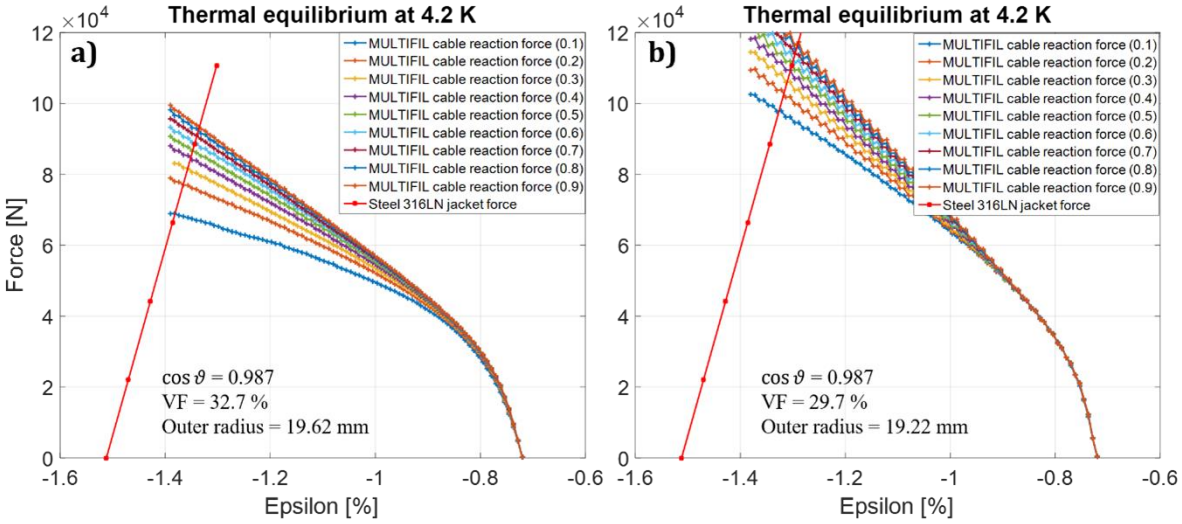

Figure IV.3.11. a) Impact of the inter-strands friction coefficient on the jacket-cable equilibrium at CD for VF=32.7 %; b) impact of the inter-strands friction coefficient on the jacket-cable equilibrium at CD for VF=29.7 %.

In this case as well, it is possible to fit the plots based on in the equation (IV.7) to find a new set of (α, β, γ) parameters, providing the longitudinal stiffness of the cable as a function of the friction coefficient. From the study of the (α, β, γ) parameters variation with FC, β was almost constant and set at 18 MPa. Differently from the VF case, both α and γ are not constant and they vary with FC as:

$$\begin{matrix} \alpha = -27.\ln(FC) + 70\ [MPa] \\ \gamma = 636\ .FC^{0.24}[MPa] \end{matrix} . \qquad (IV.9)$$

This approach can be generalized to find the longitudinal rigidity for any VF and FC, by the following set of parameters:

$$\begin{matrix} \alpha = -27.\ln(FC) + 70\ [MPa] \\ \beta = 15\ [MPa] \\ \gamma = (1.24.10^5\ VF^2 - 9.1.10^4\ VF + 1.7.10^4).FC^{0.24}\ [MPa] \end{matrix} . \qquad (IV.10)$$

Figure IV.3.12 reports the comparison between the curves given by equation (IV.7), Figure IV.3.12a), and the linear fit of equation (IV.9), Figure IV.3.12b).

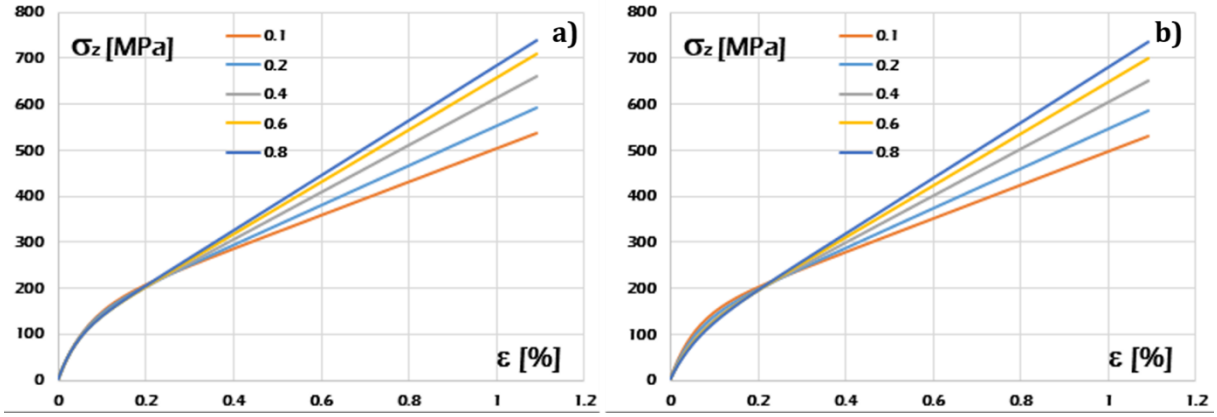

Figure IV.3.12. Comparison between the fitting function result for different friction coefficients (a) and the linear fit as a function of friction coefficient (b).

Finally, after the CD loading, an assessment of the T_{cs} at the EM peak by means of the THELMA code is presented in Figure IV.3.13.

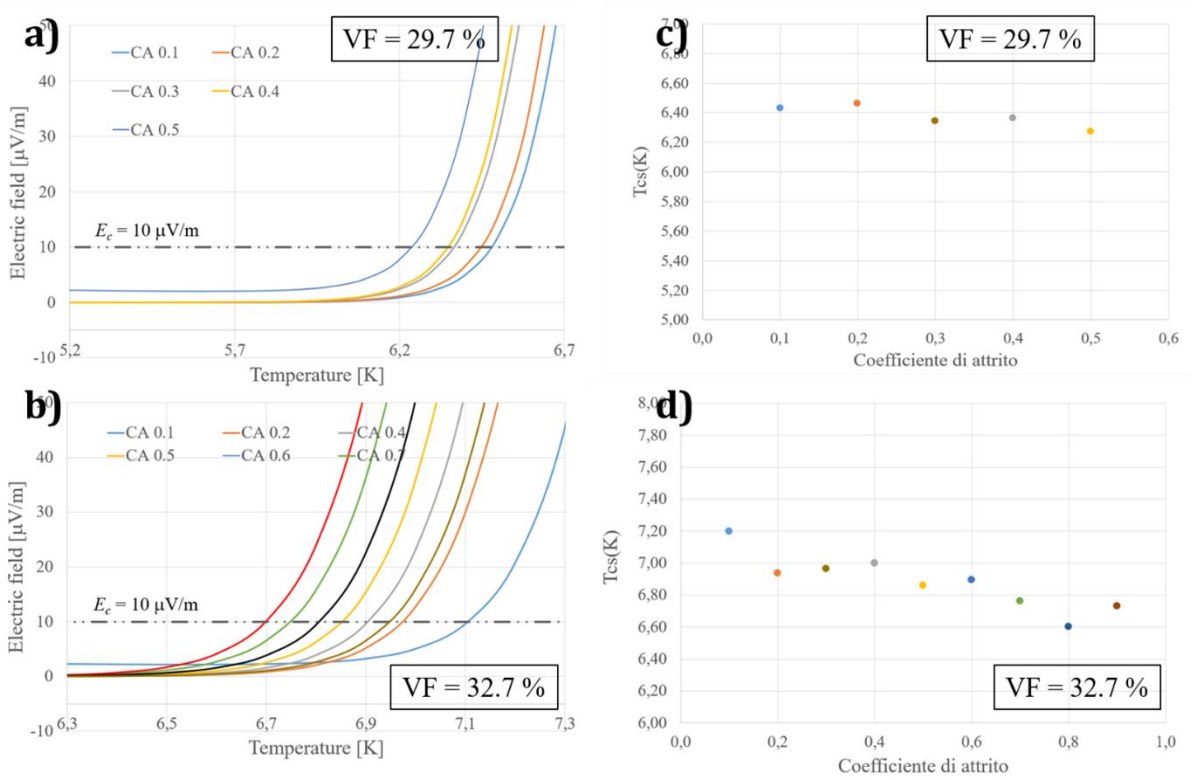

Figure IV.3.13. a) and b) (T,E) characteristics for different FCs at VF=29.7% and 32.7% respectively; c) and d) T_{cs} plots as a function of the FC at VF=29.7% and 32.7% respectively.

The FC study shows that for the more compacted cable at 29.7 % of VF, the T_{cs} tends to be more stable than for the greater VF. These results show that for looser cables, the FC has a greater impact on the determination of the T_{cs}. It seems reasonable to deduce that the lower impact of the FC on the more compacted cable is linked to its locked behavior. Therefore, the looser cables (greater VFs) would benefit from the increase of the FC for the cyclic behavior.

IV.3.2.2 Full cable model

For computational time reasons, two FCs were investigated for the full cable model: the nominal value used in all the previous simulations 0.1 and the (Bajas 2011)'s value of 0.25.

Figure IV.3.14 reports the geometrical comparison after CD of the two case studies. The geometry does not seem to present remarkable differences between the two different models.

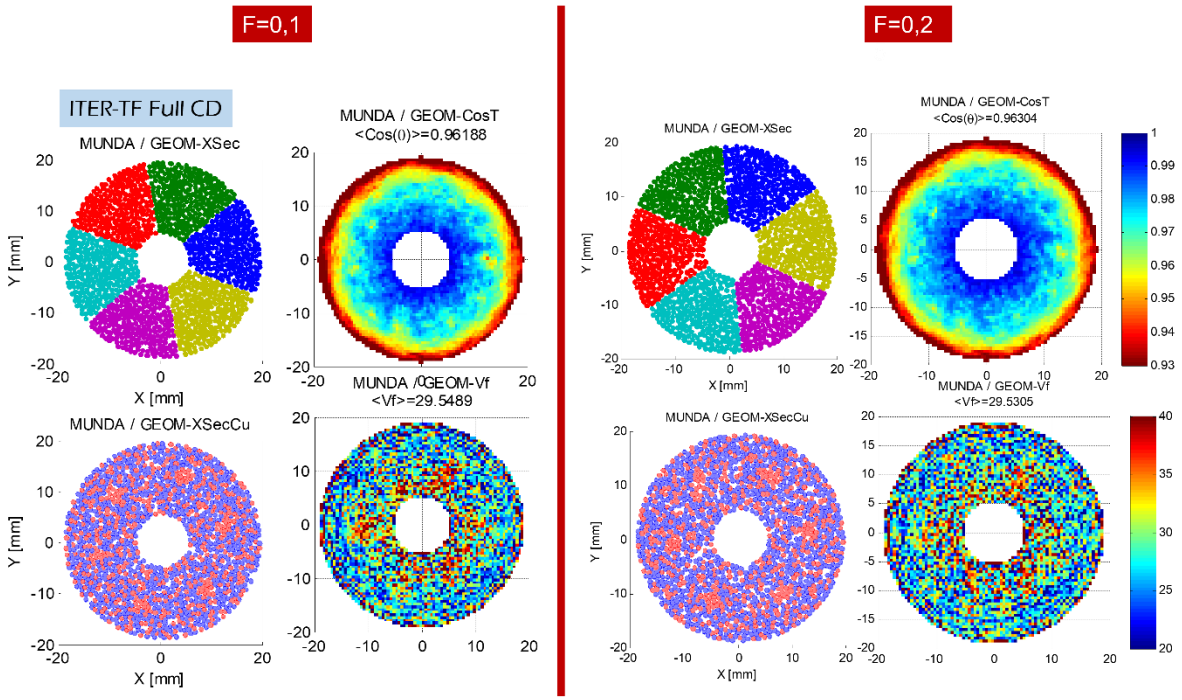

Figure IV.3.14. Impact of the FC on the geometrical parameters after CD.

Table IV.3.3 summarizes the main mechanical results for several loadings.

Table IV.3.3. Mechanical characterization after CD and EM cycles for two FCs cables.

		ε_{ap} [%]	ε_{ax} [%]	ε_b [%]	γ^b [-]	ε_{pl} [%]	ε_{el} [%]	η^{pl} [-]
FC=0.1	CD	–0.672	–0.262	0.335	1.23	–0.177	–0.0847	2.09
	1st EM	–0.0676	–0.274	0.398	1.45	–0.282	0.0076	37.10
	4th EM	–0.0169	–0.276	0.439	1.59	–0.288	0.0185	24.41
	5th EM	–0.0169	–0.278	0.444	1.60	–0.290	0.0117	24.79
FC=0.25	CD	–0.655	–0.34	0.32	0.94	–0.24	–0.098	2.45
	1st EM	–0.0676	–0.34	0.37	1.09	–0.34	–0.0017	200
	4th EM	–0.0338	–0.34	0.41	1.2	–0.36	0.0116	31
	7th EM	0	–0.34	0.43	1.26	–0.36	0.015	24

Figure IV.3.15 and Figure IV.3.16 report qualitative comparison of the strain maps for the two case studies at the first EM peak and the fifth EM peak respectively.

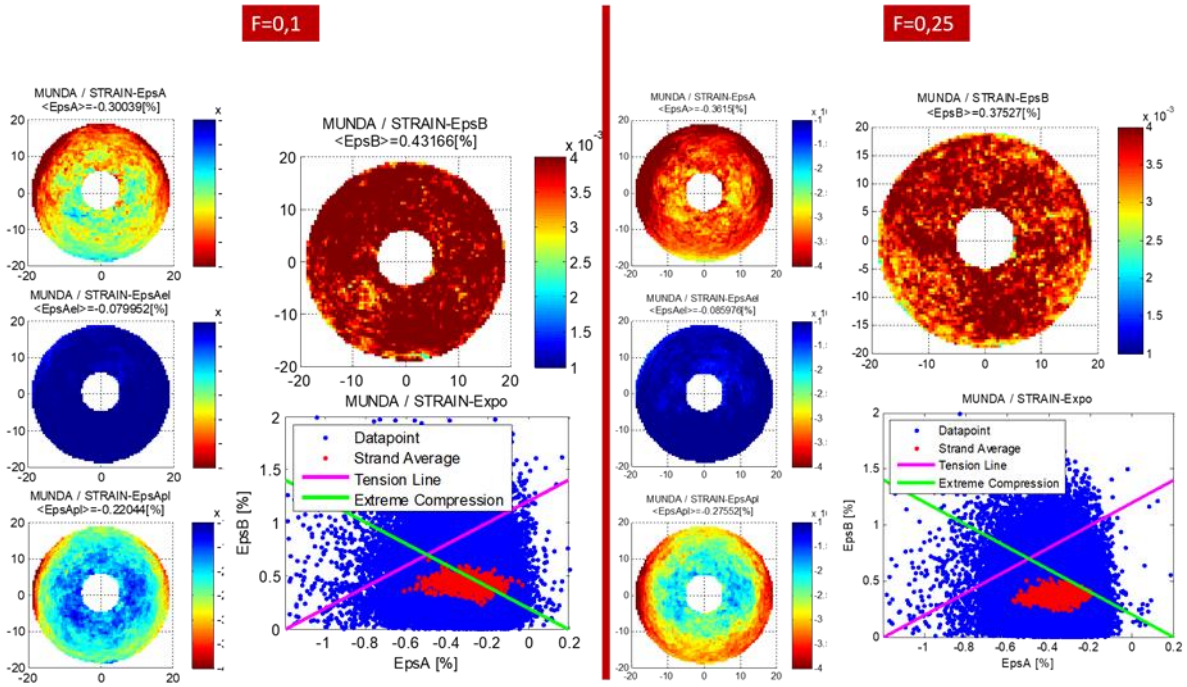

Figure IV.3.15. Comparison between FC=0.1 and 0.25 of cumulative polar maps of strains at the first EM cycle peak.

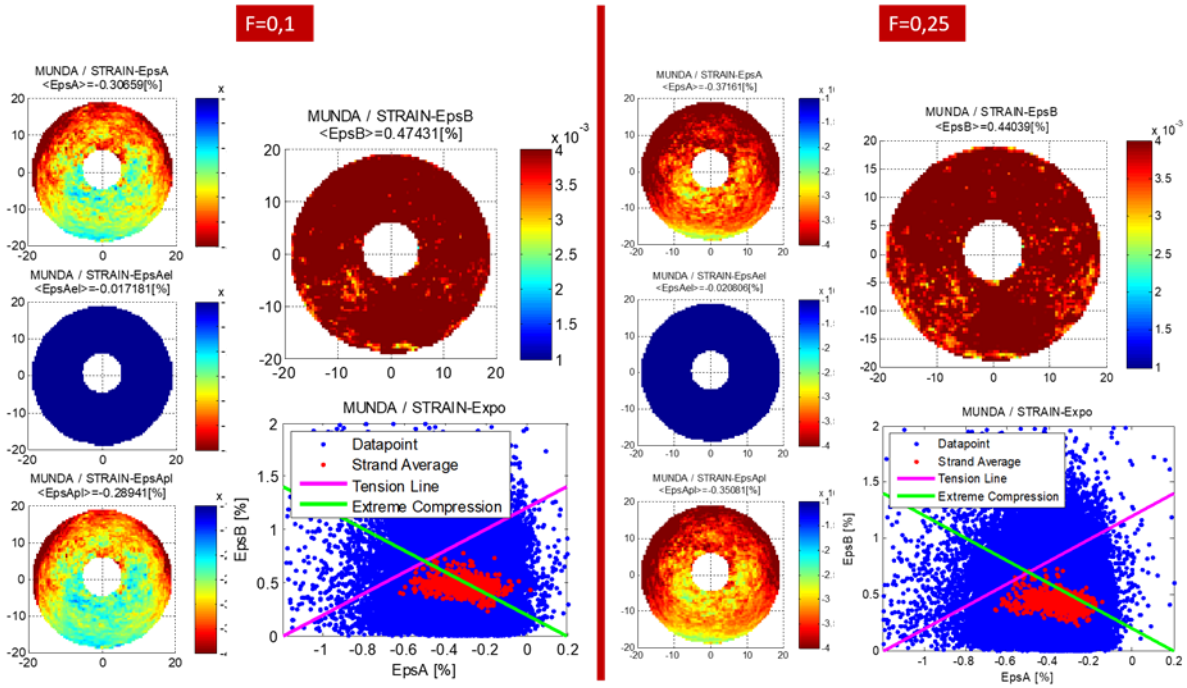

Figure IV.3.16. Comparison between FC=0.1 and 0.25 of cumulative polar maps of strains at the 5th EM cycle peak.

The higher friction coefficient makes the full cable stiffer (as for the petal), which translates to a globally more compressive state and less exposure to tensile strains and so to the risk of the filaments fractures. The EM cycles amplify this behavior and the wires have more tendency to move for the low FC cable as shown by the plot of the local VF as a function of the angular position in Figure IV.3.17. Nevertheless, it looks like this difference

is reduced as the EM cycles accumulate, and already after 5 EM cycles, the curves are quite similar.

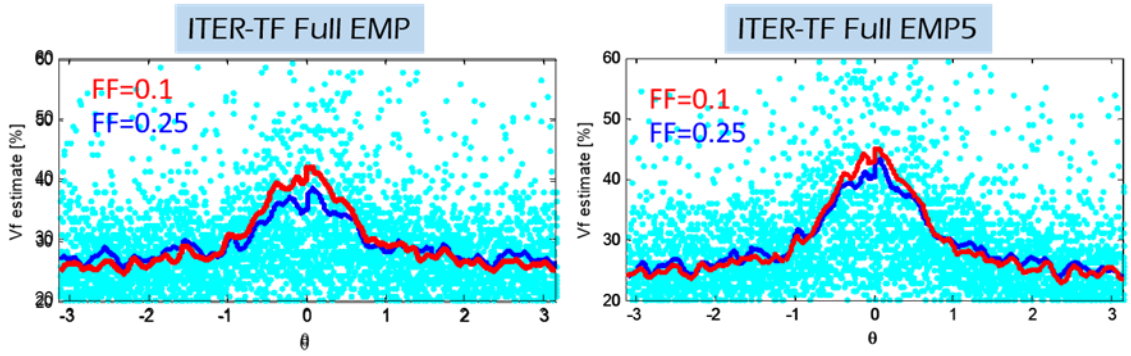

Figure IV.3.17. Plot of the local VF as a function of the angular position for two different FCs at the 1st and 5th EMPs.

IV.3.3 Conclusion

The performed parametric studies show a clear transition from the locked to the loose behavior through the evolution of fractures, contacts and bending ratio. The code indicates very different behaviors of the cable as a function of its compaction as expected by (Bessette 2014) and (Chiletti 2020).

The friction coefficient is set at 0.1 and all the main studies have been performed at this value. However, the real friction between strands in contact is unknown, and probably more complex than a simple friction coefficient. Future work and investigations, with a tribometer for example, are recommended to deduce a contact model for the simulations.

IV.4 CHAPTER – STUDY AND COMPARISON OF OTHER CICCs DESIGNS

This chapter aims to highlight the versatility of MULTIFIL to model fusion cables that was reached thanks to this Ph.D. work. The simulated cables are made of Nb_3Sn wires, and so the same material constitutive laws are used, although it would be possible to implement material constitutive laws of NbTi, for example. Figure IV.4.1 reports the case studies modelled by MULTIFIL for this dissertation.

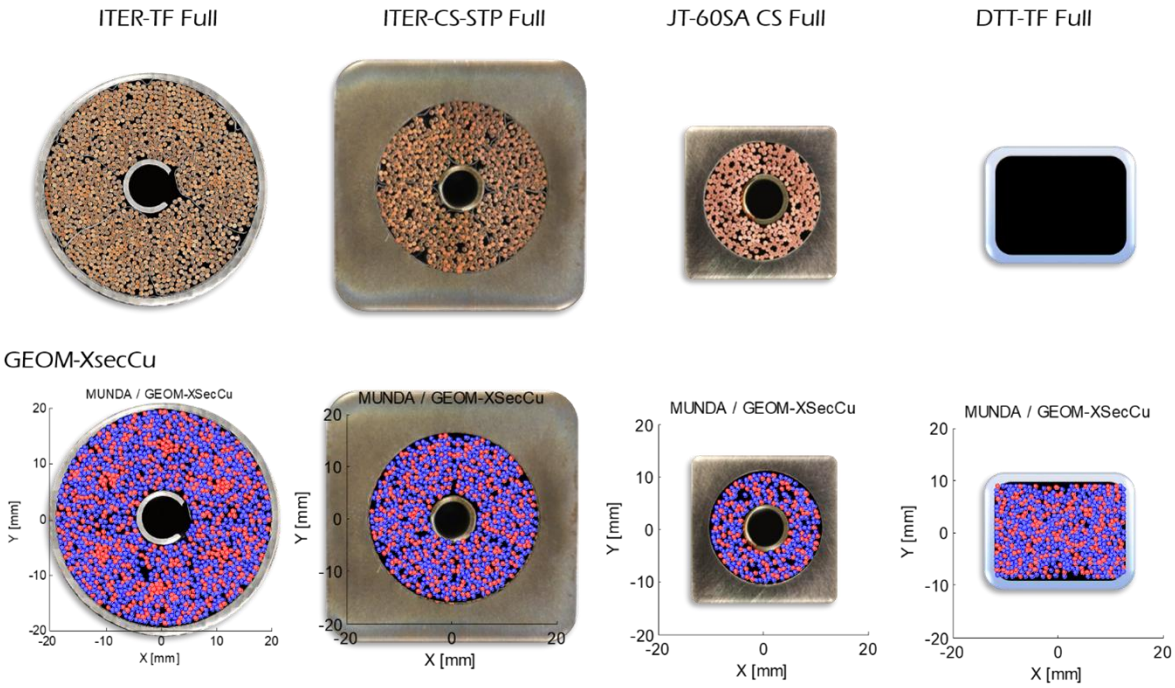

Figure IV.4.1. Nb_3Sn fusion cables simulated with MULTIFIL and compered to the corresponding real cable.

Section IV.4.1 provides the main design information about the simulated cables, while section IV.4.2 provides a comparative study of the geometries and presents some of studies. Finally, section IV.4.3 presents the geometry of the JT60SA TF CICC.

IV.4.1 Nb_3Sn full cable test cases

Table IV.4.1 reports all the input parameters for the MULTIFIL simulations to achieve a cable comparable to the corresponding nominal designs. Three different Nb_3Sn

cables have been modelled and compared to the ITER TF CICC (Bessette 2014), (Yoshida 2010), (Giannini 2021).

Table IV.4.1. MULTIFIL case studies input parameters compared to their nominal design.

	ITER CS STP design	**Full cable model**
Cabling layout	(2Nb_3Sn+1Cu)x3x4x4x6	
Central spiral diameter	9 mm	
Cable diameter	32.6mm	32 mm
Cr coated wire diameter	0.83 mm	
Wires number	864	
Wires friction	[-]	0.1
Jacket outer dimensions	49x49 mm	
Mean twist angle	0.945	0.935
Void fraction	33 %	33 %
Length	900 m	0.30 m
Operating conditions	(13 T, 45 kA)	
	JT60SA CS design	**Full cable model**
Cabling layout	(2Nb_3Sn+1Cu)x3x6x6	
Central spiral diameter	9 mm	
Cable diameter	21mm	20.738 mm
Cr coated wire diameter	0.82 mm	
Wires number	324	
Wires friction	[-]	0.1
Jacket outer dimensions	27.9x27.9 mm	
Mean twist angle	[-]	0.946
Void fraction	34 %	34 %
Length	11.5 km	0.30 m
Operating conditions	(8.9 T, 20 kA)	
	DTT TF design	**Full cable model**
Cabling layout	((2Nb_3Sn+1Cu)x2+3 Nb_3Sn)x3x4+3Cux4)x5	((2Nb_3Sn+1Cu)x3x3x4+3Cux 4)x5
Cable dimensions	25x18.3 mm	24.84x18 mm
Cr coated wire diameter	0.82 mm	
Wires number	600	
Wires friction	[-]	0.1
Jacket outer dimensions	26.9x20.2 mm	
Mean twist angle	[-]	0.967
Void fraction	26.4 %	26.7 %
Length	[-]	0.30 m
Operating conditions	(13.6 T, 31 kA)	

For each test case the numerical protocol presented in chapter III.3 was successfully applied to the manufacture simulation. Table IV.4.1 provides also an overview of the typical information required by the MUTLIFIL code for fusion cables. The

jacket information is used for the CD/WUCD simulations. In some cases, the mean twist angle was unknown and so in this sense the code was useful to predict it.

It must be noticed that the DTT TF CICC design foresees two different baseline triplets: one made of 3 Nb_3Sn wires and two others made of 1 Cu wire and 2 Nb_3Sn wires. The simulation considered only baseline triplets made of 1 Cu wire and 2 Nb_3Sn wires because of a MULTIFIL modelling limit. This issue can be easily solved in future works. The use of different triplets with respect to design does not affect the geometrical comparison, since the wire diameters are the same.

IV.4.2 CICCs geometrical comparison

The main goal of this section is to show the ability of the MUNDA protocol to process different input geometries and complex design configurations. Figure IV.4.2 reports the geometrical comparison highlighting the various shapes of the petals (first line) and the Cu content (second line) for each conductor.

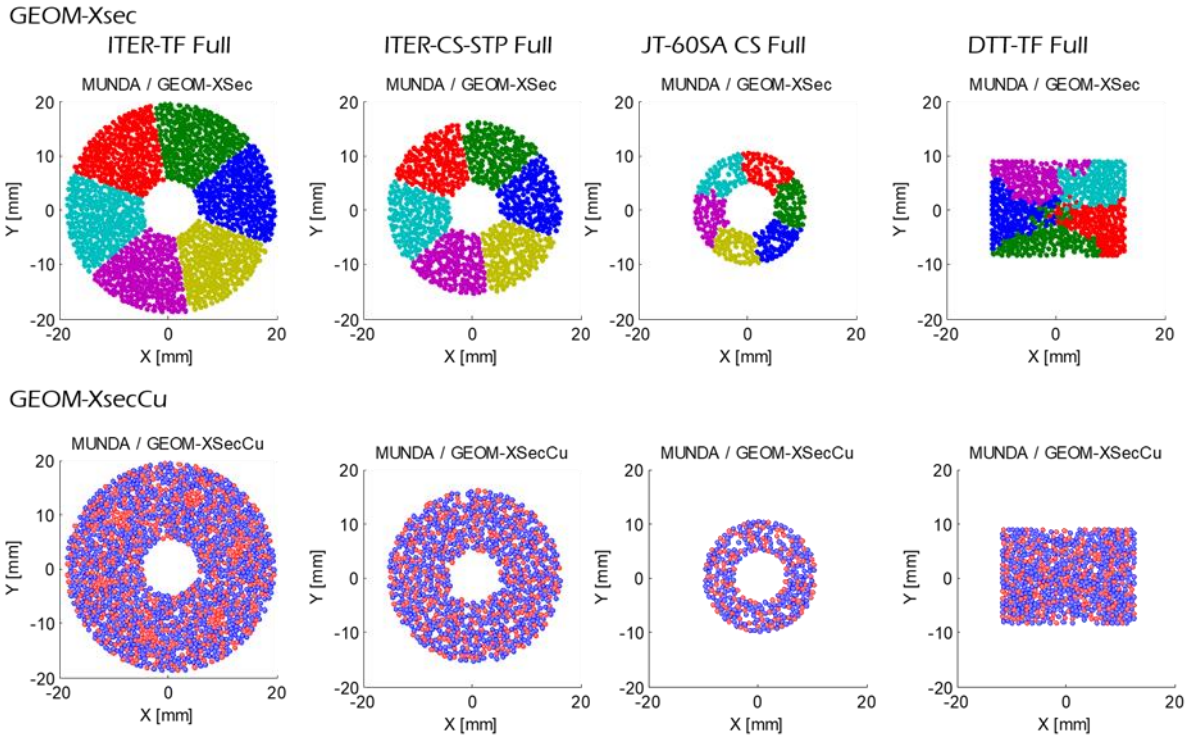

Figure IV.4.2. First line: petals identification for different designs; second line: Cu and Nb_3Sn wires identification, pink and blue respectively.

The Cu wires position shows the absence of Cu cores in the petals in JT-60SA CS and ITER CS CICCs with respect to the ITER TF CICC. However, the Cu cores are not visible for the DTT TF conductor. Moreover, due to the high compaction of the DTT TF cable, the wires of the petals tend to mix each other. The reality of this phenomenon has to be verified by examination of real DTT TF conductors. The difference of VF among the cables is visible as well.

Figure IV.4.3 reports the CPMs of the twist angle to highlight the differences in trajectories.

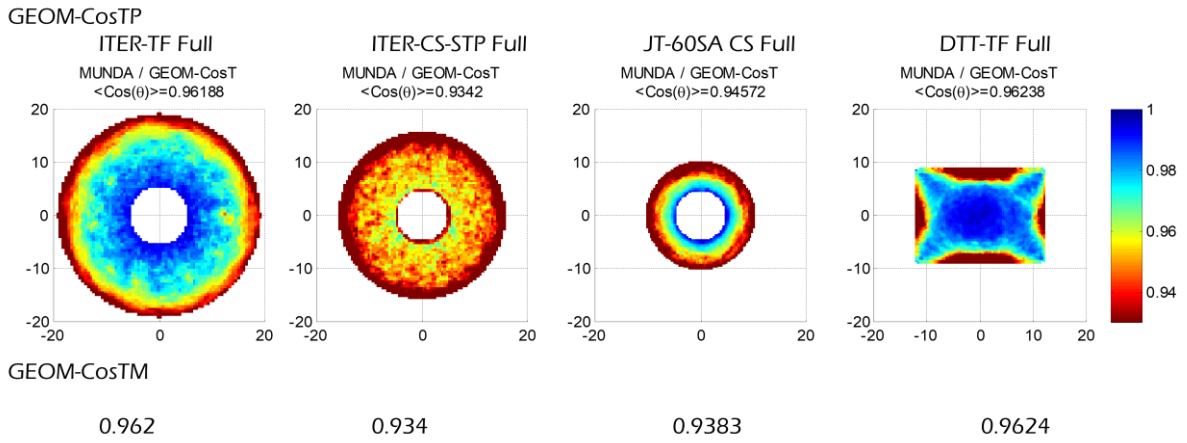

Figure IV.4.3. Cumulative polar maps of the twist angle for each Nb_3Sn conductor.

All the circular cables show, as expected from the cabling helices, a radial gradient presenting straighter wires towards the center of the cable. Clearly the ITER CS is characterized by more angle inclination with respect to the cable axis due to the Short Twist Pitch (STP) design. An interesting distribution is shown by the rectangular geometry with straighter wires up to the cable's corners. This specific distribution of the void should be confirmed, but tends to point in the direction of a "straightening" of the wires during cable compaction to this specific rectangular shape.

Figure IV.4.4 reports an assessment of the local VF as CPM (first line) and as angular distribution (second line).

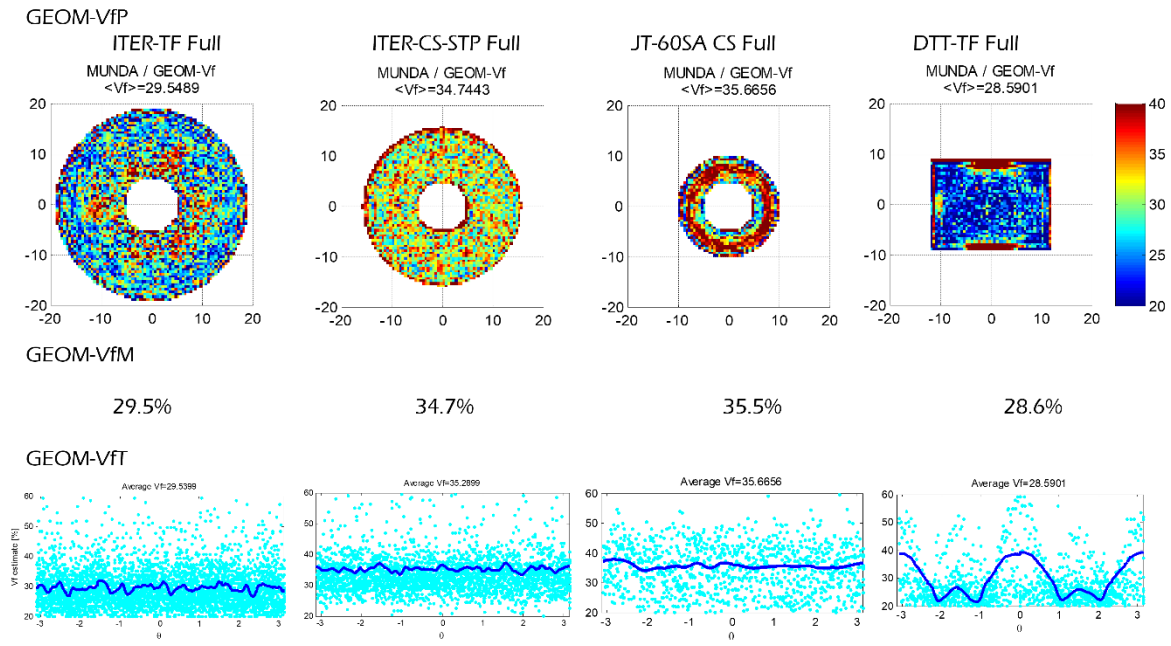

Figure IV.4.4. First line: CPM of the local VF, second line: average local VF as a function of the angular position on the cross-section.

The three circular cables show a constant VF as a function of the angular coordinate ϑ. However, the CPMs present a completely different radial distribution depending on the test case showing thus that the local VF distribution is probably a function of the dimensions and of the average VF itself. Moreover, the angular plot of local VF for the rectangular shape shows a particular distribution of VF with minimum peaks corresponding to the angles.

In conclusion, using the numerical and analysis protocol define in this Ph.D. dissertation, it is possible to simulate and compare various CICCs and get predictive values out of the models, to be confronted to real cables analysis.

IV.4.3 TF JT60SA model

This paragraph is dedicated to the geometrical analysis of the NbTi cable of the JT-60SA TF CICC (Yoshida 2010). The input parameters compared to the design are reported in Table IV.4.2.

Table IV.4.2. MULTIFIL input parameters compared to the baseline design for JT-60SA TF CICC.

	JT60SA TF design	Full cable model
Cabling layout	(2Nb_3Sn+1Cu)x3x3x3x6	
Cable dimensions	18x22 mm	17.89x21.9 mm
Cr coated wire diameter	0.83 mm	
Wires number	486	
Wires friction	[-]	0.1
Jacket outer dimensions	22x26 mm	
Mean twist angle	[-]	0.969
Void fraction	32 %	32.5 %
Length	24.4 km	0.30 m
Operating conditions	(5.56 T, 25.7 kA)	

Figure IV.4.5 reports the cross-section for the identification of the petals and Cu wires positions.

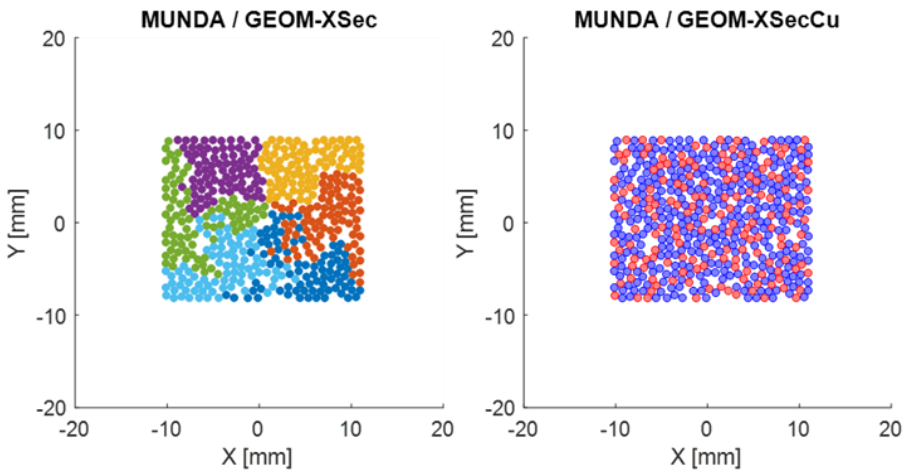

Figure IV.4.5. Left: petals identification for JT-60SA TF CICC; right: Cu and Nb_3Sn wires identification, pink and blue respectively.

With respect to what was observed for the DTT TF CICC, the petals are strongly interpenetrating each other. This effect could be a consequence of the shaping simulation without boundary between petals. Further studies and upgrades might need to be done on the numerical approach of the rectangular cables without internal wrappings in order to be representative of the real cabling procedure, where petals are pre-compacted before being cabled. A preliminary suggestion is to keep the petals separated with helical rigid tools during the outer dimensions reduction and then remove them for the further phases of the simulation.

Figure IV.4.6 reports the twist angle and local VF CPM on the first line and the angular variation of the average VF on the second line.

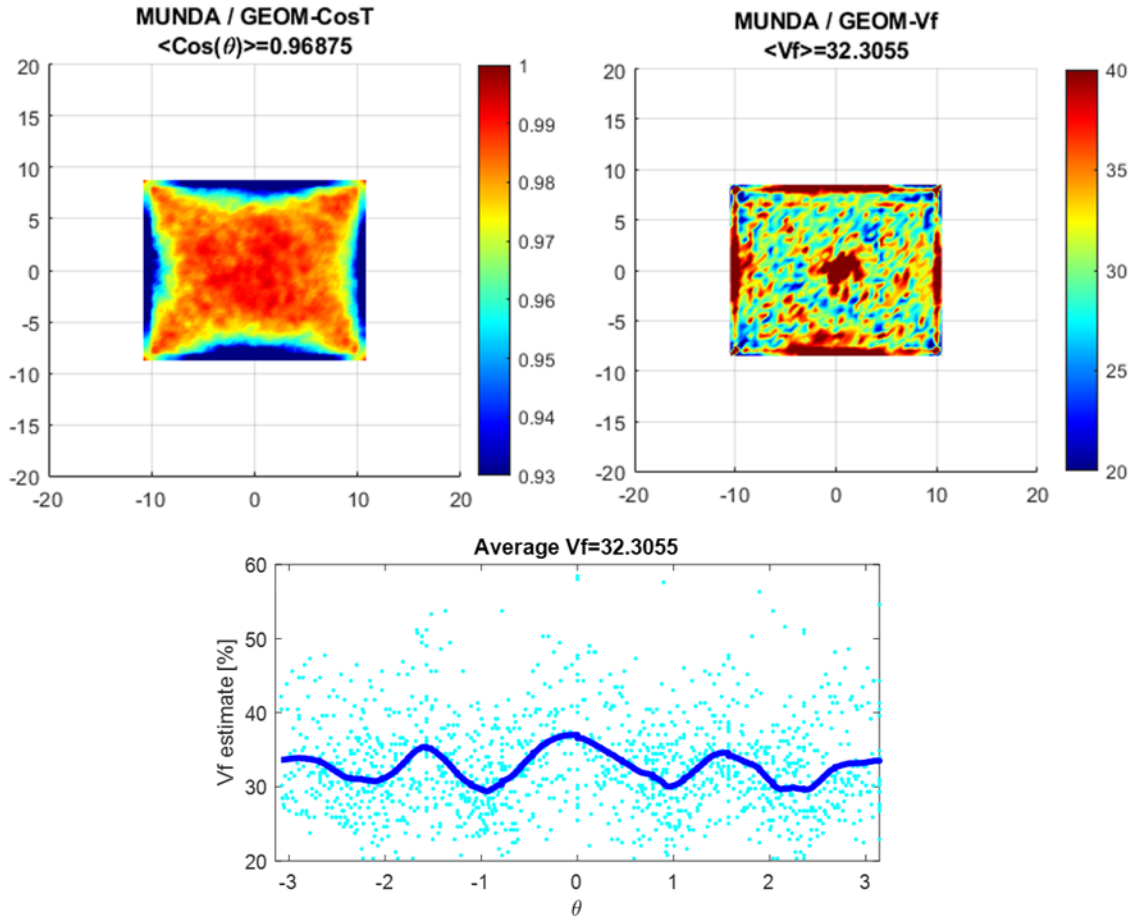

Figure IV.4.6. First line: CPMs of the twist angel and local VF; second line: average local VF as a function of the angular position on the cross-section for the JT-60SA TF CICC.

The behavior is quite similar to what was observed for the DTT TF CICC, but less amplified probably due to the larger VF.

IV.4.4 Conclusion

Both the numerical MULTIFIL protocol developed to shape fusion cables and the MUNDA post-processing protocol to study the main geometrical parameters have been successfully applied to different CICC geometries and designs.

Preliminary analyses and geometrical comparison of conductors from different fusion Tokamaks highlighted important features that could affect the electrical behavior of the cables, such as the local VF distribution.

Both the numerical and post-processing protocols are ready to be applied for a mechanical analysis of the different conductors behavior under thermal and EM loadings, similar to the studies performed for the ITER TF CICC.

CONCLUSIONS

CONCLUSION AND PERSPECTIVES

The work presented in this Ph.D. dissertation aimed at reaching an improved understanding of one of the major issues related to the ITER magnet system. The superconductor Nb_3Sn composing the TF coil wires is brittle and strain-sensitive and this peculiarity influences the current carrying capacity of the superconductor. At the same time, experimental tests showed that after 1000 cyclic loadings under nominal operative conditions (68 kA and 11.8 T), the CICCs of the TF coil are characterized by a degradation of the performances, measured by a decrease in T_{cs} which translates into operating margin reduction. However, even though several works attribute the loss of performance to reversible or irreversible mechanical phenomena occurring at the scale of the strands, it is not possible to measure the local strain inside the cables and thus to tackle the root cause of the degradation. The ITER International Organization and CEA therefore promoted the adaptation of the MULTIFIL code, which can simulate the mechanical interaction of hundreds of strands, to study the ITER CICCs in order to reproduce the thermomechanical and electromechanical loadings applied to these conductors, computing the strain maps at the level of the individual wires. A former version of the code created a sub-scale model of the TF CICC with MULTIFIL in order to simulate the conductor behavior when subjected to the same loadings as those applied to SULTAN samples. It nevertheless left many developments unfinished and many open questions remained.

This Ph.D. project, based on the work of H. Bajas tried to answer the needs of ITER and of the fusion community through the creation of a reliable model for simulating fusion cables in terms of representability and understanding of how the mechanical phenomena at the local and macroscopic scale affect the electrical performance of the conductor. Moreover, since the precise understanding of the degradation phenomenon that goes with cyclic operation is still quite debated, this Ph.D. project tackled this issue through both experimental activities and numerical modeling.

The experimental activities aimed at investigating the fatigue behavior in traction and compression of Nb_3Sn wires when submitted to thousands of cycles of uniaxial loadings. Several experimental campaigns were performed under tensile and compressive solicitations both at room and cryogenic temperature. These experimental activities allowed a full mechanical characterization of the strand properties, both its

envelope and cyclic loading curves, more detailed than the studies presented in literature for tensile tests of Nb_3Sn IT-wires for hundreds of cycles. The tensile campaigns highlighted two phenomena at RT associated with the plastic deformation of the wire. The tensile tests performed at cryogenic temperature need further improvements, but the cyclic behavior of the strain provides results in reasonable agreement with literature. The range of accumulated strain by ratcheting effect (~0.02% after 1000 cycles for traction and 250 cycles for compression) is relevant to a change in the current carrying capability, although the applied load during the uniaxial tests is higher than what is expected in strands inside a cable. Differently from traction, in compression the effect is only cumulative. Moreover, thanks to the work of this Ph.D. project a completely new experimental protocol was developed to test very brittle and small superconducting wires in compression. The first results, if compared to the tensile tests, show a reasonable behavior that would benefit from additional cross-checks and statistical treatment. The perspectives of this experimental work rely on further campaigns to confirm the compressive and cryogenic tensile results, while the cyclic tensile tests at RT can be fitted to provide mechanical constitutive laws to be implemented in numerical codes, like MULTIFIL.

Thanks to the numerical work based on the MULTIFIL code a new reliable and solid model for the simulation of the CICCs was created to assess the local and global strain state for a complex full-scale cable geometry, thanks to the integration of the new code-core in support of the fusion cable study. Moreover, numerical protocol and post-processing routines were developed ad-hoc for the MULTIFIL study of fusion cables. In particular, the Ph.D. investigation on fusion Nb_3Sn CICCs is based on two main kinds of study: phenomenological understanding of the macroscopic mechanical mechanisms affecting the global electrical performance degradation of the conductor and impact of the design parameters on the electromechanical behavior of the cable. The first point was treated by a deep analysis of the ITER TF single petal and full cable models. The second point is treated instead through a parametric study on the same case studies. The procedure, in the end, was also applied to several other Nb_3Sn CICC case studies. The ITER TF CICC model simulations highlighted more exposure to tensile strain of the full cable model than in the single petal model. Hence the single petal model used in past works could not be completely representative of the main mechanisms occurring inside a full conductor. The major effect of the EM cycles is a progressive softening of the cable due to large plasticization of the strands coupled to a release of internal frictional contacts, and a substantial change of the jacket-cable equilibrium in agreement with the jacket relaxation assessments in post-mortem SULTAN samples analyses. In light of these results, the typical initial drop (first few cycles) of the T_{cs} observed in several TF conductors could be interpreted as a compressive shift of the cable-jacket equilibrium. The full-cable model preliminary analyses show a good agreement with experimental

studies and the model seems to be able to correctly describe typical behaviors of real TF CICCs like strands displacements in low pressure side or void fraction distribution in the cable. The performed parametric studies show a clear transition from the locked to the loose behavior through the evolution of fractures, contacts and bending and plastic ratios. The friction coefficient is set at 0.1 and all the main studies have been performed at this value. However, the real friction between strands in contact is unknown, and probably more complex than a simple friction coefficient. Future work and investigations, with a tribometer for example, are recommended to deduce a more realistic contact model for the simulations. Both the numerical MULTIFIL protocol developed to shape fusion cables and the MUNDA post-processing protocol to study the main geometrical parameters have been successfully applied to other tokamak cables as well. Preliminary analyses of geometrical comparison of these conductors highlighted important mechanical features that could affect the electrical behavior of the cables, such as the local VF distribution. Future studies should focus on the mechanical study of the different conductors under thermal and EM loadings, similar to the studies performed for the ITER TF CICC.

ANNEXES

A. ANNEX – HEAT TREATMENT PROCEDURE

Several heat treatments were performed during the Ph.D. work in support to the experimental activities at the GAIM Laboratory (CEA Cadarache) in order to prepare a set of reacted Nb_3Sn strands and/or bundles ready to be tested. The heat treatment is specific to the studied strand and follows the manufacturer recommended profile.

A.1 Oven description and regulation system

The oven, illustrated in Figure A.1, is tubular and horizontal. It has four independent heating zones that are 1080 mm long. The heating chamber has an inner diameter of 275 mm and is made of refractory stainless steel. At the ends, there are all the auxiliary components and four shields to mitigate the heating towards the outside. At one end (left side in Figure A.1), there are ten thermocouples and the gas injection and at the other end (right side in Figure A.1) there are the gas extraction system and a pumping system.

Figure A.1. The CEA oven.

The thermocouples, Figure A.2a), allow measuring the temperature continuously inside the heating chamber in ten different points of the oven. The pumping system, Figure A.2b), is needed to empty the chamber from air/gas. The gas injection/extraction system is used to heat under inert gas atmosphere, in this case Argon.

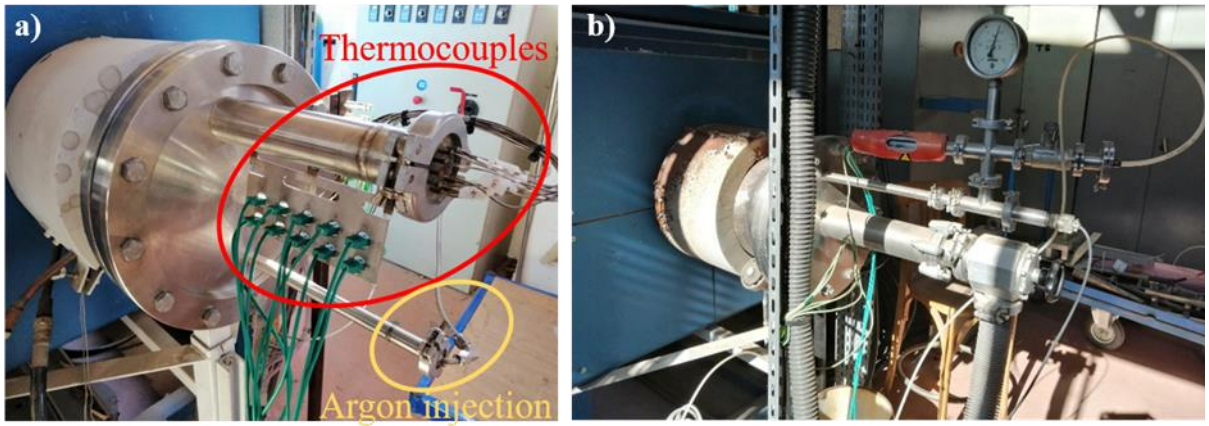

Figure A.2. a) Left end of the oven, in red the thermocouples connectors and in yellow the Argon injection system. b) Right end of the oven with the pumping system and the Argon extraction system.

A scheme of the oven with all the main components is given in Figure A.3.

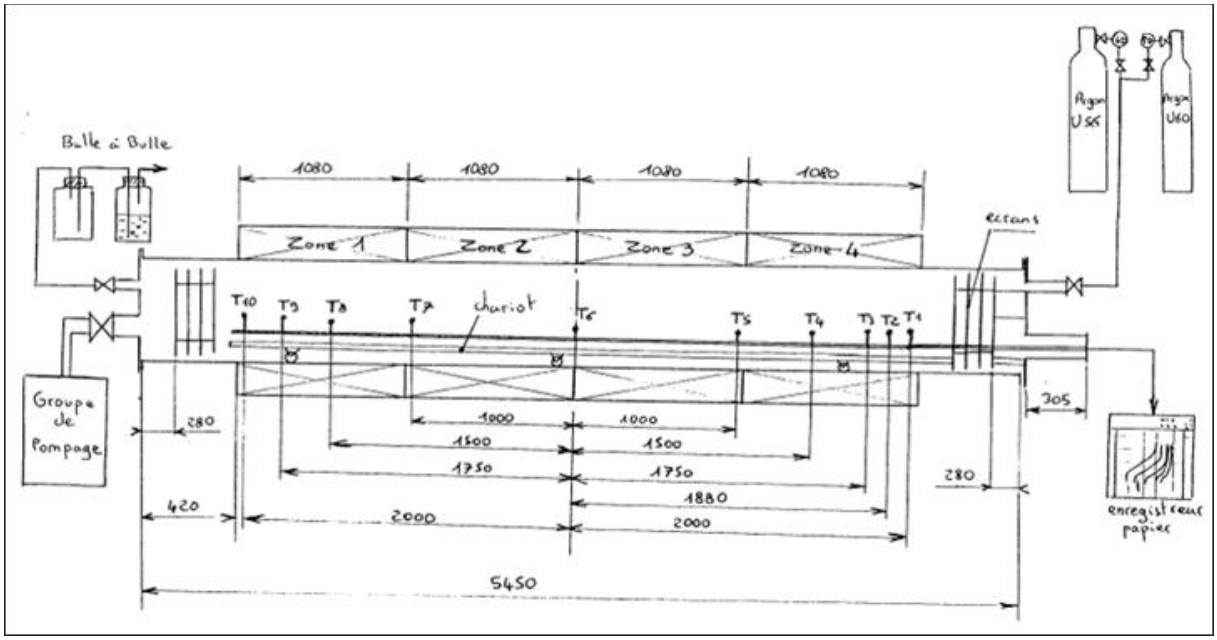

Figure A.3. Basic scheme of the oven with all the main components.

A main programmer and four slave regulators, one for each zone of the oven, ensure the temperature regulation of the oven. In particular, the main programmer gives the general instruction and each regulator has to tackle temperature variations in its own zone. A temperature security system is associated to each regulator to verify that in each zone the temperature does not exceed the limit value imposed by the operator. The local regulation is based on probes that are outside the heating chamber. At the same time, temperatures inside the heat chamber are measured for each zone in different points

thanks to the thermocouples. Figure A.4 shows the conceptual idea behind the oven regulation.

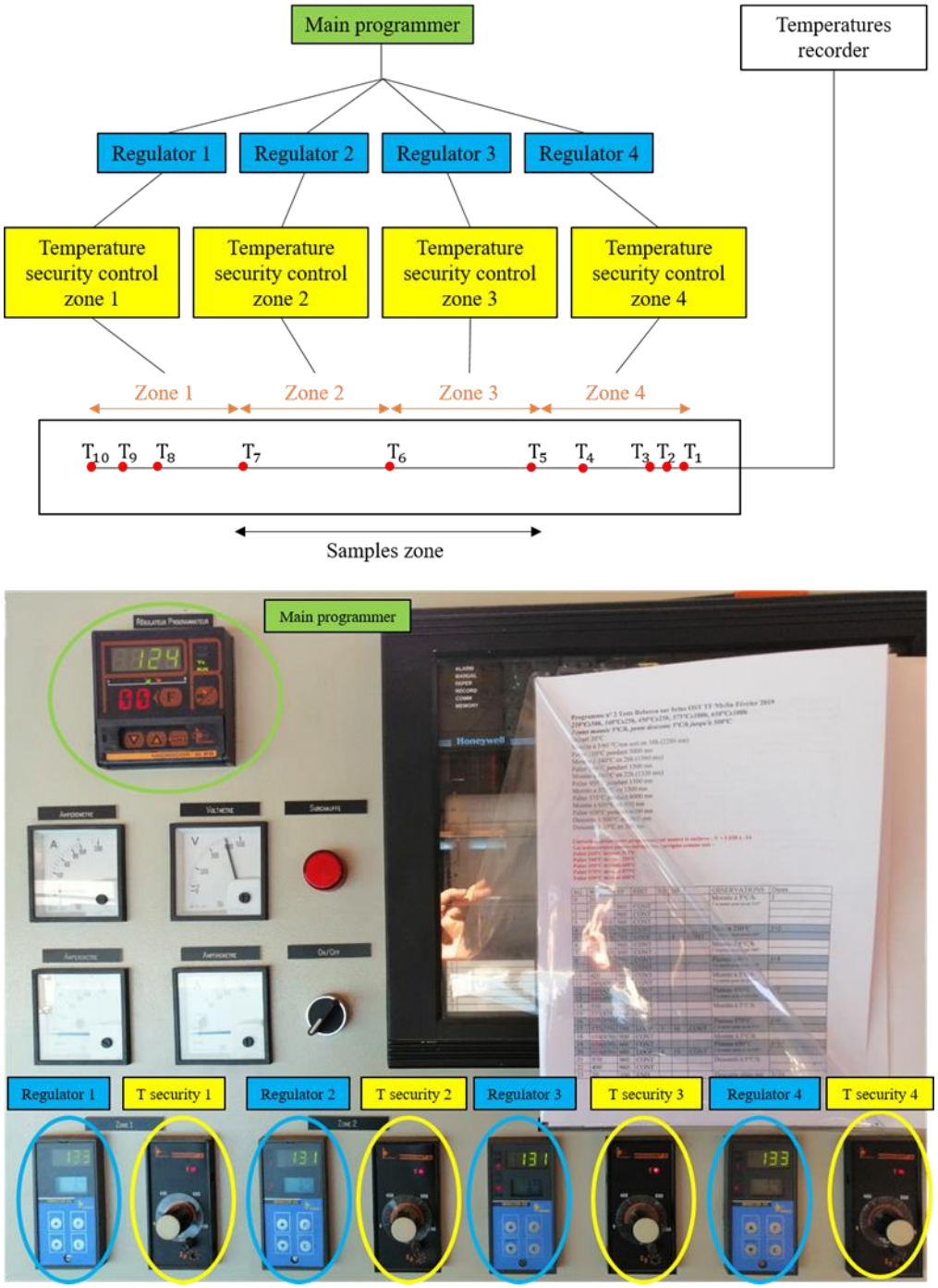

Figure A.4. Regulation system of the CEA oven based on a main programmer and four enslaved regulators controlling temperature variations in four different zones of the oven.

A.2 Samples description

The heat treatment has been always performed on OST G 01EX0571A01C Nb_3Sn strands supplied by Fusion for Energy. The samples can be fixed with the two different configurations shown in Figure A.5.

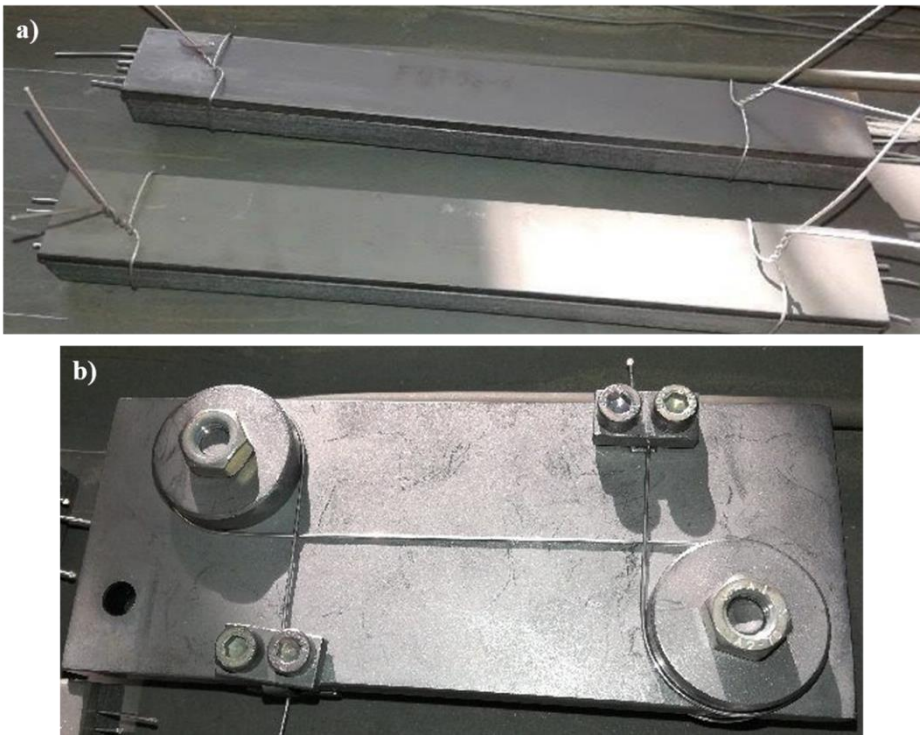

Figure A.5. a) Two holders containing each one 6 strands in a rectilinear configuration. b) Holder for the strand configuration ready to be tested.

All the strands are prepared, positioned and heat-treated in the oven avoiding any kind of displacement and subsequent bending stresses during and after the heat treatment.

Finally, all extremities of the strands are TIG-welded to avoid any tin-leakage during the heat treatment. This step is necessary just if the strands follow the internal tin method of manufacture.

A.3 Heat treatment program

The heat treatment program is the one used for a typical OST IT-strand (Boutboul 2016) and foresees 210 °C for 50 hours, 340 °C for 25 hours, 450 °C for 25 hours, 575 °C for 100 hours, 650 °C for 100 hours. The increase rate is 5 °C/h and during cool-down the decrease rate is 5 °C/h between 650 °C and 500 °C and afterwards a faster decrease in temperature following the natural cooling of the oven until the room temperature (significantly below 25 °C/h).

Because of an error between the main programmer and the enslaved regulators, it is necessary to apply the following correction to the step temperatures in order to achieve the desired temperatures: Y = 1.028 x -14. Therefore, to obtain a step of 210 °C, you have to set 202 °C in the main programmer. Table A.1 reports the details of the full heat treatment program.

Table A.1. Heat treatment program for the OST G 01EX0571A01C Nb_3Sn strands performed at CEA.

SG	WP	TP	EDIT	NB	DB		OBSERVATIONS	Dates

0	20						Ascent speed 5°C/h T to be set to have 210°	J
1	100	960	CONT					
2	180	960	CONT					
3	202(210)	360	CONT					
4	202(210)	750	CONT				Step at 210°C T to be set to have 210°	J+2
5	202(210)	750	LOOP	1	4	CONT		
6	290	960	CONT				Ascent speed 5°C/h T to be set to have 340°	
7	335(340)	600	CONT					
8	335(340)	750	CONT				Step at 340°C T to be set to have 340°	J+5
9	335(340)	750	CONT					
10	420	960	CONT				Ascent speed 5°C/h T to be set to have 450°	
11	449(450)	360	CONT					
12	449(450)	750	CONT				Step at 450°C T to be set to have 450°	J+7
13	449(450)	750	CONT					
14	530	960	CONT				Ascent speed 5°C/h	
15	577(575)	540	CONT					
16	577(575)	750	CONT				Step at 575°C T to be set to have 570°	J+9
17	577(575)	750	LOOP	3	16	CONT		
18	654(650)	900	CONT				Ascent speed 5°C/h	
19	654(650)	600	CONT				Step at 650°C T to be set to have 650°	J+13
20	654(650)	600	LOOP	4	19	CONT		
21	570	960	CONT				Descent speed 5°C/h	
22	490	960	CONT					
23	20	100	END				Descent	J+24

A.4 Oven starting protocol

The procedure to perform the heat treatment follows a specific protocol of which the main steps are here reported:

1. Placement of the samples in the central area between T7 and T5 where the temperature can be considered homogenous with a variation of +/- 2 °C.
2. Connection of the ten thermocouples to the temperature recorder and of the Argon pipe to the gas injection system of the oven (see Figure A.2).
3. Creation of an inert atmosphere without oxygen → empty the chamber from air with the pump until 0.1 Pa and then filled with Argon at atmospheric pressure. Repeat again and re-fill again with Argon until a pressure a bit higher than the atmospheric pressure.
4. Verification of the presence of leakages: in the extraction pipe, there are two electrodes making plasma and during the pumping phase when the chamber is near to vacuum, the plasma barely shines due to the few amounts of gas. If alcohol is

squirted on the critical points of possible leakage, the plasma brightness increases instantly if there is an effective leakage.

5. Choose and start the heat treatment program.
6. Switch the temperatures recorder connected to the thermocouples.

A.5 Performed heat treatment

Here in Figure A.6 an example of the temperature plot during the heat treatment. In particular, the plot refers to the probes T5 and T6 corresponding to the placement of the samples in the oven.

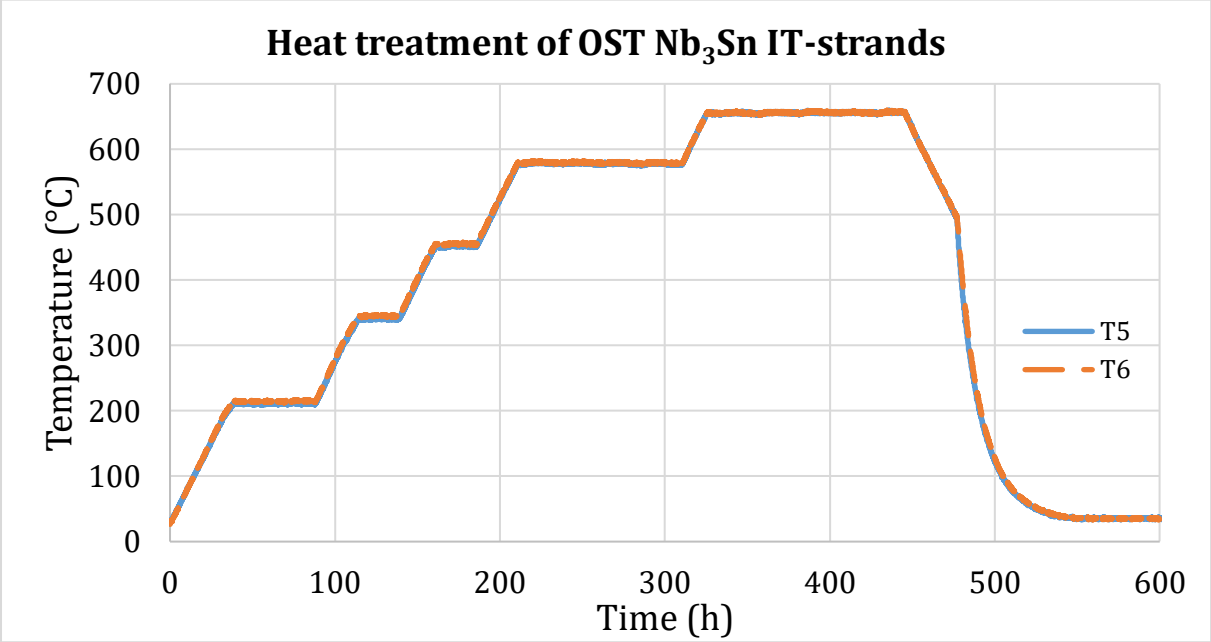

Figure A.6. Temperature plot for probes T5 and T6 during the heat treatment of OST Nb_3Sn IT-strands.

B. ANNEX – EXPERIMENTAL DEVICES DESIGN

During the Ph.D. project several tools were designed to adapt the tensile machine at the GAIM Lab, in order to be able to perform the required tests. This annex reports all the detailed plans of the designed devices during the Ph.D. for clarity and deeper understanding of the experimental procedures.

In particular, the section B.1 presents the design of the devices to apply the compressive forces to the bundle and of the cryogenic box. The box was designed to be able to host the tensile clamping system presented in section B.2 and the compressive tests. However, in order to be able to use the box for tensile tests it is important to add almost 20 Kg of weights since the box is not fixed on the bottom for insulating reasons. As anticipated in section II.3.1, the correct application of the uniaxial compressive force is essential for the success and reliability of the result.

Concerning the tensile tests, it was necessary to design a specific device able to clamp the Nb_3Sn wire with the SCUTT device (tubes + soldered balls, illustrated in paragraph II.2.1.1) and to keep the strand aligned with the axis of the machine. The first design is the one exposed in section B.2, the upper clamp slides along a fixed guide while the lower clamp is fixed. However, this design, achieved during the first year of the Ph.D., changed in the meanwhile and during the following years, it was adapted to fit in the cryogenic box. The last version is the one in Figure II.2.9, where the vertical component of the fix holder was removed and the base has a circular groove to facilitate the sample installation without bending the wire. Finally, two components were designed (section B.3) to consider in the tensile line the 1 kN load cell instead of the 100 kN load cell integrated in the tensile machine.

B.1 Cryogenic box and compressive tools

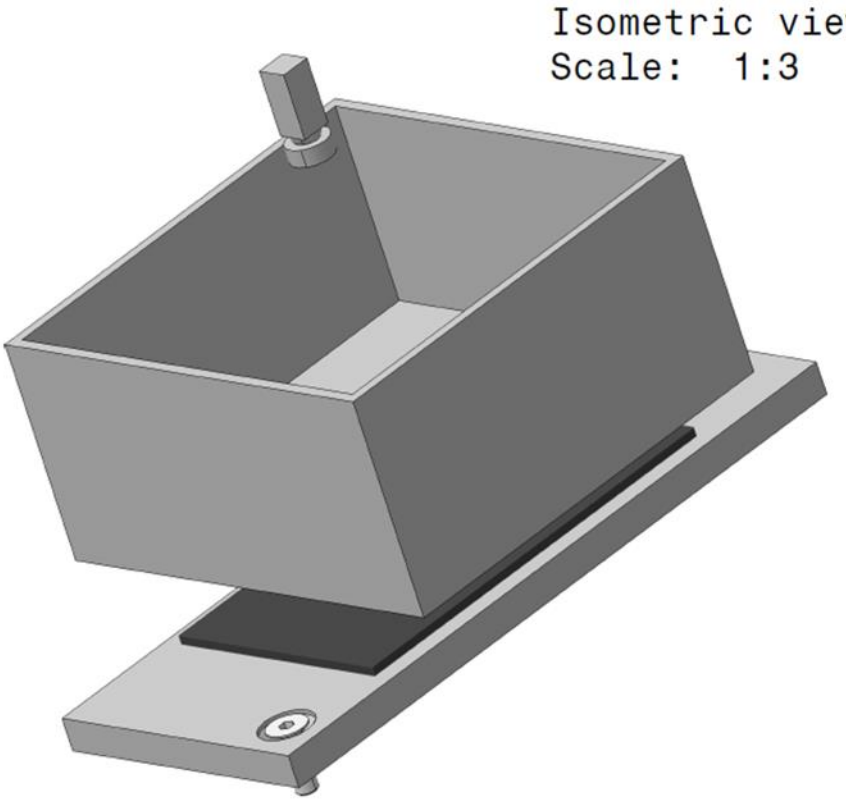

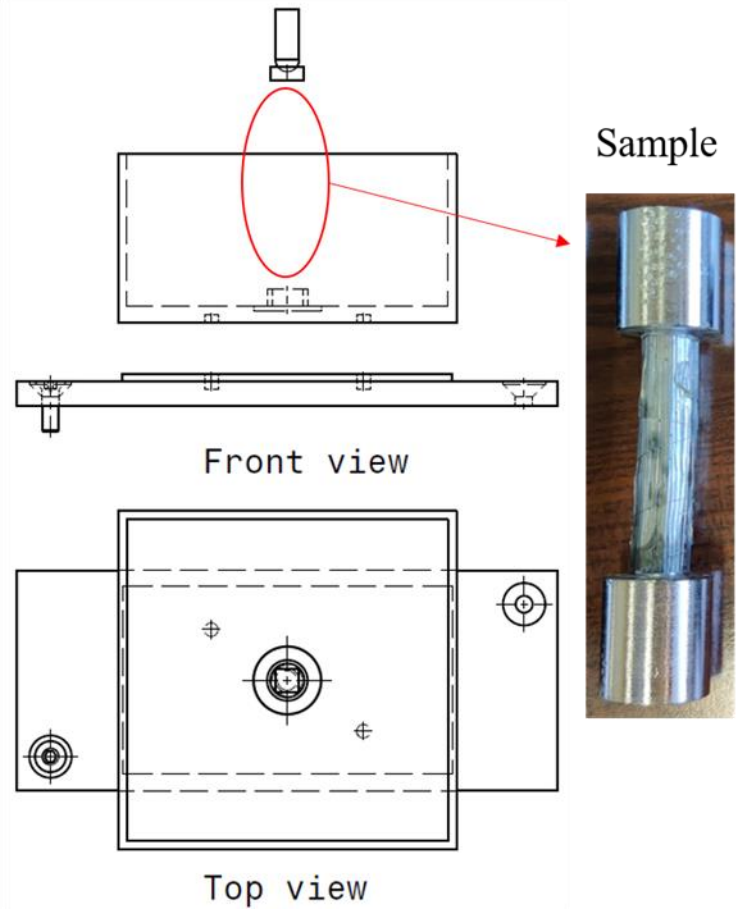

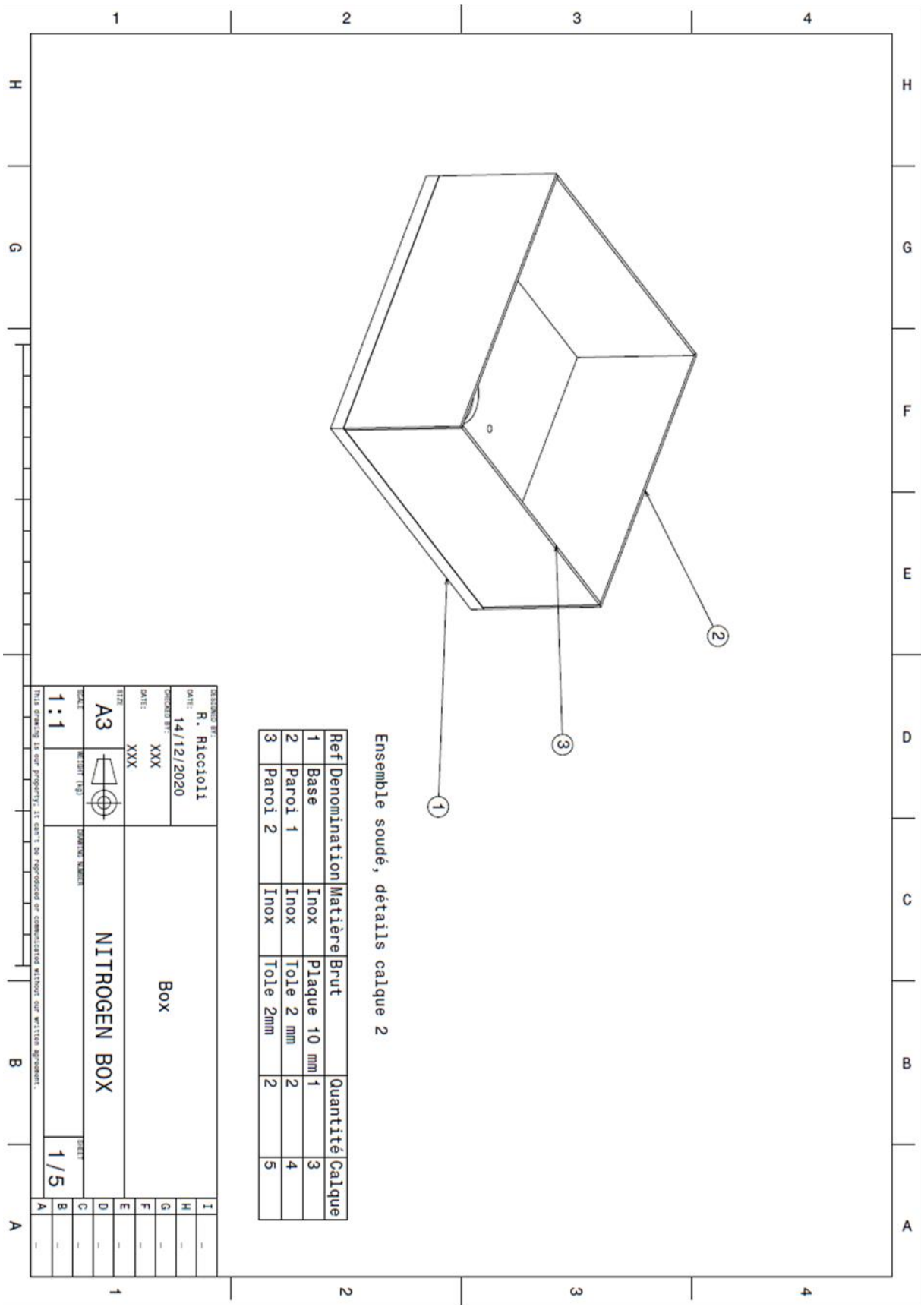
1
2
3
4
H
G
F
E
D
C
B
A
Ensemble soudé, détails calque 2
Ref Denomination Matière Brut Quantité Calque
1 Base Inox Plaque 10 mm 1 3
2 Paroi 1 Inox Tole 2 mm 2 4
3 Paroi 2 Inox Tole 2mm 2 5
DESIGNED BY: R. Riccioli
DATE: 14/12/2020
CHECKED BY: XXX
DATE: XXX
SIZE: A3
SCALE: 1:1
WEIGHT (kg)
DRAWING NUMBER
SHEET 1/5
Box
NITROGEN BOX
This drawing is our property; it can't be reproduced or communicated without our written agreement.

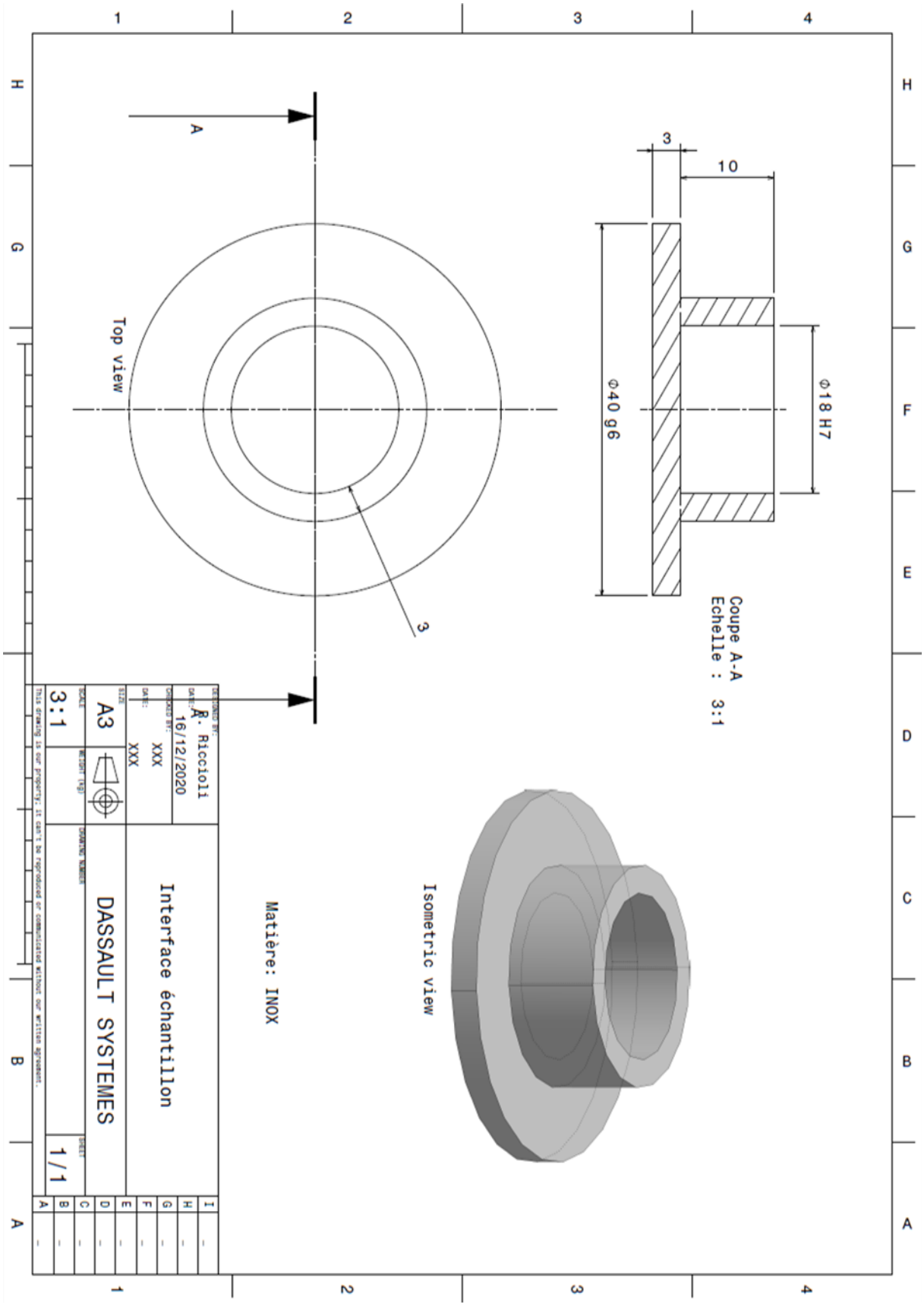
A
Top view
3
3
10
Φ40 g6
Φ18 H7
Coupe A-A
Echelle : 3:1
Isometric view
Matière: INOX
DESIGNED BY: A. Riccioli
DATE: 16/12/2020
CHECKED BY: XXX
DATE: XXX
SIZE: A3
SCALE: 3:1
WEIGHT (kg):
DRAWING NUMBER:
Interface échantillon
DASSAULT SYSTEMES
SHEET: 1/1
This drawing is our property; it can't be reproduced or communicated without our written agreement.

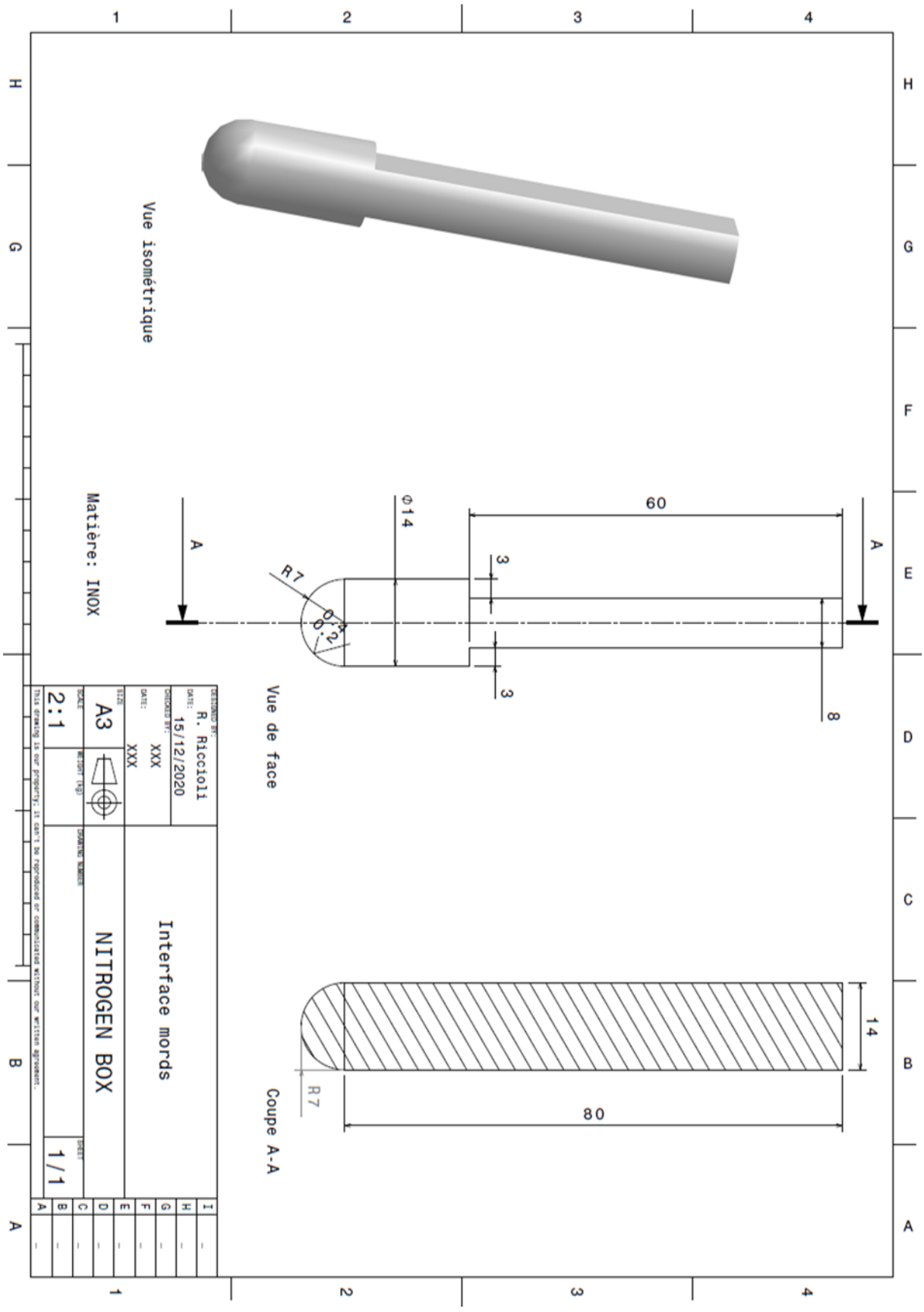
Vue isométrique
Matière: INOX
A
A
Φ14
60
3
3
8
R7
Vue de face
14
R7
80
Coupe A-A
Interface mords
NITROGEN BOX
R. Riccioli
15/12/2020
XXX
XXX
A3
2:1
1/1

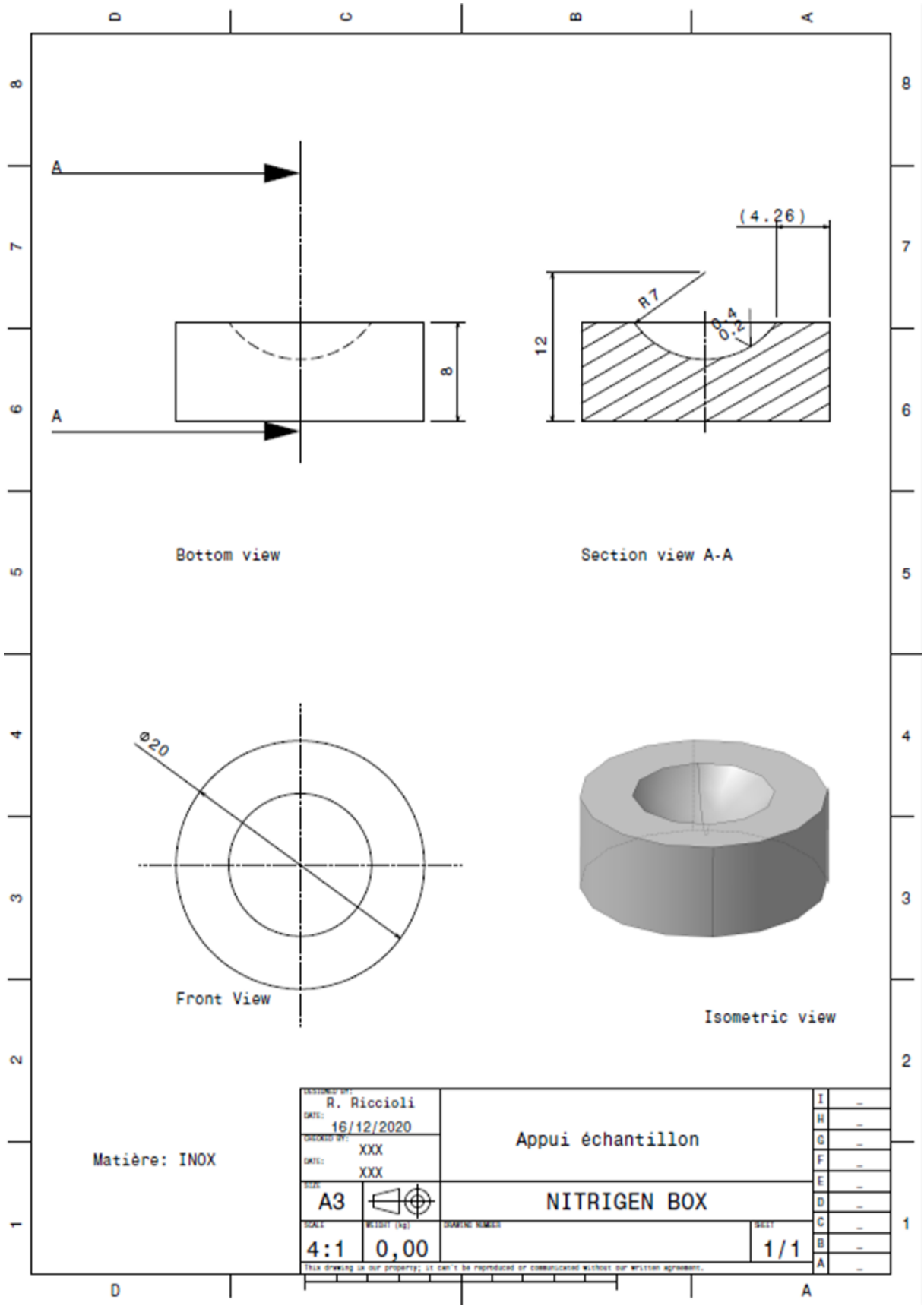
A
A
8
Bottom view
(4.26)
R7
0.4
0.2
12
Section view A-A
Ø20
Front View
Isometric view
Matière: INOX
R. Riccioli
16/12/2020
XXX
XXX
Appui échantillon
NITRIGEN BOX
A3
4:1
0,00
1/1

B.2 Tensile clamping device

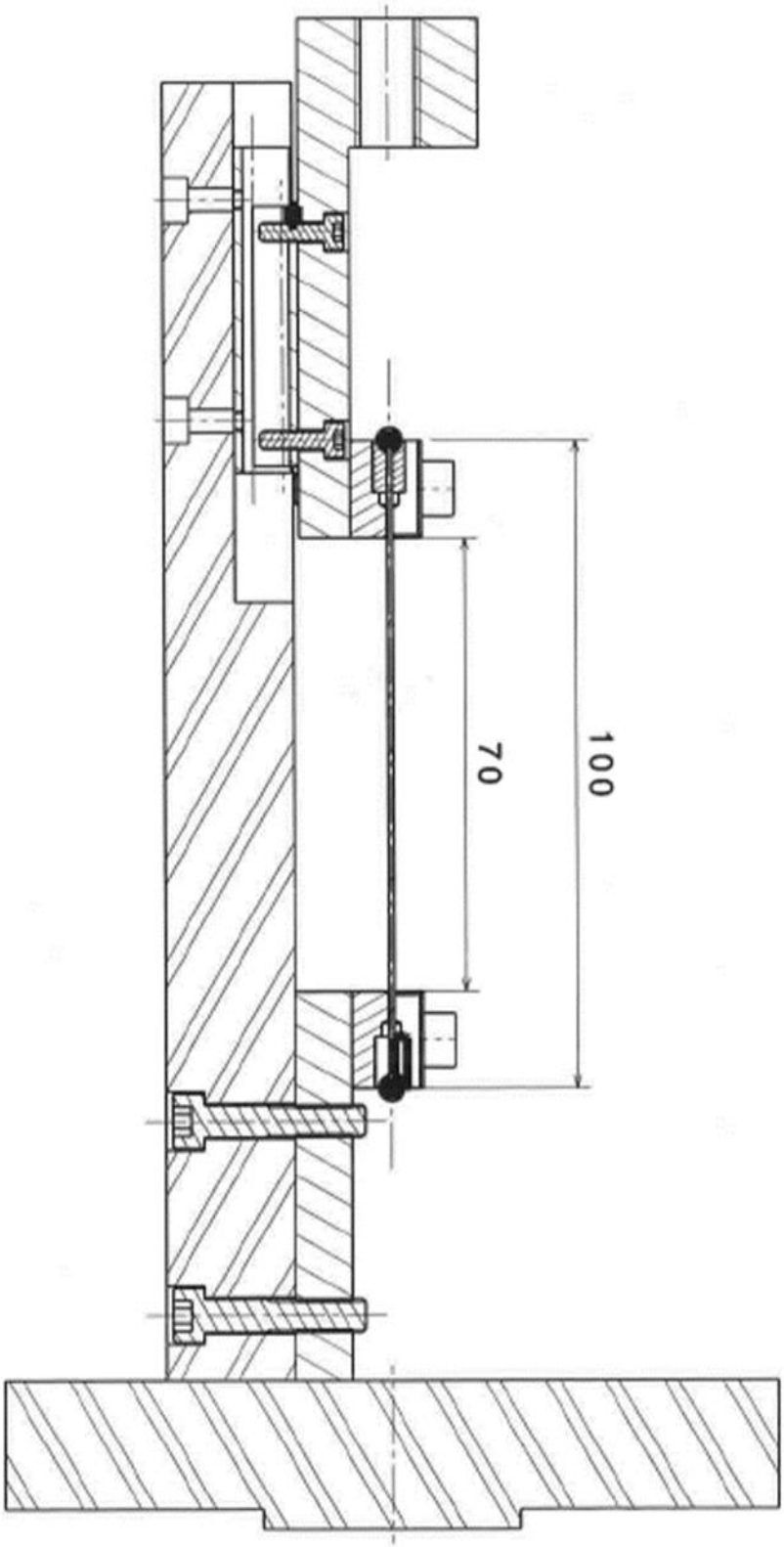

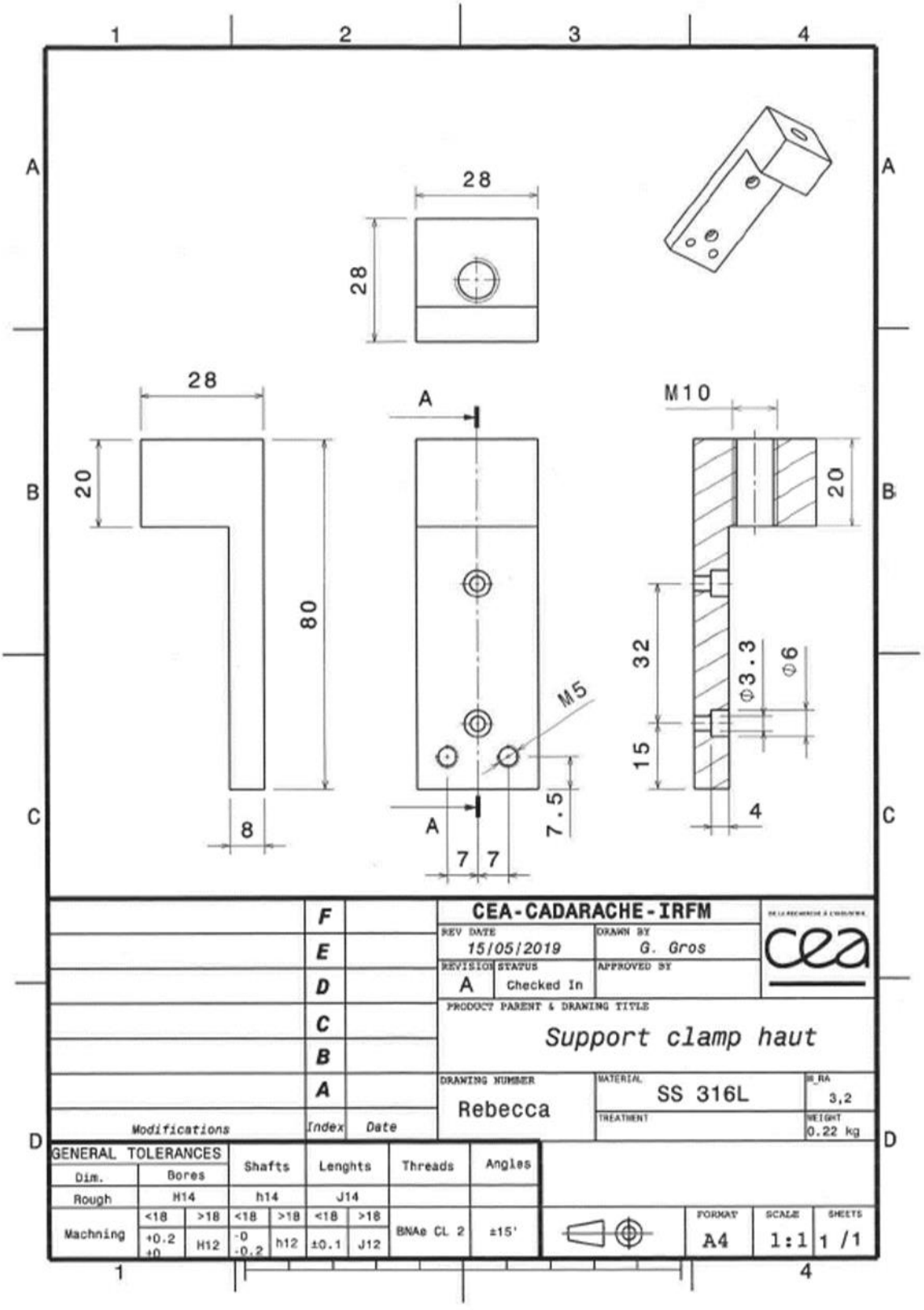

Modifications	Index	Date
	F	
	E	
	D	
	C	
	B	
	A	

CEA-CADARACHE-IRFM

REV DATE: 15/05/2019

DRAWN BY: G. Gros

REVISION: A

STATUS: Checked In

APPROVED BY:

PRODUCT PARENT & DRAWING TITLE: *Support clamp haut*

DRAWING NUMBER: Rebecca

MATERIAL: SS 316L

R_RA: 3,2

TREATMENT:

WEIGHT: 0.22 kg

GENERAL TOLERANCES								
Dim.	Bores		Shafts		Lenghts		Threads	Angles
Rough	H14		h14		J14			
Machning	<18	>18	<18	>18	<18	>18	BNAe CL 2	±15'
	+0.2 +0	H12	-0 -0.2	h12	±0.1	J12		

FORMAT: A4

SCALE: 1:1

SHEETS: 1 /1

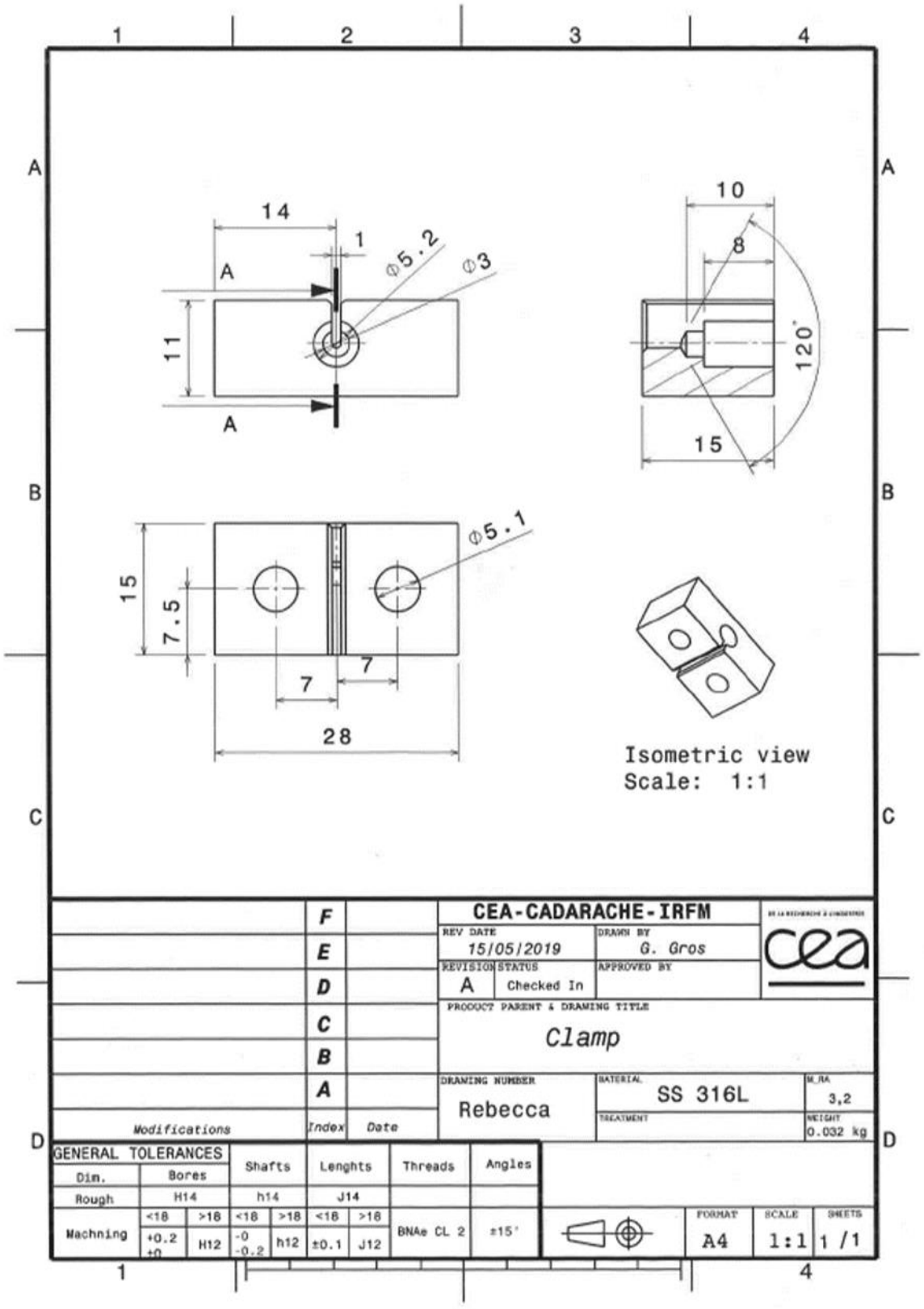
14
1
Ø5.2
Ø3
A
11
A
10
8
120°
15
15
7.5
Ø5.1
7
7
28
Isometric view
Scale: 1:1
CEA-CADARACHE-IRFM
REV DATE 15/05/2019
DRAWN BY G. Gros
REVISION STATUS A Checked In
APPROVED BY
PRODUCT PARENT & DRAWING TITLE
Clamp
DRAWING NUMBER Rebecca
MATERIAL SS 316L
TREATMENT
Ra 3,2
WEIGHT 0.032 kg
Modifications
Index
Date
GENERAL TOLERANCES
Dim. Bores Shafts Lenghts Threads Angles
Rough H14 h14 J14
Machning <18 +0.2 +0 >18 H12 <18 -0 -0.2 >18 h12 <18 ±0.1 >18 J12 BNAe CL 2 ±15'
FORMAT A4
SCALE 1:1
SHEETS 1 /1

B.3 Load cell adaptors

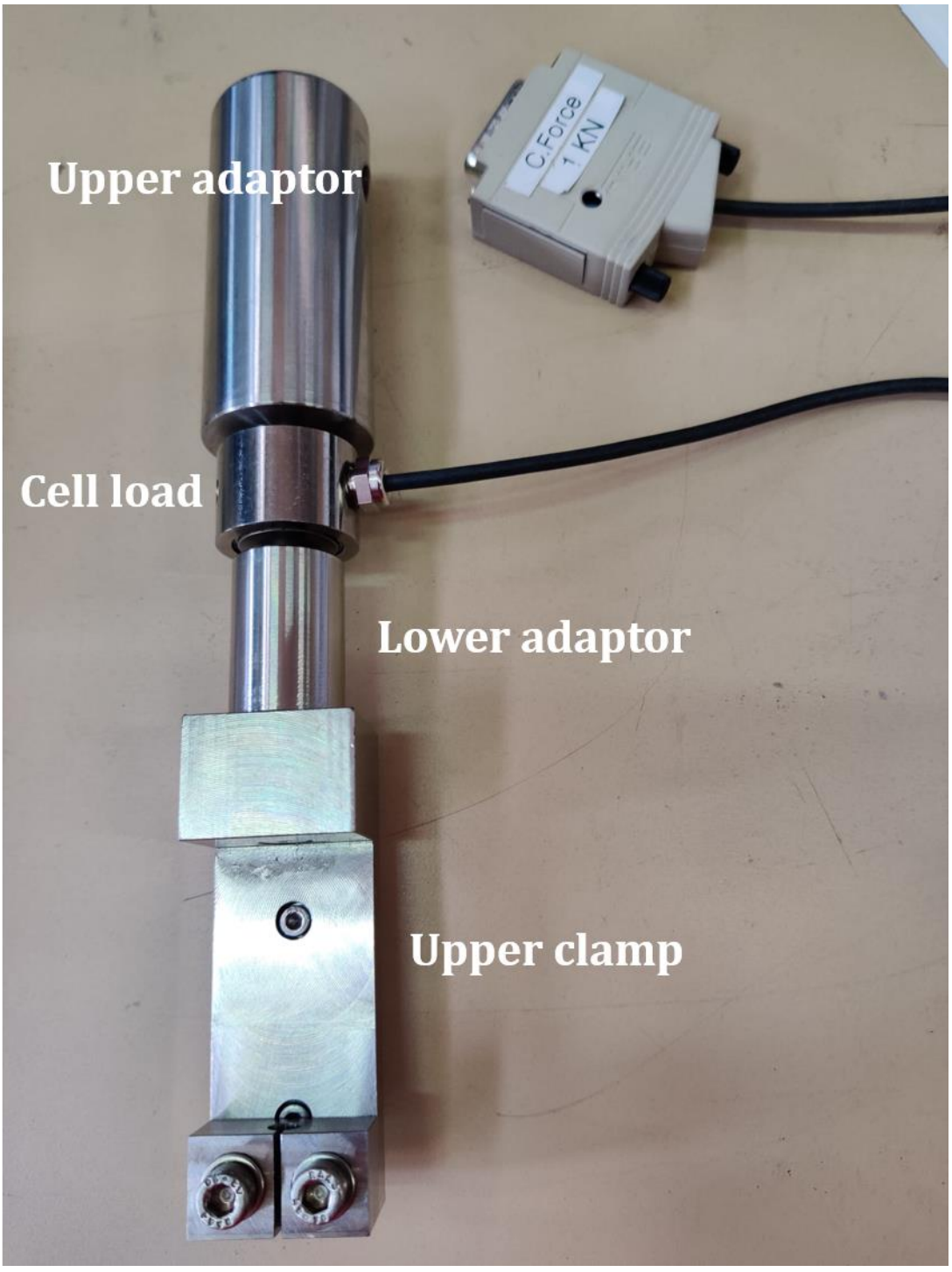

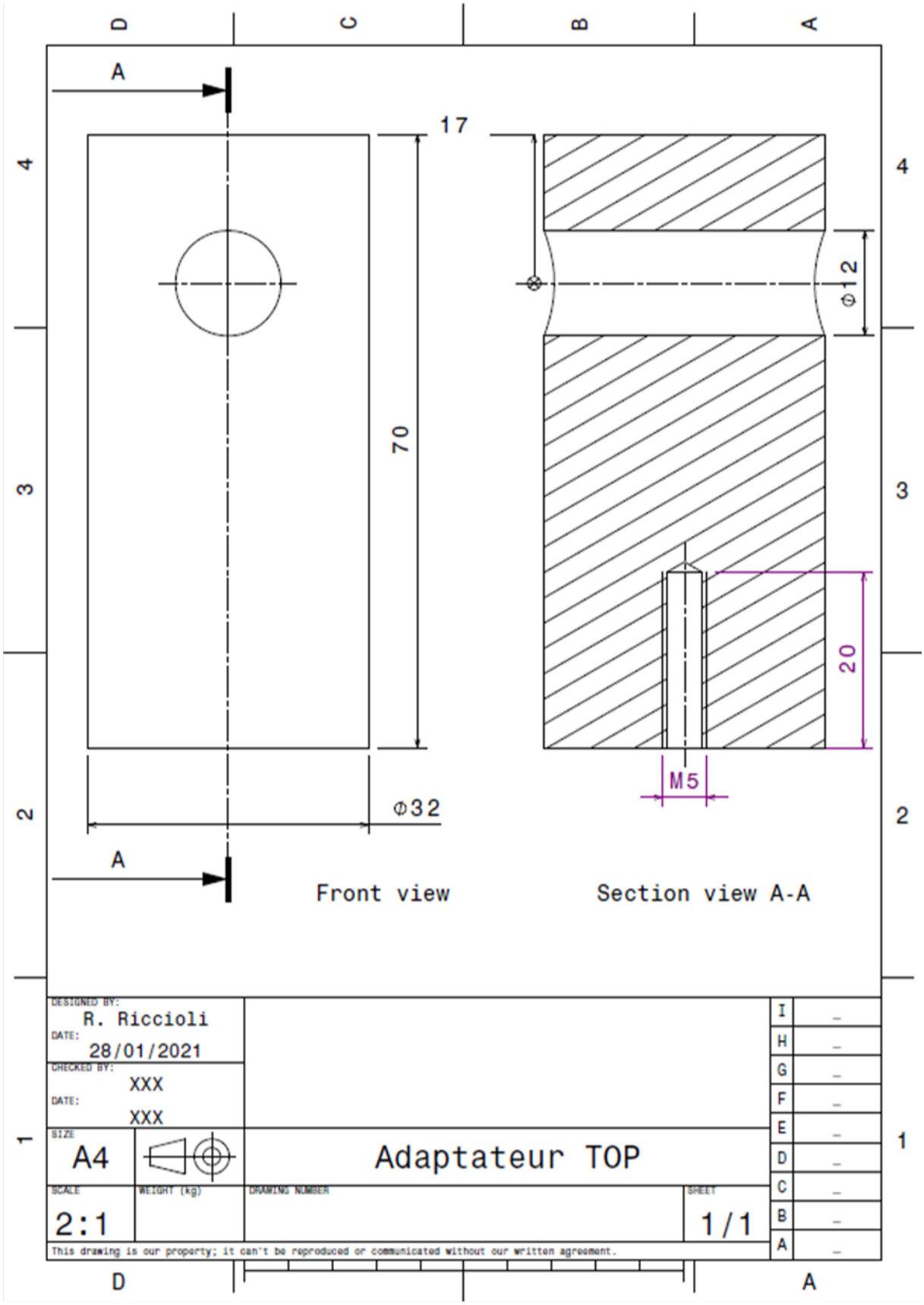
A
17
70
Φ12
20
M5
Φ32
A
Front view
Section view A-A
DESIGNED BY:
R. Riccioli
DATE:
28/01/2021
CHECKED BY:
XXX
DATE:
XXX
SIZE
A4
Adaptateur TOP
SCALE
2:1
WEIGHT (kg)
DRAWING NUMBER
SHEET
1/1
This drawing is our property; it can't be reproduced or communicated without our written agreement.

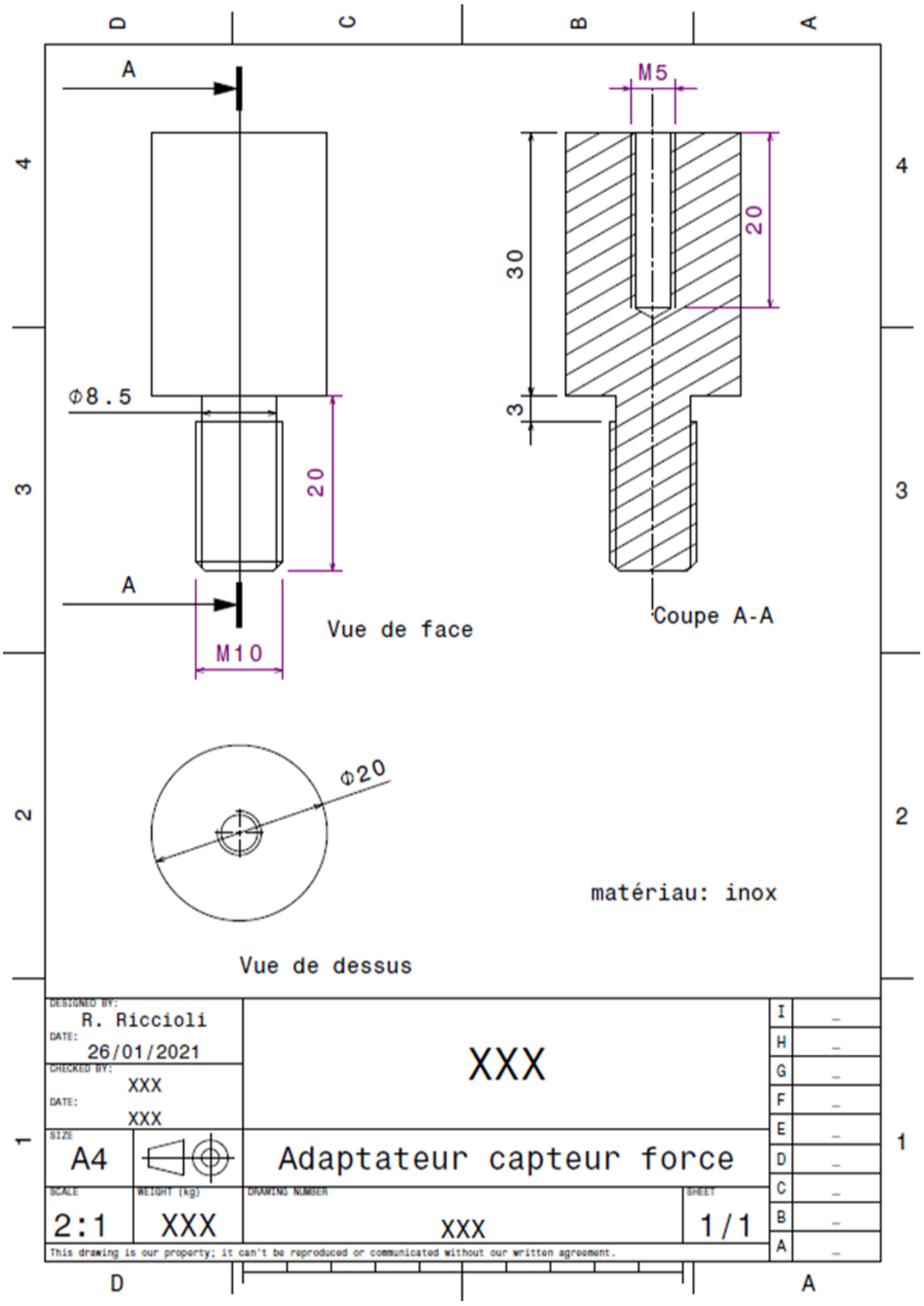
A
M5
30
20
3
ϕ8.5
20
A
M10
Vue de face
Coupe A-A
ϕ20
matériau: inox
Vue de dessus
DESIGNED BY: R. Riccioli
DATE: 26/01/2021
CHECKED BY: XXX
DATE: XXX
XXX
SIZE A4
Adaptateur capteur force
SCALE 2:1
WEIGHT (kg) XXX
DRAWING NUMBER XXX
SHEET 1/1
This drawing is our property; it can't be reproduced or communicated without our written agreement.

BIBLIOGRAPHY

(Bajas 2010) – H. Bajas *et al, Numerical Simulation of the Mechanical Behavior of ITER Cable-In-Conduit Conductors*, IEEE Transactions on Applied Superconductivity, vol. 20, n. 3, (2010), pp. 1467-1470.

(Bajas 2011) – H. Bajas, *Numerical simulation of the mechanical behavior of the ITER cable-in-conduit conductors,* Ph.D. dissertation, (2011).

(Bajas 2012) – H. Bajas *et al, Finite element modelling of cable-in-conduit conductors,* Superconductor Science and Technology, vol. 25, n. 5, (2012).

(Bessette 2014) – D. Bessette, *Design of a Nb3Sn Cable-in-Conduit Conductor to Withstand the 60 000 Electromagnetic Cycles of the ITER Central Solenoid*, IEEE Transactions on applied superconductivity, vol. 24, n. 3, (2014).

(Boso 2013) – D. P. Boso, *A simple and effective approach for thermo-mechanical modelling of composite superconducting wires,* Superconductor Science and Technology, (2013).

(Boutboul 2014) – T. Boutboul *et al*, *Status of the procurement of the European superconductors for the ITER magnets,* IEEE Transactions on Applied Superconductivity, vol. 24, n. 3, (2014).

(Boutboul 2016) – T. Boutboul *et al, European Nb3Sn superconducting strand production and characterization for ITER TF coil conductor*, IEEE Transactions on Applied Superconductivity, vol. 26, n. 4, (2016).

(Breschi 2008) – M. Breschi *et al, Electromagnetic Modeling of the Jacket in Cable-in-Conduit Conductors*, IEEE Transactions on applied superconductivity, vol. 18, n.1, (2008).

(Breschi 2011) – M. Breschi *et al, Evaluation of Effective Strain and n-Value of ITER TF Conductor Samples*, IEEE Transactions on applied superconductivity, vol. 21, n. 3, (2011).

(Breschi 2012a) – M. Breschi *et al, Results of the TF conductor performance qualification samples for the ITER project*, Superconductor Science and Technology, (2012).

(Breschi 2012b) – M. Breschi *et al, Modeling of the electro-mechanical behavior of ITER Nb3Sn cable in conduit conductors*, Superconductor Science and Technology, vol. 25, n. 5, (2012).

(Breschi 2015) – M. Breschi *et al, Electromechanical Modeling of Nb_3Sn Superconducting Wires Subjected to Periodic Bending Strain,* IEEE Transactions on Applied Superconductivity, vol. 25, n. 3, (2015).

(Breschi 2017) – M. Breschi *et al, Performance analysis of the toroidal field ITER production conductors,* Superconductor Science and Technology, (2017).

(Bruzzone 2002) – P. Bruzzone *et al*, *Upgrade of Operating Range for SULTAN Test Facility*, IEEE Transactions on applied superconductivity, vol. 12 n. 1, (2002).

(Calzolaio 2013) – C. Calzolaio *et al*, *Monitoring of the Thermal Strain Distribution in CICCs During the Cyclic Loading Tests in SULTAN,* IEEE Transactions on applied superconductivity, vol. 23 n. 3, (2013).

(Chiletti 2020) – M. Chiletti *et al*, *Void Fraction Influence on CICCs Coupling Losses: Analysis of Experimental Results With MPAS Model*, IEEE Transactions on applied superconductivity, vol. 30 n. 4, (2020).

(Ciazynski 2007) – D. Ciazynski, *Review of Nb_3Sn conductors for ITER*, Fusion Engineering and Design, (2007), pp. 488-497.

(Ciazynski 2010) – D. Ciazynski and A. Torre, Analytical formulae for computing the critical current of an Nb3Sn strand under bending. *Superconductor Science and Technology*, (2010).

(Ciotti 2006) – M. Ciotti *at al*, *THELMA code electromagnetic model of ITER superconducting cables and application to the ENEA stability experiment*, Superconductor Science and Technology, vol. 19, (2006), pp. 987-997.

(Decool 2008) – P. Decool *et al*, *Investigation on Thermal Strain in Full Size ITER Conductors*, IEEE Transactions on Applied Superconductivity, vol. 18, n.2, (2008).

(Desai 2018) – P. R. Desai *et al*, *Effect of slenderness ratio on Euler critical load for elastic columns with ANSYS,* Journal of Engineering Research and Application, (2018), pp. 40-43.

(Devred 2012) – A. Devred *et al*, *Status of ITER conductor developement and production*, IEEE Transactions on Applied Superconductivity, vol. 22, n.3, (2012).

(Devred 2014) – A. Devred *et al*, *Challanges and status of ITER conductor production*, Superconductor science and technology, (2014).

(Devred 2017) – A. Devred, *Superconductors & Magnets for ITER: 10 years summary,* ITER Organization, Presentation for CEA-Cadarache, (2017).

(Du 2021) – W. Du *et al*, *Establishment of 3D multistage models of superconducting cable based on discrete element method,* Superconductor Science and Technology, (2021).

(Durville 1998) – D. Durville, *Modélisation du comportement mécanique de câbles métalliques,* Revue européenne des éléments finis, *7*, pp. 9-22, (1998).

(Dylla 2016) – M. T. Dylla *et al*, *Fracture Strength Distribution of Individual Nb_3Sn Filaments*, IEEE Transactions on Applied Superconductivity, vol. 26, n. 8, (2016).

(Evans 2018) – L. Evans, *The Large Hadron Collider: a marvel of technology,* EPFL press, Lausanne, (2018).

(Gao 2019) – Z. Gao *et al*, *Study on the effective Young's moduli of CICC strand with multi-stage structures*, Fusion Engineering and Design, (2019), pp. 66-77.

(Gao 2020) – Z. Gao *et al*, *Contact behavior and tensile stiffness in CICC with CWS design*, Fusion Engineering and Design, (2020).

(Giannini 2021) – L. Giannini *et al*, *Design Studies, Magnetic Calculations and Structural Assessment For the DTT Central Solenoid*, IEEE Transactions on Applied Superconductivity, vol. 31, n. 5, (2021).

(Green Albert Edward Naghdi 1974) – P. M. Green Albert Edward Naghdi *et al*, *On the theory of rods. I. Derivations from the three-dimensional equations,* Proceedings of the Royal Society of London. Series A, Mathematical and Physical Sciences, vol. *337*, (1974), pp. 451-483.

(Ham 2020) – C. Ham *et al, Filamentary plasma eruptions and their control on the route to fusion energy,* Nature reviews physics 2, (2020), pp. 159-167.

(Hemmi 2012) – T. Hemmi *et al*, *Test Results and Investigation of Tcs Degradation in Japanese ITER CS Conductor Samples,* IEEE Transactions on Applied Superconductivity, vol. 22, n. 3, (2012).

(Hillairet 2021) – J. Hillairet *et al*, *Tokamak Dimensioning*, (Last update 2021).

(IEC/CEI 61788-19 2013) – IEC/CEI 61788-19, *Superconductivity - Part 19: Mechanical properties measurement - Room temperature tensile test of reacted Nb_3Sn composite superconductors.* Geneve, (2013).

(Ilyin 2006) – Y. Ilyin *et al*, *Axial Tensile Stress-Strain Characterization of a 36 Nb_3Sn Strands Cable,* IEEE Transactions on Applied Superconductivity, vol. 16, n. 2, (2006).

(Ilyin 2007) – Y. Ilyin *et al*, *Scaling law for the strain dependence of the critical current in an advanced ITER Nb_3Sn strand,* Superconductor science and technology, vol. 20, n. 3, (2007), pp. 187-191.

(ITER Organization web site) – *iter.org*.

(ITER Organization 2005) – ITER Organization, *DRG1 annex - Superconducting Material Database - Art 5. Thermal, Electrical and Mechanical properties of materials at cryogenic temperatures,* Technical report, (2005).

(ITER Organization 2008) – ITER Organization, *Annex B - ITER TF Conductor Procurement Package 1.1P6A,* Technical report, (2008).

(ITER Organization 2015) – ITER Organization, *Parameter table of the TFEU13 Sultan sample - internal use,* Technical report, (2015).

(Jha 2009) – A. L. Jha *et al*, Single-crystalline superconducting MgB_2 nanowires. *Superconductor Science and Technology*, (2009).

(Khachan) – J. Khachan *et al*, http://www.physics.usyd.edu.au, *School of Physics.*

(Lee 2018) – P. J. Lee *et al*, https://nationalmaglab.org/magnet-development/applied-superconductivity-center/plots, *National High Magnetic FIeld Laboratory - Applied Superconductivty Center*, (2018).

(Lenoir 2017) – G. Lenoir, *Caractérisation et modélisation du comportement mécanique de matériaux supraconducteurs,* Ph.D. dissertation, (2017).

(Lenoir 2019) – G. Lenoir *et al*, *Mechanical Behavior Laws for Multiscale Numerical Model of Nb_3Sn Conductors*, IEEE Transactions on Applied Superconductivity, vol. 29, n. 5, (2019).

(Li 2013) – Y. X. Li *et al*, *Modeling for mechanical response of CICC by hierarchical approach and ABAQUS simulation*, Fusion Engineering and Design, (2013).

(Mitchell 2002) – N. Mitchell, *Analysis of the effect of Nb_3Sn strand bending on CICC superconductor performance*, Cryogenics, (2012), pp. 311-325.

(Mitchell 2003) – N. Mitchell, *Summary, assessment and implications of the ITER model coil test results,* Fusion Engineering and Design, (2003), pp. 971-993.

(Mitchell 2005a) – N. Mitchell, *Operating strain effects in Nb3Sn cable-in-conduit conductors*, Superconductor Science and Technology, (2005), pp. S396-S404.

(Mitchell 2005b) – N. Mitchell, *Finite element simulations of elasto-plastic processes in Nb_3Sn strands*, Cryogenics, (2005), pp. 501-515.

(Mitchell 2005c) – N. Mitchell, *Modeling of the Effect of Nb_3Sn Strand Composition on Thermal Strains and Superconducting Performance,* IEEE Transactions on Applied Superconductivity, vol. 15, n. 2, (2005).

(Mitchell 2008) – N. Mitchell, *The ITER magnet system,* IEEE Transactions on Applied Superconductivity, vol. 18, n. 2, (2008).

(Mitchell 2017) – N. Mitchell *et al*, *The ITER magnet system: configuration and construction status*, Fusion Engineering and Design, (2017), pp. 17-25.

(Mitchell 2020) – N. Mitchell *et al*, *The use of Nb_3Sn in fusion: lessons learned from the ITER production including options for management of performance degradation*, Superconductor Science and Technology, (2020).

(Miyagi 2012) – D. Miyagi *et al*, *Analysis of 3-D Locations of All Strands in CIC Conductor*, IEEE Transactions on Applied Superconductivity, vol. 22, n. 3, (2012).

(Miyoshi 2009) – Y. Miyoshi *et al*, *Distinct voltage-current characteristics of Nb_3Sn strands with dispersed and collective crack distributions*, Superconductor Science and Technology, (2009).

(Nijhuis 2006) – A. Nijhuis *et al*, *Transverse load optimization in Nb_3Sn CICC design; influence of cabling, void fraction and strand stiffness*, Superconductor Science and Technology, (2006), pp. 945-962.

(Nijhuis 2004) – A. Nijhuis *et al*, *Change of interstrand contact resistance and coupling loss in various prototype ITER NbTi conductors with transverse loading in the Twente Cryogenic Cable Press up to 40,000 cycles*, Cryogenics, (2004), pp. 319-339.

(Nijhuis 2005) – A. Nijhuis *et al*, *Impact of Void Fraction on Mechanical Properties and Evolution of Coupling Loss in ITER Nb_3Sn Conductors Under Cyclic Loading*, IEEE Transactions on Applied Superconductivity, vol. 15, n. 2, (2005).

(Nijhuis 2008) – A. Nijhuis, *A solution for transverse load degradation in ITER Nb_3Sn CICCs: verification of cabling effect on Lorentz force response*, Superconductor Science and Technology, vol. 21, (2008).

(Nijhuis 2014) – A. Nijhuis, *TARSIS and Pacman Ic(strain) tests on second sample of OST G 01EX0571A01C TF Nb3Sn strand,* University of Twente report, (2014).

(Nyilas 2005) – A. Nyilas *et al*, *Strain sensing systems tailored for tensile measurement of fragile wires*, Superconductor Science and Technology, (2005).

(Osamura 2008) – K. Osamura *et al*, *International round robin test for mechanical properties of Nb_3Sn superconductive wires at room temperature,* Superconductor Science and Technology, vol. 21, (2008).

(Qin 2010) – J. Qin *et al*, *A 3D numerical model study for superconducting cable pattern*, Fusion Engineering and Design, (2010), pp. 109-114.

(Qin 2011) – J. Qin *et al*, *A novel numerical mechanical model for the stress–strain distribution in superconducting cable-in-conduit conductors,* Superconductor Science and Technology, (2011).

(Riccioli 2019) – R. Riccioli *et al*, *Mechanical Modeling and First Case Study on ITER TF CICC Loading Cases With Upgraded Finite Element Code Simulations*, IEEE Transactions on Applied Superconductivity, vol. 29, n. 5, (2019).

(Riccioli 2020) – R. Riccioli *et al*, *Advanced modeling of electromagnetic loading of cable-in-conduit conductors for fusion magnets*, IEEE Transactions on Applied Superconductivity, vol. 30, n. 4, (2020).

(Riccioli 2021) – R. Riccioli *et al*, *Study of the ITER TF CICC Mechanical Behavior Under Cool-Down and Repetitive EM Loadings*, IEEE Transactions on Applied Superconductivity, vol. 31, n. 5, (2021).

(Sanabria 2012) – C. Sanabria *et al*, *Evidence that filament fracture occurs in an ITER toroidal field conductor after cyclic Lorentz force loading in SULTAN*, Superconductor Science and Technology, (2012).

(Sanabria 2016) – C. Sanabria *et al*, *Metallographic autopsies of full-scale ITER prototype cable-in-conduit conductors after full cyclic testing in SULTAN: III. The importance of strand surface roughness in long twist pitch conductors,* Superconductor Science and Technology, vol. 29, (2016).

(Sanabria 2017) – C. Sanabria, *A new understanding of the ehat treatment of Nb-Sn superconducting wires,* PhD dissertation, (2017).

(Sheth 2011) – M. K. Sheth, *Fatigue Behavior of Nb#Sn Composite Strands Used for Iter Magnets.* Ph.D. dissertation, (2011).

(Shibata 2011) – H. Shibata, *Superconducting single-proton detectors*, NTT Technical Review, (2011).

(Tixador 1995) – P. Tixador, *Les supraconducteurs,* HERMES, Paris, (1995).

(Torre 2011) – A. Torre *et al*, *Mechanical-Electrical Modeling of Stretching Experiment on 45 Nb_3Sn Strands CICCs*, IEEE Transactions on Applied Superconductivity, vol. 21, n. 3, (2011), pp. 2042-2045.

(Torre 2013) – A. Torre *et al, Coupled Mechanical-Electrical Modeling of the TARSIS Experiment*, IEEE Transactions on Applied Superconductivity, vol. 23, n. 3, (2013).

(Torre 2014) – A. Torre *et al, Mechanical and Electrical Modeling of Strands in Two ITER CS Cable Designs*, IEEE Transactions on Applied Superconductivity, vol. 24, n. 3, (2014).

(Van den Eijnden 2005) – N. C. Van den Eijnden *et al*, *Axial tensile stress–strain characterization of ITER model coil type Nb_3Sn strands in TARSIS*, Superconductor Science and Technology, (2005).

(Wang 2016) – X. Wang *et al*, *Mechanical behaviors of multi-filament twist superconducting strand under tensile and cyclic loading*, Cryogenics, vol. 73, (2016), pp. 14-24.

(Wilson 1983) – M. N. Wilson, *Superconducting Magnets,* Oxford Science Publications, (1983).

(Xue 2020) – S. Xue *et al*, *The effect of strain and filament fracture on the transport properties of ITER cable-in-conduit conductors,* AIP Advances, (2020).

(Yagotintsev 2019) – K. A. Yagotintsev *et al*, *Overview of verification tests on AC loss, contact resistance and mechanical properties of ITER conductors with transverse loading up to 30 000 cycles,* Superconductor Science and Technology, vol. 32, (2019).

(Yoshida 2010) – K. Yoshida *et al*, *Design and Construction of JT-60SA Superconducting Magnet System*, J. Plasma Fusion Research, (2010).

(Yue 2018) – D. Yue *et al*, *Theoretical analysis for the mechanical behavior caused by an electromagnetic cycle in ITER Nb_3Sn cable-in-conduit conductors,* Acta Mechanica Sinica, (2018), pp. 614-622.

(Zani 2021) – L. Zani *et al*, *Extensive Analyses of Superconducting Cables 3D Geometry With Advanced Tomographic Examinations,* IEEE Transactions on Applied Superconductivity, vol. 31, n. 5, (2021).